

Laser Spectroscopic Techniques and Related Instrumentation for Studies on Lanthanides and Actinides

By

Mukesh Lal Shah

(Enrolment No PHYS01201104004)

Bhabha Atomic Research Centre, Mumbai-400085

India

A thesis submitted to the Board of Studies in Physical Sciences

In partial fulfillment of requirements

For the Degree of

DOCTOR OF PHILOSOPHY

of

HOMI BHABHA NATIONAL INSTITUTE



February, 2016

Homi Bhabha National Institute

Recommendations of the Viva Voce Committee

As members of the Viva Voce Committee, we certify that we have read the dissertation prepared by Mukesh Lal Shah entitled "Laser Spectroscopic Techniques and Related Instrumentation for Studies on Lanthanides and Actinides" and recommend that it may be accepted as fulfilling the thesis requirement for the award of Degree of Doctor of Philosophy.

Chairman- Dr N K Sahoo




Date: 15/2/2016

Guide/Convener- Dr K G Manohar



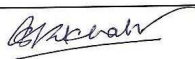
Date: 15/02/2016

Member 1- Dr S Dixit



Date: 15/2/16

Member 2- Dr S G Nakhate



Date: 15/02/2016

External examiner- Dr A K Rai



Date: 15/02/2016

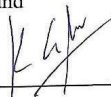
Final approval and acceptance of this dissertation is contingent upon the candidate's submission of the final copies of the dissertation to HBNI.

I hereby certify that I have read this dissertation prepared under my direction and recommend that it may be accepted as fulfilling the dissertation requirement.

Date 15/02/2016

Place BARC/Trombay

Guide



Dr K G Manohar

STATEMENT BY AUTHOR

This dissertation has been submitted in partial fulfillment of requirements for an advanced degree at Homi Bhabha National Institute (HBNI) and is deposited in the Library to be made available to borrowers under rules of the HBNI.

Brief quotations from this dissertation are allowable without special permission, provided that accurate acknowledgement of source is made. Requests for permission for extended quotation from or reproduction of this manuscript in whole or in part may be granted by the Competent Authority of HBNI when in his or her judgment the proposed use of the material is in the interests of scholarship. In all other instances, however, permission must be obtained from the author.



(Mukesh Lal Shah)

DECLARATION

I, hereby, declare that the investigation presented in the thesis has been carried out by me. The work is original and has not been submitted earlier as a whole or in part for a degree/diploma at this or any other Institution /University.

A handwritten signature in blue ink, appearing to read 'mshah', is written over a horizontal line.

(Mukesh Lal Shah)

List of Publications

List of publications through Journals

1. "Spectroscopic measurements of plasma temperatures and electron number density in a uranium hollow cathode discharge lamp", M L Shah, B M Suri and G P Gupta, *Eur. Phys. J. D* **69**, 16 [2015]
2. "Investigations of high-lying even-parity energy levels of atomic samarium using simultaneous observation of two-color laser-induced fluorescence and photoionization signals", M L Shah, A C Sahoo, A K Pulhani, G P Gupta, B M Suri and Vas Dev, *Eur. Phys. J. D* **68**, 235 [2014]
3. "Homogeneity testing and quantitative analysis of manganese (Mn) in vitrified Mn-doped glasses by laser-induced breakdown spectroscopy (LIBS)", V. K. Unnikrishnan, R Nayak, V B Kartha, C Santhosh, M S Sonavane, R G Yeotikar, M L Shah, G P Gupta, and B M Suri, *AIP Advances*, **4**, 097104 [2014]
4. "Measurements of excited-state-to-excited-state transition probabilities and photoionization cross-sections using laser-induced fluorescence and photoionization signals", M L Shah, A C Sahoo, A K Pulhani, G P Gupta, B Dikshit, M S Bhatia, B M Suri, *J. Quant. Spectros. & Rad. Transfer*, **142**, 9-16, [2014]
5. "Measurement of radiative lifetime in atomic samarium using simultaneous detection of laser-induced fluorescence and photoionization signals", A C Sahoo, M L Shah, P K Mandal, A K Pulhani, G P Gupta, Vas dev, B M Suri, *Pranama, Journal of Physics*, **82**, 403-408, [2014]

6. "Quantitative elemental analysis of steel using calibration-free laser-induced breakdown spectroscopy", M L Shah, A K Pulhani, G P Gupta, B M Suri, *Applied Optics*, **51**, 4612-4621, [2012]
7. "Study of even-parity autoionization resonances of atomic uranium by three-color optogalvanic spectroscopy", M. L. Shah, P. K. Mandal, Vas Dev, and B. M. Suri, *J. Opt. Soc. Am. B*, **29**, 1625-1630, [2012]
8. "Measurement of photoionization cross-section in atomic uranium using simultaneous observation of laser-induced photoionization and fluorescence signals", M L Shah, G P Gupta, Vas Dev, B Dikshit, M S Bhatia, B M Suri, *J. Opt. Soc. Am. B* **29**, 600-606, [2012]
9. "Measurements of radiative lifetime of high-lying odd parity energy levels of U I", R.C. Das, P.K. Mandal, M.L. Shah, A.U. Seema, D.R. Rathod, Vas Dev, K.G. Manohar, B.M. Suri, *J. Quant. Spectros. & Rad. Transfer* **113**, 382-386, [2012]
10. "Measurements of radiative lifetimes, branching fractions, and absolute transition probabilities in atomic samarium using laser-induced fluorescence", M. L. Shah, A. K. Pulhani, G P Gupta and B. M. Suri, *J. Opt. Soc. Am B*, **27**, 423-431, [2010]
11. "Measurement of photoexcitation cross-section of uranium by saturation method", M L Shah, R C Das, P K Mandal, D R Rathod, Vas Dev, K G Manohar and B M Suri, *Pramana - Journal of Physics* **75**, 1141-44, [2010]
12. "Measurement of total angular momentum values of high-lying even-parity atomic states of samarium by spectrally resolved laser-induced fluorescence technique", A K Pulhani, M L Shah, G P Gupta and B M Suri, *Pramana - Journal of Physics* **75**, 1135-40, [2010]

List of publication through Book

1. M L Shah, A K Pulhani, G P Gupta, B M Suri “Laser spectroscopy for nuclear applications”, Chapter 3, Spectroscopic techniques for security, forensic and environmental applications edited by Y Dwivedi, S B Rai, J P Singh, Nova publishers, New York, USA, [2014]

List of publications through BARC News Letter

1. “Simultaneous observation of laser-induced photoionization and fluorescence signals in atomic uranium”, M L Shah, G P Gupta, Vas Dev, B Dikshit, M S Bhatia, B M Suri, Founder's day special issue, BARC News Letter , Issue No 314, 287-290, [2013]
2. “Measurement of total angular momentum values of high-lying even-parity atomic states of samarium by spectrally resolved laser-induced fluorescence technique”, A K Pulhani, M L Shah, G P Gupta and B M Suri, Founder's day special issue, BARC News Letter, Issue No 311, 300-303 [2010]
3. “Studies on linearity in indigenously developed reflectron time of flight mass spectrometer for atomic spectroscopy”, R. C. Das, M. L. Shah, D. R. Rathod, P K Mandal, Vas Dev, K. G. Manohar and B. M. Suri, Founder's day special issue, BARC News Letter, Issue No 311, 278-281, [2010]

List of publications through Symposia

1. “Measurement of radiative lifetime in atomic samarium using simultaneous detection of laser –induced fluorescence and photoionization signals”, A C Sahoo, M L Shah, P K Mandal, A K Pulhani, G P Gupta, Vas Dev, B M Suri, Proceedings of 21st DAE-BRNS National Laser Symposium (NLS-21), BARC, Mumbai, Feb. 6- 9 [2013]

2. “Simultaneous observation of laser-induced photoionization and fluorescence signals”, M. L. Shah, G. P. Gupta, Vas Dev, B. Dikshit, M. S. Bhatia and B. M. Suri, Proceedings of National Laser Symposium (NLS-20), 9-12 Jan 2012, Anna, University, Chennai [2012]

(This paper was adjudged as best paper).

3. “Time-resolved measurements of electron density and temperature in laser produced steel plasma using emission spectroscopy”, G. P. Gupta, M. L. Shah, A. K. Pulhani, B. M. Suri, Proceedings of 26th National symposium on plasma science and technology (Plasma 2011), Birla Institute of Technology Mesra, Patna campus 20-23 Dec. [2011]

4. “A New Technique for Atomic Parameter Measurement in Resonance Ionization Mass Spectrometry: Applications to Lifetimes of U I Energy Levels”, R. C. Das, P. K. Mandal, M. L. Shah, D. R. Rathod, Vas Dev, K. G. Manohar and B. M. Suri, Proceedings of ISMAS International Discussion Meet on Elemental Mass Spectrometry in Health and Environmental Sciences, 114-117 [2011]

5. “Measurement of photo excitation cross-sections of excited state to excited state transition of uranium by saturation method”, P K Mandal, M L Shah, R C Das, Vas Dev,

K G Manohar, B M Suri, Proceedings of DAE-BRNS National Laser Symposium-NLS-19, RRCAT, Indore, December 1- 4 [2010].

6.“Lifetime Measurements of Uranium Energy Levels in A Resonance Ionization Mass Spectrometry Setup”, R. C. Das, M. L. Shah, P. K. Mandal, D. R. Rathod, Vas Dev, K. G. Manohar and B. M. Suri, Proceedings of DAE-BRNS National Laser Symposium-NLS-09, BARC, Mumbai, January 13- 16 [2010]

7.“Isotope selective excitation of atoms in an indigenously developed reflectron time-of-flight mass spectrometer based resonance ionization mass spectrometry setup”, R. C. Das, M. L. Shah, D. R. Rathod, Vas Dev, K. G. Manohar and B. M. Suri; Proceedings of Ninth DAE-BRNS National Laser Symposium-NLS-09, BARC, Mumbai, January 13- 16 [2010]

8.“Measurement of total angular momentum values of high-lying even-parity atomic states of samarium by spectrally resolved laser-induced-fluorescence technique”, A. K. Pulhani, M. L. Shah, G. P. Gupta, B. M. Suri, Proceedings of Ninth DAE-BRNS National Laser Symposium-NLS-09, BARC, Mumbai, January 13- 16 [2010]

(This paper was awarded as best paper).

9.“Measurement of photo excitation cross-sections of uranium by saturation method” M. L. Shah, R. C. Das, P. Mandal, D. R. Rathod, Vas Dev, K. G. Manohar and B. M. Suri; Proceedings of Ninth DAE-BRNS National Laser Symposium-NLS-09, BARC, Mumbai, January 13- 16 [2010]

To my Father for his

Blessings,

Love

&

Everything.....

Acknowledgements

I would like to thank my guide Dr K G Manohar for his able guidance, constructive comments and wonderful support throughout the course of this work.

I would like to express my sincere appreciation towards Dr. B. M. Suri, for introducing me to the inspiring, fascinating and ingenious field of laser spectroscopy. His excellent knowledge about the subject, literature and advanced instrumentation provided me the right platform for the present work.

I would like to thank my Doctoral Committee for their reviews and suggestions, which helped me a lot in improving the quality and quantity of the thesis.

I am very grateful to Dr. G. P. Gupta for his untiring support during experimental and theoretical work. This work would not have been possible without his excellent theoretical and analytical skills. I am thankful to him for his support during the preparation of the communicated research manuscripts and the thesis. I am indebted to him for the moral support he has extended during the entire work.

I am sincerely obliged to Dr Vas Dev for his kind support and encouragement. I feel fortunate to have worked with him. I am thankful to him for teaching me the experimental basics and tricks regarding laser spectroscopy. I sincerely acknowledge him for fruitful scientific discussions.

I am grateful to Dr A K Pulhani for his sustained cooperation and useful scientific discussions during the entire work. His dissertation provided the foundation for the current work and made the task easy for me.

I sincerely thank Dr N. K. Sahoo for his continuous support and encouragement. I am also thankful to him and his Division for designing and developing many optical components, which were not commercially available. It would have been difficult to conduct experiments without his timely help.

I sincerely thank Dr A. K. Mohanty and Dr S. Basu, Former and Present Dean Academic, Physical and Mathematical Sciences, Homi Bhabha National Institute, Mumbai, for their timely support and encouragement.

I am thankful to Shri A. C. Sahoo and Shri P. K. Mandal for their support in conducting experiments. I am also thankful to Shri G. Zende for his support in preparation of the hollow cathode discharge lamp. I am thankful to Smt B. Sodhi and Smt S. Uparkar for their support.

My special thanks are due to Dr L. M. Gantayet, Dr A. K. Das, Dr. K. Dasgupta, Dr. D. J. Biawas, for their support and encouragement during the course of this work. I am also thankful to Dr. S. K. Sarkar, Dr. P. N. Bajaj, Dr. M. S. Bhatia, Dr. S. Sinha, Dr. A. K. Nayak, Dr G. K. Bhowmick, Dr. A. K. Ray, Dr. S. Kumar, Dr. K. Patel, Dr. S. Thakur and other senior colleagues of my institute for stimulating and fruitful discussions, timely suggestions and encouragement.

I am thankful to my friends, Dr. V. S. Rawat, Dr. R Bhatt, Dr. R. C. Das, Dr. B. Dikshit, Dr. G. K. Sahu, Dr. S. Pradhan, Dr. S. Baruah, Dr. B. Jana, Mr. A.K. Tak, Mr. A. Majumder, Mr. T. B. Pal, Mr N. Kawade, Mr. S. Rao, Mr. J. Thomas, and Mr. A. Ghosh, for their generous support and cooperation.

I am always grateful to my father for his everlasting blessings for me, which always made things easy. It would not have been possible without his encouragement and

support. I am indebted to my mother for her best wishes. She has always been a stress reliever for me. I am thankful to my mother-in-law for the encouragement and support.

I am very thankful to my wife Richa for her patience, care and wishes, which helped me in completing the Ph. D thesis.

Finally, I would like to convey my thanks to my elder brother, bhabhiji, sisters, jijaji and their children, for the moral support they have provided to me. I am also thankful to Richesh for his co-operation.

Last but not the least, I am thankful to all of those who helped me directly or indirectly in this work but could not find a specific mention.

Contents

Title	Page No
Synopsis	i
List of Figures	xi
List of Tables	xv
Chapter 1: Introduction	1
1.0 Introduction to Spectroscopy	1
1.1 Spectroscopy of atoms	3
1.1.1 Atomic Spectroscopy of Lanthanides and Actinides	5
1.1.2 Atomic Spectroscopic Techniques for Lanthanides and Actinides	6
1.2 Laser Spectroscopy of atoms	7
1.3 Laser Spectroscopic Techniques for Studying Atoms	9
1.3.1 Atomic Spectroscopy using Multi-Mode Lasers	10
1.4 Motivation and description of Present Work	11
Chapter 2: Laser- induced photoionization and fluorescence techniques	17
2.1 Laser-induced photoionization	17
2.1.1 Atomic spectroscopy of uranium	18
2.1.2 Present work using laser-induced photoionization	20
2.1.2.1 Measurement of radiative lifetime of atomic uranium by LIP	20
2.1.2.1.1 Experimental setup for measurement of radiative lifetime	21

2.1.2.1.2	Results and discussion	22
2.2	Laser-induced fluorescence	23
2.2.1	Atomic spectroscopy of samarium	24
2.2.2	Present work using laser-induced fluorescence	25
2.2.2.1	Experimental setup and development of spectrometer	27
2.2.2.2	Results and discussion	31
2.2.2.2.1	Radiative lifetimes of odd-parity and even-parity energy levels	32
2.2.2.2.2	Excited-level-to-ground-level transition probabilities	33
2.2.2.2.3	Excited-level-to-excited-level transition probabilities	33
2.2.2.2.4	Assignment of J-values	34
2.2.2.3	Systematic uncertainties in the measurements	34
2.3	Simultaneous laser-induced fluorescence and photoionization signals	37
2.3.1	Experimental details	38
2.3.2	Methodology	38
2.3.3	Results and discussion	41
Chapter 3:	Theoretical analysis of simultaneous laser-induced fluorescence and photoionization signals using density matrix formalism	66
3.1	Density matrix equations for interaction of laser light with two-level atom system	68
3.2	Density matrix equations for interaction of laser light with an open three-level atom system	79
3.3	Density matrix equations for interaction of laser light with real atomic	

beam system	81
3.4 Simultaneous observation of laser-induced photoionization and fluorescence signals in atomic uranium	82
3.4.1 Experimental details	85
3.4.2 Theoretical analysis using density matrix (DM) formalism	86
3.4.3 Results obtained after analysis of experiments	92
3.5 Simultaneous observation of laser-induced photoionization and fluorescence signals in atomic samarium	95
3.5.1 Experimental details	96
3.5.2 Theoretical analysis using density matrix (DM) formalism	97
3.5.3 Results obtained after analysis of experiments	98
3.6 Conclusions	101
Chapter 4: Laser optogalvanic spectroscopy technique	117
4.1 Spectroscopic measurements of plasma temperatures and electron number density in a uranium hollow cathode discharge lamp	118
4.1.1 Experimental details	120
4.1.2 Theory	122
4.1.2.1 Temperature of neutral species	122
4.1.2.2 Atomic excitation temperature	123
4.1.2.3 Electron number density	124
4.1.2.4 Condition for Local Thermodynamic Equilibrium (LTE)	
Plasma	124
4.1.3 Results and discussions	125

4.1.3.1	Emission spectrum	125
4.1.3.2	Temperature of neutral species	125
4.1.3.3	Atomic excitation temperature	127
4.1.3.4	Electron number density	127
4.1.3.5	LTE condition	128
4.1.4	Conclusion	128
4.2	Study of even-parity autoionization resonances of atomic uranium by three- color optogalvanic spectroscopy	129
4.2.1	Introduction	129
4.2.2	Experimental details	132
4.2.3	Results and discussions	133
4.3	Conclusions	137
Chapter 5: Laser-induced breakdown spectroscopy		154
5.1	Introduction	154
5.2	Experimental setup	162
5.3	Plasma characterization	165
5.3.1	Determination of plasma temperature	165
5.3.2	Determination of electron number density n_e	166
5.3.3	Determination of density ratio of the species of a particular element	167
5.3.4	Determination of density ratio of the species of different Elements	167
5.3.5	Criterion for optically thin and LTE plasma	167

5.4	Quantitative elemental analysis	168
5.5	Results and discussion	171
5.5.1	Emission spectra	171
5.5.2	Time delay for optically thin and LTE plasma	172
5.5.3	Plasma temperature	173
5.5.4	Electron number density	174
5.5.5	Density ratios of the species of particular and different Elements	174
5.5.6	Quantitative elemental analysis	175
5.6	Conclusions	176
	Summary and future scope of work	185
	References	187
	Chapter 1	187
	Chapter 2	190
	Chapter 3	200
	Chapter 4	204
	Chapter 5	209

Synopsis

Spectroscopy is the study of the interaction of electromagnetic radiation with matter. Spectroscopy is a sufficiently broad field covering many sub-disciplines, each with numerous implementations of specific spectroscopic techniques. Various techniques and their implementations can be classified in several ways. Types of spectroscopy can be distinguished by the nature of the interaction between the energy and the mater. The interaction of electromagnetic radiation or light with the matter leads to absorption, emission and scattering of radiation. The radiation matter interaction may change the impedance or couple the quantum states of the mater. Spectroscopy is also a scientific measurement technique. It measures light that is emitted, absorbed, or scattered by materials and can be used to study, identify and quantify materials because the spectrum of a substance is as unique to that substance as a fingerprint to a human being. It has made significant impact on various fields of basic and applied sciences, and also led to several technological advances. The spectral data recorded in spectroscopic measurements help us in understanding the energy level structure of atoms and molecules, as well as their atomic and molecular properties. The quantitative values of these properties provide detailed information about shape, flexibility and electronic arrangement in atoms and molecules. Thus, spectroscopy has emerged as a very powerful tool for atomic and molecular structure studies. It has contributed a lot to our understanding of the universe-our earth, atmosphere, sun, interstellar space and distant stars, which used to be treated as mystery or supernatural phenomenon few centuries back.

The absorption and emission spectroscopic techniques were used earlier for studying atomic spectra. These techniques have their own limitations in terms of studying high-lying excited states of atoms. The absorption cross-sections happen to be smaller as one move up in the energy level ladder, so the detection of these high-lying states becomes difficult. The excited states, which have the same parity as that of a ground state, become inaccessible due to the selection rules. Moreover, one has to use complex vacuum-ultraviolet spectrometers, if the spectra lie in the vacuum-ultraviolet region. Earlier, the typical emission/absorption sources used for studying various elements were hollow cathode discharge lamps, electrodeless discharge lamps, flames and plasmas. These atom sources contain species, such as excited atoms, ions and multi-atomic species in a variety of states. This puts a stringent requirement on spectrometers' resolution. The assignment of atomic states also becomes complex because many excited high-lying states decay to low-lying states. So, it is very difficult to get complete spectroscopic information by conventional sources and techniques.

The invention and subsequent development of the laser has revolutionized the spectroscopy and opened many new branches of spectroscopy. The wavelength tunability, high intensity, narrow spectral width and low divergence of lasers have not only simplified the resulting spectra but also made those experiments possible, which could not be done before due to the lack of intensity or insufficient resolution. Comparing the conventional source to a tunable laser source, the power per unit wavelength of the tunable laser is much greater than that of the white-light source, thus allowing easier detection. This increase in power density with lasers leads to an increase in

sensitivity of many orders of magnitude as compared to that of conventional sources.

The lanthanides and actinides are used in many areas of science and technology, including nuclear power programs, high temperature superconductivity, communication and display industry, medical and biochemical applications, material science, laser industry, fundamental aspects of atomic and nuclear structure, etc. The uranium and plutonium being fissile materials attract a lot of attention by nuclear industry for nuclear power programs. The lanthanides are also known as the “rare-earth” metals, however this nickname is not very accurate as many of the lanthanides are abundant in the earth’s crust, with some present in even greater quantities than lead. All of the actinides are radioactive and therefore are toxic and difficult to study. The lanthanides and actinides are part of a unique section of the periodic table having partially filled f orbital. In the lanthanide and actinides series the 4f and the 5f shell, respectively, are progressively filled with electrons. Owing to the high degeneracy of the f shells (14 spin orbitals) a rather large number of possible electronic states may arise. The situation becomes more complicated, because an open s, p, or d, shell frequently accompanies the open f shell. A large number of low-lying electronic states make a rationalization of the electronic structure of lanthanide and actinide compounds rather difficult. The situation from a spectroscopy point of view is even more complicated owing to the numerous isotopes occurring for some lanthanides and actinides, which cause a huge number of spectral lines. Moreover, the odd isotopes possess hyperfine structure. All these make the atomic emission and absorption spectra of these elements are very complex, with a large number of spectral lines. In some cases, the ground state of these elements is also multiplet, and

there are many close low-lying metastable energy levels. These elements are refractory, not so easily produced in the vapor state, which is the requirement for studying their atomic spectra. To generate the sufficient atomic number densities, high temperature operations are required. But, at these high temperatures, the population is thermally distributed among various low-lying metastable energy levels resulting in the low quantum state number density. These elements are also highly chemically reactive. Moreover, many of these elements are available only in small quantities, or are radioactive, which has to be handled in small quantities. Therefore sophisticated spectroscopic techniques are required to extract the spectral information of these elements. Laser-based spectroscopic techniques provide some of the best techniques for studying these elements.

As mentioned above, the lanthanides and actinides possess a very large number of energy levels between the ground state and the continuum. These energy levels are excited stepwise by using one or more than one photons from tunable lasers depending upon ionization potential of the elements. The involved photo-excitation cross-sections for stepwise transitions are appreciably large, owing to bound-bound transitions. Therefore, the excited levels can be easily accessed by available continuous wave (cw) and pulse tunable lasers. The excited atoms are then observed by detecting ions by further exciting the atoms above continuum, by detecting fluorescence from the excited levels, or by detecting the change in the discharge impedance. All these techniques of laser-induced photoionization spectroscopy, laser-induced fluorescence spectroscopy, and laser optogalvanic spectroscopy have been used for several elements by various researchers. The elemental information can also be obtained by focusing a pulse laser into the material

of interest to generate the plasma and subsequently collecting the emission containing characteristic atomic and ionic lines. This spectroscopic technique is known as laser-induced breakdown spectroscopy.

The laser spectroscopic techniques employed to study the complex atomic spectra of lanthanides and actinides include laser photoionization spectroscopy, laser-induced fluorescence, laser optogalvanic spectroscopy and laser-induced breakdown spectroscopy. Atomic beams, hollow cathode discharge lamps, and plasmas are used as atom sources for laser spectroscopy experiments. The spectra from these sources are generally too complex for easy analysis. But, the tunable, narrow line width and high power lasers make spectroscopy of any selected species easy even in these systems.

Laser spectroscopy of these elements includes measurements of atomic parameters, such as energy levels, total angular momentum values of these energy levels, photo-excitation cross-sections/photo-ionization cross-sections, radiative lifetimes of the energy levels, and branching fractions of different decay channels of an excited state, isotope shifts and hyperfine structures as well as measurement of elemental concentrations of samples. Most of these atomic parameters are required in many areas of science, such as atomic physics, plasma physics, laser chemistry, atmospheric sciences and is also of importance in the determination of solar and stellar abundances of elements and in the search for new laser materials. The atomic parameters mentioned above also play vital roles in realizing various other goals, such as laser isotope separation, qualitative and quantitative elemental analysis, rare isotope detection etc.

The present Ph. D. thesis deals with the development of above-mentioned laser spectroscopic techniques, methodologies and related instrumentation for the

measurement of elemental concentrations and atomic parameters to study lanthanides and actinides. In this thesis, laser spectroscopy experiments to measure atomic parameters on uranium and samarium are reported using laser optogalvanic spectroscopy, laser-induced fluorescence spectroscopy and laser photoionization spectroscopy. For the first time, laser-induced fluorescence and laser-induced photoionization techniques are used simultaneously to develop new methodologies to measure the atomic parameters. The density matrix (DM) based theoretical calculations have been used to validate the experimental results. These experiments have led to the identification of new energy/ autoionization levels of uranium and samarium atoms and the assignment of total angular momentum values to these levels. The radiative lifetimes of high-lying energy levels, and excited-level-to-excited-level absolute transition probabilities and photoionization cross-sections are also determined for many atomic transitions of uranium and samarium. The calibration-free laser-induced breakdown spectroscopic technique has been developed and used to analyze multi-elemental concentrations of a steel sample. The thesis has been organized into five chapters, elaborating the work carried out on the above-mentioned themes. The chapter-wise description of the work is given below.

Chapter 1 describes introduction of spectroscopy and importance of atomic spectroscopic investigations in general as well as for lanthanides and actinides. The problems and limitations associated with conventional absorption and emission techniques for understanding atomic spectra of lanthanides and actinides have been discussed. The necessity and impact of the laser-based spectroscopic techniques including laser-induced photoionization, laser-induced fluorescence, laser optogalvanic spectroscopy and laser-induced breakdown spectroscopy techniques have been described

in this chapter. A brief description of the present work based on the experimental and theoretical investigations is presented at the end of this chapter,.

Chapter 2 starts with a brief description of laser-induced photoionization (LIP) and laser-induced fluorescence (LIF) techniques, the development and the use of these techniques for the measurements of atomic parameters. Various experimental systems used in the present laser spectroscopy experiments are briefly described. The methodology of the LIF and LIP experiments carried out in atomic uranium and samarium is presented. The experimental results obtained for various atomic parameters such as the energy levels, their radiative lifetimes, branching fractions of different decay channels of an excited level, transition probabilities are also described in this chapter.

By combining together both the LIF and LIP techniques for simultaneous detection and utilization of LIF and LIP signals not only helped in developing new methodologies but also helped in getting complete spectral information apart from the measurements of atomic parameters.

In this chapter the observed resonances in the two-color laser-induced fluorescence experiments on atomic samarium are compared with our own results obtained simultaneously using two-color three-photon ionization experiments. As both the signals (LIF and LIP) are obtained under similar experimental conditions (laser power, oven temperature etc.), the comparison becomes more authentic than comparison of results by two techniques under different experimental conditions. The observation of features in the two spectra recorded simultaneously validates the complementary nature of these two techniques. The LIP and LIF signals have also been studied as a function of the second-step laser power to investigate the behavior of both the signals under varying

laser powers. To the best of our knowledge, we have used for the first time the simultaneous laser-induced fluorescence and photoionization signals for studying high-lying even-parity energy levels.

Chapter 3 describes the simultaneous LIP and LIF signals recorded in atomic uranium and samarium and analysis of these signals using DM calculations to deduce the atomic parameters. The DM formalism for three-level atomic systems has been discussed in detail in the present chapter. The LIP and LIF signals simultaneously recorded in atomic uranium for two specific cases have been analyzed using the DM formalism. The experimental results have been compared with the DM calculations to deduce the photoionization cross-section for the $33801.06\text{-}50701.59\text{ cm}^{-1}$ transition of atomic uranium. Two-color, three-photon photoionization and two-color fluorescence signals recorded simultaneously in atomic samarium as a function of the second-step laser power helped us in developing a new methodology for the measurements of two important atomic parameters in a single experiment. The DM formalism has been employed to analyze these signals. Two-color laser-induced fluorescence was used to measure the second-step transition probability. The second-step transition probabilities obtained was used to infer the photoionization cross-section. Thus, the methodology combining two-color, three-photon photoionization and two-color fluorescence signals in a single experiment has been established for the first time to measure the second-step transition probability as well as the photoionization cross-section.

Chapter 4 describes the laser optogalvanic spectroscopy technique. The optogalvanic spectroscopy using a hollow cathode discharge lamp (HCDL) is a much simpler technique in comparison to its other counterparts but still able to provide useful

information. The plasma parameters in see-through type homemade uranium HCDL, which was used for laser spectroscopy experiments, have been investigated. The temperature of neutral species, the excitation temperature and the electron number density have been measured. The three plasma parameters have been measured simultaneously for the first time in the HCDL.

This chapter also describes our investigation on the even-parity autoionization resonances of atomic uranium in the energy region $52850\text{-}53350\text{ cm}^{-1}$, using three-color optogalvanic spectroscopy technique in a U-Ne HCDL characterized above with three pulsed dye lasers. To the best of our knowledge, this is the first report of observation of even-parity autoionization states in atomic uranium lying at more than 2000 cm^{-1} above the ionization limit. We have used four different excitation schemes starting from the lowest metastable state of uranium at 620 cm^{-1} ($^5K_5^0$). We have identified 102 new even-parity autoionization resonances in atomic uranium and assigned probable total angular momentum (J) values to these resonances.

In chapter 5 starts with a brief historical review of Laser-induced breakdown spectroscopy (LIBS), also called laser-induced plasma spectrometry or laser spark spectrometry. The development of the LIBS system for elemental analysis of samples, which consists of a high resolution and broad-range Echelle spectrograph coupled to an intensified charge coupled device (ICCD) to detect and quantify elements of interest, is discussed in this chapter.

The chapter also describes the quantitative elemental analysis of a steel sample using calibration-free laser-induced breakdown spectroscopy (CF-LIBS). A Q-switched Nd:YAG laser (532 nm wavelength) is used to produce the plasma by focusing it onto a

steel sample in air at atmospheric pressure. The time-resolved spectra of a steel sample consisting of atomic and ionic emission lines of the steel elements are recorded using an Echelle grating spectrograph coupled with a gated intensified charge-coupled device camera, which are used for the plasma characterization and the quantitative analysis of the sample. The time delay where the plasma is in local thermodynamic equilibrium as well as optically thin, necessary for elemental analysis, is deduced. An algorithm for the CF-LIBS relating the experimentally measured spectral intensity values with the basic physics of the plasma is developed and used for the determination of Fe, Cr, Ni, Mg and Si concentrations in a steel sample. The analytical results obtained from the CF-LIBS technique agree well with the certified values of the elements in the sample with a relative uncertainty $< 5 \%$.

The summary and future scopes of work are briefly discussed at the end of the thesis.

List of Figures

Fig. 2.1: Experimental setup for measurement of radiative lifetime

Fig. 2.2: Exponential fit of photoionization signal of high-lying odd-parity energy level of uranium at 34071.24 cm^{-1} ($\tau = 157 \pm 11 \text{ ns}$)

Fig 2.3: Experimental setup for laser-induced fluorescence experiments

Fig.2.4: Spatially-resolved LIF signal at different delay times with respect to laser pulse

Fig. 2.5: Experimental time-resolved single-color LIF decay signal with an exponential fit. The lifetime for this level (18225.13 cm^{-1}) is measured to be $143 \pm 10 \text{ ns}$

Fig. 2.6: Spectrally resolved LIF showing three different decay channels from the excited energy level at 18475.28 cm^{-1} . In the inset, the solid line represents laser-induced

excitation and the dotted lines represent the observed fluorescence

Fig. 2.7: Experimental setup for simultaneous observation of two-color laser-induced fluorescence and two-color three-photon photoionization signals

Fig. 2.8: Energy level diagram for two-color, three-photon photoionization and two-color laser-induced fluorescence. The second laser is scanned to access the energy levels between 36500 and 36875 cm^{-1}

Fig. 2.9: Signal-to-noise ratio improvement using wavelength filter in laser-induced fluorescence signal

Fig. 2.10: Simultaneous recording of two-color laser-induced fluorescence and two-color, three-photon photoionization signal along with uranium optogalvanic signal and Fabry-Perot etalon fringes for wavelength calibration of spectra

Fig. 2.11: Two-color laser-induced fluorescence spectra as a function of the second-step laser power

Fig. 2.12: Two-color, three-photon photoionization spectra as a function of the second-step laser power

Fig.3.1: Energy level diagram for an ideal two-level atom

Fig. 3.2: Energy level diagram for an open two-level atom with decays and photoionization

Fig. 3.3: Energy level diagram for an open three-level atom with decays and photoionization

Fig. 3.4: Experimental setup for simultaneous observation of LIF and RIS signals

Fig. 3.5: Energy level diagram for single-color, three-photon photoionization and single-color laser-induced fluorescence when

(A) The laser is tuned to resonance in first step transition ($0-16900.38\text{ cm}^{-1}$),

(B) The laser is detuned from resonance in first step transition by 0.15 cm^{-1} , so that it becomes two-photon resonant at 33801.06 cm^{-1}

Fig. 3.6: Simultaneously observed LIF and RIS signals for the two specific cases

(A) The laser was resonant to the first-step transition ($0 - 16900.38\text{ cm}^{-1}$),

(B) The laser was near-resonant to the first-step transition with a slight detuning

(0.15 cm^{-1}), so that it became two-photon resonant at 33801.06 cm^{-1} ,

(C) Laser-induced background scattering signal in the absence of atomic beam

Fig. 3.7: Variation of photoionization efficiency with photoionization cross-section for

the two specific cases of laser detuning

Fig. 3.8: Variation of fluorescence efficiency with photoionization cross-section for the two specific cases of laser detuning

Fig. 3.9: Experimental setup for simultaneous observation of two-color laser-induced fluorescence and two-color three-photon photoionization signals

Fig. 3.10: Energy level diagrams for two-color, three-photon photoionization and two-color laser-induced fluorescence for two photoionization pathways (a) and (b)

Fig. 3.11: Variation of two-color laser-induced fluorescence efficiency with intensity of the second-step laser for three values of A_{32} , using the photoionization cross-section $\sigma_3 = 1 \times 10^{-16} \text{ cm}^2$. Photoionization pathway of Fig. 2(a) is considered for the results in this figure

Fig. 3.12: Variation of two-color laser-induced fluorescence efficiency with intensity of the second-step laser for three values of A_{32} , using the photoionization cross-section $\sigma_3 = 1 \times 10^{-17} \text{ cm}^2$. Photoionization pathway of Fig. 2(a) is considered for the results in this figure

Fig. 3.13: Variation of two-color, three-photon photoionization efficiency with intensity of the second-step laser for three values of σ_3 , using $A_{32} = 3 \times 10^5 \text{ s}^{-1}$.

Photoionization pathway of Fig. 2(a) is considered for the results in this figure

Fig. 4.1: Schematic of the uranium hollow cathode discharge lamp

Fig. 4.2: Experimental setup for recording the emission from the HCD lamp

Fig. 4.3: A part of a typical spectrum from the U-Ne HCD lamp

Fig. 4.4: A typical recorded profile of the Ne I spectral line at 640.22 nm

Fig. 4. 5: Boltzmann plot made using seven U I transitions. The solid line is a linear fit.

The slope gives the temperature equal to (0.284 ± 0.014) eV

Fig 4.6: Experimental setup used for three-color optogalvanic spectroscopy

Fig 4.7: a. Typical temporal wave form of resonant single-color optogalvanic signal.

b. Two-color optogalvanic signal.

c. Three-color optogalvanic signal

Fig. 4.8: Schematic of the different excitation schemes used for observation of autoionization states of uranium atoms

Fig. 4.9: A portion of typical three-color, three-photon autoionization spectra using scheme D in the energy region $53295\text{--}53327\text{ cm}^{-1}$

a. Fabry-perot etalon fringes

b. Autoionization spectra with resonances marked with asterisk (*)

c. Two-color spectra recorded by blocking second laser (λ_2)

Fig. 5.1: Experimental set-up for LIBS studies

Fig. 5.2: Spectrum of Hg-Ar lamp before intensity calibration

Fig. 5.3: Spectrum of Hg-Ar lamp after intensity calibration

Fig. 5.4: Schematic of the CF-LIBS algorithm

Fig. 5.5: LIBS spectra of a steel sample at a delay time of 1000 ns, covering (A) atomic lines of Fe, Cr, Ni, Mn, and Si (B) ionic lines of Fe used in the analysis

Fig. 5.6: Boltzmann plot made using seven Fe I transitions, considering the intensities at a delay time of 1000 ns. The continuous line represents the results of a linear best fit. The slope gives the temperature equal to 0.875 ± 0.044 eV

List of Tables

Table 2.1 Measured branching fractions and transition probabilities of the transitions

from the stepwise-excited even-parity energy level at 34935.5 cm^{-1} to various lower odd-parity levels using two-color laser-induced fluorescence with $\lambda_1 = 591.64 \text{ nm}$ and $\lambda_2 = 563.36 \text{ nm}$.

Table 2.2 Assigned values of the total angular momentum J to each of the stepwise-

excited even-parity energy levels in atomic samarium based on examination of J-values of the lower odd-parity levels to which a stepwise-excited even-parity level decays, removing the ambiguity from the proposed J-values in Ref [60].

Table 2.3 High-lying even-parity energy levels of atomic samarium

Table 3.1 Theoretical ratios of LIF and RIS signals for several values of the

photoionization cross-section σ_3 .

Table 3.2 Measured atomic parameters using simultaneous photoionization and

fluorescence signals

Table 4.1 Spectroscopic data for uranium atomic (U I) and ionic (U II) lines used in the

analysis (see text for references).

Table 4.2 Electron number density measurement using several uranium atomic (U I) lines

and uranium ionic line (U II) at 605.17 nm .

Table 4.3 New autoionization resonances using three-color, three-photon photoionization

spectroscopy in a hollow cathode discharge tube.

Table 5.1 Wavelength, lower and upper energy levels, upper level degeneracy, transition

probability for the atomic and ionic emission lines used in the analysis.

Table 5.2 Values of T, n_e , $n_{\text{Cr I}}/n_{\text{Fe II}}$, $n_{\text{Ni I}}/n_{\text{Fe II}}$, $n_{\text{Si I}}/n_{\text{Fe II}}$, $n_{\text{Mn I}}/n_{\text{Fe II}}$ and $n_{\text{Fe II}}/n_{\text{Fe I}}$ in the

LIBS plasma determined from the LIBS spectral line intensities as experimental results at a delay time of 1000 ns.

Table 5.3 Comparison of the elemental contents of the steel sample obtained from the CF-LIBS analysis with their certified values and the corresponding relative uncertainty.

Chapter 1

Introduction

1.0 Introduction to spectroscopy

Spectroscopy is a branch of science dealing with the interaction of electromagnetic radiation with matter. When the matter is properly energized, it may reemit the absorbed energy as electromagnetic radiation having frequencies characteristic of the radiating species and with intensity proportional to the number of particles participating in radiation. The frequencies radiated serve to identify the radiating species, giving rise to qualitative analytical spectroscopy. The amount of radiation gives a measure of the quantity of the matter responsible for the radiation, giving rise to quantitative analytical spectroscopy. Over the last several decades, spectroscopy has been applied to qualitative and quantitative determination of elements in solid, liquid and gaseous samples. Most of our knowledge about the structure of atoms and molecules is based on spectroscopic investigations. When the matter is energized with electromagnetic radiation, the basic phenomena of absorption, emission, scattering of the radiation and polarization effects with plane-polarized radiation are employed for spectroscopic studies. These studies have provided fascinating possibilities for a deeper understanding of the fundamental properties of the building blocks of matter. Thus, spectroscopy has made an outstanding contribution to atomic and molecular physics, chemistry, biology, medicine, environmental protection and energy research. In fact, it has contributed a lot to our understanding of the universe - earth, atmosphere, sun, interstellar space and distant stars which used to be treated as mystery or supernatural phenomenon few centuries back. Spectroscopic investigations can be fundamental or applied in nature,

which allow us to measure certain quantities (wavelengths, intensities, etc.). These quantities are then used to evaluate fundamental atomic parameters, like energy levels, radiative life time of energy levels, transition probabilities, angular momentum etc. These atomic parameters are useful in several disciplines of science and technology, such as atomic physics, astrophysics, plasma physics and laser physics. In the field of applied spectroscopy, the spectroscopic information is used for qualitative and quantitative analysis in various applications like combustion diagnostics, remote sensing of environment, photo-physical and photochemical processes, etc. Various techniques and their implementations can be classified in several ways. Types of spectroscopy can be distinguished by the nature of interaction between the energy and the mater. The interaction of electromagnetic radiation with the matter leads to absorption, emission and scattering of radiation. So, the spectroscopy is classified by either the nature of interaction, e.g., absorption spectroscopy, emission spectroscopy and scattering spectroscopy, or by the technique employed, e.g., ionization spectroscopy, photo-acoustic spectroscopy, optogalvanic spectroscopy, breakdown spectroscopy, etc. Spectroscopy can also be classified in terms of the electromagnetic spectrum used for the spectroscopic investigations, e.g., infrared spectroscopy, visible spectroscopy or X-ray spectroscopy. The choice of the spectral range of the radiation is done on the basis of phenomena to be studied. When laser as a light source is employed in the spectroscopy, the resultant spectroscopy is known as laser spectroscopy. When laser interacts with matter it produces the phenomenon of absorption, emission, discharge change, breakdown etc., giving rise to laser-induced photoionization spectroscopy, laser-induced fluorescence spectroscopy, laser optogalvanic spectroscopy and laser-induced breakdown spectroscopy and so on.

1.1 Spectroscopy of atoms

The study of the electromagnetic radiation absorbed and emitted by atoms to explore the atomic structure is known as atomic spectroscopy. The atomic absorption spectra for most elements originate from the transition of atoms from ground state to excited states on account of laser energy absorption. The atomic emission originates when atoms in the matter excited to higher energy states on account of laser energy absorption deexcite to lower states. In atomic spectroscopy experiments, the spectrum, which is a collection of broad and narrow bands of light absorbed by or emitted from atoms, is recorded. The recorded spectra reveal a lot of information related to atoms depending on the type of the measurements. The atomic energy level information is obtained by the wavelength measurements of the spectral lines. The line intensities are proportional to the transition probabilities which describe how strongly the two levels of the atomic transition are coupled. The widths of the spectral lines give information about the collision processes, the inter-atomic potentials and the velocity distributions of the atoms. Zeeman and Stark splitting of spectral lines by external magnetic and electric fields give information about magnetic and electric moments, respectively. The hyperfine structure of the spectral lines provides information about the interaction between the nucleus and the electron cloud, which helps in the determination of nuclear spin, nuclear magnetic dipole and electric quadrupole moment. Time-resolved measurements are used to measure excited-state lifetimes, to investigate dynamic and collision processes and various energy and charge transfer mechanisms, etc. Spectrally resolved measurements provide information, which can be useful for the branching fraction measurements and for the determination of atomic level energy values. The

spatially resolved measurements allow us to study the spatial and density variations in samples. The variation of the signal amplitude as a function of excitation source power is used for the measurement of atomic cross-sections. Time-resolved and spectrally-resolved spectra also allow us to carry out the qualitative and quantitative elemental analysis by choosing a proper time window where spectrally resolved spectra can be used for quantitative elemental analysis.

The experimental setup for atomic spectroscopy consists of an atom source, an excitation radiation source, an analyzer and a detection system. In earlier times, hollow cathode and electrodeless discharge lamps, sliding sparks and heat-pipe ovens were used as an atomic source for atomic spectroscopy. The spectral resolution, time resolution and the detection sensitivity in a spectroscopic experiment are crucial for attaining the substantial spectral information. Due to the advancement in instrumentation in the recent years, the use of new atom sources, optical sources, optical devices, sensitive detectors, fast electronics and image intensifiers have significantly extended the resolution and sensitivity limits. As a result many new spectroscopic techniques, such as Fourier transform spectroscopy, optical pumping, level-crossing techniques, double-resonance techniques, multi-photon techniques, etc., have contributed to the better understanding of the atomic spectra. Laser ablation and subsequent emission collection using gated cameras have opened up the opportunity for multi-elemental qualitative and quantitative analysis not only in laboratories but also at industrial environment or real work site. There still remain many unexplored areas where work has to be done, especially on the complex spectra of neutral and ionized atoms of lanthanides and actinides.

1.1.1 Atomic spectroscopy of Lanthanides and Actinides

Lanthanides in the periodic table include elements from Lanthanum (atomic number 57), to Lutetium (atomic number 71). Actinides include elements from Thorium, (atomic number 90), to Lawrencium (atomic number 103). Transuranics are the elements with atomic number higher than that of uranium, U (atomic number 92). These elements are produced artificially by bombarding heavy elements with neutrons. Transuranics form most of the actinides. These elements are unstable, with half-lives ranging from millions of years to fraction of seconds. The lanthanides and actinides are part of a unique section of the periodic table having partially filled f orbital. In the lanthanide and actinides series the 4f and the 5f shell, respectively, are progressively filled with electrons [1]. A large number of possible electronic states may arise due to the high degeneracy of the f shells (14 spin orbitals). The situation becomes more complicated, because an open s, p, or d, shell frequently accompanies the open f shell. The large number of low-lying electronic states makes a rationalization of the electronic structure of lanthanide and actinide compounds rather difficult. The situation from a spectroscopy point of view is even more complicated owing to the numerous isotopes occurring for some lanthanides and actinides, which cause a huge number of spectral lines. Moreover, the odd isotopes possess hyperfine structure. All these make the atomic emission and absorption spectra of lanthanides and actinides very complex, with a large number of spectral lines. The ground state of atoms of these elements is also multiplet in some cases, and there are many close low-lying metastable energy levels. Some of these elements are refractory and not so easily produced in the vapor state, which is the requirement for studying their atomic spectra. To generate the appreciable atomic number densities of these elements (~

10^8 atoms/cm³ or more), high temperature operations are required. But, at these high temperatures, the population is thermally distributed among various low-lying metastable and multiplet ground states in some cases, resulting in the lower number density in these states. It makes the signal intensity arising from a particular energy level very weak. These elements are also highly chemically reactive and, hence, handling chemically reactive species at higher temperatures also becomes quite difficult. In addition, many of these elements are available only in small amounts, or are radioactive. Elucidation of the spectra of these elements is difficult. It, therefore, requires sophisticated spectroscopic techniques and instrumentation. Laser-based spectroscopic techniques provide some of the best techniques for their studies.

1.1.2 Atomic spectroscopic techniques for Lanthanides and Actinides

As mentioned earlier, sparks, flames, hollow cathode and electrodeless discharge lamps were used as sources for absorption and emission spectroscopy experiments of these elements. These sources have been used as light sources as well as atomic sources. The emitted radiation from the source has been analyzed for the spectral information in emission spectroscopy experiments. The excitation of atoms by another light sources having sufficient intensity at excitation wavelength has been employed in absorption spectroscopy experiments. Absorption / emission spectra from these sources were photographed by a spectrograph, and the spectral lines were recorded for identification and analysis [2]. High-resolution optical spectroscopy was performed by employing Fabry-Perot interferometer. Meggers reviewed most of the literature of atomic spectroscopy published till that date in 1963 [3]. Argonne National Laboratory has provided more precise atomic spectra with extended spectral ranges using a 30 feet

spectrograph [4,5]. The National Bureau of Standards, now known as National Institute of Standards and Technology (NIST) has used the normal incidence vacuum spectrograph to study spectra of highly ionized atoms [6], which led to excellent compilations done by National Bureau of Standards Monographs [7-10]. The first spectrum, using Fourier transform spectrometer (FTS), of thorium and holmium at high resolution has been recorded in 1970 [11]. Later, numerous FTS investigations have been carried out [12-16]. These classical absorption / emission spectroscopy investigations were limited either by resolving power of the wavelength dispersing instruments, or by the intensity of the light source. These techniques were not capable of exploring the high-lying energy regions (above 30000 cm^{-1}) as the energy levels in these energy regions were not sufficiently populated. It is required to observe atomic transitions from these high-lying energy levels.

1.2 Laser spectroscopy of atoms

Atomic spectroscopy got a big boost only after the invention of tunable dye laser in 1966 [17]. The crucial experimental parameters in atomic spectroscopy are intensity as well as spectral brightness. Lasers have very high spectral brightness. Lasers can also be focused to very small areas and thus provide very intensity. These properties make lasers very suitable for atomic spectroscopy experiments. The unique properties offered by lasers not only allowed the evolution of completely new techniques but also allowed the established spectroscopic techniques to be applied more precisely [18]. Lasers being highly monochromatic helped improving the resolution of measurements. The high spectral brightness opened the new branch of spectroscopy, the non-linear spectroscopy, which is based on saturation phenomena, or multi-photon transitions [18]. Lasers capable

of delivering short pulses in nano-, pico- or femto-second time domain, made the time resolved studies possible. The time-resolved investigations can be used to measure radiative lifetimes of the energy levels. These properties also allowed a new branch of spectroscopy to emerge, laser- induced breakdown spectroscopy (LIBS), which utilizes laser-ablation based atomic/ionic sources [19]. The specific areas of a sample can be probed due to the high directionality of the laser beam. Thus, lasers made a huge multifold impact on the field of spectroscopy. Tunability is a crucial criterion for a laser to be used in spectroscopy experiments. Although many lasers including solid state lasers, optical parametric oscillators, semiconductor lasers can be made tunable but the dye lasers in their various modifications in visible and ultra-violet spectral region are still the most widely used lasers for spectroscopy experiments. The organic dye molecules dissolved in liquids make the active medium for dye lasers. The tuning range of dye laser depends on the individual dye and pump laser used. By using different dyes, a wide wavelength range from 300 -1000 nm can be covered. The tunable range can be extended from vacuum ultra-violet to infrared region by wavelength doubling or mixing techniques.

The dye lasers used for laser spectroscopy can be operated in pulsed mode by pumping it with another pulsed laser or flash lamp. It can also be operated in continuous wave (cw) mode by pumping it with argon ion / Ti-sapphire laser. Dye lasers can also be used either in multimode or single-mode depending upon the experimental requirement. Laser intensity required for saturating an atomic transition is of the order of few $\mu\text{W}/\text{cm}^2$ to tens of mW/cm^2 for different steps, which can be achieved easily by both cw and pulsed dye lasers. The line-width of the dye laser is another crucial parameter, which

dictates the obtained frequency resolution in spectroscopic experiments. The cw lasers generally have narrow line-width of the order of MHz or even lower whereas the pulsed lasers are broad with line width in the range of GHz. Thus, the cw lasers are generally used for high resolution atomic spectroscopy experiments. The line-width of the pulsed lasers can also be reduced for improving the resolution in the experiments but the lower limit for the line-width of the pulsed lasers is mainly determined by the Fourier transformation of the time-dependent laser intensity, which yields, for laser pulses with a duration τ , a spectral line-width given by $\Delta\nu = \frac{1}{2\pi\tau}$.

However, the final resolution obtained in a laser spectroscopy experiment, depends on the convolution of the laser line-width and the atomic width of the spectral line. The origin of the atomic width of the spectral line is due to many broadening mechanisms inside the atom source, which include natural broadening, Doppler broadening, collisional broadening, power broadening etc [18].

1.3 Laser spectroscopic techniques for studying atoms

Laser spectroscopic techniques can be classified into two categories, Doppler-limited or Doppler-free techniques. If the resolution obtained in spectroscopy experiments is limited by the Doppler width of the atomic absorption line, the technique is known as Doppler-limited technique, otherwise it is known as Doppler-free technique. Laser-based absorption spectroscopy, fluorescence spectroscopy, photoionization spectroscopy, photoacoustic spectroscopy, optothermal, optogalvanic spectroscopy are examples of the Doppler-limited spectroscopic techniques, which can be used with pulsed lasers, and are very useful for studying highly-excited levels, Rydberg levels and

autoionizing energy levels of atoms. These techniques can also be used for measurements of radiative lifetimes, branching fractions, photoexcitation and photoionization cross-sections, etc [18]. Doppler-free spectroscopic techniques overcome the limit set by the Doppler broadening and thus high-resolution spectroscopy can be performed. Such techniques are termed as non-linear spectroscopic techniques. Saturation spectroscopy, polarization spectroscopy and multi-photon spectroscopy are examples of Doppler-free spectroscopy techniques. The cw laser based non-linear spectroscopy is well suited for high-resolution investigations, which can provide information about isotope shifts and hyperfine structures [18, 20-21]. Some of the techniques can be kept in a separate category like laser-induced breakdown spectroscopy, where laser is used to generate ablation based atomic or ionic source. However detection efficiency can be enhanced by laser-induced fluorescence by exciting the atomic/ionic transitions using another laser tuned to that particular transition [19].

1.3.1. Atomic spectroscopy using multi-mode lasers

By tuning the laser wavelength to an atomic transition between two energy levels, the population of atoms can be transferred from lower energy level to upper energy level. In this way, large population densities in the upper energy level can be attained. Because of this population transfer from the lower energy level, the upper energy level can serve as initial energy level for further excitation. Thus, the spectroscopy of excited energy levels can be performed by stepwise excitation of atoms. The experiments with tunable multi-mode lasers are aimed to determine the energy-level structure in high-lying energy regions accessible through step-wise excitation. These high-lying energy levels are inaccessible by other classical spectroscopic techniques.

The pulsed lasers are capable of generating very intense short pulses, allowing time-resolved studies to be done. The time-resolved studies can provide the measurement of radiative lifetime of excited states. The spectrally-resolved studies can provide the measurement of branching fractions. Combining these two atomic parameters, one can deduce the transition probabilities. By stepwise excitation, these measurements can be done for excited energy levels. Thus, the radiative lifetime for excited energy levels and transition probabilities for transitions between excited energy levels can be measured. The time-resolved studies can also be done using a laser ablation source in combination with a gated detector such as intensified charge coupled device (ICCD) camera. These studies can be useful in determination of elemental composition of materials [19].

1.4 Motivation and description of the present work

The data on atomic spectroscopy of lanthanides and actinides are far from complete. The literature survey revealed that these elements still have unexplored high-lying energy regions and many atomic parameters are unknown which could be of vital importance in both basic and applied studies. The high energy regions are not well studied due to the inaccessibility of these regions by commonly used technique of emission spectroscopy. This is due to the fact that the atomic sources used for emission spectroscopy have very low population in these high-lying energy levels. Moreover, the decay from these high-lying energy levels was to low-lying energy levels emitting only a few photons for a given decay transition, and thus, making detection difficult. With the advent of lasers and improvement in spectroscopic instrumentation, it became possible to selectively produce, investigate and detect specific energy levels of atomic, ionic and isotopic species. Lasers coupled with improved time-gated detectors not only made

measurements of atomic parameters possible but also made the multi-elemental analysis possible. It became possible even without generating calibration curves and utilizing calibration free laser-induced breakdown spectroscopy techniques.

In this thesis, various laser spectroscopic techniques, methodologies and related instrumentation have been developed for the measurements of atomic parameters and quantitative elemental analysis. In this work, laser spectroscopic studies have been reported for samarium and uranium employing laser-based photoionization, fluorescence and optogalvanic spectroscopic techniques. The multi-color resonant excitations have been used to explore the high-lying energy levels by employing fluorescence, ionization or optogalvanic spectroscopic techniques. These high-lying energy levels have also been explored by simultaneously using laser-induced fluorescence and photoionization techniques. These studies led us to identify new energy levels, both in the explored and unexplored energy regions. It also led us to measure many other important atomic parameters. These results have been presented in this thesis. The fluorescence from the excited state has been temporally and spectrally resolved, to measure radiative lifetimes and branching fractions, which in combination helped in deducing excited-state-to-ground-state and excited-state-to-excited-state absolute transition probabilities. For the first time, laser-induced fluorescence and photoionization techniques have been used simultaneously to study high-lying energy regions. It has been established that both techniques should be used in a complimentary way for identification of atomic energy levels.

The results obtained using simultaneous laser-induced fluorescence and photoionization techniques have been analyzed using density matrix formalism. This has

led us to develop new methodologies for the measurements of important atomic parameters. A new calibration-free laser-induced breakdown spectroscopy approach has been developed for multi-elemental composition analysis. This technique has been used to analyze elemental concentrations of a steel sample. The all above-mentioned results have been compared with the earlier works reported in the literature and also with the other known methods. The description of other chapters in this thesis is as follows.

Chapter 2 discusses laser-induced photoionization (LIP) including resonance ionization spectroscopy (RIS) and resonance ionization mass spectroscopy (RIMS) techniques in brief. It also briefly describes laser-induced fluorescence (LIF) technique. The experiments and experimental systems employed for atomic spectroscopy of uranium and samarium using these techniques has also been discussed. The methodology of the LIF and LIP experiments carried out in atomic uranium and samarium is presented. The results on measurements of many important atomic parameters including energy levels and their angular momentum values, radiative lifetimes, branching fractions, transition probabilities, photoexcitation/photoionization cross-sections, etc. have been presented in this chapter.

This chapter describes simultaneous utilization of LIF and RIS techniques to generate full spectral information. The observation of features in the two spectra recorded simultaneously validates the complementary nature of these two techniques. The RIS and LIF signals have also been studied as a function of the second-step laser power to investigate the behavior of both the signals under varying laser powers. To the best of our knowledge, simultaneous laser-induced fluorescence and photoionization signals have been used here for the first time for studying high-lying even-parity energy levels.

Chapter 3 describes the use of simultaneous LIF and RIS techniques for the development of new methodologies to deduce photoexcitation/ photoionization cross-sections. The experimental results have been theoretically analyzed by using density matrix (DM) formalism. The DM formalism for two and three-level atomic systems has been discussed in detail in the present chapter. The experimental results have been compared with the DM calculations to deduce the photoionization cross-section for the $33801.06\text{-}50701.59\text{ cm}^{-1}$ transition of atomic uranium. Two-color laser-induced fluorescence was used to measure the second-step transition probability. The second-step transition probabilities obtained was used to infer the photoionization cross-sections. Thus, the methodology combining two-color, three-photon photoionization and two-color fluorescence signals in a single experiment has been established for the first time to measure the second-step transition probability as well as the photoionization cross-section. Two important atomic parameters have been measured in a single experiment by simultaneously recording two-color, three-photon photoionization and two-color fluorescence signals of atomic samarium as a function of the second-step laser power.

Chapter 4 deals with optogalvanic spectroscopy technique, which relies on its simplicity. The technique employs a simple device called hollow cathode discharge lamp (HCDL), which can be used as an atomic vapor source as well as ion detector. It is an attractive tool to extract useful spectral information. This technique is a boon, especially for studying the refractory elements where generation of atomic beam is difficult. In this chapter, the plasma parameters have been investigated in see-through-type homemade uranium HCDL. The temperature of neutral species, the excitation temperature and the electron number density have been measured.

This chapter also describes the investigation of even-parity autoionization resonances of atomic uranium in the energy region $52850\text{--}53350\text{ cm}^{-1}$, using three-color optogalvanic spectroscopy technique in a U-Ne HCDL with three pulsed dye lasers. To the best of our knowledge, this is the first report of observation of even-parity autoionization states in atomic uranium lying at more than 2000 cm^{-1} above the ionization limit. Total 102 new even-parity autoionization resonances in atomic uranium have been identified. The probable total angular momentum (J) values to these resonances have also been assigned.

Chapter 5 reviews the laser-induced breakdown spectroscopy technique (LIBS), capable of remote, real-time multi-elemental analysis. The development of the LIBS system for multi-elemental analysis of samples consists of a high resolution and broad-range Echelle spectrograph coupled to an intensified charge-coupled device (ICCD) to detect and quantify elements of interest. The details of the LIBS experimental setup and methodology adopted for the elemental analysis is discussed in this chapter.

The present chapter also describes the quantitative elemental analysis of a steel sample using calibration-free laser-induced breakdown spectroscopy (CF-LIBS). A Q-switched Nd:YAG laser (532 nm wavelength) is used to produce the plasma by focusing it onto a steel sample in air at atmospheric pressure. The time-resolved spectra of a steel sample consisting of atomic and ionic emission lines of the steel elements are used for the plasma characterization and the quantitative analysis of the sample. The time delay relative to the laser pulse where the plasma is in local thermodynamic equilibrium as well as optically thin, necessary for the elemental analysis, is deduced. An algorithm for the CF-LIBS relating the experimentally measured spectral intensity values with the basic

physics of the plasma is developed and used for the determination of Fe, Cr, Ni, Mg and Si concentrations in a steel sample. The analytical results obtained from the CF-LIBS technique agree well with the certified values of the elements in the sample with a relative uncertainty $< 5\%$.

Brief summary and future scope of work is given at the end of the thesis.

Chapter 2

Laser-induced photoionization and fluorescence techniques

In the laser-induced photoionization (LIP) spectroscopy technique, neutral atoms of an element are selectively raised to an excited atomic state of the atoms by a laser resonantly tuned to the excitation energy of the transition. The excited atoms are further photoionized from their resonant state by an additional laser tuned to provide enough energy to raise the excited atoms over the ionization threshold of that element. This process of photoionization of atoms is called resonance ionization spectroscopy (RIS). RIS, when coupled with a mass spectrometer, is known as resonance ionization mass spectrometry (RIMS). Laser-induced fluorescence (LIF) is another spectroscopic technique that excites atoms by precisely tuned lasers and detects the relaxation of an excited state by spontaneous emission of fluorescence radiation to lower states. Both, RIS/RIMS and LIF are excellent tools for investigating high-lying energy levels. Very useful information on atomic structure as well as laser-atom interaction dynamics have been derived from these techniques. These techniques are discussed in detail in the following sections.

2.1 Laser-induced photoionization

As mentioned above, in laser-induced photoionization (LIP) technique, the atoms excited in one or two-steps are further excited above the continuum and subsequently ionized. Since the resonant excitation steps are involved in photoionization, the term resonance ionization spectroscopy (RIS) is often used for the process. This is also known as multi-step photoionization spectroscopy technique as multiple steps might be involved depending upon the ionization potential of the atom under investigation. So, single or

multi-step resonant excitation followed by ionization is carried out by irradiation with tunable laser light and resulting electrons or ions are detected by the detector. RIS is a very sensitive technique. In principle, every absorbed laser photon gives rise to a detected ion or electron, with 100% efficiency. As an extension to RIS, the ions generated by resonant excitations are further mass analyzed by a mass spectrometer, and this spectroscopy is known as resonance ionization mass spectroscopy (RIMS). The techniques of RIS and RIMS, because of their high sensitivity are widely used. Janes et al. [1] have reported the capability of RIS technique to study heavy atoms in 1975. RIMS as a spectroscopic tool was reported by Carlson et al. [2] in 1976. Hurst et al [3] have reported the capability to detect single atom in the interaction zone in 1979. V. S. Letokhov [4] discussed key characteristics and applications of laser photoionization spectroscopy in 1985. Since then, these photoionization techniques have been developed as very sensitive techniques and the developments have been reviewed extensively in the literature [5-12]. It has been used by various researchers for studying atomic spectra of various atoms [2, 13-15], ultra-sensitive detection of trace elements [16, 17], studying nuclear structure [18, 19], nuclear research [20, 21], isotope production [22] and various other applications [23, 24].

2.1.1 Atomic spectroscopy of uranium

The natural uranium, a mixture of largely two isotopes, U^{238} accounting for about 99.3% and U^{235} about 0.7%, is found in the earth's crust. The isotope U^{235} is fissile. Its nucleus can split into two nuclei under certain conditions, yielding fission. The uranium fuel is assembled in such a way in a nuclear reactor that a controlled fission chain reaction can be achieved. The other uranium isotope U^{238} is a fertile material as it can

capture one of neutrons in the core of reactor to become (indirectly) Pu^{239} , which is again a fissile material. Thus uranium is very important element for harnessing nuclear energy. Uranium is chosen as one of the actinide elements for spectroscopic studies. Uranium is the heaviest of all the naturally occurring elements. The elemental and isotopic composition of uranium in samples obtained from the uranium ore, nuclear waste and each step involved in nuclear fuel cycle needs to be monitored carefully for achieving nuclear as well as environmental safeguards. The efficient and selective multi-step laser photoionization pathways need to be identified for carrying out the elemental and isotopic composition analysis, trace analysis and isotope separation programs. Thus, highly efficient and selective photoionization schemes have to be formulated, which require the complete knowledge of all the spectroscopic parameters of involved atomic energy levels and atomic transitions.

Uranium has very dense and complex atomic spectra. It has a radon core and six optical electrons. Uranium atomic transitions are used as wavelength references throughout the uv to near-ir spectral range. Precision interferometric studies using optogalvanic spectroscopy, have yielded wavelength standards, with accuracy at the 0.0003 cm^{-1} level.

Using various techniques, a lot of spectroscopic data has been generated and reported on atomic parameters of uranium in the literature [2, 12-15, 25-35], but still the spectroscopic information available is far from complete. Thus, the primary interest for this study was to develop or setup techniques capable of measuring various atomic parameters.

2.1.2 Present work using laser-induced photoionization

The knowledge of atomic parameters such as radiative lifetimes, photoexcitation/photoionization cross-sections, branching fractions, transition probabilities are crucial in many areas of basic science, such as atomic physics, plasma physics and atmospheric sciences. These parameters are used for determination of solar and stellar abundances of elements, for searching the new laser materials, etc. The accurate values of these parameter are also very important for choosing efficient photoionization schemes for atomic vapor laser isotope separation process and trace analysis as these parameters determine the laser fluences needed for the transition steps involved in the photoionization process.

2.1.2.1 Measurement of radiative lifetime of atomic uranium by LIP

The radiative lifetime of atomic energy levels is an important atomic parameter as it governs the dynamics of excitation and all the applications involving laser excitation look for this fundamental property of atomic level. The radiative properties of atoms and ions are of great importance in astrophysics, plasma physics and laser physics. The natural lifetime determines the fundamental limit of resolution in spectroscopic investigations. The measurements of radiative lifetimes of energy levels and branching fractions provide a reliable method for determining the absolute transition probabilities of atom and, therefore, are important in many fields of science and technology. It is also important in deciding the efficient photoionization schemes for trace analysis and isotope separation process. Radiative lifetime is crucial for searching the new laser materials. Measurements of radiative lifetimes are usually done by employing laser-induced fluorescence (LIF) or laser-induced photoionization (LIP) techniques. Using LIF

techniques Miron et al. [29] have carried out most extensive work on U I energy levels and radiative lifetimes. Carlson et al. [2], Hackel et al. [34] and Avril et al. [35] have measured radiative lifetimes using LIP. In this Section, the results on measurements of radiative lifetimes of high-lying odd-parity energy levels of atomic uranium using the pump probe technique have been discussed [31].

2.1.2.1.1 Experimental setup for measurement of radiative lifetime

The experimental set-up is shown in Fig.2.1. It consists of Nd-YAG (Model YG 980) pumped dye lasers (Model TDL 90), indigenously developed reflectron type time-of-flight mass spectrometer, digital oscilloscope, homemade U-Ne hollow cathode discharge lamp and a fast photodiode. Uranium atomic beam was generated by resistive heating of uranium metal in tantalum crucible in a vacuum chamber evacuated to a pressure less than 10^{-7} Torr. Uranium atoms thus produced were excited and photoionized by three-color three-photon photo ionization scheme using Nd-YAG pumped dye laser system. Resulting photoion signal was detected using Micro-channel plate (MCP) in a reflectron type time-of-flight mass spectrometer. The delay can be varied using a delay generator. The detectors MCP1 and MCP2 are used in the axial (linear) and off-axis (reflected) positions respectively for ion signal detection. The signals from the MCP are recorded by the oscilloscope capable to transfer the data to the computer for subsequent processing and analysis. Each data is averaged over 128 pulses on a 500 MHz oscilloscope and recorded. Here, the first and second lasers are used as the pump lasers to excite the uranium atoms to a highly excited odd-parity level through a two-step excitation process involving resonant first and second-step transitions. The third laser probes the population of the highly excited level by photoionizing the excited

uranium atoms. The photoionization signal is recorded as a function of the time delay between pump and probe lasers. The radiative lifetime of an energy level is obtained by fitting the data to an exponential decay curve.

2.1.2.1.2 Results and discussion

The typical decay curves of the energy level at $34,071.24 \text{ cm}^{-1}$ is shown in Fig. 2.2. The radiative lifetimes of nine high-lying odd-parity energy levels of atomic uranium have been measured [31]. The measured values match well with those reported in the literature for short lifetime values [29]. The measured lifetimes 1469 ns and 2099 ns for the energy levels $34,128.47 \text{ cm}^{-1}$ and $34,048.45 \text{ cm}^{-1}$, respectively, are substantially higher as compared to those reported by Miron et al [29] as 900 and 1080 ns. Mirron et al. [29] have carried out the measurements in the presence of argon as a buffer gas. So, the atomic collisions are likely to depopulate the excited atoms, resulting in reduction of the measured lifetime values. Although they have extrapolated their results to zero Argon pressure, there could be residual errors in the extrapolated values when compared with a collisionless atomic beam in a high vacuum environment, as in our experiment. In addition, they have not mentioned anything about the interaction volume. For the energy levels particularly with relatively long life-times, the atoms may move out of the interaction volume before being probed. In our experiments, this effect was negligible for those energy levels whose radiative lifetimes were much less than the transit time of atoms through the interaction zone, which was about $10 \text{ }\mu\text{s}$ (atomic beam travelling through the pump beam diameter of 4 mm with an average velocity of $4 \times 10^2 \text{ m/s}$). The radiative lifetime values for the energy levels 34944.10 , 34953.82 , and 34999.5 cm^{-1} have been measured for the first time as 318 ± 27 , 47 ± 2 and $647 \pm 44 \text{ ns}$ respectively.

2.2 Laser-induced fluorescence

In the laser-induced fluorescence (LIF) spectroscopy technique, laser is used for inducing a resonant transition from a lower energy level to a higher energy level of atoms and subsequent emission of photons due to spontaneous de-excitation of the excited level to lower levels detected by photon detectors [36]. This spectroscopy technique can be used in two different ways by recording either the excitation or fluorescence spectrum. The excitation spectrum is obtained when the laser wavelength is scanned across the spectral range of the absorption lines, the total fluorescence intensity monitored as a function of the laser wavelength. It represents an image of the absorption spectrum, therefore directly reflects the absorption spectrum with respect to line positions. The fluorescence spectrum is obtained when the laser wavelength is tuned to one transition and the spectrum, which corresponds to the allowed transitions towards lower energy levels, is recorded. If collection of the emitted photons is integrated over whole interaction volume, time and frequency of emitted photons, it is called integrated fluorescence. By properly choosing the spectroscopic instrumentation and optics, the integrated fluorescence can be resolved either spectrally or temporally or spatially giving vital information in each case.

The technique of fluorescence spectroscopy is a very sensitive technique in visible, ultraviolet and near infrared regions. LIF spectroscopy has been employed for a wide range of applications related to analytical sciences [37, 38], diagnostic processes [39, 40, 41], and atomic and molecular physics [29, 42-44]. In this work, atomic parameters of samarium have been measured using LIF technique.

2.2.1 Atomic spectroscopy of samarium

Samarium (Sm) has many electrons in d and f shells, so it is well known for its large number of atomic transitions, with strong oscillator strengths in the visible region. Due to its rich energy level structure, Sm is one of the major dopants for optical amplifications such as laser amplifiers and communication devices, like other lanthanides, namely neodymium and erbium. It is also used in magnets and some metal alloys. Samarium when blended with cobalt for a stronger alloy resists demagnetization. Samarium is also used as an additive in glass to absorb infrared energy. Optical properties of Sm-doped material are of great interest in the field of photonics.

The alkali atoms have been studied so far extensively for coherent population trapping, which is widely used in different applications, such as magnetometry, metrology, etc. The rare earth atoms have an advantage because their hyperfine structure energy levels are deeply shielded and, therefore, ground sub-levels have much higher energy splitting. Atomic samarium offers a versatile environment for studying the atomic coherence, or coherent atom-field interactions [45]. Samarium has an energy level structure, which is suitable for studying electromagnetically induced transparency experiments [46-48]. Samarium has pairs of narrowly separated opposite-parity energy levels. The mixing between these opposite-parity level pairs, which is caused by the neutral current interaction, is largely enhanced and, thus, it is the strong candidate for parity violation experiments [47, 48]. Moreover, Sm has a large number of stable isotopes, which also enable the measurements of atomic parity violation experiments with different isotopes. Samarium has usefulness in trace analysis [49]. The atomic vapor laser isotope separation (AVLIS) of samarium is finding attention as samarium is used as an

improved burnable poison for commercial nuclear power reactor [50]. In this study, samarium (Sm) has been chosen because of scarcity of spectroscopic information related to it in the literature. The LIF technique developed and used here has a general applicability. It can be applied to any of lanthanides and actinides.

2.2.2 Present work using laser-induced fluorescence

As mentioned in section 2.1.2.1, that radiative lifetime is very important atomic parameter. The radiative lifetime measurements are commonly done by monitoring time-resolved LIF [29, 51-57] from an atomic beam with a fast detector like photomultiplier tube (PMT). Laser-based methods for measurement of absolute transition probability use either laser-induced fluorescence (LIF) or laser-induced photoionization (LIP) as mentioned in earlier sections. Carlson et al. [2] have described a branching-fraction-lifetime ($\beta - \tau$) method for determining absolute transition probabilities by independently measuring branching fractions (β) and radiative lifetimes (τ) using time-resolved optical pumping, probed by time-resolved laser-induced photoionization (LIP). This method has a distinctive advantage of being independent to laser beam quality, such as temporal profile, intensity and linewidth, unlike most of the other methods. They have used this method to obtain accurate values of transition probability for atomic transitions in uranium. Hackel and Rushford [34] have refined this method and measured the branching fraction and the accurate absolute transition probability in atomic uranium. In the above works the β - τ method is applied for optical transitions between excited and ground states. The branching fractions are also measured by either monitoring the LIF spectrum in an atomic beam or the emission spectrum of a hollow cathode discharge lamp with a Fourier-transform spectrometer (FTS) [32].

Measurement of absolute transition probability for atomic transitions between excited-level-to-excited-level is difficult and complex. The β - τ method using time-resolved LIP technique was used by Bisson et al. [58] for measurement of absolute transition probabilities of excited-level-to-excited-level optical transitions in atomic cerium and gadolinium. They have discussed advantages and limitations of their method. Petit et al. [32] and Avril et al. [35] have used LIP to measure the lifetimes and LIF to measure the branching fractions for determining the absolute transition probabilities of uranium atomic transitions originating from the 34659 cm^{-1} excited energy level.

Total angular momentum value (J) is fundamentally important in choosing possible excitation schemes and, hence, assignment of its value to each energy level of the excitation pathways is of great significance. There are several experimental methods to determine J of a given atomic energy level, e.g., Zeeman effect, hyperfine splitting in absorption lines, spectrally resolved fluorescence from the level, excitation to same level via multiple excitation pathways and polarization combination methods. Zeeman Effect and hyperfine splitting in absorption lines [59] can be applied to ground or low-lying atomic energy levels, which can be populated by single excitation source. Multiple excitation pathways [60, 61] or spectrally resolved fluorescence technique [29, 62] can be successfully employed for assigning a unique J value to high-lying energy levels. Identification of J for autoionization energy levels uses polarization combination method [63].

The motivation for the substantial effort on the spectroscopic data of rare earth atoms and ions arises primarily from stellar elemental abundance studies. Komarovskii and Smirnov [64] have used electron beam for excitation and measured the branching

fractions of different decay channels in atomic samarium. Using these measurements and lifetimes reported earlier [51, 52], they have determined absolute transition probabilities for excited-state-to-ground-state Sm I atomic transitions in the wavelength range 350-650 nm. To the best of our knowledge, there is no data reported in the literature on excited-state-to-excited-state transition probability in atomic samarium.

In this Section, development of LIF spectrometer for the measurement of atomic parameters of samarium is reported [65]. The LIF has been temporally resolved to measure the lifetimes of excited energy levels. It is spectrally resolved using a monochromator to determine the different decay channels, and thus branching fractions. The lifetime and branching fraction data has been combined to deduce ground-level-to-excited-level and excited-level-to-excited-level absolute transition probabilities of several atomic transitions. The LIF technique has also been used to uniquely assign the total angular momentum values (J).

2.2.2.1 Experimental setup and development of spectrometer

The lasers employed remain same, Q-switched Nd:YAG laser (Quantel YG980) pumped dye lasers (Quantel TDL90), as mentioned in earlier Sections. For detection of temporally and spectrally resolved laser-induced fluorescence, intensified charge couple device camera (ICCD) camera of high temporal resolution (< 1 ns) and moderate gains ($> 10^4$) has been used. ICCD camera when coupled with a monochromator has the capability of simultaneous temporal and spectral measurements. The experimental set-up used for this study is shown in Fig.2.3. This consists of Q-switched Nd:YAG pumped dye lasers, atomic beam chamber, fluorescence collection assembly, monochromator, PMT and gated ICCD camera coupled with a personal computer. The samarium atomic beam was

generated in a vacuum chamber maintained at a background pressure of $\sim 10^{-5}$ torr by resistive heating of samarium metal kept in a tantalum crucible at ~ 1000 °C. The samarium vapors come out effusively from a 0.5 mm hole in the crucible lid. The Sm atoms of this low-density atomic beam in the interaction zone were resonantly excited by dye lasers at right angle to the atomic beam. The pulse duration, repetition rate and linewidth of the dye laser were 7 ns, 20 Hz and 0.05 cm^{-1} (1.5 GHz) respectively. The fluorescence light emitted from excited upper levels was collected perpendicularly to both laser and atomic beams and focussed onto the entrance slit of the 0.5 m monochromator (Acton SpectraPro, 2500i) by a suitable lens assembly.

The monochromator consists of three interchangeable 500-nm blaze gratings having 300, 600 and 1200 lines/mm. The resolution of the spectrograph with 300 lines/mm grating is roughly 0.1 nm. Most of the work was done using this grating. Spectral ranges with a higher line density were also scanned using the 1200 lines/mm grating, which has a resolution of about 30 pm. Wavelength/pixel calibration of the spectrograph was performed by using Hg/Ar lamp. This lamp was inserted in the atomic beam chamber along the beam path, before the experiment. The Hg/Ar calibration lamp used produces sharp lines in the spectral range 253-1700 nm. Easily identifiable mercury and argon spectral emission lines are listed on the lamp housing, which are known in the literature. Camera parameters are adjusted in a manner that several peaks of lamp are displayed. By carefully positioning the cursor at one of the peaks, so that it is at the point of maximum intensity, which gives the pixel number which is being displayed in status bar. This step is repeated for all the peaks displayed. These pixel and wavelength values are inserted in the in-built software program to perform linear regressions. It provides

linear dispersion scale in terms of wavelength. Now the calibration is checked with respect to temperature stabilized He –Ne laser. If it displays the exact wavelength, then calibration process is completed, otherwise all process requires to be repeated till it gives the exact wavelength of any stabilized wavelength source. Cross-checking of this wavelength calibration was also done by first and second excited step wavelengths of dye laser 1 and 2 and decay channel wavelengths which are previously observed transitions from that level. Dye laser wavelengths are also cross-checked by 1.5 m high resolution monochromator. All the gratings were calibrated separately. A NIST-certified Deuterium Tungsten Halogen lamp with well known continuous spectral distribution was also used to get the relative spectral transfer function of the detection system. The uncertainty of calibration of lamp with the uncertainty of the response of spectrometer using this lamp is about 6%. For the grating having 300 lines/mm, the covered wavelength range was 130 nm for single coverage. So, multiple acquisitions have been carried out to cover the LIF spectrum in the wavelength range 300-900 nm. A sufficient amount of overlap was set between successive acquisitions to reconstruct the entire spectrum. In order to take into account the intensity fluctuations during the different steps of acquisition, relative corrections were made on the parts of spectrum by matching the spectral lines of the overlapped spectra. These parts of the spectrum were merged and the relative normalization was applied to the entire spectrum. The monochromator employed has two output slits, providing the possibility to detect fluorescence alternately either with a PMT or through a gated ICCD camera. LIF light from resonantly excited samarium atoms can be spectrally and temporally resolved using a monochromator and a gated ICCD camera (4 Quik E, Standard computer optics, Inc), respectively. Resonant

wavelength acquisition was performed using PMT-based detection system and wavelength was optimized for maximum LIF signal. The wavelengths chosen for the first- and second-step excitations were already used in our earlier work [60], where wavelength calibration was done using a U-Ne hollow cathode lamp and fabry perot etalon fringes. It was further cross-checked that the appropriate first energy level is excited by the laser by comparing the observed decay channels with the previously observed transitions from that level.

For observation and optimization of two-color LIF, single-color LIF signal was first optimized and the second laser was tuned for maximum two-color LIF signal. It was confirmed that the second laser excited atoms in the level populated by the first laser by blocking the first laser beam and checking that the signal disappeared. After optimization, LIF emission was directed towards the ICCD camera and it was pre-triggered by 40 ns for compensating its internal trigger propagation delay time. A fast photodiode was used to observe the laser pulse in the interaction zone with respect to trigger pulse. Different neutral density filters, whenever required, were inserted in the exciting laser path to avoid the saturation effects and to ensure a linear response of the detection system. It displays all resonant and non-resonant decay channels within the spectral range of monochromator.

For measurement of excited-level-to-ground-level transition probabilities, we have measured radiative lifetimes and branching fractions of low-lying odd-parity energy levels using single-color laser excitation. Laser was scanned in the wavelength region 556 – 572 nm to resonantly excite Sm atoms to the excited odd-parity energy levels in the energy region 17769.71-19990.25 cm^{-1} . We have confirmed that the right energy level is

populated by observing the known decay channels from that level. For measurement of excited-state-to-excited-state transition probabilities, we have used two-color two-step resonant excitation. For excited-level-to-excited-level transition probabilities measurements, the first-step excitation laser was tuned to 591.6 nm to excite the samarium atoms from 293 cm^{-1} to 17190 cm^{-1} and the second-step excitation laser was tuned from 558 – 568 nm to further excite Sm atoms from the first excited level to different second-excited high-lying even parity energy levels.

2.2.2.2 Results and discussion

One of the resonant or non-resonant decay channels was chosen to measure the lifetime of the excited state. The fluorescence counts were recorded as a function of delay between the trigger pulse of ICCD and the opening of ICCD shutter for the exposure. Exposure time and delay of gate pulse with respect to trigger can be varied from 1 ns – 80 sec and 0 ns – 80 sec, respectively with minimum step of 0.1 ns. For the lifetime measurements, delay between the trigger pulse of ICCD and the opening of ICCD shutter for the exposure was varied till signal falls to just above the noise level. Background of ICCD camera was suitably subtracted from the actual fluorescence counts. The plot of the corrected fluorescence counts versus this delay was fitted exponentially to get the radiative lifetime of the excited level. The ICCD gain is set such that the maximum intensity during predetermined gate exposure time after excitation laser pulse does not saturate the ICCD camera. We have used the exposure time of 10 ns. With these conditions we could get counts corresponding to an average of 25 laser pulses per data point. Experiment was repeated fifteen times for each excited level of interest under different experimental conditions of laser pulse energy, atomic beam number density, etc.

to overcome any systematic error. The average of these measurements was adopted as the final radiative lifetime of the excited upper level. The statistical uncertainty in the lifetime values is estimated from the spread in the fitted lifetime values. Radiative lifetime values were also checked with other decay channels but the values remained same within the experimental errors.

Branching fractions of optical transitions from each excited level were determined from LIF light intensities of different decay channels to lower energy levels. Branching fraction was obtained for each decay channel from line intensities through $\beta_{ki} = I_{ki} / \sum_i I_{ki}$, where I_{ki} is intensity of the spectral line and sum is taken over all lower levels (i) to which upper level (k) decays. The spectra showing the fluorescence decay channels were recorded after the delay of 25 - 30 ns with respect to laser trigger pulse in order to cut down the contribution of laser scattering to resonant fluorescence. Experiment was repeated fifteen times under different experimental conditions as in the case of lifetime measurements. The average of these measurements was used to determine the branching fractions.

Transition probability A_{ki} was obtained from the measured values of lifetime and branching fraction using the expression $A_{ki} = \beta_{ki} / \tau$, where τ is the radiative lifetime of the excited level and β_{ki} is the branching fraction for the $k \rightarrow i$ transition

2.2.2.2.1 Radiative lifetimes of odd-parity and even-parity energy levels

Single-color laser excitation followed by time-resolved LIF was used to measure radiative lifetimes of seven odd-parity energy levels in the energy region 17769.71 - 19990.25 cm^{-1} . Fig. 2.4 shows spatially resolved LIF signal at different delays time with respect to laser pulse. Figure 2.5 shows a typical time-resolved single-color LIF decay

signal from the 18225.13 cm^{-1} energy level with an exponential fit. The radiative lifetimes of seven odd-parity energy levels in atomic samarium have been measured, which agree well with the earlier reported values [52]. We have further extended the measurements of radiative lifetimes of stepwise-excited even-parity energy levels reported in Ref. [60] using time-resolved two-color LIF. The measured radiative lifetimes of the six stepwise-excited even-parity energy levels are new as no data for these levels are reported in the literature.

2.2.2.2.2 Excited-level-to-ground-level transition probabilities

The absolute transition probabilities of 21 excited-level-to-ground-level transitions of Sm I were determined from the measured lifetimes of the first-excited level as mentioned above and the measured branching fractions of the fluorescence decay channels terminating on one of the levels of the $4f^6 6s^2 \text{ } ^7\text{F}$ ground septet. Figure 2.6 shows a typical single-color LIF spectrum from the excited level at 18475.28 cm^{-1} . We could observe all three-decay channels from each of seven excited energy levels allowed by selection rules. The values measured here are found to match well with those reported in the literature [64].

2.2.2.2.3 Excited-level-to-excited-level transition probabilities

High-lying even-parity energy levels of samarium atoms were selectively populated by two-step laser excitation. Lower odd-parity energy levels to which a stepwise-excited even-parity level decays via fluorescence decay channels were identified using the energy level information available in the literature [67]. The decay channels from stepwise-excited even-parity energy levels 34814.4 , 34924.0 , 34935.5 , 34972.1 , 35072.6 , 35092.1 cm^{-1} have been observed. Table 2.1 list the observed decay

channels from stepwise-excited even-parity energy levels 34935.5 cm^{-1} , measured branching fractions and absolute transition probabilities. Fluorescence decay channels, which are due to two-step resonant excitation (involving λ_1 and λ_2), are used for obtaining the values of branching fractions. With these sets of experiments absolute transition probabilities for 51 excited-state-to-excited-state transitions in atomic Sm have been determined for the first time, as they are not reported in the literature so far.

2.2.2.2.4 Assignment of J-values

Examination of J values of the lower energy levels to which the stepwise-excited even-parity energy level decays via fluorescence decay channels has led us to assign unique J values to the six stepwise-excited even-parity energy levels. Table 2.2 lists the stepwise-excited even-parity energy levels and their unique angular momentum values thus obtained. This technique of J identification is relatively simpler and does not require excitation to the same energy level by different excitation routes.

2.2.2.3 Systematic uncertainties in the measurements

The difficulty in measuring the absolute transition probabilities employing most of the conventional techniques is due to either the uncertainties in measurement of absolute number densities of the interacting atoms or the intensity of laser photons used for excitation. Lifetime-branching fraction method used in this paper is intrinsic in nature and the value of measured transition probability does not depend on accurate measurement of number density of atoms and photons but on the error in measurement of lifetimes of the excited levels and the branching fractions. The accuracy of the measurement of atomic transition probability using this method depends on how accurately the lifetime and branching fraction measurements are made.

The statistical uncertainty in our measurements of lifetime is $\sim \pm 10\%$, based on the spread in the fitted lifetime values to the time-dependent LIF signals. Apart from this statistical uncertainty, there could be various effects causing systematic uncertainties in the lifetime measurements, such as radiation trapping, collisional depopulation, atomic motion, cascade repopulation and depopulation, Zeeman and hyperfine quantum beats [54]. The radiation trapping is insignificant in our experiments carried out in a Sm atomic beam with number density in the laser-interaction zone $\sim 10^{11}$ atoms/cm³. We have not observed any change in the measured values of lifetime even at higher permissible oven temperature or number density. The collisional depopulation of excited levels is also insignificant in the present work as it has been carried out in a vacuum chamber evacuated to a pressure of 10^{-5} torr. We have not found the evidence of collisional quenching even at a pressure of 10^{-4} torr. As far as the atomic motion effect is concerned, the lifetime can be shortened owing to the fact that the radiative atoms can move out into a region of lower collection efficiency. This effect is negligible in the case of short-lived levels with lifetime less than 200 ns as the transit time of atoms is few microseconds. Since our measured lifetime values are less than 200 ns, the systematic error due to this effect is negligible. The selective excitation of levels using lasers eliminates the possibility of cascade repopulation from higher-lying levels. There could be some modulations in the observed fluorescence intensity due to Zeeman and hyperfine quantum beats. The residual magnetic field in the interaction zone due to current flowing in the heater for generation of Sm atomic beam was very small (~ 60 mG). The natural abundance of odd Sm isotopes is about $\sim 28\%$, so only 28% of the total fluorescent signal can be modulated due to hyperfine quantum beats. We have not observed any modulation

in the fluorescence decay curves due to these effects. Our values of the lifetimes are free from the common systematic errors. Thus, the systematic uncertainties have been neglected because any possible small contribution due to systematic errors would not change the uncertainty beyond the statistical value of 10%.

The accuracy of the branching fraction measurements requires very wide wavelength coverage to the maximum range possible for simultaneous measurements of all spectral decay channels and knowledge of the energy level spectrum, especially for complex atoms. Missing branches to unknown levels, unobserved decay channels due to low line-strengths or incomplete wavelength coverage can have significant effects on the branching fraction values obtained.

The statistical uncertainty in our β measurements estimated from the spread of β -values measured under different experimental conditions is $\leq 10\%$. The spread is minimum $\sim 5\%$ for the strong transitions and maximum 10% for weak transitions. The maximum value of 10% is taken for estimation of uncertainties. The uncertainty of calibration of the lamp with the uncertainty of the response of spectrometer using this lamp is about 6 %. These two uncertainties are combined in quadrature with the uncertainty in lifetime measurements to give the uncertainty of $\sim 15\%$ in the measurement of transition probabilities. This estimate of uncertainty is without considering the infrared (IR) transitions.

The non-observation of allowed transitions in the IR region is a systematic uncertainty in the branching fraction measurement, limiting its accuracy. Biemont et al. [68] have observed in the spectrum of Sm III that the IR transitions are mostly weak transitions and do not give a significant contribution. But, if there are many transitions of

weak intensity - a distinct possibility that they could add up to as much as 20% or more of total decay as mentioned by Wickliffe et al. [69] in the nearby spectrum of Dy I. Although the contribution of IR transitions to uncertainty is dependent on element and transition, this could lead to a systematic uncertainty ranging from negligibly small value to 20 % or more in the branching fraction measurements of Sm transitions considered, in addition to the statistical uncertainties. Similarly overall uncertainties in transition probability measurements will increase due to contribution from IR transitions.

2.3 Simultaneous laser-induced fluorescence and photoionization signals

We have mentioned in our earlier work [60] that laser-induced photoionization (LIP) and laser-induced fluorescence (LIF) techniques can be used in a complementary manner for better understanding of atomic spectra. It was stated on the basis of comparison of resonances observed in our two-color fluorescence spectra with the two-color, three-photon photoionization spectra observed by different authors [61, 70]. Since the experiments employing these techniques of LIF and RIS were performed under different experimental conditions, direct comparison of the results was difficult. However, simultaneous use of these techniques can help in better understanding of spectra. But simultaneous detection of LIP and LIF signals has been rarely used for studying these elements [39].

In order to compare the results obtained in LIF with those obtained in RIS under similar experimental conditions (laser power, atom number density etc.), the two-color laser-induced fluorescence and two-color, three-photon photoionization signals have been simultaneously monitored in atomic samarium. This work is presented in this section [71]. The observation of features in the two spectra recorded simultaneously validates the

complementary nature of these two techniques. To the best of our knowledge, simultaneous laser-induced fluorescence and photoionization signals have been used for the first time to study high-lying even-parity energy levels. The LIP and LIF signals have also been studied as a function of the second-step laser power to investigate the behavior of both the signals under varying laser powers.

2.3.1 Experimental details

The detail of the experimental set up is already mentioned in section 2.2.2.1 of this Chapter. Modifications have been made to detect the photoion signal. The experimental setup for simultaneous detection of RIS and LIF signals is shown in Fig. 2.7. The photoion signal was detected using a parallel-plate configuration and applying – 1 kV to the plates across a load of 5 k Ω . The photoion detection system was in cross-configuration with laser and atomic beams, like the fluorescence collection assembly. Because of the fluorescence assembly being in a straight line with the photoion system, one of the plates was made of fine wire mesh with light transmission efficiency of about 80% so that the maximum of fluorescence light passed through it and reached the fluorescence collection assembly, consisting of a couple of plano-convex lenses.

2.3.2 Methodology

In the chosen photoionization pathway (Fig. 2.8), samarium atoms from one of the ground state septet at 1489.55 cm⁻¹ (J=3) were excited to odd-parity energy level at 19009.52 cm⁻¹ (J=2) by the first laser. The first-step laser wavelength was fixed by observing the non-resonant fluorescence signal from the energy level at 19009.52 cm⁻¹ decaying to energy level at 811.92 cm⁻¹. Once the first-step laser induced fluorescence is optimized, the second laser was scanned to further excite the atoms to the intermediate

even-parity levels between $36510\text{-}36875\text{ cm}^{-1}$. Another photon of the second laser was good enough to raise the atoms above continuum (ionization potential $\sim 45519\text{ cm}^{-1}$) leading to photoionization. The photoionization signal along with the fluorescence signal from the second-excited even-parity energy level was simultaneously recorded as a function of the second-step laser power. The monochromator was set in such a way that it cuts off the laser scattering from the first and second-step lasers. The sum of non-resonant fluorescence falling in the band pass of the monochromator has been detected through PMT. A portion of the two-color laser-induced fluorescence spectrum is shown as the top spectrum in Fig. 2.9. In the present work, the monochromator is used as a filter which cuts down the contributions from the first and second-step lasers. The monochromator central wavelength was kept at 520 nm and slits are set in such a way that it provides a band pass of 40 nm (± 20 nm with respect to central wavelength). Reducing the band pass may also limit collection of decaying fluorescence channels. So, the contributions from the lasers cannot be fully nullified as the monochromator does not sharply cut off beyond the band pass and some contribution from the lasers still reaches the output slit of monochromator. So, the fluctuations in laser always provide noisy base line as shown in the top spectrum of Fig. 2.9. In this situation, the detection of weak signals becomes difficult. To improve the signal-to-noise (S/N) ratio, a notch filter, which cuts off sharply between 550-600 nm and pass the other wavelength has been introduced in the input slit of the monochromator. The notch filter cuts down the laser contributions completely and allows the monochromator to be used in higher band pass and throughput mode. The monochromator now is used not only as a second filter but it remains as an integral part of experimental setup as in our earlier work for acquiring the first-step laser

wavelength by optimizing the fluorescence from the first excited state [60]. The notch filter is placed only after the first-step wavelength is acquired by optimizing single-color fluorescence. The background noise for LIF signals was about 5% of maximum signal without filter. The noise was reduced to 1%, when a notch filter is used. The improvement in the S/N ratio is evident from the middle spectrum of Fig. 2.9. For filtering out the single color features, the spectrum is repeated with first-step laser blocked as shown in the bottom spectrum of Fig. 2.9. For absolute wavelength calibration, an optogalvanic signal from U-Ne hollow-cathode discharge lamp, induced by scanning dye laser, was recorded. Interference fringes, produced by a part of the dye laser beam in an air-spaced etalon (free spectral range = 0.5 cm^{-1}) and detected by a photodiode, were simultaneously recorded, to provide dispersion scale. At one of the strong two-color fluorescence features, we attempted to observe the two-color, three-photon photoionization signal simultaneously. To ensure the sequential absorption of photons from two dye lasers, temporal pulse of second-step dye laser was delayed to an extent that both the dye-laser pulses were separated in time domain, i.e., temporally non-overlapping. So, the second-step laser is delayed with respect to the first-step laser by 7 ns (FWHM of laser pulse duration). Both the laser beams were then spatially aligned with respect to each other and with the atomic beam. For maximum excitation efficiency, both the dye lasers were ensured to be spatially overlapping.

Two-color fluorescence and two-color, three-photon photoionization signals of Sm along with uranium optogalvanic signal and Fabry-Perot etalon fringes have been processed through four different boxcar averagers for spectrum recording. Figure 2.10 shows various signals and Fabry-Perot etalon fringes recorded using a photodiode. The

spectra from top to bottom represent Fabry-Perot etalon fringes (free spectral range 0.5 cm^{-1}), uranium optogalvanic signal, two-color laser-induced fluorescence and two-color, three photon photoionization signals respectively. The experiments were repeated and spectra between $36510\text{-}36875 \text{ cm}^{-1}$ were recorded several times.

2.3.3 Results and discussion

The two-color fluorescence and two-color, three photon photoionization signals have been analyzed. The results have been compared with those reported in the literature. Although most of the features were observed in both the spectra, we observed that some of the resonant features in two-color fluorescence spectra were non-observable in two-color, three-photon photoionization spectra and vice versa. Similar situation was reported in our earlier paper, where a plausible explanation was given regarding the origin of both the signals [60]. The two-color laser-induced fluorescence signal is proportional to the product of $\sigma_1 I_1$ and $\sigma_2 I_2$. Here, σ_1 and σ_2 are the first and second-step transition cross-sections and I_1 and I_2 are the first and second-step laser intensities respectively. The two-color, three-photon photoionization signal is proportional to the product of $\sigma_1 I_1$, $\sigma_2 I_2$ and $\sigma_3 I_2$, where σ_3 is the photoionization cross-section for the third-step transition as another photon of the second-step laser is used to ionize the atom from the second-excited energy level. In that work, we have compared our two-color fluorescence results with the two-color, three-photon photoionization results of other researchers [61, 70]. Since in our earlier work [60], the comparison of LIF and RIS signals were based on different experimental conditions (laser power, atom number density etc.), in this work, we recorded both the signals together under the similar experimental conditions. The missing features in two-color fluorescence in comparison to two-color, three-photon

photoionization signal can be due to the weak second-step cross-section, however a strong autoionization connection can make it observable in two-color, three-photon photoionization signal. The other reasons like improper optical alignment between fluorescence collection optics, monochromator, PMT, poor S/N ratio and fluorescence falling outside the band pass of filter can also lead to non-detection of fluorescence signal. As we have mentioned earlier, by introducing an additional filter in the fluorescence collection path, which cuts down completely the scattering contribution from the lasers, helped us to improve the signal-to-noise-ratio. By carefully aligning the optical components to improve fluorescence collection efficiency, we could observe all the features in the two-color laser-induced fluorescence spectra, which were observed in the two-color, three-photon photoionization spectra. The missing features in two-color, three-photon photoionization spectra in comparison to two-color fluorescence can arise due to weak second-step cross-section and absence of strong autoionization for termination in the final step through another photon of the second laser. To confirm the given explanation, we have recorded the two-color fluorescence and two-color, three-photon photoionization signals as a function of second-step laser (λ_2) power. The second-step laser power was attenuated by introducing neutral density filters in the path of second-step dye laser keeping the first laser power same throughout the experiments. A portion of the two-color fluorescence and two-color, three-photon photoionization signals at 10%, 30%, 100% powers of second-step laser is shown in Figs. 2.11 and 2.12 respectively. The first-step laser energy was about $30 \mu\text{J}/\text{cm}^2$. The second laser was tuned within the available dye tuning range from 558 nm to 572 nm. The maximum pulse energy at 565 nm was about $400 \mu\text{J}/\text{cm}^2$, which represents the 100% power in Figs. 2.11

and 2.12. The background noise of less than 1% of maximum signal was attained in all the spectra (Figs. 2.10-2.12). Total maximum of five features are visible in the representative scan of Figs 2.11 and 2.12. At 10% power level of the second laser, only four and two features out of five are visible in the respective fluorescence and photoionization spectra. As the power was increased, all the five features appeared in both the spectra. But if one would have recorded the two-color, three photon photoionization spectra at 10% laser power, only two features could have been obtained, whereas the resultant fluorescence spectra could have provided four features in the same region. All the spectra shown in the Figs. 2.11 and 2.12 are recorded using the same sensitivity except the top spectra (signals at 10% power) of Figs 2.11 and 2.12. These spectra are recorded at higher sensitivity by a factor of 2. So, the signals should be treated as half in the relative scale. However, good S/N ratio is necessary for the detection of weak signals in both the spectra. Hence, the two-color, three-photon photoionization spectroscopy technique, which is the most sensitive technique, can result in incomplete spectral information unless the power requirement to saturate the final ionization step terminating to continuum is fulfilled. However, in the two-color fluorescence, the laser pulse energy requirement to saturate the second-step transition necessary to be fulfilled, is much less (from few $\mu\text{J}/\text{cm}^2$ to few hundred $\mu\text{J}/\text{cm}^2$) than the pulse energy requirement to saturate the third or final ionization step transition terminating in continuum or weak autoionization state (from few hundred $\mu\text{J}/\text{cm}^2$ to few thousand $\mu\text{J}/\text{cm}^2$). It is also evident from the top spectra of Figures 2.11 and 2.12 respectively, where the fluorescence spectra provided more number of features. We could observe all the high-lying even-parity energy levels possible by angular momentum selection rule ($\Delta J=0, \pm 1$), which are

reported in the literature [61, 71-78] except the one at 36536.8 cm^{-1} [73, 75, 78]. The plausible reason for the non-observance of this level may be the weak transition probability for the $19009.52\text{-}36536.8 \text{ cm}^{-1}$ transition. Moreover, this transition also falls at the end the dye tuning curve in the present study. The Table 2.3 compares our results with those reported in the literature. Only those features are considered for energy level assignment, which have the signal-to-noise-ratio better than five. The minimization of experimental errors is crucial in order to ensure the accuracy of experiment data, has been done in the current work. The possible errors could arise from absolute calibration of spectrum and nonlinearity in the dye laser scan. As mentioned above, the wavelength of the dye laser is absolutely calibrated with optogalvanic spectra of uranium neon hollow-cathode lamp whose spectral lines are known accurately. It is also relatively calibrated by the transmission spectrum of a Fabry–Perot etalon to correct the nonlinearity in each scan. The uranium provides rich spectra so many uranium lines are used as the reference lines along with Fabry Perot etalon fringes for energy value assignment of even-parity energy levels of atomic samarium. Furthermore, every spectrum has been repeated several times to reduce the statistical errors. The energy values (wavenumbers) listed in the Table 2.3 is an average of measurements on several spectra recorded. The results are reproducible to within $\pm 0.20 \text{ cm}^{-1}$. We have also obtained resonances at 36741.44 and 36848.43 cm^{-1} , which are not reported in the literature. The plausible reason for the observance of these levels may be the moderate or strong transition probability for the $19009.52\text{-}36741.44$ and $19009.52\text{-}36848.43 \text{ cm}^{-1}$ transition. So, two new even-parity energy levels based on these resonances are reported here with probable angular momentum (J) values 1-3, as the intermediate odd-parity energy level (19009.52 cm^{-1})

has the J value of 2. For all other energy levels, unambiguous J- values are taken from the literature. All the energy levels reported in Table 2.3 have been observed by both the techniques except the energy level at 36848.43 cm^{-1} , which was observed only with LIF.

Using the above mentioned experimental setup, radiative lifetime of atomic samarium for the energy level 19009.52 cm^{-1} has been measured using both LIP and LIF techniques [78]. The two-color fluorescence and two-color, three photon photoionization signals were recorded on a digital oscilloscope as a function of delay between pump and probe lasers. The resultant decay curves provide the lifetime values of 19009.52 cm^{-1} level using the both techniques. The results were found to be same within the experimental errors by both the techniques and match well with those reported in the literature [52,65]. The measured lifetime value for the energy level of samarium at 19009.52 cm^{-1} was found to be $47\pm 4\text{ ns}$. It is established from this that the lifetime can be measured by employing any of these techniques. For the lifetime measurement of first-excited state energy levels using photoionization technique, the energy of first laser and twice the energy of second laser should be more than the ionization potential of material. But, these conditions need not to be fulfilled using fluorescence technique. On the other hand, for the measurements of lifetime for the second-excited state energy levels, if the sum of first, second and third laser energy is more than ionization potential of material, fluorescence technique cannot be used but the photoionization technique can be used. So, using laser-induced fluorescence and photoionization techniques simultaneously, lifetime of all energy levels can be measured, irrespective of lasers energies and ionization potential of material.

In this work, the two-color laser-induced fluorescence and two-color, three-photon photoionization spectra of atomic samarium in the energy region 36510-36875 cm^{-1} have been recorded simultaneously. Total 21 resonances have been obtained in this energy region. By comparing our results with those reported in the literature, two new energy levels at 36741.44 and 36848.43 cm^{-1} have been obtained. Although, the resonance ionization spectroscopy is most sensitive spectroscopy technique, but in some cases the spectra obtained using two-color, three-photon photoionization technique can provide the incomplete energy level information unless the stringent pulse energy requirement to saturate the ionization step, which is terminating in continuum or weak autoionization state, is fulfilled. As the energy requirement to saturate the second-step transition is much less than the third-step transition, the two-color fluorescence can provide more useful energy level information. In some cases, the weak second-step transition may be difficult to be observed in two-color fluorescence, but if the ionization-step is terminating in strong autoionization resonance, then it can be observed using two-color, three-photon photoionization technique easily. These facts were experimentally observed, when both the signals were recorded at different second-step laser (λ_2) energies and the given explanation was authenticated experimentally. If the pulse energy is good enough to saturate the respective transitions, signals can be obtained by any technique. But, the energy requirements cannot always be fulfilled due to limited pulse energy available and some of the weak transitions can fall at the edge of the dye tuning range. So, the complete energy level information can be obtained when both the two-color laser-induced fluorescence and two-color, three-photon photoionization techniques are used simultaneously to investigate the high-lying energy levels of atoms.

The radiative lifetime of the odd-parity energy level 19009.52 cm^{-1} of Sm I has been measured using simultaneous laser-induced fluorescence and photoionization signals by employing the pump-probe technique. The emphasis was not to generate volume of new data but to compare laser-induced fluorescence and photoionization techniques for such measurements. The lifetime values obtained using laser-induced fluorescence and photoionization techniques match well with each other and with those reported in the literature. To the best of our knowledge, this is for the first that laser-induced fluorescence and photoionization techniques are used simultaneously to measure lifetime and the results are compared with each other as well as with other reported values. The technique used here can be universally applicable for other energy levels of interest as well as for other materials.

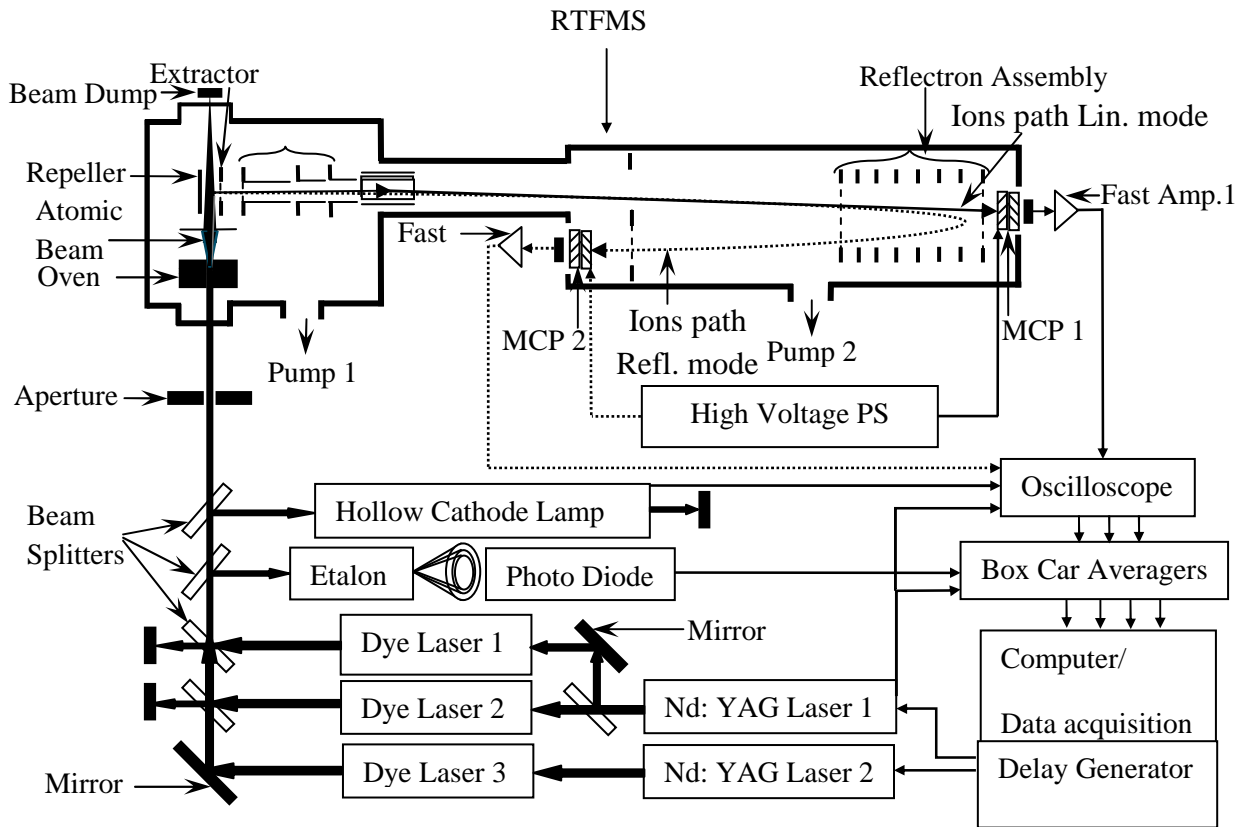


Fig. 2.1: Experimental setup for measurement of radiative lifetime

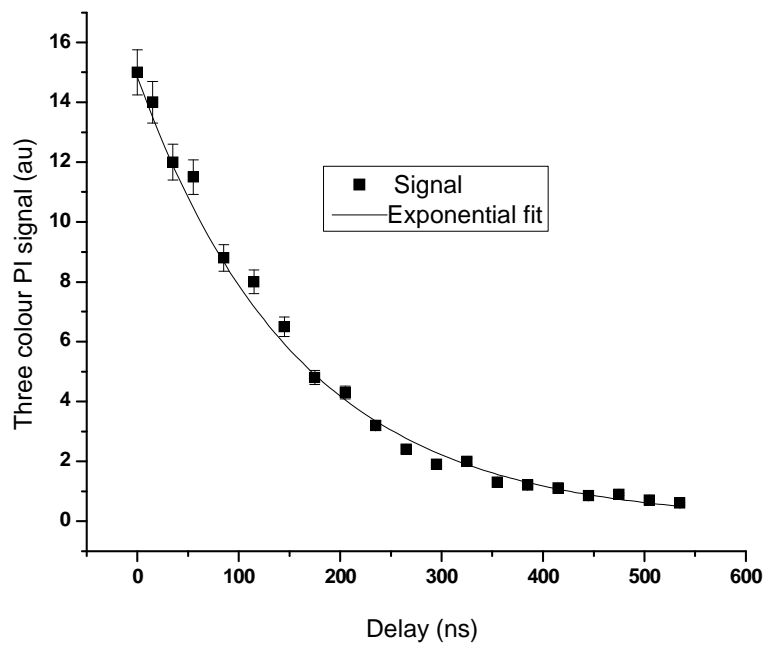


Fig. 2.2: Exponential fit of photoionization signal of high lying odd-parity energy level of uranium at 34071.24 cm^{-1} ($\tau=157\pm11 \text{ ns}$)

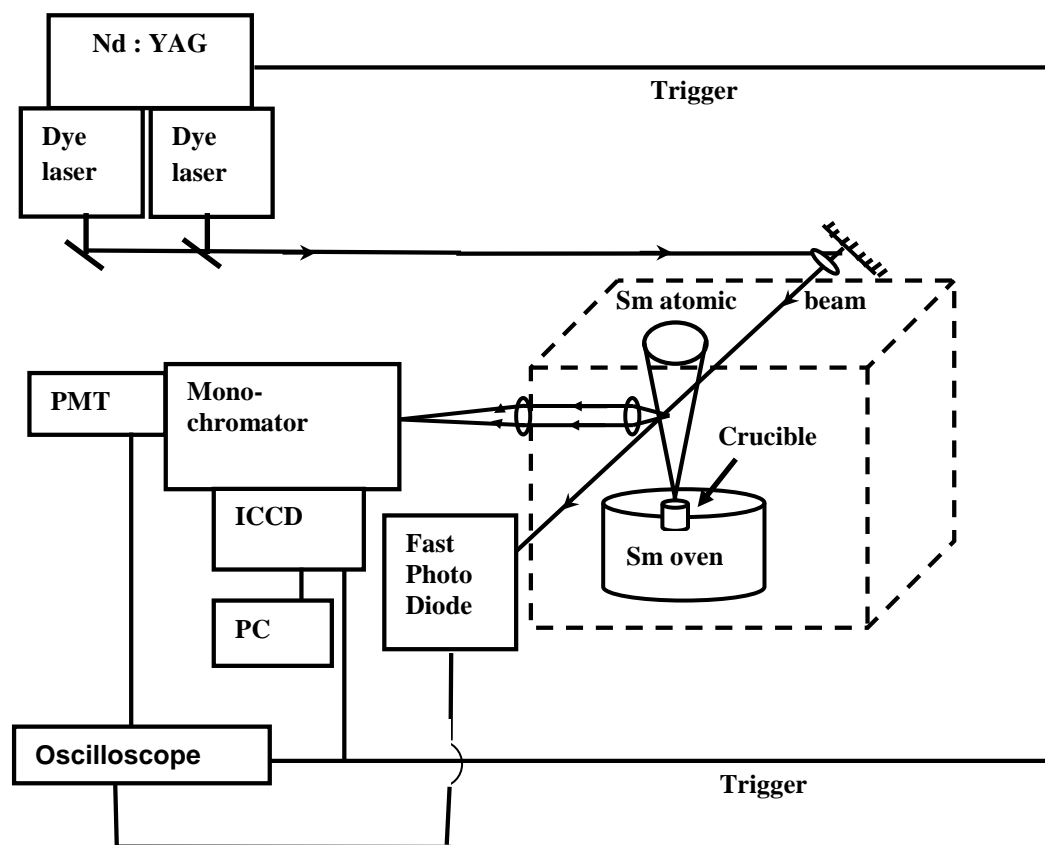


Fig 2.3: Experimental setup for laser-induced fluorescence experiments



LIF signal at 30 ns delay



LIF signal at 80 ns delay



LIF signal at 120 ns delay

Fig. 2.4: Spatially-resolved LIF signal at different delays time with respect to laser pulse

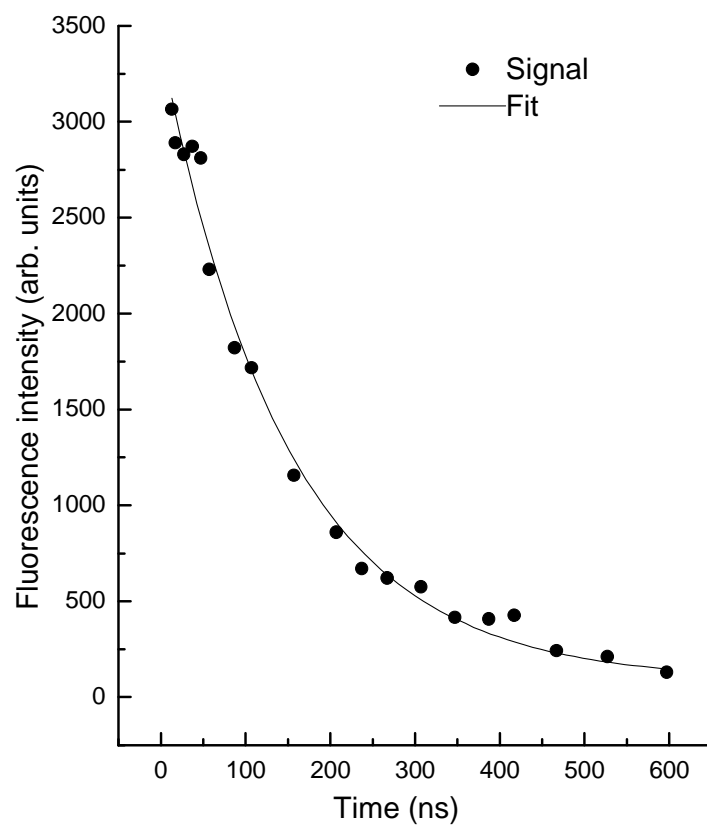


Fig. 2.5: Experimental time-resolved single-color LIF decay signal with an exponential fit. The lifetime for this level (18225.13 cm^{-1}) is measured to be 143 ± 10 ns

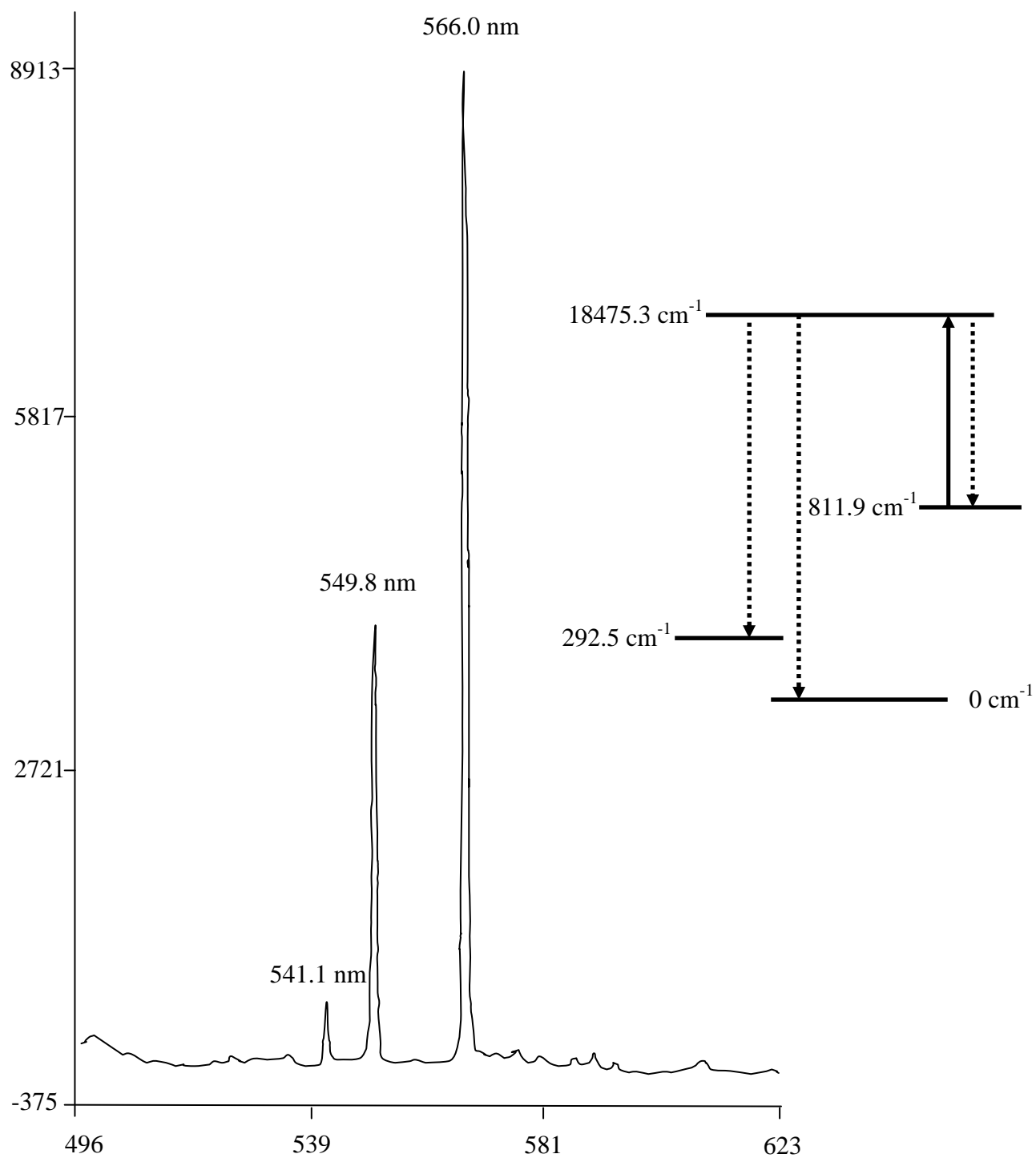


Fig. 2.6: Spectrally resolved LIF showing three different decay channels from the excited energy level at 18475.28 cm^{-1} . In the inset, the solid line represents laser-induced excitation and the dotted lines represent the observed fluorescence

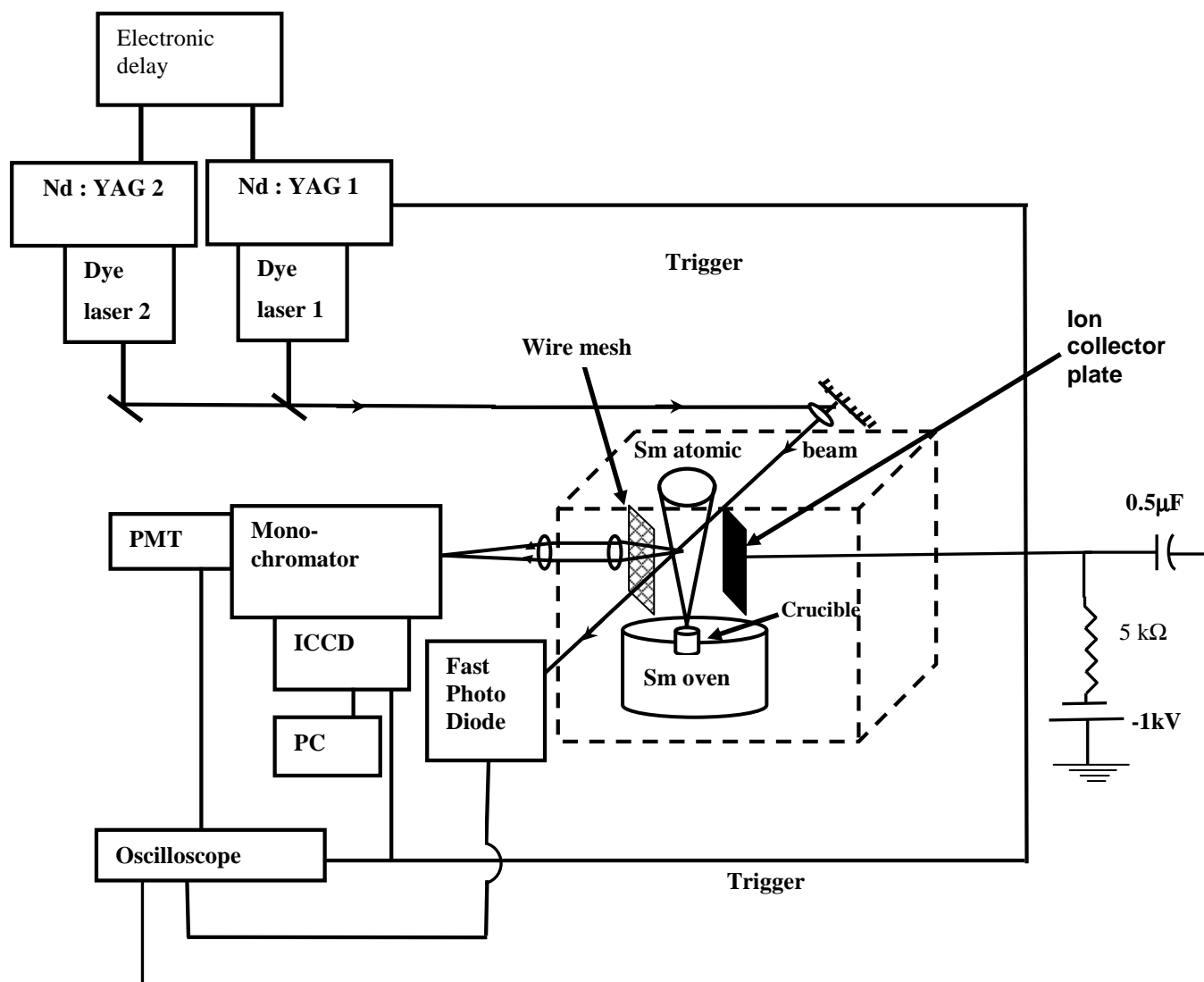


Fig. 2.7: Experimental setup for simultaneous observation of two-color laser-induced fluorescence and two-color three-photon photoionization signals

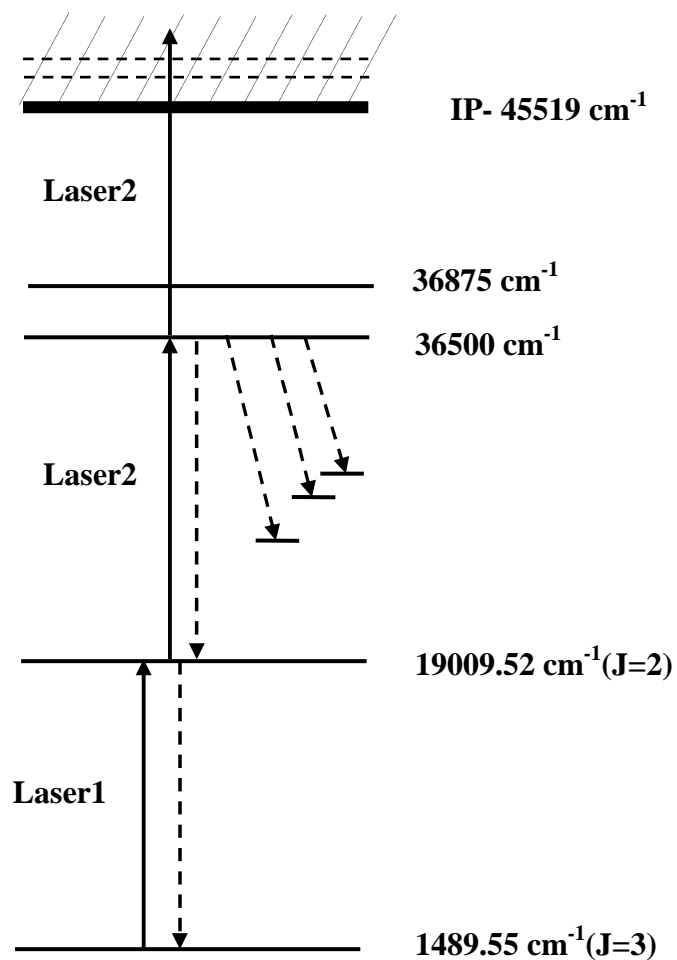


Fig. 2.8: Energy level diagram for two-color, three-photon photoionization and two-color laser-induced fluorescence. The second laser was scanned to access the energy levels between 36500 and 36875 cm^{-1}

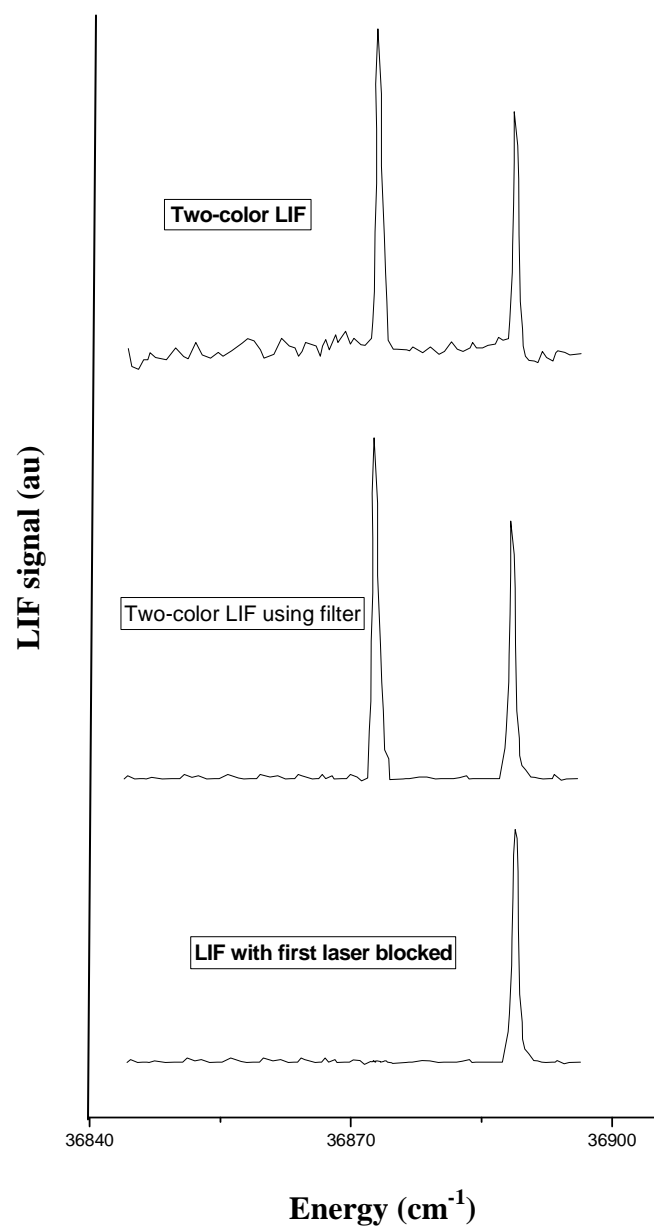


Fig. 2.9: Signal-to- noise ratio improvement using wavelength filter in laser-induced fluorescence signal

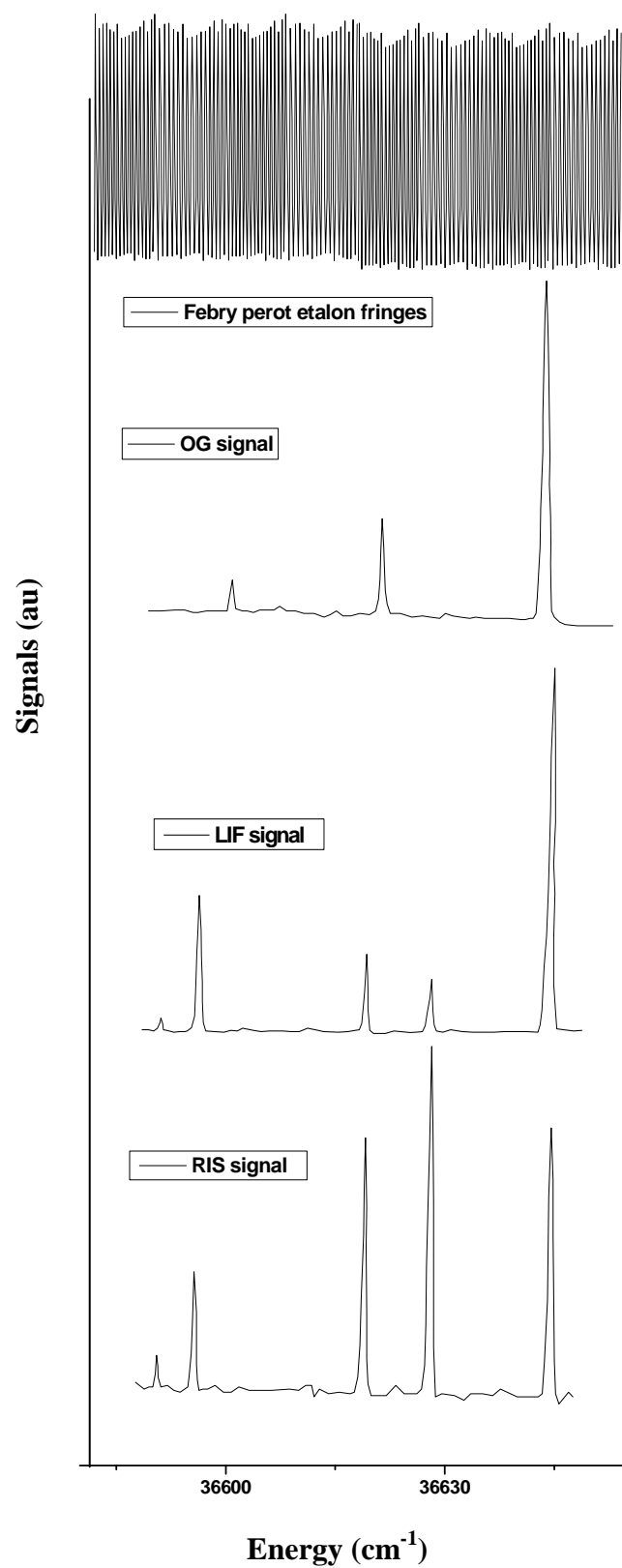


Fig. 2.10: Simultaneous recording of two-color laser-induced fluorescence and two-color, three-photon photoionization signal along with uranium optogalvanic signal and Fabry-Perot etalon fringes for wavelength calibration of spectra

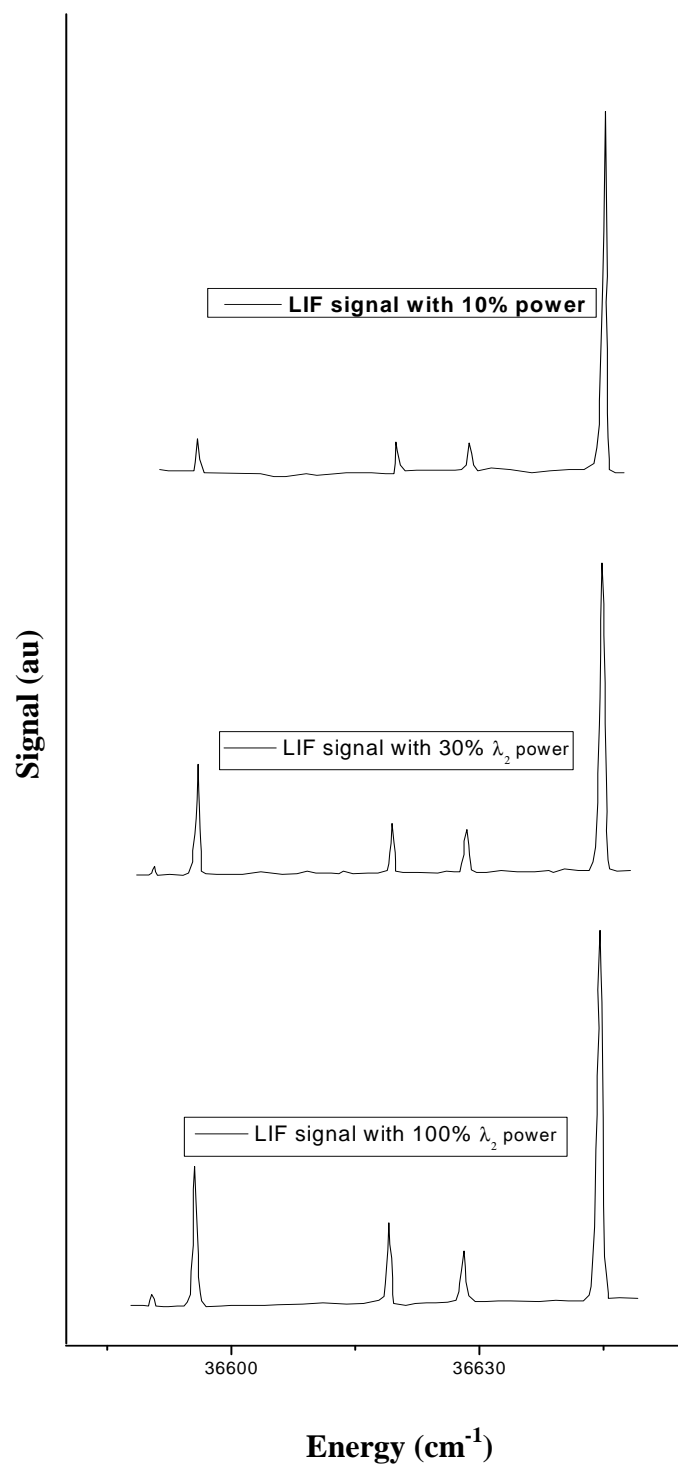


Fig. 2.11: Two-color laser-induced fluorescence spectra as a function of second-step laser power

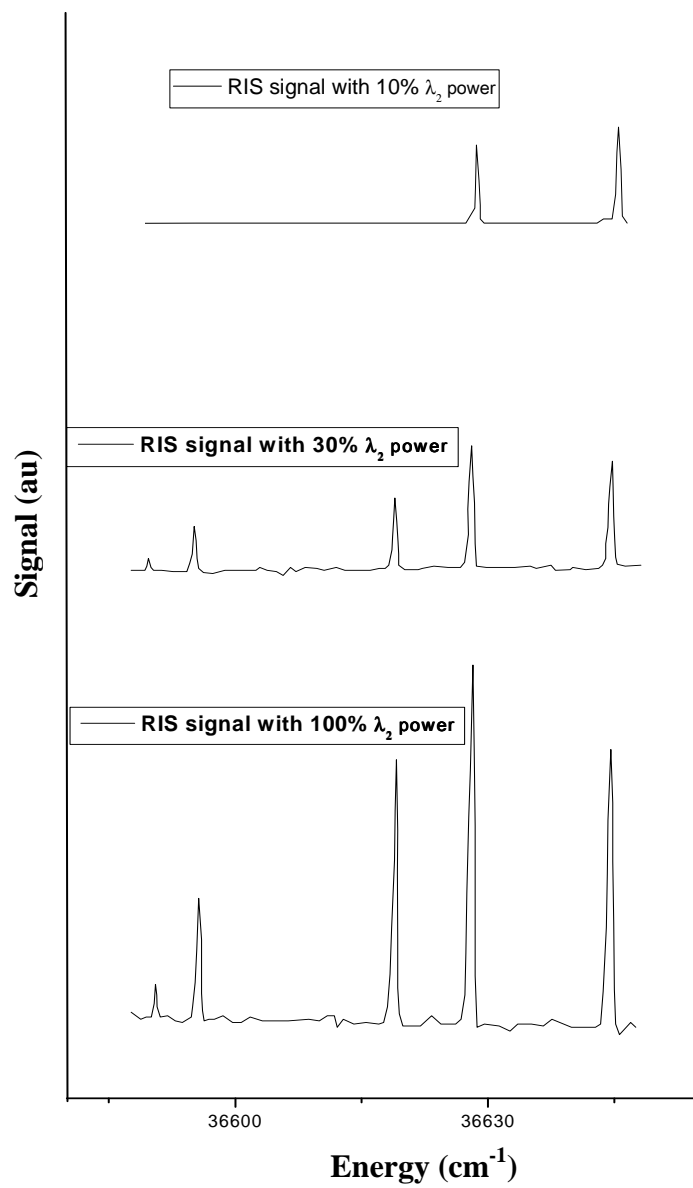


Fig. 2.12: Two-color, three-photon photoionization spectra as a function of second-step laser power

Table 2.1 Measured branching fractions and transition probabilities of the transitions from the stepwise-excited even-parity energy level at 34935.5 cm^{-1} to various lower odd-parity levels using two-colour laser-induced fluorescence with $\lambda_1 = 591.64 \text{ nm}$ and $\lambda_2 = 563.36 \text{ nm}$.

Energy of lower level (cm^{-1})	J-value of lower level	Fluorescence wavelength (nm)	Intensity (arb. units)	Branching fraction	Transition probability (10^6 s^{-1})
14380.50	2	486.3	315	0.084	1.1
14863.85	1	498.1	101	0.027	0.3
14915.83	3	514.6	177	0.047	0.6
15567.32	2	516.1	1302	0.346	4.4
16116.42	2	531.2	321	0.085	1.1
16748.30	3	549.7	326	0.087	1.1
17769.71	1	582.4	265	0.071	0.9
17830.80	3	584.4	315	0.084	1.1
18209.04	3	597.7	281	0.075	1.0
18328.64	3	602.0	361	0.096	1.2

Table 2.2 Assigned values of the total angular momentum J to each of the stepwise-excited even-parity energy levels in atomic samarium based on examination of J-values of the lower odd-parity levels to which a stepwise-excited even-parity level decays, removing the ambiguity from the proposed J-values in Ref [60].

Even-parity energy level (cm ⁻¹)	J -value
34814.4	2
34924.0	2
34935.5	2
34972.1	3
35072.6	1
35092.1	3

Table 2.3 High-lying even-parity energy levels of atomic samarium

S	Energy value from our	Reported values	Reported J-values
No	measurements (cm ⁻¹)	(cm ⁻¹)	
1	36515.19	36515.18 ^b	2
		36515.40 ^c	2
		36515.39 ^d	2
		36515.18 ^e	2
		36515.40 ^g	2
2	36535.44	36535.13 ^b	3
		36535.30 ^c	3
		36535.30 ^g	3
3	36565.29	36565.62 ^b	1
		36565.50 ^c	1
		36565.28 ^d	1
		36565.02 ^e	1
		36565.50 ^g	1
4	36571.94	36572.90 ^b	3
		36572.00 ^c	3
		36572.09 ^d	3
		36572.00 ^g	3
5	36587.29	36587.50 ^b	3

		36587.40 ^c	3
		36587.27 ^d	3
		36587.40 ^g	3
6	36592.74	36593.53 ^b	2
		36592.80 ^c	2
		36592.71 ^d	2
		36592.65 ^e	2
		36592.80 ^g	2
7	36618.94	36619.00 ^b	2
		36618.10 ^c	2
		36618.88 ^d	2
		36618.80 ^g	2
8	36628.14	36628.70 ^b	1
		36628.40 ^c	1
		36228.64 ^d	1
		36628.09 ^e	1,2
		36628.40 ^g	1
9	36644.56	36644.41 ^b	1
		36644.60 ^c	1
		36644.59 ^d	1
		36644.28 ^e	1,2
		36644.60 ^g	1

10	36682.46	36682.46 ^b	3
		36682.50 ^c	3
		36682.57 ^d	3
		36682.16 ^f	3
		36682.50 ^g	3
11	36701.54	36701.64 ^b	2
		36701.80 ^c	2
		36701.40 ^e	1,2
		36701.80 ^g	2
12	36741.44	-	1-3
13	36759.84	36760.30 ^b	2
		36760.10 ^c	2
		36759.84 ^e	1,2
		36760.10 ^g	2
14	36763.19	36763.20 ^b	3
		36763.20 ^c	3
		36762.99 ^f	3
		36763.20 ^g	3
15	36776.58	36776.80 ^b	3
		36776.50 ^c	3
		36776.39 ^f	3
		36776.50 ^g	3

16	36777.93	36778.73 ^b	2
		36778.20 ^c	2
		36778.20 ^g	2
17	36812.43	36812.80 ^b	3
		36812.80 ^c	3
		36812.63 ^f	3
		36812.80 ^g	3
18	36834.18	36834.70 ^b	1
		36834.90 ^c	1
		36834.55 ^e	1,2
		36834.60 ^g	1
19	36848.43	-	1-3
20	36855.53	36855.41 ^a	2,3
		36855.40 ^b	3
		36855.60 ^c	3
		36855.17 ^f	3
		36855.60 ^g	3
21	36873.33	36873.60 ^b	2
		36873.50 ^c	2
		36873.50 ^g	2

a-[Ref 72], b-[Ref 75], c-[Ref 78], d-[Ref 74], e-[Ref 76], f-[Ref 77], g-[Ref 78]

Chapter 3

Theoretical analysis of simultaneous laser-induced fluorescence and photoionization signals using density matrix formalism

The density matrix (DM) formalism [1-5] is well known to be the most accurate method to describe multi-step photoionization and photoionization of atoms by narrowband lasers as it incorporates the coherences induced between the atomic energy levels by the narrowband laser fields. It is an elaborate method involving detailed computational procedure. In order to derive the relevant equations of the DM formalism for the three-step photoionization process, we first consider a two-level atom system interacting with a pulsed narrowband laser and then generalize the formalism for a three-level atom system interacting with two pulsed narrowband lasers. The semi-classical approach is utilized to study laser-atom interaction [1]. In this approach, the laser radiation incident upon an atom is described by a classical electromagnetic (EM) plane wave, $\vec{E} = \vec{E}_0 \cos(kz - \omega t)$, whereas the atom is treated quantum-mechanically. Since the wavelength (λ) of light of our interest is much larger than the diameter of atom ($d \sim 0.5$ nm), the phase of the EM wave remains practically the same within the volume of the atom owing to the fact that $kz = \frac{2\pi z}{\lambda} \ll 1$ for $z \leq d$. Hence, one can omit spatial derivatives of the field amplitude. This is called the dipole approximation. In a coordinate system with its origin in the centre of the atom, one can assume $kz \approx 0$ within the atomic volume. Thus, the EM wave in the dipole approximation reduces to $\vec{E} = \vec{E}_0 \cos(kz - \omega t) = \frac{1}{2} \vec{E}_0 e^{-i\omega t} + c.c.$, where c.c. stands for the complex conjugate.

In quantum mechanics, a state of maximum knowledge is called a pure state. A wave function denoted by $|\Psi\rangle$ is utilized in the description of information of a pure state. The probability of finding the system in a specific state is obtained from $|\Psi|^2$. The wave function $|\Psi\rangle$ is expressed in terms of eigen functions φ_i , which are orthogonal to each other, i.e.

$$\langle \varphi_n | \varphi_m \rangle = \delta_{nm} \quad (3.1)$$

$$|\Psi\rangle = \sum_{i=1}^n c_i |\varphi_i\rangle \quad (3.2)$$

where $|c_i|^2$ is the probability of the system being in a state with an eigen function φ_i .

$$\delta_{mn} = 1, \text{ if } m = n \text{ and } \delta_{mn} = 0 \text{ if } m \neq n.$$

For instance, if one consider a two-level atom system, the wave function $|\Psi\rangle$ is written as

$$|\Psi\rangle = c_1 \varphi_1 + c_2 \varphi_2 \quad (3.3)$$

where φ_1 and φ_2 are the eigen functions of the two levels ‘1’ and ‘2’.

The density matrix operator “ ρ ” is the product of two state vectors

$$\begin{aligned} \rho &= |\Psi\rangle\langle\Psi| \\ &= \begin{pmatrix} \varphi_1 \\ \varphi_2 \end{pmatrix} (\varphi_1 \quad \varphi_2) \end{aligned} \quad (3.4)$$

which form a 2 x 2 matrix,

$$\rho = \begin{pmatrix} \rho_{11} & \rho_{12} \\ \rho_{21} & \rho_{22} \end{pmatrix} \quad (3.5)$$

For an n level atom, the density matrix is thus a n x n matrix.

The density matrix elements are related to observable quantities. The diagonal matrix elements ρ_{11} and ρ_{22} represent the probabilities of finding the atoms of the system in the levels $|1\rangle$ and $|2\rangle$, respectively. The non-diagonal matrix elements describe the coherences induced by the laser fields causing transition between the atomic levels.

3.1 Density matrix equations for interaction of laser light with a two-level atom system

The simplest problem involving laser-atom interaction is the coupling of a two-level atomic system with a laser light. Let us consider two energy levels $|1\rangle$ and $|2\rangle$ with energies E_1 and E_2 respectively of a two-level atom system (Fig. 3.1), interacting with an external monochromatic laser field [1]. Laser frequency ω is close to the transition frequency $\omega_{21} \equiv (E_2 - E_1)/\hbar$ with $\Delta = \omega_{21} - \omega$ as the laser detuning from the transition frequency. Here $\hbar = h/2\pi$, h being the Planck constant. If $\Delta = 0$, the transition induced by the laser field between the two-levels is in exact resonance with the laser frequency.

Time-independent atomic Hamiltonian (H_0) of a free atom without the laser field is written as

$$H_0 = \frac{\hbar^2}{2m} \nabla^2 + V(r) \quad (3.6)$$

where the first term incorporates kinetic energy $\frac{p^2}{2m}$ and $V(r)$ represents the static binding potential. Energy can be imparted to or taken from a quantum system only if system can jump from one state $|1\rangle$ to another state $|2\rangle$. A change from one state to another is induced if an external time-dependent field F_{ext} acts on this two-level atom system. The total Hamiltonian in the presence of the time-dependent field is expressed as

$$H = H_0 + V_{\text{ext}}(r, t) \quad (3.7)$$

where V_{ext} is some external (time varying) potential, which describes the interaction of the atom with the field and which reduces in the dipole approximation to .

$$V = \vec{p} \cdot \vec{E} = \vec{p} \cdot \vec{E}_0 \cos(\omega t) \quad (3.8)$$

where V is the scalar product of the dipole operator $\vec{p} = -e\vec{r}$ and the electric field \vec{E} . The time-dependent Schrodinger equation for the laser-atom system can be written as

$$\left(-\frac{\hbar^2}{2m} \nabla^2 + V(r) + V_{\text{ext}}(r, t) \right) \Psi(r, t) = i\hbar \frac{\partial \Psi}{\partial t} \quad (3.9)$$

The general solution $\Psi(r, t)$ of this equation can be expressed as a linear superposition of φ_n 's

$$\Psi(r, t) = \sum_{n=1}^{\infty} c_n(t) \varphi_n(r) \quad (3.10)$$

Since $\Psi(r, t)$ is time dependent, the specific sets of coefficients c_n which are used to write Ψ out of φ_n 's must also change in time, i.e. c_n 's are time dependent.

Applying this to the Schrodinger equation, one obtain

$$\sum_{n=1}^{\infty} c_n [H_0 + V_{\text{ext}}] \varphi_n(r) = \sum_{n=1}^{\infty} i\hbar \frac{dc_n \varphi_n(r)}{dt} \quad (3.11)$$

Using the fact that the $\varphi_n(r)$ is the solution set for time-independent Schrodinger equation, we have

$$H_0 \varphi_n = E_n \varphi_n \quad (3.12)$$

$$\sum_{n=1}^{\infty} c_n [E_n + V_{\text{ext}}] \varphi_n(r) = \sum_{n=1}^{\infty} i\hbar \frac{dc_n \varphi_n(r)}{dt} \quad (3.13)$$

Members of the set of functions $[\varphi_n(r)]$ that represents all possible solutions of the time-independent Schrodinger equation are complete, orthogonal and normalized. One uses the term orthonormal to express combination of orthogonality and unit normalization.

$$\begin{aligned}\langle \varphi_m | \varphi_n \rangle &= \int_{\text{all space}} d^3r \varphi_m^*(r) \varphi_n(r) = 0 \quad (\text{for } m \neq n) \\ \langle \varphi_n | \varphi_n \rangle &= \int_{\text{all space}} d^3r \varphi_n^*(r) \varphi_n(r) = 1 \quad (\text{for } m = n)\end{aligned}\tag{3.14}$$

The functions $\varphi_n(r)$ have unit self projections and one uses Kronecker delta symbol.

$$\begin{aligned}\langle \varphi_m | \varphi_n \rangle &= \int_{\text{all space}} d^3r \varphi_m^*(r) \varphi_n(r) = \delta_{mn} \\ \delta_{mn} &= 1 \quad \text{if } m = n \\ \delta_{mn} &= 0 \quad \text{if } m \neq n\end{aligned}\tag{3.15}$$

Taking projection of both sides of the equation onto one of the basic functions $\varphi_m(r)$, one obtains

$$\begin{aligned}i\hbar \frac{dc_m}{dt} &= E_m c_m + \sum_n c_n \int \varphi_m^*(r) V_{\text{ext}} \varphi_n(r) d^3r \\ &= E_m c_m + \sum_n V_{mn}(t) c_n\end{aligned}\tag{3.16}$$

where $V_{mn}(t) = \int \varphi_m^*(r) V_{\text{ext}} \varphi_n(r) d^3r$ is the matrix element of V_{ext} between states m and n . This equation is called the time-dependent Schrodinger equation and knowledge of c 's can be used to reconstitute the exact time-dependent wave function $\Psi(r,t)$.

The orthogonality relation yields

$$\int_{\text{all space}} \varphi_m^*(r,t) \varphi_n(r,t) d^3r = 1 \quad \text{for } m = n\tag{3.17}$$

This implies

$$\begin{aligned}
\int \left(\sum_m c_m \varphi_m \right)^* \left(\sum_m c_m \varphi_m \right) d^3r &= 1 \\
\sum_m c_m^* \sum_m c_m \langle \varphi_m | \varphi_m \rangle &= 1 \\
\sum_m c_m^* c_m \langle \varphi_m | \varphi_m \rangle &= 1 \\
\sum_m c_m^* c_m &= 1 \\
\sum_m |c_m|^2 &= 1
\end{aligned} \tag{3.18}$$

Each term in this equation is identified as the state probability. The squared amplitude $|c_m|^2$ is the probability that the quantum system is in its m th state at time t . The sum of the probabilities of the system in all the states is unity at time t .

Let the electron of an atom interact with an external laser field to create the externally induced potential,

$$V_{ext}(r, t) = -e\vec{r} \cdot \vec{E}(t) \tag{3.19}$$

where \vec{r} is electron-nuclear distance. The integral V_{mn} is written as

$$V_{mn} = -e\vec{E} \cdot \int \varphi_m^* \vec{r} \varphi_n d^3r \tag{3.20}$$

Since \vec{r} has odd-parity, the integrals V_{mm} and V_{nn} vanish when integrating over all coordinates from $-\infty$ to $+\infty$. The quantity $D_{mn} = D_{nm} = -e \int \varphi_m^* \vec{r} \varphi_n d^3r$ is called the atomic dipole matrix element. As mentioned earlier, The EM wave in the dipole approximation is written as

$$E(t) = \frac{1}{2} E_o e^{-i\omega t} + c.c. \tag{3.21}$$

The externally induced potential is responsible for the coupling of the two states, inducing transition between the energy levels in the atom that are separated by $\Delta E \approx \hbar\omega$ due to laser radiation at frequency ω . Here, $\Delta E = E_2 - E_1$.

For a two-level system,

$$\Psi(r, t) = c_1(t)\phi_1(r) + c_2(t)\phi_2(r)$$

and the Schrodinger equation reduces to

$$\begin{aligned} i\hbar \frac{dc_1(t)}{dt} &= E_1 c_1(t) + V_{11} c_1(t) + V_{12} c_2(t) \\ i\hbar \frac{dc_2(t)}{dt} &= E_2 c_2(t) + V_{21} c_1(t) + V_{22} c_2(t) \end{aligned} \quad (3.22)$$

Since the diagonal matrix elements V_{11} and V_{22} of the interaction is zero owing to the fact that \vec{r} has odd-parity, Eq. (3.22) reduces to

$$\begin{aligned} i\hbar \frac{dc_1(t)}{dt} &= E_1 c_1(t) + V_{12} c_2(t) \\ i\hbar \frac{dc_2(t)}{dt} &= E_2 c_2(t) + V_{21} c_1(t) \end{aligned} \quad (3.23)$$

These equations give the time-dependent probability amplitudes $c_1(t)$ and $c_2(t)$ of the atomic states $|1\rangle$ and $|2\rangle$. This means that the value $|c_1(t)|^2$ gives the probability of finding the system in level 1 at time t .

The probability that the system is found in one or the other of these two states is unity at time t , i.e.

$$|c_1(t)|^2 + |c_2(t)|^2 = 1$$

The integrals $V_{12}(t)$ and $V_{21}(t)$ can be written as

$$V_{12}(t) = -e\vec{r} \cdot \frac{1}{2} \left(\vec{E}_0 e^{-i\hat{\omega}t} + c.c. \right)$$

$$V_{21}(t) = -e\vec{r} \cdot \frac{1}{2} \left(\vec{E}_0 e^{-i\hat{\omega}t} + c.c. \right) \quad (3.24)$$

The matrix elements of the electron displacement are defined as

$$r_{12} = \int \varphi_1^*(r) r \varphi_2(r) d^3r$$

$$r_{21} = \int \varphi_2^*(r) r \varphi_1(r) d^3r$$

Before inserting the integrals V_{12} and V_{21} in the Schrodinger equation, certain conventions are adopted and one works with frequencies, rather than energies,

$$\omega_{21} = \frac{E_2 - E_1}{\hbar} \quad (3.25)$$

$$\Delta = \omega_{21} - \omega \quad (3.26)$$

$$\Omega_{12} = e(r_{12}) \frac{E_0}{\hbar} \quad (3.27)$$

$$\Omega_{21} = e(r_{21}) \frac{E_0}{\hbar} \quad (3.28)$$

Ω_{12} or Ω_{21} is field-atom interaction energy in frequency units and is known as “Rabi frequency”. Even though $r_{21} = r_{12}^*$ but one cannot write $\Omega_{21} = \Omega_{12}^*$ since E_0 may be complex (e.g. for circularly polarized light). $\Omega_{21} = \Omega_{12}^*$ only when E_0 is real for a linearly polarized light which is the case of our interest.

With these conventions, by inserting matrix elements in the Schrodinger equation, one obtains

$$\begin{aligned} i \frac{dc_1}{dt} &= -\frac{1}{2} \left(\Omega_{12} e^{-i\omega t} + \Omega_{21}^* e^{+i\omega t} \right) c_2 \\ i \frac{dc_2}{dt} &= \omega_{21} c_2 - \frac{1}{2} \left(\Omega_{21} e^{-i\omega t} + \Omega_{12}^* e^{+i\omega t} \right) c_1 \end{aligned} \quad (3.29)$$

In the absence of any radiation field, $\Omega_{12} = 0$ and, hence, these differential equations reduce to

$$\begin{aligned} i \frac{dc_1}{dt} &= 0 \\ i \frac{dc_2}{dt} &= \omega_{21} c_2 \end{aligned}$$

which have the solution

$$\begin{aligned} c_1(t) &= c_1(0) \\ \text{and } c_2(t) &= c_2(0) e^{-i\omega_{21}t} \end{aligned} \quad (3.30)$$

From these one can form the trial solutions for the case when the laser field is present.

$$\begin{aligned} c_1 &= c_1(t) \\ c_2 &= c_2(t) e^{-i\omega t} \end{aligned} \quad (3.31)$$

One can then find the equations of motion for the coefficients c_1 and c_2 as

$$\begin{aligned} i \frac{dc_1}{dt} &= -\frac{1}{2} \left(\Omega_{12} e^{-2i\omega t} + \Omega_{21}^* \right) c_2 \\ i \frac{dc_2}{dt} &= (\omega_{21} - \omega) c_2 - \frac{1}{2} \left(\Omega_{21} + \Omega_{12}^* e^{+2i\omega t} \right) c_1 \end{aligned} \quad (3.32)$$

The terms containing $e^{\pm 2i\omega t}$ oscillate so rapidly as compared to any other time variation in the equations so that they can be assumed to average out to zero over any realistic time interval. Thus, these terms can be discarded. This is known as “Rotating wave approximation”. Thus, the equations of motion in the rotating wave approximation reduces to

$$\begin{aligned} i \frac{dc_1}{dt} &= -\frac{1}{2} (\Omega_{21}^*) c_2 \\ i \frac{dc_2}{dt} &= (\omega_{21} - \omega) c_2 - \frac{1}{2} \Omega_{21} c_1 \end{aligned} \quad (3.33)$$

The density matrix elements for a two-level atom system are defined as

$$\begin{aligned} \rho_{11} &= c_1 c_1^* = |c_1|^2 \\ \rho_{22} &= c_2 c_2^* = |c_2|^2 \\ \rho_{12} &= c_1 c_2^* \\ \rho_{21} &= c_2 c_1^* \end{aligned} \quad (3.34)$$

ρ_{11} and ρ_{22} define the level occupation probabilities while ρ_{21} and ρ_{12} describe the coherences between the two states induced by the laser field. The equations of motion for the density matrix elements for an ideal closed two-level atom are obtained from the above equations of motion for coefficients c_1 and c_2 as

$$\frac{d}{dt} \rho_{11} = i \frac{\Omega}{2} (\rho_{21} - \rho_{12}) \quad \frac{d}{dt} \rho_{22} = i \frac{\Omega}{2} (\rho_{12} - \rho_{21})$$

$$\begin{aligned}\frac{d}{dt}\rho_{21} &= i\frac{\Omega}{2}(\rho_{11} - \rho_{22}) - i\Delta\rho_{21} \\ \frac{d}{dt}\rho_{12} &= i\frac{\Omega}{2}(\rho_{22} - \rho_{11}) + i\Delta\rho_{12}\end{aligned}\tag{3.35}$$

The above equations are set of coupled differential equations describing the oscillation of the population between the two levels of a closed two-level atom considered. In the case where $\Delta = 0$, the population oscillates between the two-levels with the frequency known as Rabi frequency. With increase in the field strength of the electromagnetic field, the amplitude of the oscillation increases. With increased detuning Δ , the amplitude of the oscillation decreases. In reality, there is no closed two-level atom system. There are various damping processes that will cause these oscillations to die out with time. These are:

1. Elastic collisions: The elastic collisions among atoms do not change state populations but do cause dephasing (loss of coherence).
2. Inelastic collisions: The inelastic atom-atom collisions change state populations and also cause dephasing.
3. Photoionization/Photoexcitation of atoms from the upper level to higher levels
4. Radiative decay due to
 - (i) Spontaneous emission within the excitation ladder of a two-level system
 - (ii) Spontaneous emission outside the excitation ladder of a two-level system

Since laser-based spectroscopic experiments are commonly done in a collision-free atomic beam environment, the radiative decay processes and photoionization/photoexcitation from the upper level are only considered for further discussion.

The equations of motion for the density matrix element for a two-level atom with these damping processes, called as an open two-level atom are phenomenologically written using the following two principles [1-3]:

1. For the diagonal elements, the damping terms are added corresponding to what is expected from rate equations i.e. the rate of change is increased or decreased by the sum of rates for all possible channels of populations that flow into or out from that state.
2. The off-diagonal elements are decreased by sum of all half rates for decay out of either of the two coupled states.

Using these principles, one can write the density matrix equations for an open two-level system with radiative decays and photoionization.

Fig. 3.2 shows an open two-level atom consisting of the energy states $|1\rangle$ (ground state), and $|2\rangle$ (first excited state) coupled by a monochromatic lasers of frequency ω , nearly resonant with the $|1\rangle - |2\rangle$ transition of frequency ω_{21} . The detuning of the laser is denoted by $\Delta = \omega_{21} - \omega$. The Rabi frequency for the transition is denoted by Ω_R , describing the laser field coupling strength for the transition. The parameter Γ equal to the half of the Einstein coefficient for spontaneous emission denotes the radiative relaxation rates within the excitation ladder whereas γ denotes the radiative relaxation rate out of the excitation ladder. The parameter γ denotes the half rate of photoionization from the upper level having a radiative lifetime T_2 . The DM equations are thus obtained for an open two-level atom as

$$\frac{d}{dt}\rho_{11} = i\frac{\Omega_R}{2}(\rho_{21} - \rho_{12}) + A_{21}\rho_{22}$$

$$\begin{aligned}
\frac{d}{dt}\rho_{22} &= i\frac{\Omega_R}{2}(\rho_{12} - \rho_{21}) - (2\gamma_I + \frac{1}{T_2})\rho_{22} \\
\frac{d}{dt}\rho_{21} &= i\frac{\Omega_R}{2}(\rho_{11} - \rho_{22}) - (i\Delta + \frac{A_{21}}{2} + \gamma_I)\rho_{21} \\
\frac{d}{dt}\rho_{12} &= i\frac{\Omega_R}{2}(\rho_{22} - \rho_{11}) - (-i\Delta + \frac{A_{21}}{2} + \gamma_I)\rho_{12}
\end{aligned} \tag{3.36}$$

Here, A_{21} is the Einstein coefficient for spontaneous emission from state $|2\rangle$ to state $|1\rangle$.

and $\gamma_I = \frac{\sigma_i I}{2\hbar\omega}$ is the photoionization rate from the state $|2\rangle$ with I as laser intensity and

σ_i as the cross-section for photoionization from the state $|2\rangle$. In the above equation, laser is considered as a monochromatic light source. In reality the laser has a finite line-width, which is assumed to arise from phase fluctuations of the laser field. It is thus necessary to have allowance of the finite laser line-width in the above equation. The effect of finite laser line-width is incorporated in the DM equation through the term γ_L by use of the phase-diffusion model [6-10]. In this model the laser spectrum is assumed to be Lorentzian near the centre with full width at half maximum (FWHM) of $\Delta\omega_{las}$ and has a cutoff at \approx frequency β ($>\Delta\omega_{las}/2$). The term γ_L is expressed as [10]

$$\gamma_L = 2\Delta\omega_{las} \frac{\beta^2}{\beta^2 + \Delta^2} \tag{3.37}$$

Considering the finite laser line-width, the relevant DM equations are obtained as

$$\frac{d}{dt}\rho_{11} = i\frac{\Omega_R}{2}(\rho_{21} - \rho_{12}) + A_{21}\rho_{22}$$

$$\begin{aligned}
\frac{d}{dt}\rho_{22} &= i\frac{\Omega_R}{2}(\rho_{12} - \rho_{21}) - (2\gamma_I + \frac{1}{T_2})\rho_{22} \\
\frac{d}{dt}\rho_{21} &= i\frac{\Omega_R}{2}(\rho_{11} - \rho_{22}) - (i\Delta + \frac{A_{21}}{2} + \gamma_I)\rho_{21} \\
\frac{d}{dt}\rho_{12} &= i\frac{\Omega_R}{2}(\rho_{22} - \rho_{11}) - (-i\Delta + \frac{A_{21}}{2} + \gamma_I)\rho_{12}
\end{aligned} \tag{3.38}$$

A normalized frequency cutoff parameter $\beta_c (= \beta/\Delta\omega_{\text{las}})$ having a value greater than 0.5 is thus introduced into the laser spectrum for correction of the ideal Lorentzian laser shape, which leads to nonphysical results. For a monochromatic excitation laser (laser linewidth \ll atomic natural linewidth), γ_L is set to zero in the DM equations.

3.2 Density matrix equations for interaction of laser light with an open three-level atom system

The parameters relevant to the DM formalism of three-step photoionization scheme are shown in Fig.3.3. Consider an open three-level atom consisting of the energy states $|1\rangle$ (ground state), $|2\rangle$ (first excited state) and $|3\rangle$ (second excited state) coupled by two monochromatic lasers. Laser 1 of frequency ω_1 is nearly resonant with the $|1\rangle - |2\rangle$ transition of frequency ω_{21} . Laser 2 of frequency ω_2 is nearly resonant with the $|2\rangle - |3\rangle$ transition of frequency ω_{32} . The detuning of laser 1 is denoted by $\Delta_1 = \omega_{21} - \omega_1$ whereas that of laser 2 is denoted by $\Delta_2 = \omega_{32} - \omega_2$.

The Rabi frequency for the first-step transition is denoted by Ω_1 and describes the laser field coupling strength for the corresponding transition. Similarly, the Rabi frequency for the second-step transition is denoted by Ω_2 . It describes the laser field coupling strength for the corresponding transition. The parameters Γ_1 and Γ_2 equal to half

of the Einstein coefficients for spontaneous emission denote the radiative relaxation rates within the excitation ladder and γ_1 and γ_2 denote the radiative relaxation rates out of the excitation ladder. The parameter γ_I describes the rate of photoionization from the upper excited state $|3\rangle$ to the ion state $|4\rangle$. The photoionization process in the third-step is incoherent. This assumption makes it possible to use the DM formalism for an open three-level atom for atomic excitation and treat photoionization as one of the relaxation mechanisms in the formalism for describing the three-step photoionization.

Extending the procedure discussed for an open two-level atom to an open three-level atom, one can derive the equations of motions for the time evolution of the DM elements for three-step photoionization of atoms, which are obtained as follows:

$$\frac{d}{dt} \rho_{11} = i \frac{\Omega_1}{2} (\rho_{21} - \rho_{12}) + A_{21} \rho_{22}$$

$$\frac{d}{dt} \rho_{22} = i \frac{\Omega_2}{2} (\rho_{32} - \rho_{23}) + i \frac{\Omega_1}{2} (\rho_{12} - \rho_{21}) + A_{32} \rho_{33} - \frac{1}{T_2} \rho_{22}$$

$$\frac{d}{dt} \rho_{33} = i \frac{\Omega_2}{2} (\rho_{23} - \rho_{32}) - \frac{1}{T_3} \rho_{33}$$

$$\frac{d}{dt} \rho_{32} = i \frac{\Omega_2}{2} (\rho_{22} - \rho_{33}) - i \frac{\Omega_1}{2} \rho_{31} - [i\Delta_2 + 0.5(\frac{1}{T_2} + \frac{1}{T_3}) + \gamma_{L2}] \rho_{32}$$

$$\frac{d}{dt} \rho_{23} = \frac{d}{dt} \rho_{32}^*$$

$$\frac{d}{dt} \rho_{31} = i \frac{\Omega_2}{2} \rho_{21} - i \frac{\Omega_1}{2} \rho_{32} - [i(\Delta_1 + \Delta_2) + 0.5(\frac{1}{T_2}) + \gamma_{L1} + \gamma_{L2}] \rho_{31}$$

$$\frac{d}{dt} \rho_{13} = \frac{d}{dt} \rho_{31}^*$$

$$\begin{aligned}\frac{d}{dt}\rho_{21} &= i\frac{\Omega_1}{2}(\rho_{11} - \rho_{22}) + i\frac{\Omega_2}{2}\rho_{31} - [i\Delta_1 + 0.5(\frac{1}{T_1}) + \gamma_{L1}]\rho_{21} \\ \frac{d}{dt}\rho_{12} &= \frac{d}{dt}\rho_{21}^*\end{aligned}\tag{3.39}$$

The terms γ_{L1} and γ_{L2} , accounting for the finite line width of the lasers causing incoherence damping of the Rabi oscillations in the first-step and second-step transitions, respectively are expressed as [10]

$$\gamma_{L1} = 2\Delta\omega_{las1} \frac{\beta^2}{\beta^2 + \Delta_1^2}\tag{3.40}$$

$$\gamma_{L2} = 2\Delta\omega_{las2} \frac{\beta^2}{\beta^2 + \Delta_2^2}\tag{3.41}$$

Here $\Delta\omega_{las1}$ ($\Delta\omega_{las2}$) is the full-width-half-maximum (FWHM) linewidth of the first-step (second-step) laser and β is a cut-off frequency introduced into the laser spectrum to obtain realistic values from the Lorentzian laser line profile assumed in deriving Eqs (3.40) and (3.41).

3.3 Density matrix equations for interaction of laser light with a real atomic beam system

The density matrix formalism developed in the previous section is applicable only to an ideal atomic system where all the atoms have the same interaction times and the same resonant detuning. In laser spectroscopic experiments the atomic beam is generated through a thermal atomic beam source. In such situations the atoms have velocity distributions and finite angular divergence resulting in a distribution of Doppler-shifted laser detunings. Thus, to obtain the ionization yield of a real atomic beam system, or for

modeling of a real atomic beam system, it is necessary to integrate the DM equations over the angle-velocity distribution. This is handled by considering the position as a transformation of velocity and time, with an appropriately chosen common zero-time at a position before the atoms enter the laser beams. The resulting density matrix equations of motion are integrated over the interaction time and over the angle-velocity distribution to obtain the resulting ion signal. Bushaw et al. [4] have carried out extensive DM calculations for two-step excitation in real calcium atomic beam irradiated by CW lasers. They have taken into account a distribution of Doppler-shifted laser detunings and interaction times. For interaction of atoms with pulsed lasers, as is the case in our experiments, all atoms have the same interaction time equal to the pulse duration. Hence, one has to account only for the distribution of the Doppler-shifted laser detunings, which are functions of the angle and velocity.

The Doppler broadening is characterized by the velocity distribution function of the atoms moving along the laser propagation direction. When the atom is moving with a velocity component v_y in the laser propagation direction, the laser detuning Δ with respect to the transition frequency gets modified as the effective laser detuning frequency Δ^{eff} expressed as $\Delta^{eff} = \Delta - \frac{\omega_{21}}{c} v_y$, where c is the speed of light.

3.4 Simultaneous observation of laser-induced photoionization and fluorescence signals in atomic uranium

Resonance ionization spectroscopy and laser-induced fluorescence techniques can be used in a complementary manner for better understanding of atomic spectra [11]. Simultaneous use of two techniques is very rare. Yi et al. [12] have detected both RIS and

LIF signals simultaneously for monitoring the efficiency of the photoionization process in atomic gadolinium. Broglia et al. [13] have carried out simultaneous detection of optogalvanic (OG) and fluorescence signals in a uranium hollow cathode discharge lamp (HCDL) to investigate the possibility of the application of OG detection to study the saturation of atomic transitions. As mentioned earlier, we [14] have recently investigated high-lying even-parity energy levels of atomic samarium using simultaneous RIS and LIF techniques.

The RIS technique deals with laser photo-excitation of atoms from ground or low-lying energy levels to an ionic state through multi-step resonant excitations depending upon the ionization potential (IP) of atoms. The multiple photons of same wavelength from one laser or different wavelengths from different lasers in a time sequence can be used in the process. The probability of photoexcitation and photoionization depends on various atomic parameters, such as energy levels, angular momenta, lifetimes, branching ratios and transition probabilities or cross-sections. Many laser parameters, such as laser wavelength, intensity, pulse width and line width also affect photoionization efficiency. The atoms left in the intermediate excited states after irradiation by excitation and ionization lasers decay back to lower energy levels, emitting the fluorescence radiation. The LIF signal strength is directly proportional to the atomic population left in the excited state. Thus, the observation of LIF signals along with RIS signals indicates incomplete ionization of atoms present before laser irradiation. Using LIF, the photoionization efficiency of every step involved in excitation and ionization process can be monitored. Hence, the simultaneous detection of LIF and RIS signals plays an important role for monitoring the photoionization process. The study of the

photoionization of the excited states of atoms offers an opportunity to investigate the photoionization process, which requires the knowledge of the photoionization cross-section. The experimental methods for the measurement of photoionization cross-section from highly excited states of atoms are based on the observation of saturation in RIS signals and depletion in LIF signals resulting from photoionization [15, 16].

In the present chapter, the results of simultaneous observation of RIS and LIF signals in atomic uranium have been presented [17]. Both the signals were monitored for two specific cases. In the first case, the dye laser was made resonant to the first-step transition ($0-16900.38 \text{ cm}^{-1}$) and in the second case, the laser was slightly detuned by 0.15 cm^{-1} from the first-step transition so that it became two-photon resonant at 33801.06 cm^{-1} . The atoms in the 33801.06 cm^{-1} energy level were further excited by the absorption of a third photon from the same laser to the autoionization state at 50701.59 cm^{-1} . Manohar et al. [18] have reported this autoionization state at 50701.6 cm^{-1} , which is the same state as mentioned above within the measurement accuracy of $\pm 0.1 \text{ cm}^{-1}$. However, they have not mentioned the width of this autoionization state.

The DM equations mentioned in Sections 3.1 to 3.3 of this chapter have been utilized to analyze the RIS and LIF signals observed in the two specific experimental cases. From the DM calculations, the ratios of photoionization as well as fluorescence signals in the two specific cases, considering several values of the photoionization cross-section have been obtained. By comparing these theoretical ratios with the experimentally measured ratios, the photoionization cross-section for the $33801.06-50701.59 \text{ cm}^{-1}$ transition has been obtained.

3.4.1 Experimental details

The experimental setup for simultaneous detection of RIS and LIF signals is shown in Fig. 3.4. It consists of a high temperature atomic vapor source in a vacuum chamber, a dye laser (Quantel TDL 90) pumped by a Q-switched Nd:YAG (Quantel YG 980) laser, a U-Ne HCDL, a photo-multiplier tube (PMT), a 0.5 m monochromator, a 1.5 m high-resolution monochromator, a pyrometer, a high voltage power supply and an oscilloscope. The vacuum chamber is maintained at a pressure of $\sim 5 \times 10^{-6}$ mbar. A pencil-type electron gun of 8 kW power (32 kV, 250 mA) is mounted in the vacuum chamber at an angle of 45° relative to the horizontal axis. The electron beam is turned through another 45° by an external magnetic field so as to ensure normal incidence of electron beam on the surface of the material to be evaporated. In the study reported here, uranium block has been used as a target material. At the electron beam impact point with a spot diameter of ~ 7 mm on the target, high temperature (~ 2600 K) as a result of the electron beam heating process is generated giving rise to copious evaporation of the target material from the surface. Uranium vapor was allowed to expand freely up to a distance of ~ 30 cm. The atoms coming from the source were collimated to a relatively small full angular divergence of 12° through two slits ($1 \text{ cm} \times 10 \text{ cm}$) located at heights ~ 10 cm and ~ 25 cm from the source to create a collimated atomic beam in which spectroscopic investigations were carried out. The pulse duration, repetition rate and line width of the dye laser were 7 ns, 20 Hz and 0.05 cm^{-1} (1.5 GHz), respectively. The laser pulse energy in the interaction zone was 2.5 mJ. The laser beam diameter in the interaction zone was 5 mm. The laser beam passed through the atomic beam of uranium in cross-configuration. The laser wavelength was monitored using the 1.5 m high-

resolution monochromator. Resonance and near-resonance excitation was ensured with the help of OG signal which was monitored by passing the laser beam through the HCDL during the experiments. The fluorescence light emitted from the first-excited level was collected in a direction perpendicular to both laser and atomic beams and focussed onto the entrance slit of the 0.5 m monochromator (Acton SpectraPro, 2500i) by a suitable lens assembly. The photoion signal was detected using a parallel-plate configuration and applying -2 kV to the plates across a load of $5\text{ k}\Omega$. The photoion detection system was in cross-configuration with laser and atomic beams, like the fluorescence collection assembly. Because of the fluorescence assembly being in a straight line with the photoion system, one of the plates was made of fine wire mesh with light transmission efficiency of about 80% so that the maximum of fluorescence light passed through it and reached the fluorescence collection assembly, which consists of a couple of plano-convex lenses. The first lens collimated the fluorescence light and the second lens focused it on to the entrance slit of the 0.5 m monochromator, which consists of three interchangeable 500 nm blazed gratings having 300, 600 and 1200 lines/mm. The resolution of the spectrograph with 300 lines/mm grating is roughly 0.1 nm, which has been used in this study. The monochromator here is used as a filter. The output slit of the monochromator was coupled with a PMT (gain of 10^7).

3.4.2 Theoretical analysis using density matrix (DM) formalism

The basic processes involved in our single-color, three-photon photoionization experiments are described by DM formalism, considering single-color, three-step and three-photon photoionization scheme as shown in Fig. 3.5. As mentioned earlier, the DM formalism gives the most accurate description of multi-step photoionization process by

narrowband lasers as it incorporates the coherences induced between the atomic levels by narrowband laser excitations as is the case for the experimental result being analyzed here. We consider that the photoionization process occurs in a level scheme consisting of ground state 1, first excited state 2, second excited state 3 and autoionization state 4. A rigorous description of the three-step photoionization scheme requires a DM of 4×4 dimension. However, the description is reduced to a DM of 3×3 dimension if the autoionization state is incoherently coupled to the upper excited state, which is justified because generally the spontaneous decay rate from the autoionization state is much larger than the photoexcitation rate between the second excited state and the autoionization state. We have assumed that the width of the autoionization state is broad enough to take care of laser detuning in both the excitation schemes considered in Fig. 3.5. If it is not the case, then the signal in case A of Fig. 3.5 would be very difficult to be observed as photoionization through continuum increases the laser energy requirement by orders of magnitude in comparison to autoionization state. As the signals could easily be observed in both the cases, one can say that the autoionization width is broad enough to take care of laser detuning of 0.45 cm^{-1} considered here in the two excitation schemes. In this case the three-step photoionization process is described by a three-level open system where the laser radiation producing photoionization introduces only damping in the three-level system with a half-rate of $\gamma_I (= \sigma_3 I_{las} / 2\hbar\omega_{las})$, where I_{las} is the laser pulse intensity with frequency ω_{las} , σ_3 is the photoionization cross-section from the second-excited state and $\hbar = h/2\pi$ with h as the Planck constant. The DM equations of motion for the time evolution of the DM elements ρ_{nm} for a three-level open atom interacting with a pulsed

narrowband laser, relevant to the single-color three-photon photoionization experiment of interest, as discussed in sections 3.2-3.3 are:

$$\frac{d}{dt} \rho_{11} = i \frac{\Omega_1}{2} (\rho_{21} - \rho_{12}) + A_{21} \rho_{22} ,$$

$$\frac{d}{dt} \rho_{22} = i \frac{\Omega_2}{2} (\rho_{32} - \rho_{23}) + i \frac{\Omega_1}{2} (\rho_{12} - \rho_{21}) + A_{32} \rho_{33} - \frac{1}{T_2} \rho_{22} ,$$

$$\frac{d}{dt} \rho_{33} = i \frac{\Omega_2}{2} (\rho_{23} - \rho_{32}) - \left(2\gamma_I + \frac{1}{T_3} \right) \rho_{33} ,$$

$$\frac{d}{dt} \rho_{32} = i \frac{\Omega_2}{2} (\rho_{22} - \rho_{33}) - i \frac{\Omega_1}{2} \rho_{31} - [i\Delta_2^{eff} + 0.5(\frac{1}{T_2} + \frac{1}{T_3}) + \gamma_{L2} + \gamma_I] \rho_{32} ,$$

$$\frac{d}{dt} \rho_{23} = \frac{d}{dt} \rho_{32}^* ,$$

$$\frac{d}{dt} \rho_{31} = i \frac{\Omega_2}{2} \rho_{21} - i \frac{\Omega_1}{2} \rho_{32} - [i(\Delta_1^{eff} + \Delta_2^{eff}) + 0.5(\frac{1}{T_2}) + \gamma_{L1} + \gamma_{L2} + \gamma_I] \rho_{31} ,$$

$$\frac{d}{dt} \rho_{13} = \frac{d}{dt} \rho_{31}^* ,$$

$$\frac{d}{dt} \rho_{21} = i \frac{\Omega_1}{2} (\rho_{11} - \rho_{22}) + i \frac{\Omega_2}{2} \rho_{31} - [i\Delta_1^{eff} + 0.5(\frac{1}{T_1}) + \gamma_{L1}] \rho_{21} ,$$

$$\frac{d}{dt} \rho_{12} = \frac{d}{dt} \rho_{21}^* ,$$

$$\Delta_1^{eff} = \Delta_1 - \frac{\omega_{21}}{c} v_y ,$$

$$\Delta_2^{eff} = \Delta_2 + \frac{\omega_{32}}{c} v_y ,$$

$$\Omega_j = \frac{d_j E_0}{\hbar} \text{ for } j = 1 \text{ and } 2.$$

Here E_0 is the amplitude of the electric field considered to vary in time as $\exp(-i\omega_{las}t)$, Ω_1 (Ω_2) is the Rabi frequency of the first-step (second-step) transition caused by laser, d_1 (d_2) is the dipole moment of the first-step (second-step) transition, Δ_1^{eff} (Δ_2^{eff}) is the effective laser detuning frequency of the first-step (second-step) transition when the atom is moving with a velocity component v_y in the laser propagation direction, $\Delta_1(=\omega_{21}-\omega_{las})$ is the rest frame laser detuning frequency of the first-step transition, $\Delta_2(=\omega_{32}-\omega_{las})$ is the rest frame laser detuning frequency of the second-step transition, ω_{jk} is the frequency of the j-k transition, A_{mn} is the Einstein coefficient for the spontaneous emission from the level m to the level n, T_k is the radiative lifetime of the level k and c is the speed of light. The Doppler broadening is characterized by the velocity distribution function of the atoms moving along the laser propagation direction. The diagonal matrix elements ρ_{nn} with $n = m$ represent the atomic population of the level n and the off-diagonal matrix elements ρ_{nm} with $n \neq m$ represent the coherences between the levels induced by the laser fields. The two-photon resonance is fulfilled when $\Delta_1 + \Delta_2 = 0$. The terms γ_{L1} and γ_{L2} , accounting for the finite line width of the laser causing incoherence damping of Rabi oscillations in the first-step and second-step transitions, expressed in Eqs 3.40 and 3.41 respectively as

$$\gamma_{L1} = 2\Delta\omega_{las} \frac{\beta^2}{\beta^2 + \Delta_1^2}$$

$$\gamma_{L2} = 2\Delta\omega_{las} \frac{\beta^2}{\beta^2 + \Delta_2^2}$$

Here $\Delta\omega_{las}$ is the full-width-half-maximum line width of the laser and β is a cut-off frequency introduced into the laser spectrum to obtain realistic values from the Lorentzian laser line profile assumed in deriving above equations. The value of the normalized cut-off frequency $\beta_C (= \beta/\Delta\omega_{las})$ equal to 2 is considered here as used by Gupta et al. [5,19].

The ionization yield P at the end of the laser pulse with duration T_{las} is obtained as

$$P(T_{las}) = 1 - \rho_{11}(T_{las}) - \rho_{22}(T_{las}) - \rho_{33}(T_{las}). \quad (3.42)$$

The Rabi frequency Ω_m of the m-n transition ($n = m+1$) is related to the Einstein coefficient A_{nm} and the applied laser intensity I_{las} coupling the levels m and n as [5,19,20]

$$\Omega_m (rad / s) = 8.895 \times 10^{10} \left(3 \lambda_{cm}^3 g_n A_{nm} I_{W/cm^2} / g_m \right)^{1/2}, \quad (3.43)$$

where λ_{cm} is the transition wavelength in cm, I_{W/cm^2} is the value of I_{las} in W/cm^2 and g_m (g_n) is the statistical weight of the level m (n). The dipole moment d_m of the m-n transition ($n = m+1$) is related to A_{nm} as [20]

$$A_{nm} (s^{-1}) = \frac{[d_m (Debye)]^2 g_m}{3.19 \times 10^6 \lambda_{cm}^3 g_n}. \quad (3.44)$$

The dipole moment d_1 of the 1-2 transition is related to the dipole moment d_2 of the 2-3 transition as [3]

$$\frac{d_1}{d_2} = \left(\frac{\lambda_1}{\lambda_2} \right)^{3/2} \left(\frac{g_2/g_1}{g_3/g_2} \right)^{1/2} \left(\frac{T_3}{0.9T_2} \right)^{1/2}. \quad (3.45)$$

Using Eqs. (3.44) and (3.45), one obtains

$$\frac{A_{21}}{A_{32}} = \frac{T_3}{0.9T_2}. \quad (3.46)$$

The Doppler width (FWHM), $\Delta\nu_D$, of the atomic transition line at a vapor source of temperature T (K) is given as [5]

$$\Delta\nu_D = 7.16 \times 10^{-7} \nu_0 (T/M)^{1/2}, \quad (3.47)$$

Here, M is the atomic mass number of the vapor source material and ν_0 is the transition frequency. The DM equations are solved numerically using the initial condition where ρ_{11} is set equal to unity and all other DM elements are set equal to zero at the time $t = 0$. To obtain the effective values of the DM elements for real atomic beams generated from a vapor source [5,19], these equations are integrated over the velocity and angular distribution of the atoms, resulting in a distribution of Doppler-shifted laser detuning. We have used a Maxwellian velocity distribution for the uranium atoms generated by electron beam evaporation of uranium metal with a measured evaporating surface temperature of 2600 K. Normally, at low evaporation rate, the uranium atoms evaporated in the electron beam heating process possess a Maxwellian velocity distribution. Asano et al. [21] have observed that, at evaporating surface temperatures lower than 2700 K, the velocity of uranium atoms is equal to the thermal mean velocity at the evaporating surface temperature, showing that the atomic velocity distribution at such temperatures is Maxwellian.

For the analysis of our single-color three-photon photoionization experimental results using the DM formalism, we consider the excitation scheme shown in Fig. 3.5. The experimentally measured $T = 2600$ K, $T_2 = 250$ ns [22], $T_3 = 1120$ ns [23] and other experimental conditions mentioned earlier are taken into account in the calculations. The value of A_{21} ($\approx 1/T_2$) is $4 \times 10^6 \text{ s}^{-1}$ as there is only one significant decay path of the first-

excited state at 16900.38 cm^{-1} and that is back to the ground state. The value of $A_{21}/A_{32} = 4.978$ is estimated from Eq. (3.46), which gives rise to $A_{32} = 0.8 \times 10^6 \text{ s}^{-1}$. Following the procedure discussed and employed by Bushaw et al. [4], the integration of the DM equations have been carried out to obtain the numerical results.

3.4.3 Results obtained after analysis of experiments

The $0-16900.38 \text{ cm}^{-1}$ transition at 591.5 nm in atomic uranium is well studied as it is one of the strongest atomic transitions in uranium in the visible region [18, 24, 25]. This transition also serves as a first-step transition in the RIS of ground-state atoms of uranium using single-color three-photon photoionization pathway to the autoionization state at 50701.59 cm^{-1} . Considering this transition, we have conducted the experiments for simultaneous observation of LIF and RIS signals in atomic uranium in two specific cases. In the first case, the laser was resonantly tuned to this first-step transition, which excited the uranium atoms in the ground state to the 16900.38 cm^{-1} energy level. Two photons of the same laser further photoionized the excited uranium atoms via a near-resonant intermediate state at 33801.06 cm^{-1} . The excitation scheme for this case is shown in Fig. 3.5A. Both the three-photon photoionization signal and the resonant fluorescence signal have been observed using an oscilloscope. Typical RIS and LIF signals recorded in this case are shown in Fig. 3.6A. In the second case, the laser was slightly detuned from the first-step transition by 0.15 cm^{-1} so that it became two-photon resonant at 33801.06 cm^{-1} . The excitation scheme in this case is shown in Fig. 3.5B. Typical RIS and LIF signals recorded in this case are shown in Fig. 3.6B. As evident from the figure, the RIS signal increased relative to the first case owing to the two-photon resonance transition and its connection to autoionization resonance at 50701.59 cm^{-1} [18,

24]. However, the LIF signal decreased relative to the first case, owing to detuning of the laser from the first-step resonance. In order to detect the resonant fluorescence signal, the monochromator was kept at 591.5 nm with a band pass of 1 nm. The laser scattering signal was monitored in the absence of the atomic beam in the beginning of the experiment when no electron beam heating of uranium metal was done. Typical laser scattering signal is shown in Fig. 3.6C. The scattering signal was also checked at the end of the experiment to monitor any changes in the laser power or in the detection system. The scattering signal was subtracted from the total fluorescence signals of Figs. 3.6A and 3.6B to get the actual fluorescence signal. All the experiments were done by taking an average of 64 laser pulses. The experimental ratios of RIS and LIF signals were determined by dividing the signal value measured in the first case to that in the second case. These experimental ratios were obtained by repeating the experiments six times for both the cases. The arithmetic mean of the six values of the ratios is represented as the average value of the ratio. We have taken these average values as the measured ratios. We have found the uncertainty in the signal ratios within $\pm 20\%$ from the spread in the data obtained in the six experiments. This can be attributed to the change in the experimental conditions such as fluctuations in pulse-to-pulse laser power, atomic number density and the optimization of signals for both cases. The measured ratios of LIF and RIS signals are thus deduced as 3.0 ± 0.6 and 0.5 ± 0.1 , respectively.

Using the DM formalism, we have calculated the photoionization efficiency of RIS signal and the fluorescence efficiency of LIF signal in the two specific cases of laser detuning for several values of the photoionization cross-section and the results are shown in Figs. 3.7 and 3.8. The values of laser detuning from the first- and second-step

transitions respectively are $\Delta_1 = 0 \text{ cm}^{-1}$ and $\Delta_2 = 0.30 \text{ cm}^{-1}$ (9000 MHz) in the first case and $\Delta_1 = -0.15 \text{ cm}^{-1}$ (-4500 MHz) and $\Delta_2 = 0.15 \text{ cm}^{-1}$ (4500 MHz) in the second case. The values of laser detuning in the figures are given in units of MHz. As seen from Fig. 3.7, the photoionization efficiency increases with increase in the photoionization cross-section in both the cases. It is much higher in the second case in comparison to the first case at any particular value of the photoionization cross-section considered, which is also evident in the experiments. As seen from Fig. 3.8, the fluorescence efficiency decreases with increase in the photoionization cross-section in both the cases. It is much higher in the first case in comparison to the second case at any particular value of the photoionization cross-section considered, which is also evident in the experiments. From these calculations, we have obtained the ratios of LIF and RIS signals in the two specific cases for several values of the photoionization cross-section and have shown those in Table 3.1. As noted from the table, the theoretical LIF ratio increases significantly with increase in the photoionization cross-section whereas the theoretical RIS ratio initially decreases slowly and becomes constant afterwards with increase in the photoionization cross-section. This is owing to the fact that the LIF signal involves a resonant transition in one case and a near-resonant transition in the other case whereas the RIS signal involves near-resonant transitions in both the cases. By comparing the theoretically calculated LIF and RIS ratios with the experimentally measured values, it is observed that the theoretical LIF ratio (2.9) corresponding to the photoionization cross-section of $5 \times 10^{-16} \text{ cm}^2$ matches well with the measured ratio (3.0 ± 0.6) within the experimental error whereas the theoretical RIS ratio (0.6) reasonably matches with the measured ratio (0.5 ± 0.1) within the experimental error for many values of the photoionization cross-section

including $5 \times 10^{-16} \text{ cm}^2$. Considering the uncertainties in the measured signal ratios, the value of the measured LIF ratio can vary from 2.4 to 3.6. The corresponding values of the photoionization cross-section vary from $4 \times 10^{-16} \text{ cm}^2$ to $6 \times 10^{-16} \text{ cm}^2$. Hence, the uncertainty of the photoionization cross-section is inferred to be $\pm 1 \times 10^{-16} \text{ cm}^2$. The value of the photoionization cross-section for the transition $33801.06\text{-}50701.59 \text{ cm}^{-1}$ is thus determined as $(5 \pm 1) \times 10^{-16} \text{ cm}^2$ from the comparison of the theoretical and experimental ratio of LIF signals.

3.5 Simultaneous observation of laser-induced photoionization and fluorescence signals in atomic samarium

In the two-color, three-photon photoionization process, the first laser excites the atoms to a first-excited low-lying energy level. The second laser excites it to a second-excited high lying energy level followed by a photoionization through continuum or autoionization state by the second photon of the same laser. The photoionization of the atoms in the second-excited state due to the another photon of second-step laser can be ensured by delaying the second-step laser with respect to the first-step laser by at least the laser pulse duration.

In this section, the results of simultaneous two-color RIS and LIF signals in atomic samarium for two photoionization pathways, presented in the literature [26], are discussed in this section. Laser-induced two-color, three-photon photoionization and two-color fluorescence signals have been monitored simultaneously as a function of the second-step laser pulse energy while keeping the energy of the first-step laser as constant. The two-color laser-induced fluorescence signal is proportional to the product of $A_{21}(\lambda_1)I_1$ and $A_{32}(\lambda_2)I_2$. Here, A_{21} , λ_1 , I_1 , A_{32} , λ_2 , I_2 are first and second step transition

probability, wavelength and laser intensity respectively. The two-color, three-photon photoionization signal is proportional to the product of $A_{21}(\lambda_1)I_1$, $A_{32}(\lambda_2)I_2$ and $\sigma_3(\lambda_2)I_2$, where $\sigma_3(\lambda_2)$ is the photoionization cross-section on second-step laser wavelength for the third-step transition as another photon of the second-step laser is used to ionize the atom from intermediate level. Because of the dependence of two-color, three-photon photoionization signal on photoionization cross-section, its saturation curve is expected to be different from the two-color fluorescence saturation curve. We have analyzed these signals by applying the density matrix (DM) formalism to a three-step photoionization. The value of the second-step transition probability is directly obtained from two-color fluorescence. The value of the second-step transition probability thus obtained is used to infer the value of photoionization cross-section for the third-step transition from the two-color, three-photon photoionization signal. In this way, the transition probability for the second-step and photoionization cross-section for the third-step are measured for the two photoionization pathways from simultaneous monitoring of laser-induced fluorescence and photoionization signals. To the best of our knowledge, we have used for the first time the simultaneous laser-induced fluorescence and photoionization signals for the measurement of the second-step transition probability and the photoionization cross-section for the third-step transition.

3.5.1 Experimental details

The experimental setup for simultaneous detection of RIS and LIF signals is shown in Fig. 3.9. Most of the instruments used in section 3.4.1 remain the same except the vapor generation. The samarium atomic vapor was generated in a vacuum chamber maintained at a background pressure of $\sim 10^{-5}$ torr by resistive heating of samarium metal

kept in a tantalum crucible at ~ 1000 °C. The samarium vapors came out effusively from a 0.5 mm hole in the crucible lid of 4 mm depth. The atoms coming out from the crucible hole provided a collimated atomic beam to a full angular divergence of $\sim 40^\circ$, and a reduced Doppler-width of ~ 350 MHz in the laser-atom interaction zone. The Doppler width can be reduced by a factor, which is equal to the collimation ratio of the beam. The pulse duration, repetition rate and line width of the dye laser were 7 ns, 20 Hz and 0.05 cm^{-1} (1.5 GHz), respectively. The laser beam with a diameter of 1.5 cm crossed the atomic beam of samarium at right angles. The second laser which further photoexcited and photoionized the atoms was delayed by 7 ns with respect to the first laser in order to discriminate against photoionization of atoms by another photon of the first laser. The fluorescence light emitted was collected in a direction perpendicular to both laser and atomic beams and focused onto the entrance slit of the 0.5 m monochromator (Acton SpectraPro, 2500i) by a suitable lens assembly. The photoion signal was detected using a parallel-plate configuration and applying -1 kV to the plates across a load of $5 \text{ k}\Omega$.

3.5.2 Theoretical analysis using density matrix (DM) formalism

The basic processes involved in our two-color, three-photon photoionization experiment are described by the DM formalism, considering two-color, three-step and three-photon photoionization scheme as shown in Fig. 3.10. For the analysis of our two-color three-photon photoionization experimental results using the DM formalism, which has been discussed above, we have considered two excitation pathways as shown in Fig. 3.10. The experimentally measured $T = 1000$ °C, $T_2 = 46$ ns [27], A_{21} is $6.8 \times 10^6 \text{ s}^{-1}$ [27] and other experimental conditions mentioned earlier are taken into account in the calculations. Following our work on the measurements of lifetimes of energy levels [27],

we have measured the lifetimes of the second-excited state in the photoionization pathways by recording the fluorescence at different delays after the laser pulse by employing intensified charge couple device camera (ICCD) in conjunction with a monochromator. The excited state lifetime values (T_3) are obtained as (87 ± 8) ns and (117 ± 11) ns for the even-parity energy levels of atomic samarium at 36572.0 and 36682.5 cm^{-1} respectively. Following the procedure discussed in previous section, the integration of the DM equations has been carried out and the numerical results have been obtained.

3.5.3 Results obtained after analysis of experiments

In both the photoionization pathways (Fig. 3.10), samarium atoms from the ground state septet at 1489.5 cm^{-1} ($J=3$) were excited to odd-parity energy level at 19009.5 cm^{-1} ($J=2$) by the first laser. The second laser delayed by 7 ns with respect to the first laser further excited the atoms to the intermediate even-parity level at 36572.0 cm^{-1} ($J=3$) [28] in photoionization pathway (a) and at 36682.5 cm^{-1} ($J=3$) [28] in photoionization pathway (b). A second photon of the second laser had sufficient energy to raise the atoms into the continuum (ionization potential $\sim 45519\text{ cm}^{-1}$) at 54134.5 cm^{-1} and 54355.5 cm^{-1} respectively in the first and the second path way, leading to photoionization. The intensity of the first laser was kept constant just above the saturation at $\sim 7\times 10^3\text{ W/cm}^2$ and that of the second laser was varied by inserting the neutral density filters in its path and the power was measured by a power meter (OPHIR 3A-P-V1) on each insertion. The spot size of the second laser overlapping with first laser was measured to calculate the second-step laser intensity. The photoionization signal along with the fluorescence signal from the second-excited even-parity level was

simultaneously monitored as a function of intensity of the second-step laser. The monochromator was set in such a way that it cut off the laser reflections arising from atomic beam chamber walls for the first and second-step lasers. The sum of second-step non-resonant fluorescence falling in the band pass of the monochromator has been detected through PMT. For the present work monochromator was set at 522 nm with a pass band of 20 nm (± 10 nm with respect to central wavelength), which completely cuts off the first and second-step laser reflections from the atomic vapor chamber walls as well as first-step laser-induced fluorescence. So the non-resonant second-step fluorescence from state 3 of Fig. 3.10 is only passed by monochromator, which provides a high signal-to-noise-ratio. From the integration of the DM equations, we have obtained the normalized population of different states 1, 2, 3 and 4. at the end of the laser pulse for two photoionization pathways shown in Fig. 3.10 (a) and (b). The theoretical normalized population of state 3 is represented as the two-color fluorescence efficiency as this LIF signal is proportional to the atomic population left in the state 3. Similarly, the theoretical photoionization efficiency refers to the normalized population in the ionized state 4 determined from the numerical solutions of the DM equations. The experimental fluorescence and photoionization efficiencies are obtained from the corresponding signals by equating the highest signal equal to the highest normalized population in the state 3 in case of fluorescence and equal to the highest normalized population in state 4 in the case of photoionization. For equalizing the highest value of the experimentally measured signal, the highest normalized population from the theoretical calculation is chosen in such a way that the nature of the experimental curve resembles closely with that of the theoretical curve. We have compared thus obtained theoretical and experimental

efficiencies. Fig. 3.11 shows the variation of two-color LIF efficiency with intensity of second-step laser for three values of A_{32} , using σ_3 equal to $1 \times 10^{-16} \text{ cm}^2$ for the photoionization pathway of Fig. 3.10 (a). The value of the photoionization cross-section from the second-excited level is taken equal to $1 \times 10^{-16} \text{ cm}^2$ as the value is not known in the literature. The uncertainty introduced due to scatter in data from run to run was about 5%. From the comparison of the numerical results with the experimental results, the value of $A_{32} = 3 \times 10^5 \text{ s}^{-1}$ is noted to match well these two results. In order to find out the effect of the value of unknown photoionization cross-section on the transition probability, the numerical results corresponding to Fig. 3.11 were again obtained using the photoionization cross-section value of $1 \times 10^{-17} \text{ cm}^2$ as shown in Fig. 3.12. As evident from figures 3.11 and 3.12, the transition probability value remains almost same even by changing the value of photoionization cross-section by an order of magnitude. The transition probability of the $19009.5 - 36572.0 \text{ cm}^{-1}$ transition is, thus, obtained as $3 \times 10^5 \text{ s}^{-1}$. This inferred value of A_{32} equal to $3 \times 10^5 \text{ s}^{-1}$ for the $19009.5 - 36572.0 \text{ cm}^{-1}$ transition was used to obtain the photoionization cross-section for the transition starting from even-parity energy level at 36572.0 cm^{-1} , which can terminate in continuum or at autoionization resonance at 54134.5 cm^{-1} . The photoionization cross-section for this transition was found to be $1.2 \times 10^{-17} \text{ cm}^2$ as shown in Fig. 3.13.

In order to deduce the value of A_{32} for the transition $19009.5 - 36682.5 \text{ cm}^{-1}$, the numerical results of the fluorescence efficiency for this transition of the photoionization pathway of Fig. 3.10 (b) are obtained and compared with the experimental results using the same procedure as mentioned above. From the good match of the experimental results with those obtained by the DM formalism, the transition probability of the $19009.5 -$

36682.5 cm⁻¹ transition is inferred as 2×10^5 s⁻¹. This value of A_{32} for the 19009.5 – 36682.5 cm⁻¹ transition was used to obtain the cross-section for the transition starting from even-parity energy level at 36682.5 cm⁻¹, which can terminate at continuum or at autoionization resonance at 54355.5 cm⁻¹. The photoionization cross-section for this transition was found to be 1.2×10^{-17} cm².

The value of the photoionization cross-section is found to be same and weak in both the photoionization pathways through the second-excited even parity energy levels at 36572.0 cm⁻¹ and 36682.5 cm⁻¹, so it seems more likely that the final step is terminating in continuum. Moreover, the autoionization states at 54134.5 and 54355.5 cm⁻¹ are not reported in the literature [29-31]. However, it is sure that even if these states happen to be autoionization states, they can only be the broad autoionization states with weak photoionization cross-section.

To reduce the pulse to pulse laser energy fluctuations, an average of 128 laser pulses were taken to generate the data points. Several measurements were taken to obtain the transition probability and cross-section values. The average of these values is taken as the final value. We found variation of about 20% in these values. This can be due to inaccuracy in the measurement of laser power, spot size, spectral overlap between the laser and atomic absorption line width. The results are summarized in Table 3.2 and to the best of our knowledge, these values are reported for the first time.

3.6 Conclusions

The DM formalism has been developed for real atomic systems and experimental data obtained from the simultaneous RIS and LIF signals has been analyzed using DM formalism. Simultaneous observation of RIS and LIF signals in atomic uranium has been

recorded under two specific experimental cases. The photoionization cross-section for the $33801.06\text{-}50701.59\text{ cm}^{-1}$ transition of atomic uranium has been measured as $(5 \pm 1) \times 10^{-16}\text{ cm}^2$ by comparing the experimental results with density matrix calculations. The photoionization cross-section value has been determined from the match of the theoretical ratio with the experimentally measured ratio of LIF signals.

The second-step transition probabilities for the two transitions starting from odd parity level at 19009.5 cm^{-1} in atomic samarium have been measured using two-color LIF technique. The transition probability of the $19009.5\text{-}36572.0\text{ cm}^{-1}$ transition is deduced as $(3 \pm 0.6) \times 10^5\text{ s}^{-1}$ and that of the $19009.5\text{-}36682.5\text{ cm}^{-1}$ transition is deduced as $(2 \pm 0.4) \times 10^5\text{ s}^{-1}$. The second-step transition probabilities obtained were used to infer the photoionization cross-sections from these second-excited even-parity energy levels, which can terminate in continuum or at autoionization states, using two-color, three-photon photoionization technique. The value of the photoionization cross-section from the second-excited state is found to be $(1.2 \pm 0.24) \times 10^{-17}\text{ cm}^2$ in both the photoionization pathways. The method employed here for the measurement of the second-step transition probabilities and photoionization cross-sections by simultaneously monitoring and analyzing LIF/RIS signals is used for the first time and enabled us to measure two important atomic parameters in a single experiment. Moreover, we have used only one laser in the case of atomic uranium and two lasers in the case of atomic samarium, but usually the measurement of photoionization cross-section requires three lasers. The simultaneous observation of LIF and RIS signals can facilitate investigation of photoionization dynamics.

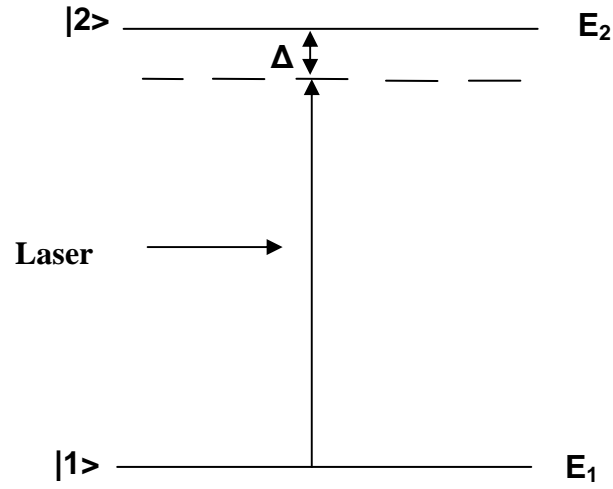


Fig.3.1: Energy level diagram for an ideal two-level atom

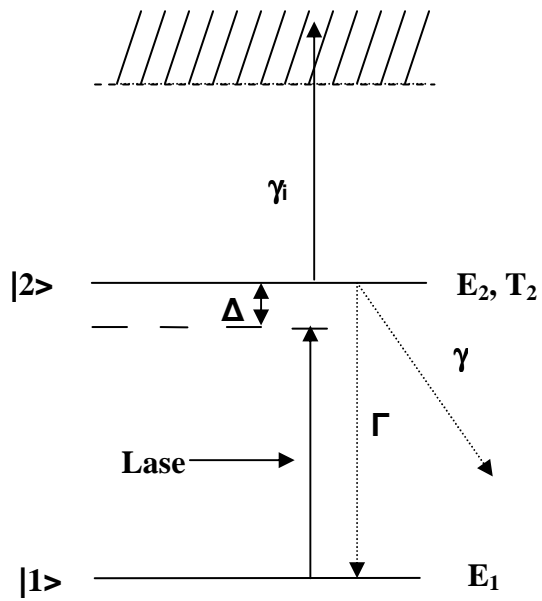


Fig. 3.2: Energy level diagram for an open two-level atom with decays and photoionization

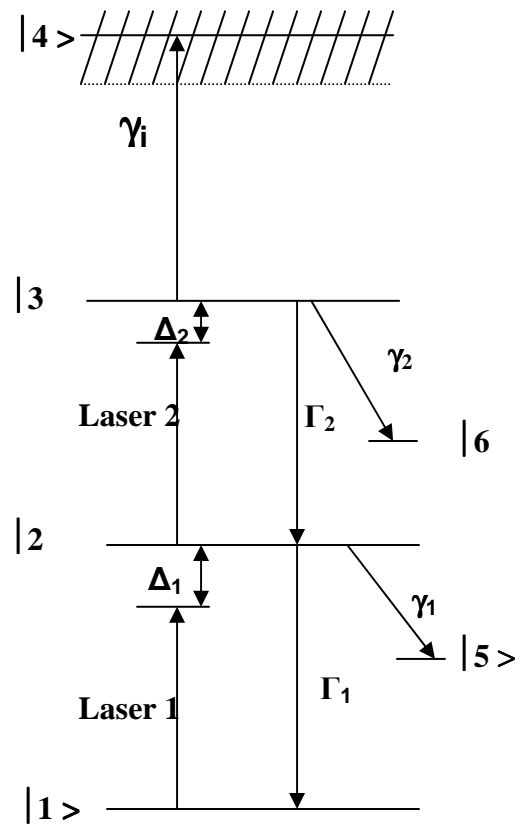


Fig. 3.3: Energy level diagram for an open three-level atom with decays and photoionization

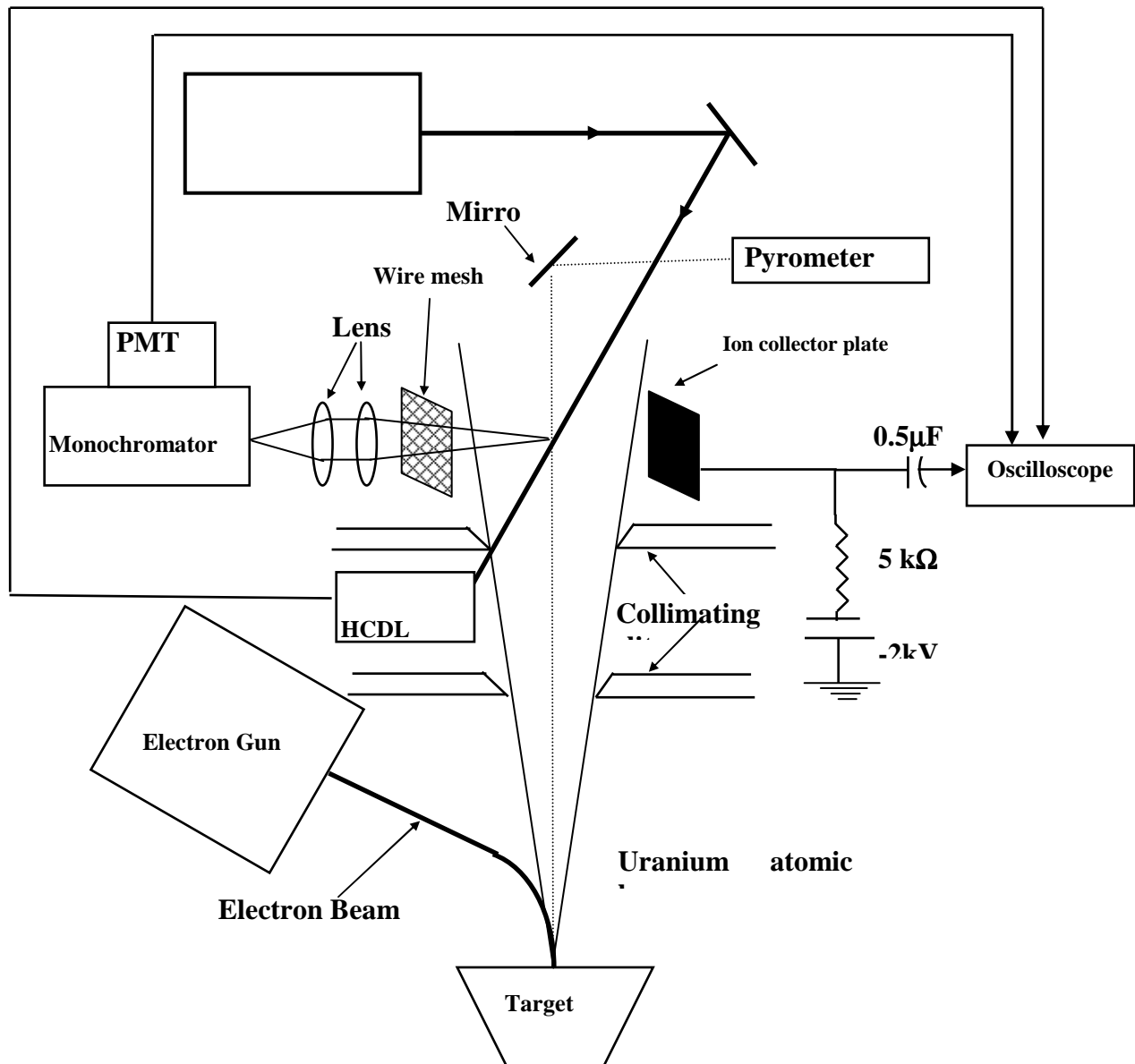


Fig. 3.4: Experimental setup for simultaneous observation of LIF and RIS signals

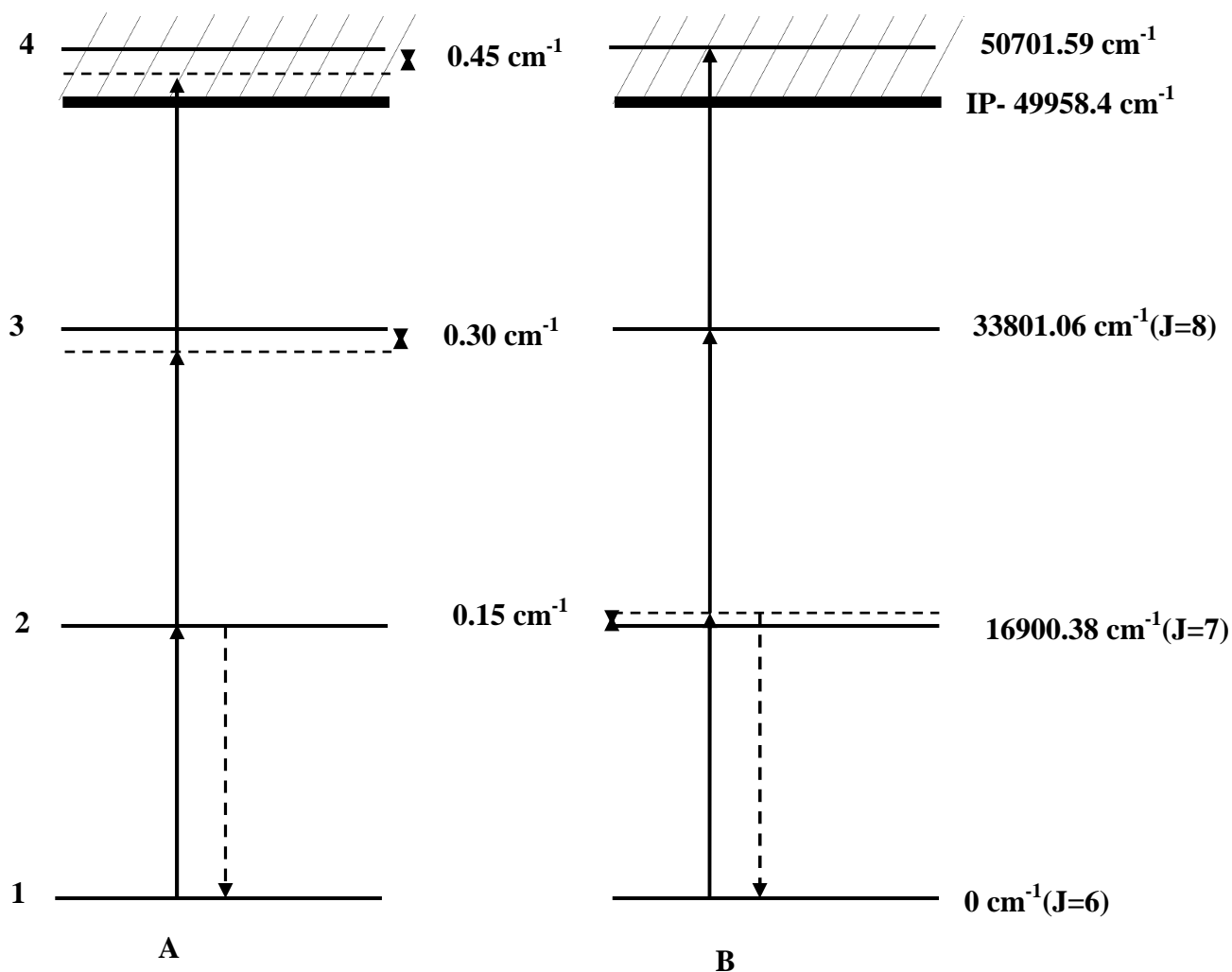


Fig. 3.5: Energy level diagram for single-color, three-photon photoionization and single-color laser-induced fluorescence when

(A) The laser is tuned to resonance in first step transition ($0\text{-}16900.38 \text{ cm}^{-1}$),

(B) The laser is detuned from resonance in first step transition by 0.15 cm^{-1} , so that it became two-photon resonant at 33801.06 cm^{-1}

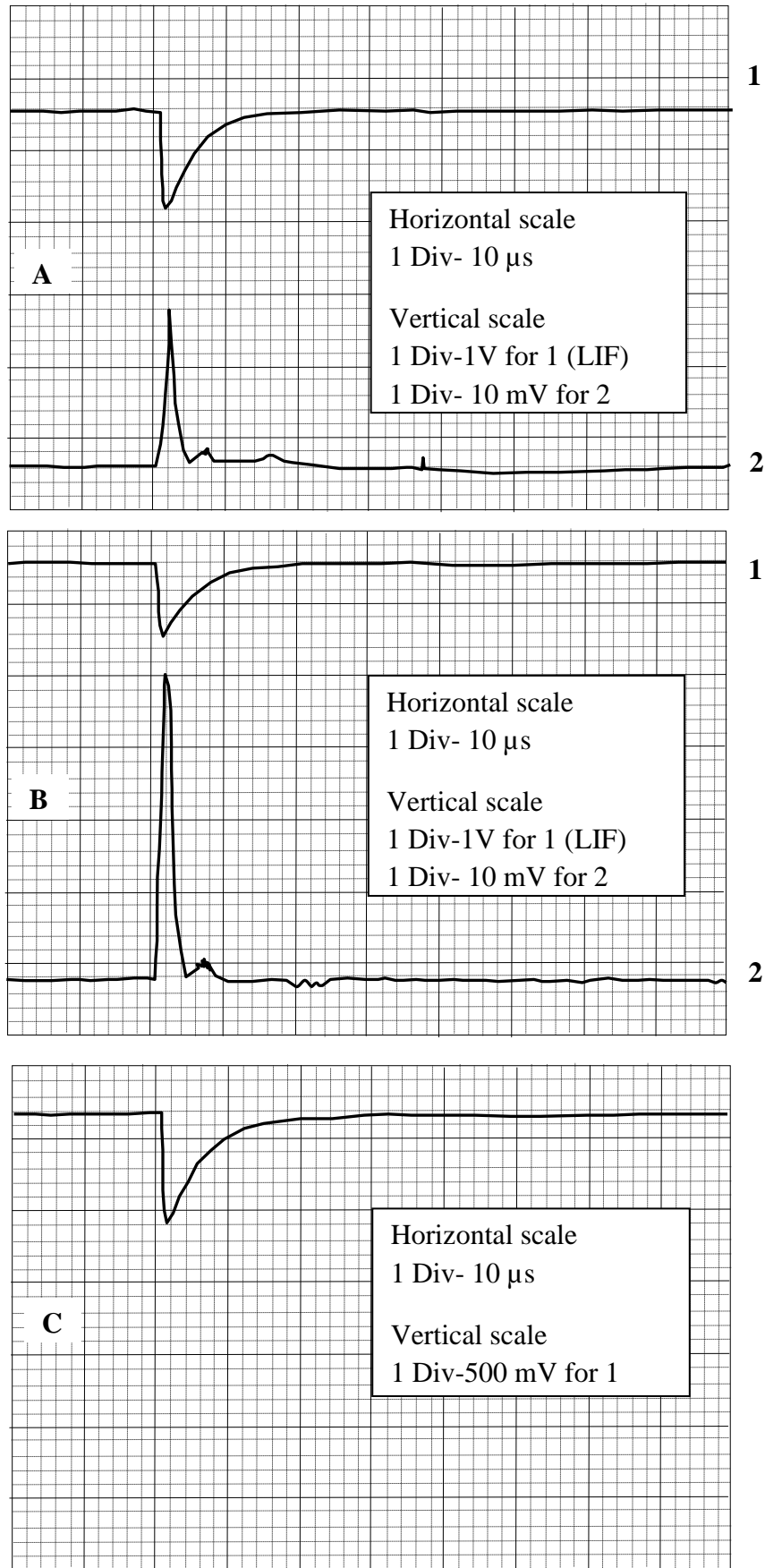


Fig. 3.6: Simultaneously observed LIF and RIS signals for the two specific cases
(A) The laser was resonant to the first-step transition ($0 - 16900.38 \text{ cm}^{-1}$),
(B) The laser was near-resonant to the first step transition with a slight detuning (0.15 cm^{-1}),
so that it became two-photon resonant at 33801.06 cm^{-1} ,
(C) Laser-induced background scattering signal in the absence of atomic beam

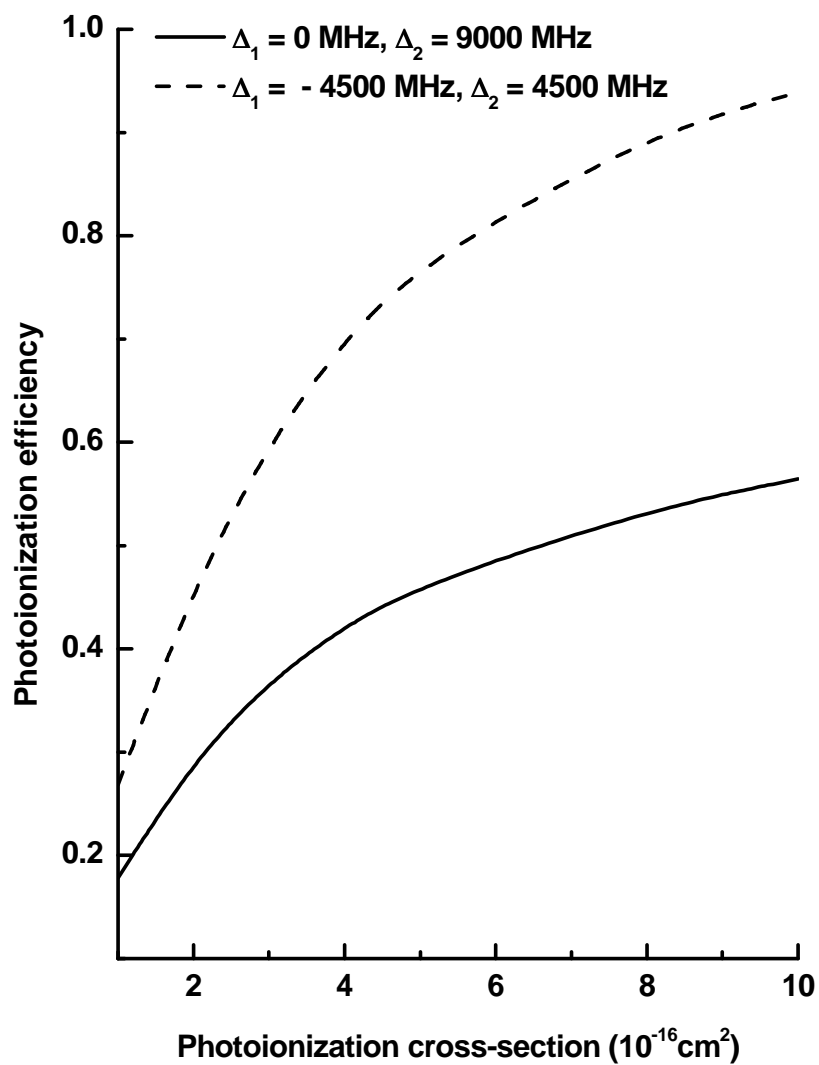


Fig. 3.7: Variation of photoionization efficiency with photoionization cross-section for the two specific cases of laser detuning

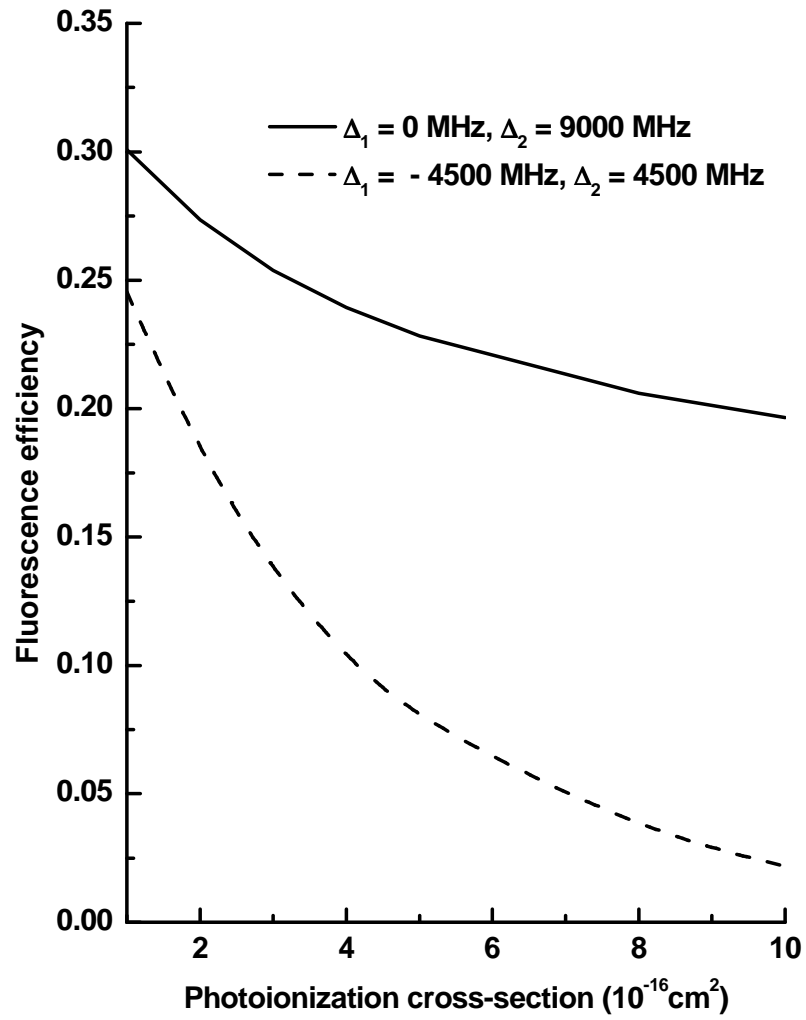


Fig. 3.8: Variation of fluorescence efficiency with photoionization cross-section for the two specific cases of laser detuning

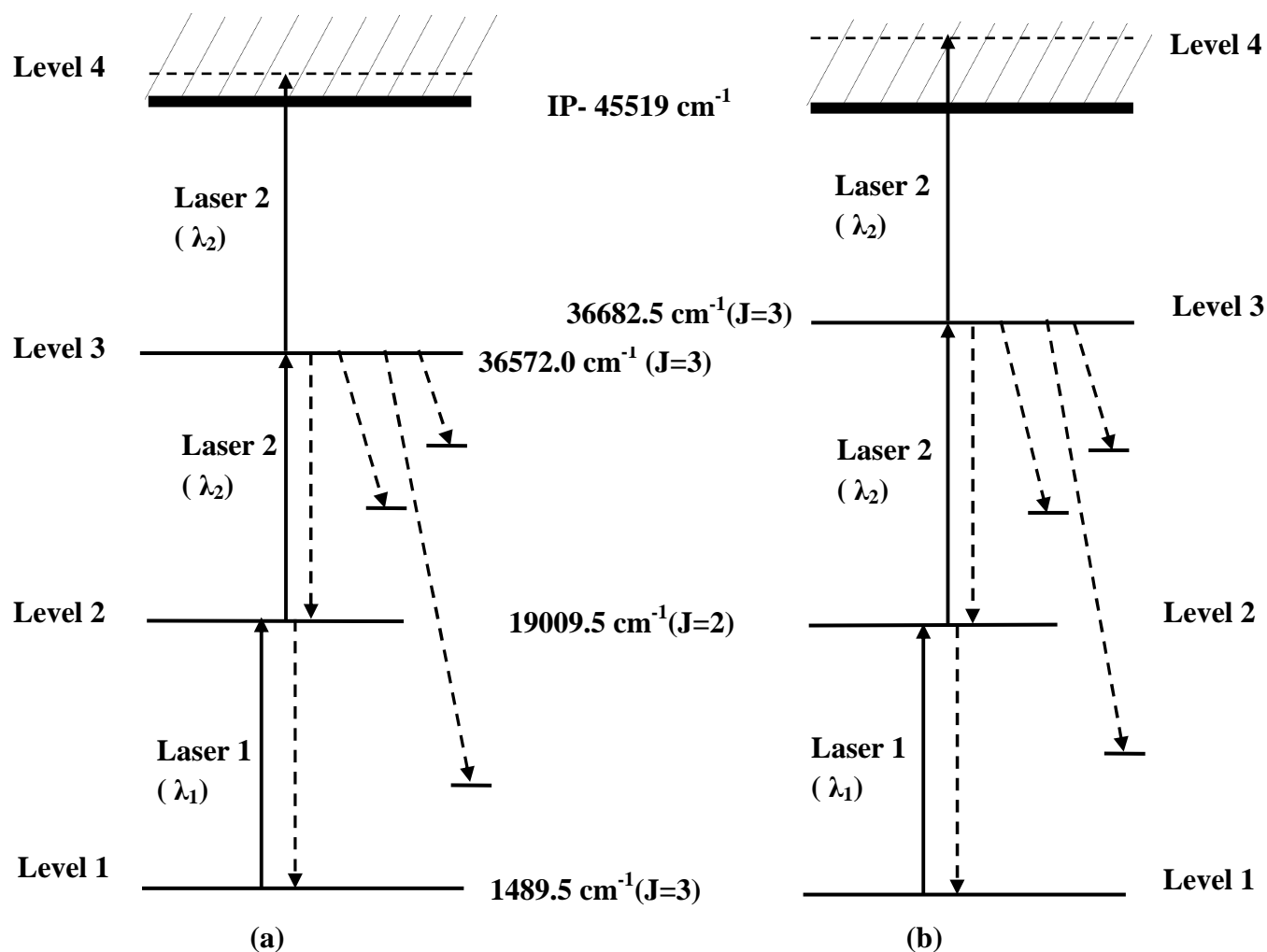


Fig. 3.10: Energy level diagrams for two-color, three-photon photoionization and two-color laser-induced fluorescence for two photoionization pathways (a) and (b)

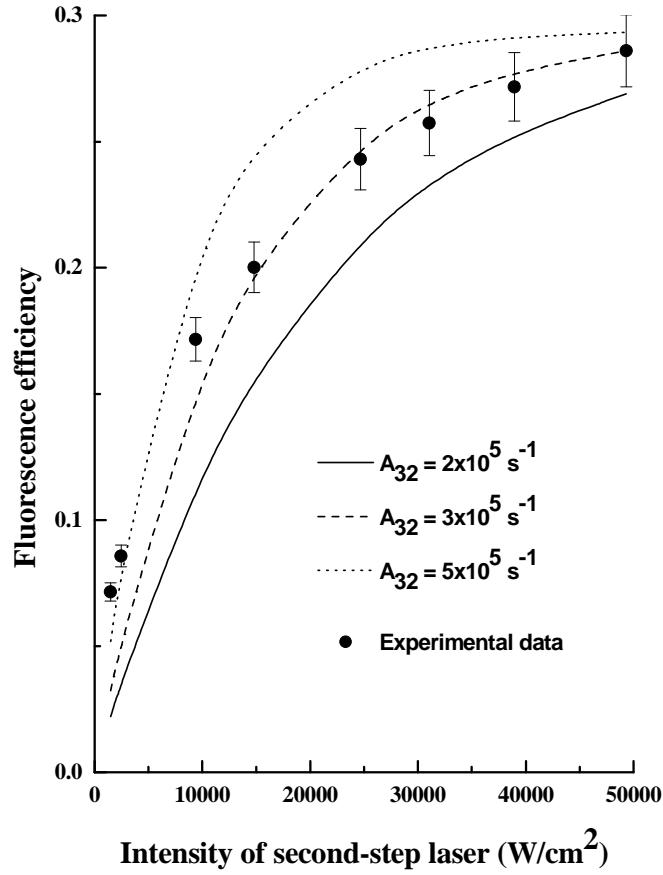


Fig. 3.11: Variation of two-color laser-induced fluorescence efficiency with intensity of the second-step laser for three values of A_{32} , using the photoionization cross-section $\sigma_3 = 1 \times 10^{-16} \text{ cm}^2$. Photoionization pathway of Fig. 2(a) is considered for the results in this figure

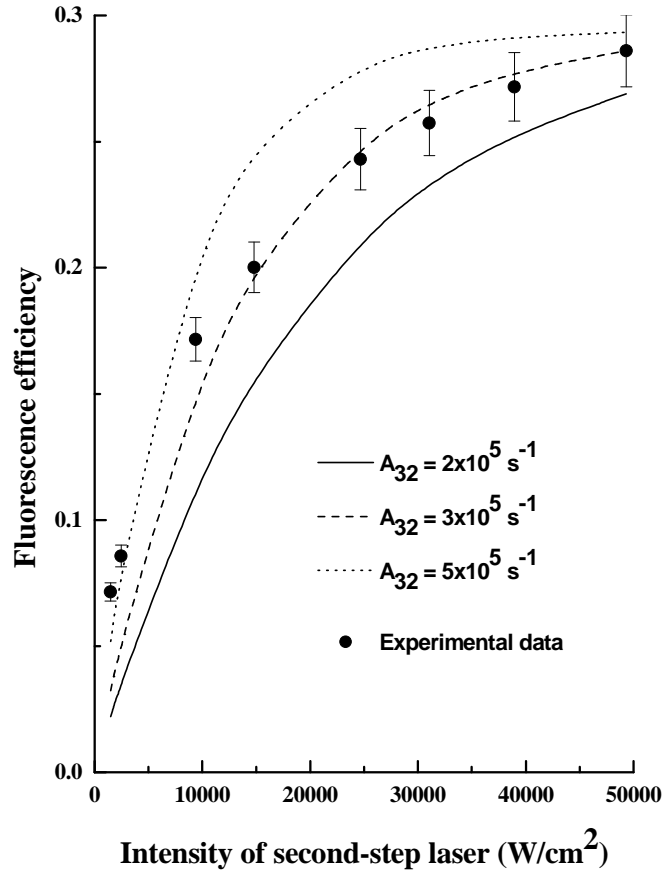


Fig. 3.12: Variation of two-color laser-induced fluorescence efficiency with intensity of the second-step laser for three values of A_{32} , using the photoionization cross-section $\sigma_3 = 1 \times 10^{-17} \text{ cm}^2$. Photoionization pathway of Fig. 2(a) is considered for the results in this figure

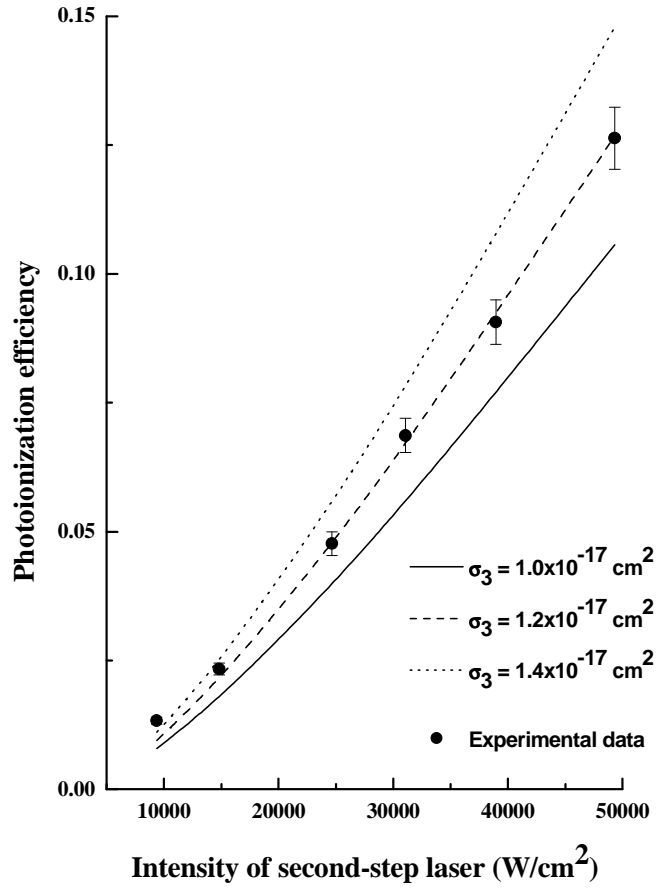


Fig. 3.13: Variation of two-color, three-photon photoionization efficiency with intensity of the second-step laser for three values of σ_3 , using $A_{32} = 3 \times 10^5 \text{ s}^{-1}$

Photoionization pathway of Fig. 2(a) is considered for the results in this figure

Table 3.1 Theoretical Ratios of LIF and RIS Signals for Several Values of the Photoionization Cross-Section σ_3 .

$\sigma_3 (10^{-16} \text{ cm}^2)$	Theoretical ratio	
	LIF	RIS
1	1.2	0.7
2	1.5	0.6
3	1.9	0.6
4	2.3	0.6
5	2.9	0.6
6	3.6	0.6
7	4.6	0.6
8	5.8	0.6
9	7.2	0.6
10	9.0	0.6

**Table 3.2 Measured atomic parameters using simultaneous photoionization and
fluorescence signals**

Sr No	Atomic parameter			Measured value
1	Transition	probability	for	$(3 \pm 0.6) \times 10^5 \text{ s}^{-1}$
	19009.5-36572.0 cm^{-1} transition			
2	Transition	probability	for	$(2 \pm 0.4) \times 10^5 \text{ s}^{-1}$
	19009.5-36682.5 cm^{-1} transition			
3	Photoionization	cross-section		$(1.2 \pm 0.24) \times 10^{-17} \text{ cm}^2$
	for 36682.5-Continuum (or at			
	54134.5 cm^{-1})			
4	Photoionization	cross-section		$(1.2 \pm 0.24) \times 10^{-17} \text{ cm}^2$
	for 36572.0-Continuum (or at			
	54355.5 cm^{-1})			

Chapter 4

Laser optogalvanic spectroscopy technique

The change in the electrical conductivity of a self-sustained gaseous discharge, when illuminated by radiation resonant with an atomic or molecular transition of the elements within it, is known as the optogalvanic effect. The optogalvanic effect was first observed by Penning in 1928. Since then, the optogalvanic effect is used as an important spectroscopy tool. The development of optogalvanic spectroscopy technique and its applications are reviewed by Barbaire et al. [1]. The high-sensitivity spectra of the species present in a gas discharge can be obtained by irradiating the discharge using a tunable dye laser. The use of a hollow-cathode discharge (HCD) lamp has made it possible to perform spectroscopy on a gas-phase sample of refractory elements produced by ionic sputtering of cathode of the lamp. The main characteristic of hollow-cathode discharge, which is a particular kind of glow discharge, is enlargement of the negative glow region. If the cathode is formed by two flat electrodes, parallel to each other and the distance between the two electrodes is quite small with respect to their typical dimensions, the two negative glows coalesce into a single negative glow displaying high radiation intensity. Usually, instead of two parallel electrodes, a cylindrical cathode is used. The strong electric field in the dark region near the cathode strongly accelerates ions against the cathode surface, producing very effective sputtering at current values of the order of 100 mA. In this way the discharge can be used as a source of free atoms of refractory elements as well as a photoion detector. Hence, optogalvanic spectroscopy technique can be used as an alternative to photoionization or fluorescence technique with much simpler experimental setup.

Commercial hollow-cathode lamps were extensively used for the first OG applications. In this chapter, investigations of the plasma parameters in a see-through type, home-made uranium HCD lamp with neon as a buffer gas using optical emission spectroscopic techniques have been discussed [2]. Identification of new even-parity autoionization levels of atomic uranium using this HCD lamp has also been discussed in this chapter [3].

4.1 Spectroscopic measurements of plasma temperatures and electron number density in a uranium hollow cathode discharge lamp

During the past several decades, the hollow cathode discharge (HCD) has been studied by both physicists and chemists. It is a particular type of glow discharge with an enlargement of the negative glow region as one of its main characteristics. With a cylindrical cathode in a HCD lamp which can be thought of as a sealed cell with a very pure buffer gas, large currents up to a few amperes are handled in the glow regime of the discharge. Because of the effective sputtering process, HCD lamp is capable of producing an atomic vapor of almost every metal of the cathode. In this way, the HCD lamps have been used as a source of free atoms of any metal, controllable by direct current in the lamp. Weakly ionized plasma produced in a low-pressure HCD lamp is stable, emitting highly-reproducible narrow spectral lines. The HCD lamps have several potential applications in plasma spectroscopy [4]. Some of the potential applications of HCD lamps include laser spectroscopy [5], optogalvanic spectroscopy [6], control and calibration of laser wavelengths [7] etc. Initially, HCD lamps have widely been used in absorption and emission spectroscopy. A detailed review of the theory and application of the HCD in the area of analytical emission spectroscopy has been carried out by Caroli

[8]. The HCD lamp has been used in our laboratory for various spectroscopic applications. Vas Dev et al. [9], Shah et al. [3] and Mandal et al. [10] have used it as a source of uranium atoms as well as detector for studying high-lying and autoionization states in atomic uranium. In our other laser spectroscopy experiments, it has been used as a tool to facilitate the wavelength acquisition and spectrum calibration [11-14].

Understanding of the plasma behaviour in the HCD lamp is important for the optimization of its applications. It requires the knowledge of plasma parameters such as the plasma temperature and the electron number density inside the HCD. The temperature parameters are neutral species temperature T_o , atomic excitation temperature T_{exc} , electron temperature T_e and ion temperature T_i [15]. The electron number density n_e in the HCD is another important plasma parameter [16,17]. When the plasma, such as the low-pressure HCD lamp plasma, is not in local thermodynamic equilibrium (LTE), all the temperatures are different from each other. The atomic excitation temperature, which describes the distribution of atoms in various energy levels as per the Boltzmann law, is higher than the neutral species temperature in the HCD lamp plasma since the atomic excitation results from the electron energy gained in the electric field applied to the lamp. The electron temperature T_e which describes the Saha ionization equilibrium and also the Maxwell distribution for the velocities of the plasma electrons is somewhat higher than the atomic excitation temperature T_{exc} . The Saha equation relates the electron number density n_e with the densities of the neutral species at a given electron temperature T_e .

Optical emission spectroscopy is a powerful tool for measurements of these plasma parameters. The atomic excitation temperature of the HCD lamp plasma is commonly determined by employing two spectroscopic methods, namely, the two-line

method and the Boltzmann plot method [16-21]. The gas temperature in a HCD lamp plasma is determined from the Doppler broadening of light-atom lines [18]. The electron number density is commonly determined using the Stark broadening of spectral lines [16, 19, 20] provided the line broadening is primarily due to the Stark effect. It can also be determined from the Saha-Boltzmann equation if the electron temperature is known [16,22,23]. Henrion et al. [18] have reported the measurements of T_{exc} and T_o in a U-Kr HCD lamp plasma. Nabavi and Koohian [21] have measured T_{exc} in a Gd-Ne HCD lamp plasma. Mahmood et al. [19] have reported the measurements of T_{exc} using the two-line and the Boltzmann plot methods and n_e using the Stark broadening of neon spectral lines in a commercial HCD lamp. They have not mentioned the material of the hollow cathode.

In this Section, measurement of the plasma parameters in a see-through type, home-made uranium HCD lamps have been discussed. The optical emission spectroscopic technique has been used for these measurements. Three plasma parameters, T_o , T_{exc} and n_e have been simultaneously measured for the first time in a moderately-low pressure hollow cathode discharge lamp [2].

4.1.1. Experimental details

We have constructed a HCD lamp as shown in Fig.4.1. The hollow cathode open at both ends is made up of uranium cylinder of 30 mm length and 8 mm inner diameter. It is supported on two tungsten rods of 2 mm thickness, which are fused with a uranium glass pinch. A tungsten ring anode of 8 mm outer diameter is mounted with the centre of the ring and the hollow cathode lying on one line, the distance between them being 3 mm. The cathode and anode are fixed in a glass envelope.

The HCD lamp was evacuated to a pressure of 10^{-5} torr and then filled with neon as a buffer gas at a pressure of about 2 torr. Using a regulated DC power supply between the electrodes, a discharge was initiated in the HCD lamp for cleaning the cathode surface by sputtering. The lamp was run for an hour and re-evacuated again. Neon gas was filled again at a pressure of about 2 torr and this process was repeated several times. This procedure served the dual purpose of baking the HCD lamp and making the cathode surface ready for efficient sputtering. After several such evacuations and refillings the HCD lamp was used for plasma characterization. The optimum running conditions of the discharge corresponded to 600 V, 100 mA and 2 torr.

The experimental set-up for recording the emission radiated from the HCD lamp plasma is shown in Fig. 4.2. The HCD lamp was mounted on a XYZ translation stage for alignment with the monochromator. The emitted light from the HCD lamp was focused by a plano-convex lens onto the input slit of a high resolution monochromator (SOPRA UHRS 1500) functioning in a double-pass configuration. The input and output slit widths of the monochromator were 12 micrometer each. The output of the monochromator was coupled to a cooled photo-multiplier tube (PMT) in a photon counting mode. The monochromator was calibrated using a stabilized He-Ne laser. A NIST-certified deuterium tungsten halogen lamp with a well-known continuous spectral distribution was used to obtain the relative spectral transfer function of the detection system. We have carried out multiple acquisitions to cover the emission spectrum in the wavelength range 490-650 nm. A sufficient amount of overlap was set between successive acquisitions to reconstruct the entire spectrum. In order to take into account intensity fluctuations during the different steps of acquisition, relative corrections were made on the parts of spectrum

by matching the spectral lines of the overlapped spectra. These parts of the spectrum were merged and the relative normalization was applied to the entire spectrum. To obtain sufficient counts, an integration time of 1 second was used. A linear response of the detection system was verified by inserting neutral density filters between the HCD lamp and the input slit of the monochromator.

4.1.2 Theory

4.1.2.1 Temperature of neutral species

The temperature T_0 of neutral species is obtained from the Doppler broadening of emission lines in cases where the Doppler broadening is the dominant broadening mechanism. This is the case in gas discharge plasmas where the electron number density is low ($\sim 10^{11} \text{ cm}^{-3}$). The full width at half-maximum (FWHM) of a Doppler-broadened spectral line is [18]:

$$\Delta\lambda_D = 7.17 \times 10^{-7} \lambda_0 \sqrt{\frac{T_0}{M}}, \quad (4.1)$$

where λ_0 is the central wavelength of the spectral line, M is the atomic mass of the element in atomic mass units and T_0 is in K. The Doppler width $\Delta\lambda_D$ is in the same units as λ_0 . Aside from the gas conditions, the line broadening includes instrumental broadening, which is almost always essential. We have incorporated this to infer the Doppler width of a spectral line.

4.1.2.2 Atomic excitation temperature

As mentioned earlier, the two-line method and the Boltzmann plot method are the two spectroscopic methods for determining the atomic excitation temperature of the HCD lamp plasma. In the two-line method, the Boltzmann relation is applied to the ratio of the

population of two excited levels, which is determined from integrated intensities of two spectral lines belonging to the same atomic species, having a common lower state and a large energy separation between the excited states. The atomic excitation temperature T_{exc} (eV) in this method is obtained using the relation [16,19]

$$\frac{I_1}{I_2} = \frac{g_1}{g_2} \frac{A_1}{A_2} \frac{\lambda_2}{\lambda_1} \exp \left[- \left(\frac{E_1 - E_2}{T_{exc}} \right) \right], \quad (4.2)$$

where the subscripts 1 and 2 refer to the two spectral lines of the same atomic species, respectively. Here I_i , λ_i , A_i , E_i , and g_i ($i = 1, 2$) represent the intensity, wavelength, transition probability, excitation energy, and statistical weight of the corresponding spectral line. The energies E_i are in the same units as T_{exc} .

In the Boltzmann plot method, the atomic excitation temperature T_{exc} (eV) is obtained from the graphical spectral analysis of many emission lines belonging to the same atomic species using the following equation [16,19,23] :

$$\ln \left(\frac{I \lambda_{ki}}{g_k A_{ki}} \right) = - \frac{1}{T_{exc}} E_k + \ln \left(\frac{hcLn}{4\pi P} \right), \quad (4.3)$$

where I is the integrated intensity of a spectral line occurring between an upper energy level k and a lower energy level i , A_{ki} is the transition probability, λ_{ki} is the transition wavelength, E_k and g_k are the energy in eV and degeneracy of the upper energy level k respectively, n is the total number density of the neutral species, h is the Planck constant, c is the speed of light, L is the characteristic length of the plasma and P is the partition function. The plot of the left-hand side of Eq. (4.3) versus E_k for several transitions is called the Boltzmann plot which yields a straight line with slope of $-1/T_{exc}$. Thus, the

value of T_{exc} in eV can be determined from the slope of the Boltzmann plot. As the Boltzmann plot method utilizes several transition lines, it is more accurate than the two-line method. Hence, we have employed only the Boltzmann plot method for deducing T_{exc} .

4.1.2.3 Electron number density

Using the spectral line intensities of a species in two consecutive charge states Z and $Z+1$ of a particular element, the plasma electron number density is determined from the Saha-Boltzmann equation expressed as [16,20,23]

$$n_e = \frac{I_Z^*}{I_{Z+1}^*} 6.04 \times 10^{21} (T_e)^{3/2} \times \exp[(-E_{k,Z+1} + E_{k,Z} - \chi_Z)/T_e] \text{ cm}^{-3}, \quad (4.4)$$

where $I_Z^* = \frac{I_Z \lambda_{ki,Z}}{g_{k,Z} A_{ki,Z}}$ and χ_Z is the ionization energy. Here, the subscript Z is used to denote the ionization stage of the species ($Z = 0$ for neutral atoms, $Z=1$ for singly ionized atoms, etc.). All the energies and T_e are in eV.

4.1.2.4 Condition for Local Thermodynamic Equilibrium (LTE) Plasma

The validity of the LTE condition can be verified using the McWhirter criterion [23],

$$n_e (\text{cm}^{-3}) \geq 1.6 \times 10^{12} T(K)^{1/2} [\Delta E(\text{eV})]^3, \quad (4.5)$$

which provides the lowest limit of the electron number density for homogeneous plasma to be in LTE. Here ΔE is the largest energy gap of the transition lines.

4.1.3. Results and discussions

4.1.3.1 Emission spectrum

We have recorded the optical emission in the wavelength range 490-650 nm radiated from the U-Ne HCD lamp operated in the glow regime of the discharge with a direct current of 2 mA and Ne gas pressure of 2 torr in the lamp. A part of a typical emission spectrum is shown in Figure 4.3. In order to obtain sufficient reproducibility of the results, we have recorded three sets of emission spectra. The line intensities averaged over the three recorded spectra are used in the present work for the plasma characterization. We have chosen seven well-resolved and non-resonant U I, one U II and one Ne I spectral lines for the analysis. The uranium lines with their intensities and other spectroscopic parameters are shown in Table 4.1. All the parameters except the transition probabilities are taken from the NIST atomic database [23]. As the transition probabilities are not available in the NIST database, we have deduced these from the oscillator strengths f_{ik} given in Ref. [18], using the relation $g_i f_{ik} = 1.4992 \times 10^{-14} \lambda_{ki}^2 g_k A_{ki}$ [25], where λ_{ki} is in nm and A_{ki} is in s^{-1} . The emission lines originating from transitions terminating on the ground level, called resonance, are not considered here as they suffer from self-absorption in the plasma. The ionization energy of U atoms is 6.194 eV [24].

4.1.3. 2 Temperature of neutral species

The sputtered uranium atoms from the cathode in the HCD lamp are in equilibrium with the neon gas atoms. This is inferred from the equilibration time which is inverse of the collision frequency of uranium atoms with neon atoms. This collision frequency is obtained from the hard-sphere interaction that provides an approximate description of atom-atom collisions. It is expressed as $Nv\sigma$ where N is the number

density of neon atoms, v is the average thermal velocity of neon atoms relative to uranium atoms and σ is the cross-section for hard-sphere interaction. The typical value of σ is $\sim 10^{-15} \text{ cm}^2$, considering atomic radius of the atoms. For neon at a pressure of 2 torr, $N = 6.4 \times 10^{16} \text{ cm}^{-3}$. Considering the neutral gas temperature equal to 1310 K as determined below, the value of v is $\sim 8.3 \times 10^4 \text{ cm/s}$. Thus, the collision frequency for collisions between uranium and neon atoms is $\sim 5.3 \times 10^6 \text{ s}^{-1}$ which yields the equilibration time of about 200 ns. Hence, with such fast equilibration, uranium is in equilibrium with neon in the HCD lamp.

Since $\Delta\lambda_D$ is significant for light atoms as evident from Eq. (4.1), we have chosen the neon line at $\lambda_0 = 640.22 \text{ nm}$, which was well separated in the emission spectrum, to determine the temperature of the neutral species. The observed spectral profile of that line is shown in Figure 4.4. The atomic mass M of neon is 20.1797. The FWHM of this Gaussian profile is 0.0042 nm. The Doppler and instrumental contribution give a Gaussian shape line profile with full width at half maximum given by [20]

$$\Delta\lambda_G = (\Delta\lambda_D^2 + \Delta\lambda_I^2)^{1/2} \quad (4.6)$$

Here, $\Delta\lambda_G$, $\Delta\lambda_D$ and $\Delta\lambda_I$ are Gaussian, Doppler and instrumental FWHM, respectively. The instrumental line width is 0.002 nm. The data fitted to Gaussian profile give the Gaussian width of 0.0042 nm. Thus, the Doppler width calculated using Eq. (4.6) gives the value of 0.0037 nm. The temperature of neutral neon species employing Eq. (4.1) is thus obtained as 1310 K at 100 mA current in our HCD lamp. From the error analysis of Eq. (4.1), the relative error in the measurement of T_0 is related to the relative error in the measurement of $\Delta\lambda_D$ as

$$\frac{\delta T_o}{T_o} = 2 \frac{\delta(\Delta\lambda_D)}{\Delta\lambda_D}. \quad (4.7)$$

As the relative error in $\Delta\lambda_D$ is about 3%, twice larger error results in the measurement of T_o . Thus the value of T_o is (1310 ± 80) K in our uranium HCD lamp at 100 mA current. Henrion et al. [18] have mentioned the neutral species temperature as 1170 K at 90 mA current in a uranium hollow cathode lamp.

4.1.3.3 Atomic excitation temperature

The atomic excitation temperature has been determined using the Boltzmann plot method. All the seven lines of U I shown in Table 4.1 have been used to generate the Boltzmann plot, which is shown in Fig. 4.5. The excitation temperature using the Boltzmann plot was obtained from the slope of the curve as (0.284 ± 0.014) eV or (3290 ± 160) K. The relative error of $\sim 5\%$ in the measurement of T_{exc} is obtained from the linear regression analysis of the plot and is the uncertainty of the slope of the linear fit in Figure 4.5.

4.1.3.4 Electron number density

All the seven uranium atomic U I lines, which were used earlier for generating the Boltzmann plot and the uranium ionic line U II at 605.17 nm are used to determine the electron number density using the Saha-Boltzmann equation given in Eq. (4.4). The electron number densities using different U I lines with the uranium ionic line at 605.17 nm are given in Table 4.2. The electron number density n_e is determined as an average value of all values given in Table 4.2 to be $(3.0 \pm 0.4) \times 10^{11} \text{ cm}^{-3}$, where the uncertainty is a sum in quadrature of the statistical uncertainty of the mean and the systematic uncertainty (10%) stemming from the uncertainty of the intensity of the U II line

common to all determinations in Table 2. In these calculations, we have taken the electron temperature equal to the excitation temperature. As the value of T_e is expected to be somewhat higher than T_{exc} , the value of n_e thus obtained is somewhat underestimated.

4.1.3.5 LTE condition

The energy gap equal to 20126 cm^{-1} for the transition $23926\text{-}3800 \text{ cm}^{-1}$ is the largest, which corresponds to ΔE equal to 2.5 eV. Considering the electron temperature equal to the excitation temperature, Eq. (4.5) yields that for HCD lamp plasma to be in LTE, the electron number density n_e should be greater than $1.4 \times 10^{15} \text{ cm}^{-3}$. Although the value of n_e in our HCD lamp is underestimated to be about $3 \times 10^{11} \text{ cm}^{-3}$, the actual value of n_e which is somewhat higher than the underestimated one is still a few orders of magnitude lower than that required for the plasma to be in LTE. Hence, the plasma in the HCD lamp is not in LTE. However, if we consider that all the upper levels of U I transitions included in Table 4.1 are in partial LTE, we obtain from Eq. (4.5) by setting the energy difference (0.55 eV) in the equation to equal the difference between the highest and lowest energies of the excited states considered that n_e must be greater than 10^{13} cm^{-3} . The linearity of the Boltzmann plot in Fig. 4.5 indicates that indeed the partial LTE is in effect, so n_e must be greater than 10^{13} cm^{-3} in our HCD lamp.

4.1.4 Conclusions

The plasma parameters in a see-through type, homemade uranium HCD lamp have been investigated. The temperature of neutral species has been measured from the Doppler broadening of the atomic spectral line of neon. The atomic excitation temperature has been measured using the Boltzmann plot method utilizing uranium atomic lines. Since the generated Boltzmann plot is a straight line, the existence of partial

LTE involving high lying atomic levels is inferred. The electron number density has been determined from the Saha-Boltzmann equation assuming the electron temperature being same as the atomic excitation temperature. For this equation, uranium atomic and ionic lines have been utilized. Thus, three plasma parameters have been measured simultaneously for the first time in a HCD lamp with neon as a buffer gas.

4.2 Study of even-parity autoionization resonances of atomic uranium by three-color optogalvanic spectroscopy

The HCD lamp described and characterized above is used for laser spectroscopy applications. The advantage of doing spectroscopy in HCD lamp lies in its simplicity. The lamp itself works as a source of atomic beam as well as photoion detector and makes the experimental setup quite simple. In this Section, the investigation on the even-parity autoionization resonances of atomic uranium in the energy region $52850\text{-}53350\text{ cm}^{-1}$, using three-color optogalvanic spectroscopy technique in U-Ne HCD lamp with three pulsed dye lasers have been described. To the best of our knowledge, this is the first report of observation of even-parity autoionization states in atomic uranium lying more than 2000 cm^{-1} above the ionization limit.

4.2.1 Introduction

The knowledge of autoionization (AI) states, which are the quasi-bound states of atom lying above the ionization limit, is important to get insight in the basic atomic physics and also to identify efficient photoionization pathways for ultra-trace elemental analysis and isotope-selective photoionization of atoms using resonance ionization spectroscopy (RIS). Multistep RIS, in general, is an excellent tool to study the complex atomic structure especially high-lying autoionization states of atoms, which are not

accessible with the conventional spectroscopic techniques. With the presence of six optically active electrons in the outer shell the electronic structure of uranium is quite complicated. Over last three decades, the uranium atom, , has been a subject of intense multistep excitation and photoionization spectroscopic investigations which resulted in identification of large number of even and odd-parity autoionization states in atomic uranium. By employing time-resolved stepwise excitation, Solarz et al. [26] have investigated high-lying atomic states of uranium within 1000 cm^{-1} of its first ionization limit I_1 (ie $f^3ds^2\ ^4T_{9/2}^0$ at $49958.4\pm0.5\text{ cm}^{-1}$) and reported the first observation of Rydberg progression whose convergence has yielded the value of I_1 which is in fair agreement with the value reported by other photoionization studies. Using similar technique, Coste et al. [27] have extended this work much beyond the first ionization limit. Their observations of Rydberg progressions near I_1 and in between I_1 and I_2 have led to accurate determination of second ionization limit I_2 (ie $f^3ds\ ^6L_{11/2}^0$ at $50247.3\pm0.5\text{ cm}^{-1}$) of uranium. Manohar et al. [28] have studied even-parity autoionization states of uranium using two-step three-photon excitation scheme in the energy region $51224\text{-}51555\text{ cm}^{-1}$ and reported the observation of large number of narrow autoionization levels. Employing two-color, two-step excitation schemes, Mago et al. [29] have reported the observation of odd-parity autoionization states of uranium in the energy region $49960\text{-}50170\text{ cm}^{-1}$. Using three-step resonance ionization mass spectroscopy (RIMS), Miyabe et al. [30] have observed over 200 even-parity autoionization states of uranium in the energy region $49930\text{-}51200\text{ cm}^{-1}$ and assigned their total angular momentum (J) values by polarization method. Bushaw et al. [31,32] and Schumann et al. [33] investigated the even-parity autoionization states in atomic uranium near ionization threshold using three-color three-

step excitation schemes. Recently, we have measured photoionization cross-section of atomic uranium for the transition between the second-excited state at 33801.06 cm^{-1} and the autoionization state at 50701.59 cm^{-1} by simultaneously observing laser-induced fluorescence and photoionization signals [14]. In spite of the voluminous work the detailed information on the autoionization states of uranium lying much above the ionization limit is scanty.

Most of this information on autoionization states of uranium mentioned above is acquired by employing the multistep RIMS in a complex atomic beam setup consisting of vacuum chamber, high temperature oven, detector, etc. required for refractory elements like uranium. Broglia et al. [34,35] have investigated the high-lying states of uranium using multistep optogalvanic spectroscopy in a much simpler system, namely, commercial hollow cathode discharge lamp (HCDL), where HCDL is used as a source of atomic vapours and resulting photoionization produced by multistep RIS is detected as a variation in the discharge current. They have shown that results obtained by this simple technique are comparable to those obtained by conventional and complex detection methods that use atomic beams. Using two-color, two-step optogalvanic spectroscopy, Kujirai et al. [36-38] have studied extensively the autoionization states of rare earth elements such as Lu, Pr, Sm, etc. Vas Dev et al.[9] have reported the investigations on the high-lying odd- parity atomic states and even-parity autoionization states of uranium in the energy regions $34500\text{-}34813\text{cm}^{-1}$ and $51400\text{-}51703 \text{ cm}^{-1}$ respectively using two-color, three-photon photoionization optogalvanic (PIOG) spectroscopy in a U-Ne HCDL. By employing similar two-color, three-photon photoionization technique, Asawari et al. [39] have reported the observation of even parity autoionization levels of uranium in the

energy region $51425\text{-}51760\text{cm}^{-1}$ and defined the J-values of about twenty autoionization levels.

In this Section, the results of investigation on the even-parity AI states of uranium in the energy region $52850\text{-}53350\text{ cm}^{-1}$ explored by using three-color optogalvanic spectroscopy technique in U-Ne HCDL with three pulsed dye lasers have been described [3]. To the best of our knowledge this is the first report of observation of even-parity autoionization states of uranium lying above more than 2000 cm^{-1} relative to the ionization limit of atomic uranium. This region has been studied using four different excitation pathways starting from the lowest metastable state of uranium at 620 cm^{-1} ($^1(^5\text{K}_5^0)$). The investigations have resulted in the identification of 102 new even parity autoionization states and the probable assignment of total angular momentum values. Twenty five out of these 102 autoionization states have been observed through more than one excitation pathway, reducing considerably the ambiguity in their J-values.

4.2.2 Experimental details

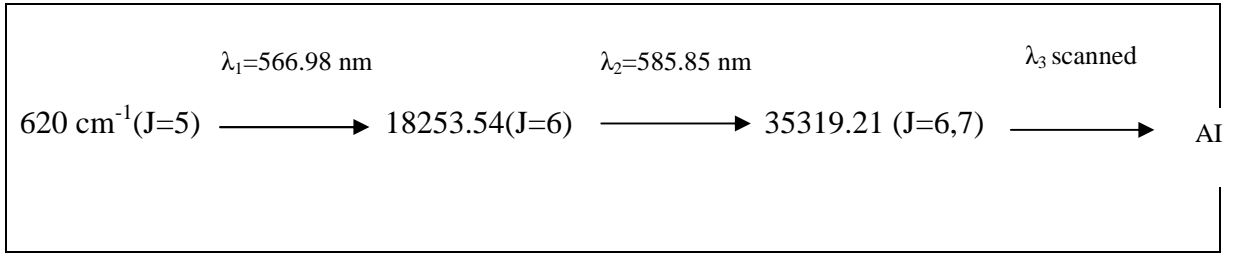
The experimental setup used for three-color optogalvanic spectroscopy is shown in Fig. 4.6. It consists of three Nd-YAG pumped dye lasers (as already described in previous chapters), a see-through-type homemade U-Ne HCDL (cathode length 30 mm, inner diameter 8 mm as described in the previous Section), a digital oscilloscope for signal monitoring and a boxcar averager for further signal processing. HCDL was operated at $\sim 50\text{ mA}$ current. The spatial overlap of three dye laser beams ($\sim 5\text{mm}$ diameter) was achieved by proper steering optics. The spatially overlapped laser beams were made to pass through the centre of the HCDL and optogalvanic signal had been detected across a $2.5\text{ k}\Omega$ ballast resistance. In order to maintain sequential excitation in

different excitation steps, temporal delay between successive lasers was kept more than laser pulse duration. The typical optogalvanic signal waveform when one laser was tuned to first-step resonant transition is shown in Fig. 4.7 a. The enhancement in the single-color optogalvanic signal is quite evident in Fig. 4.7 b, when the second laser was tuned to known second-step resonant transition. The further enhancement in two-color signal is seen, when the third laser is tuned in resonance to autoionization transition as shown in Fig. 4.7 c. The signal amplitudes mentioned here are just illustrative and enhancement depends on laser powers and the particular scheme chosen. The first and second- step dye laser powers were needed to be attenuated significantly in order to obtain high signal to background ratio. The typical signal shown here is for the autoionization resonance 53125.69 cm^{-1} using scheme A as mentioned at Sr No 48 in Table 4.3. Typical laser pulse energies used for first, second and third step transitions were about 50, 250 and 500 μJ respectively. The optimized three-color optogalvanic signal was further processed using a boxcar averager and resulting spectra along with Fabry-Perot etalon fringes (FSR 0.5 cm^{-1}) were recorded by scanning the third laser wavelength (λ_3) in the energy region of interest. During recording the three-color optogalvanic spectra, the third laser energy was varied from 100 μJ to 1 mJ depending upon the dye tuning curve. The scanning speed was 0.002 nm/sec. The energy values of autoionization peaks were calibrated by interpolation using known single-color optogalvanic peaks of uranium and the Fabry-Perot etalon fringes.

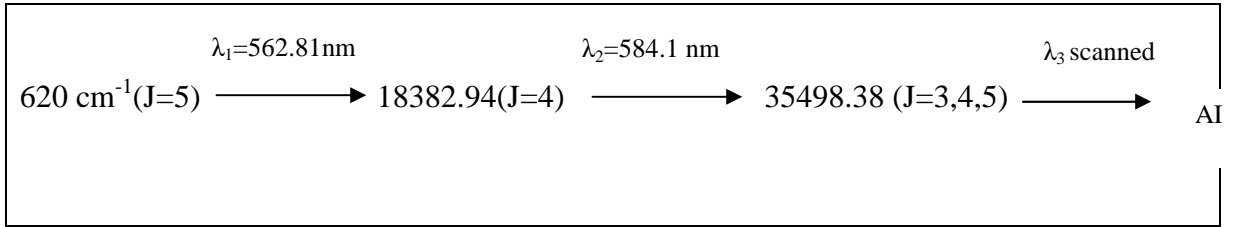
4.2.3 Results and discussions

Three-color optogalvanic spectrum has been recorded using the following four different excitation schemes as also shown in Fig. 4.8.

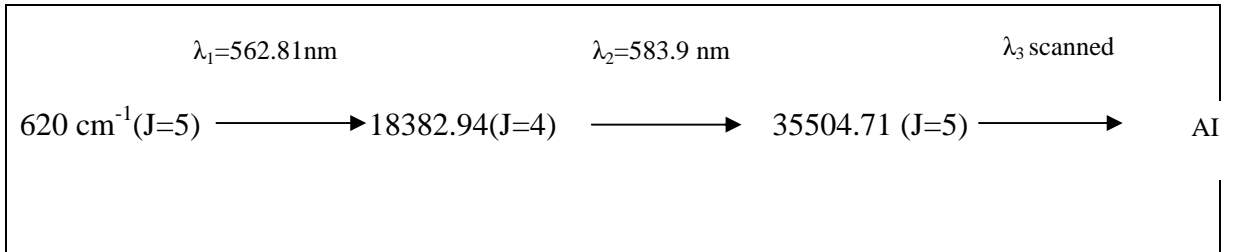
Scheme A



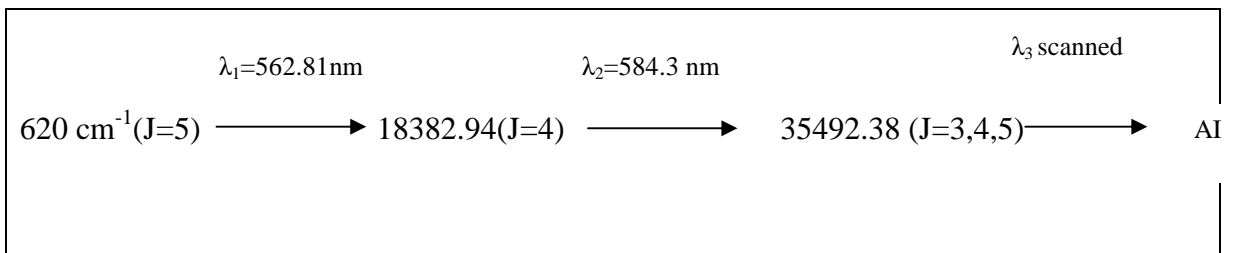
Scheme B



Scheme C



Scheme D



After fixing the wavelengths of the first and second lasers for the first and the second-step resonant transitions of a particular excitation scheme, the third laser was scanned from 560-570 nm corresponding to the energy region $52850\text{-}53350 \text{ cm}^{-1}$ using all the excitation schemes put together. Three-color, three-photon autoionization spectrum

recorded by this technique consists of resonant single-color (λ_3), two-color ($\lambda_1+\lambda_3$), and three-color ($\lambda_1+\lambda_2+\lambda_3$) optogalvanic features. To extract the three-color autoionization features from this composite spectrum, the experiment was repeated with second laser (λ_2) blocked. The resultant optogalvanic spectrum consists of single-color (due to λ_3) and two-color (due to $\lambda_1+\lambda_3$) optogalvanic features, which were filtered out from the three-color spectra to give the genuine autoionization resonances of uranium. Fig.4.9 b shows a portion of typical three-color, three photon autoionization spectra of uranium using scheme D in the energy region 53295-53327 cm^{-1} . Fabry-Perot etalon fringes and two-color optogalvanic spectrum with second laser (λ_2) blocked are shown in Fig. 4.9 a and c respectively. The traces of Fig. 4.9 b and c have been recorded at different sensitivities. The autoionization peaks are marked with the asterisk (*).

On comparison of three-color spectrum with the two-color spectrum, we have identified 102 autoionization resonances in the energy range 52850-53350 cm^{-1} after removing the overlapping autoionization resonances from different excitation schemes. Since there is no data on autoionization resonances of uranium in this energy region reported in the literature, all these resonances are new. A list of these resonances with their energy values, probable J-values and the respective excitation schemes used are given in Table 4.3. The relative intensity of the autoionization peak is shown as strong (S), Medium (M) and weak (W) for qualitative comparison, however signal strength is not normalized against the scanned third-step dye laser power. In these experiments, the intensities of the first and the second-step dye lasers were adjusted to obtain two-color optogalvanic signal of same magnitude for all the excitation schemes. Autoionization states with varying widths were observed in the autoionization spectra and accordingly

they were marked in two categories as narrow (N) and broad (B) in Table 4.3. The autoionization peaks, which are marked with asterisk (*) are also marked with S, W, N and B in Fig. 4b for the illustration purpose.

All the autoionization peaks having signal-to-background ratio less than five have been ignored. By repeating the experiments several times under different discharge conditions, the accuracy in the measurements better than $\pm 0.5 \text{ cm}^{-1}$ was obtained, but it can be slightly worse for a few broad and/or weak lines, where defining the exact peak is relatively difficult. The broadest signal width obtained was more than 5 cm^{-1} . The values of new autoionization resonances in Table 4.3 are obtained by adding the third laser energy values to the second step transition energies which are mentioned in the literature upto second decimal point of wavenumber [30].

Twenty-five out of these 102 autoionization states were populated through more than one excitation routes, so ambiguity in their J value assignment was also reduced, using electric dipole selection rules $\Delta J=0,\pm 1$. The number of autoionization states, which were observed using more than one excitation schemes, is ten through the intermediate level 35319.21 cm^{-1} (scheme A), fourteen through the intermediate level 35498.38 cm^{-1} (scheme B), thirteen through the intermediate level 35504.71 cm^{-1} (scheme C) and thirteen through the intermediate level 35492.38 cm^{-1} (scheme D). The autoionization states which were obtained through scheme A has probable J values from 5 to 8 as the intermediate level at 35319.21 cm^{-1} has J-values 6 and 7. The J- value ambiguity for those resonances is reduced from 5 to 8 to 5 and 6, which are also observed through any of other different routes (scheme B,C or D). The probable J-values for autoionization states identified through scheme B are 2 to 6 as proposed J-values of intermediate level

are 3-5. The J value ambiguity for the autoionization states, which were observed through excitation scheme B as well as A or C, is reduced from 2 to 6 to 5 and 6 and 4-6 respectively. The probable J- values for autoionization states identified through the scheme C are 4-6 as the J value of intermediate level is 5. The J value ambiguity for the autoionization states, which are obtained through scheme C and A is reduced from 4 to 6 to 5 and 6. The probable J- values for autoionization states identified through scheme D have been 2-6 as the proposed J values of intermediate level are 3-5. The J-value ambiguity for the autoionization states also obtained through scheme A or C is reduced from 2 to 6 to 5 and 6 and 4-6 respectively.

4.3 Conclusions

The three-color laser optogalvanic spectroscopy has been established as a simple and sensitive technique for studying autoionization states of uranium. The even parity autoionization states of uranium have been studied by using three-color optogalvanic spectroscopy technique in the energy region $52850\text{-}53350\text{ cm}^{-1}$. Four different excitation schemes have been used to identify 102 new autoionization resonances of uranium. The probable J-values of these newly identified states have also been assigned. Twenty five out of these 102 autoionization resonances have been populated through more than one excitation schemes, so ambiguity in their J-value assignment has been reduced. Thus, the three-color optogalvanic spectroscopy technique can be employed for studying autoionization resonances of any other element of interest.

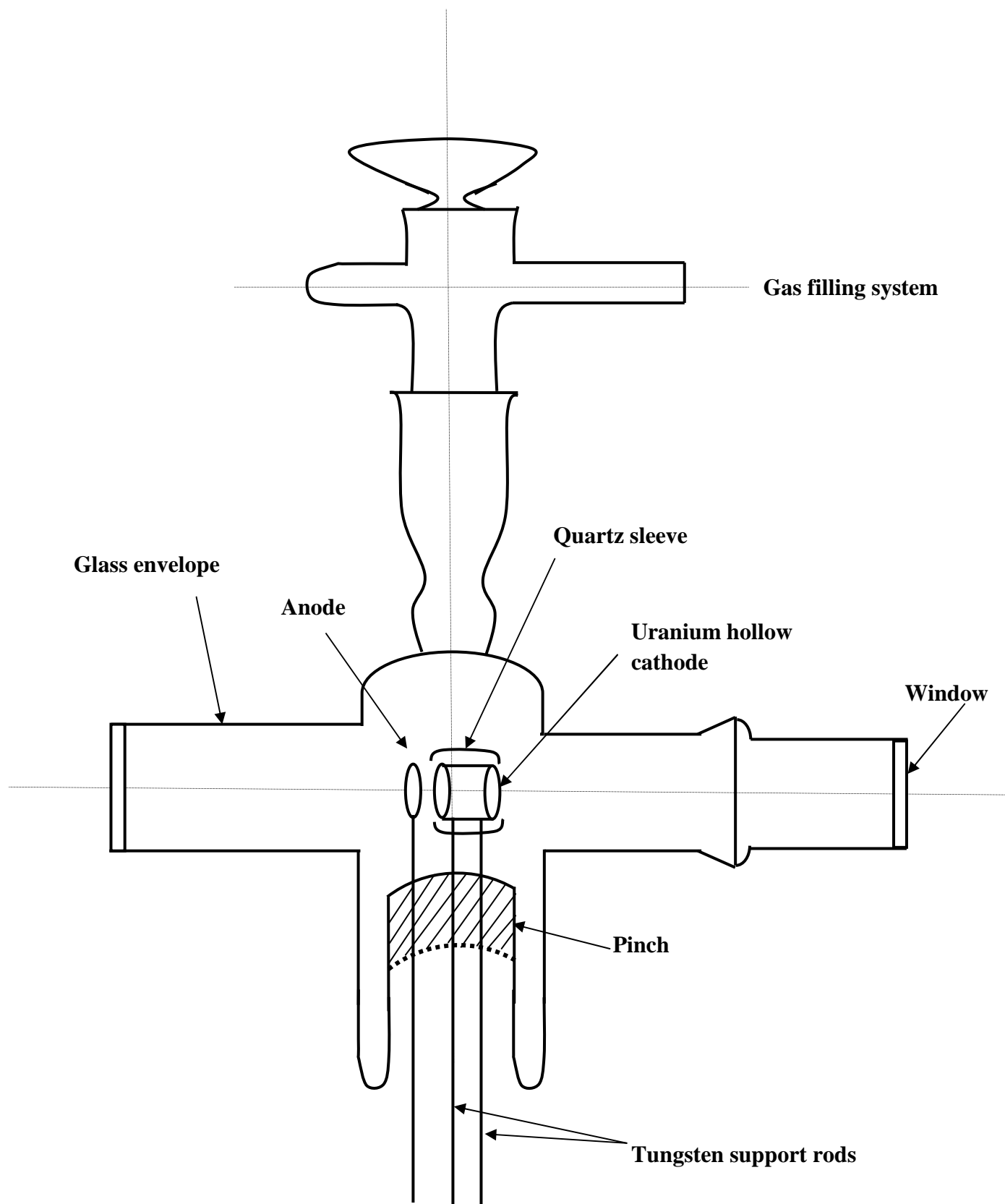


Fig. 4.1: Schematic of the uranium hollow cathode discharge lamp

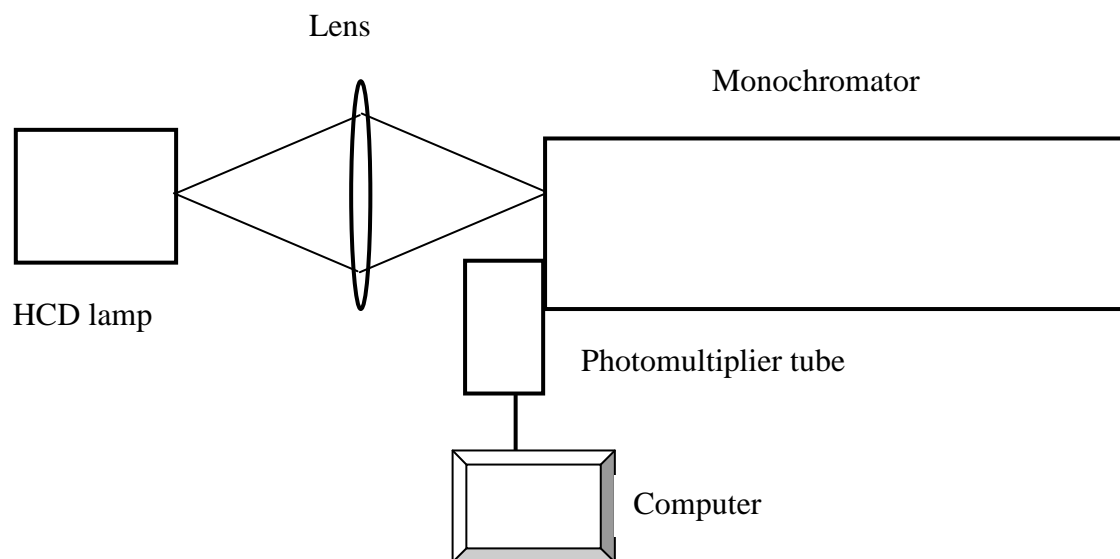


Fig. 4.2: Experimental setup for recording the emission from the HCD lamp

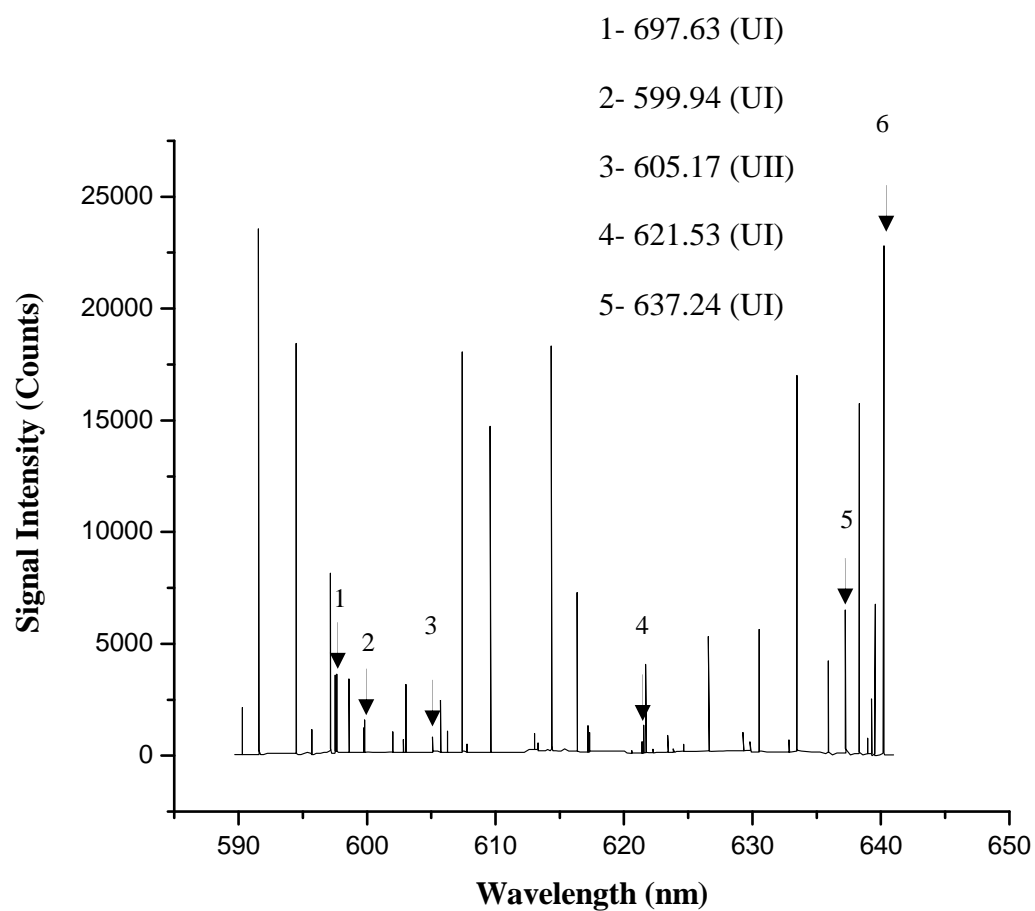


Fig. 4.3: A part of a typical spectrum from the U-Ne HCD lamp

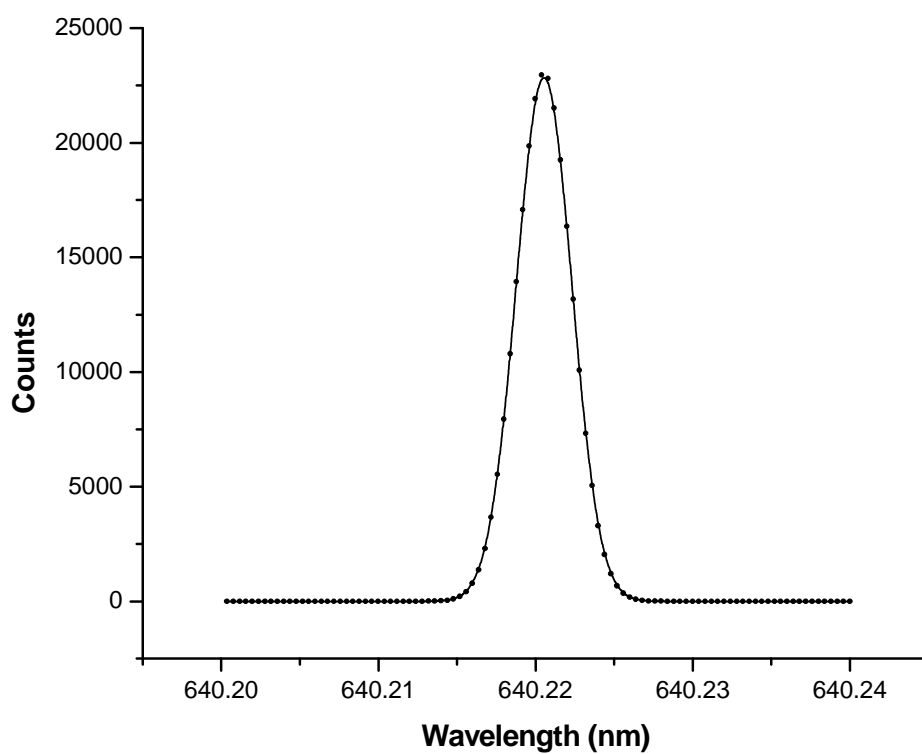


Fig. 4.4: A typical recorded profile of the Ne I spectral line at 640.22 nm

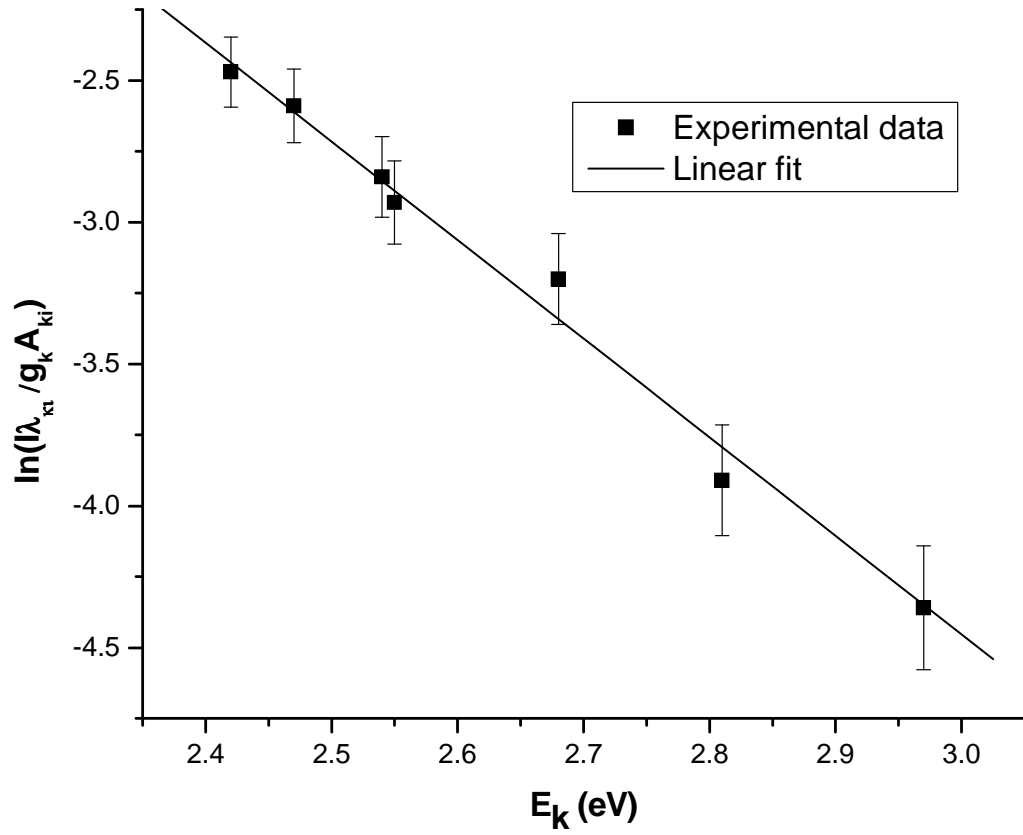
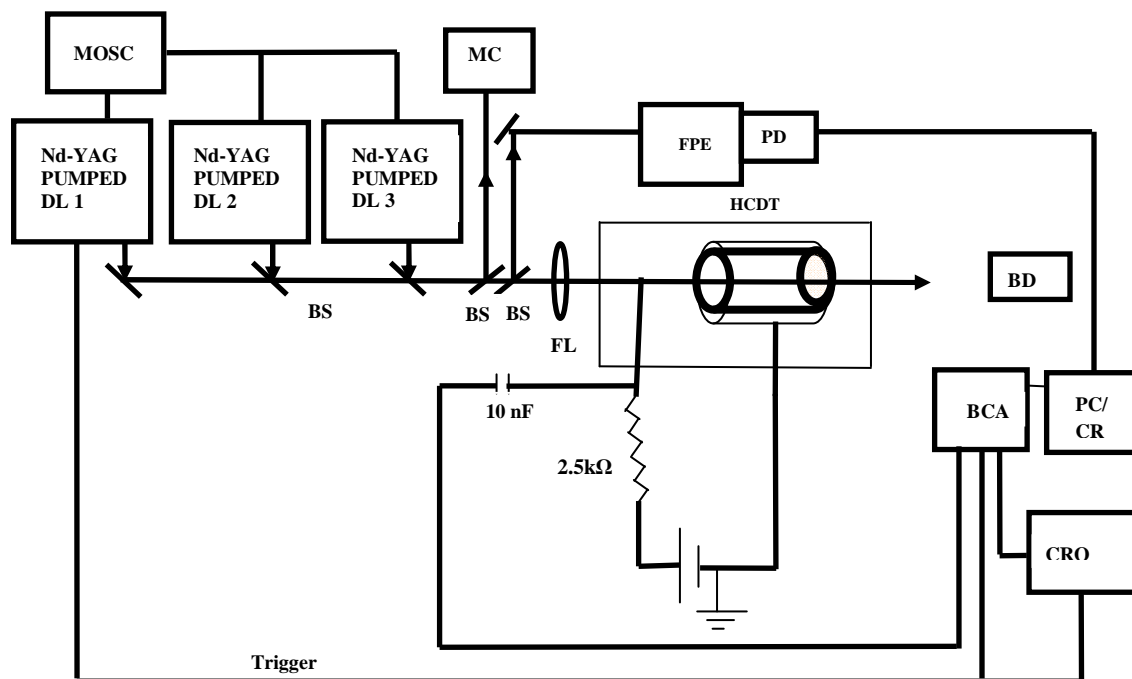


Fig.4. 5: Boltzmann plot made using seven U I transitions. The solid line is a linear fit. The slope gives the temperature equal to (0.284 ± 0.014) eV



FPE- Fabry perot etalon, PD- Photodiode, MOSC- Master oscillator, MC-Monochromator, DL- Dye laser, BD-Beam dump, HCDT-Hollow cathode discharge tube, FL-Focusing lens,

Fig 4.6: Experimental setup used for three-color optogalvanic spectroscopy

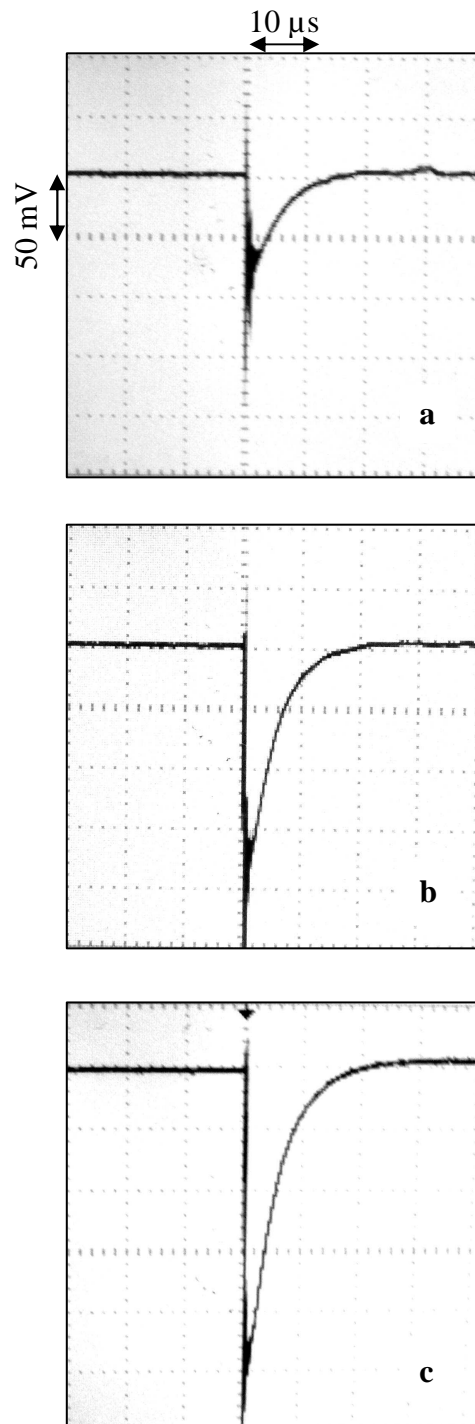


Fig 4.7 a: Typical temporal wave form of resonant single-color optogalvanic signal.

b. Two-color optogalvanic signal.

c. Three-color optogalvanic signal

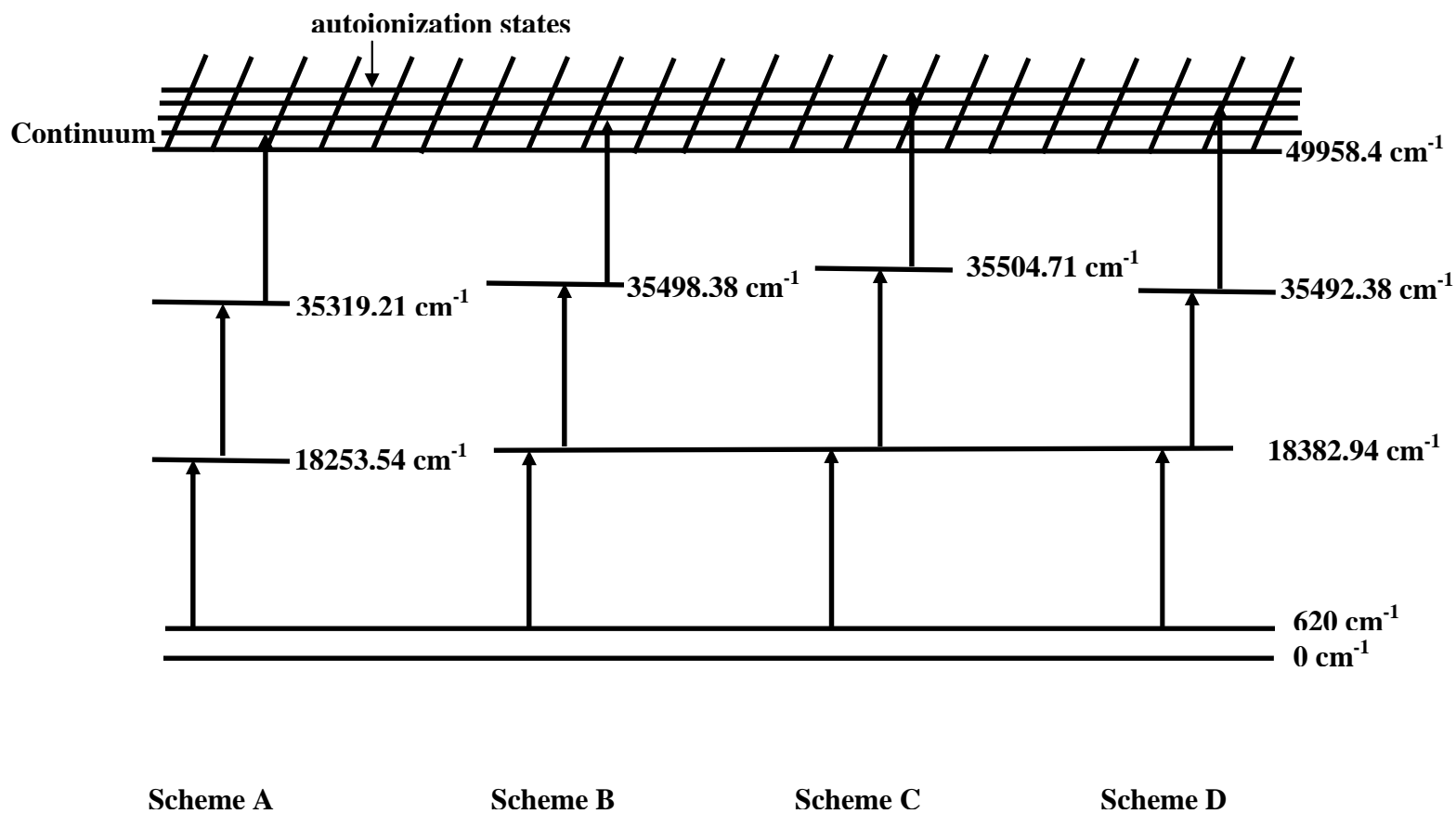


Fig. 4.8: Schematic of the different excitation schemes used for observation of autoionization states of uranium atoms

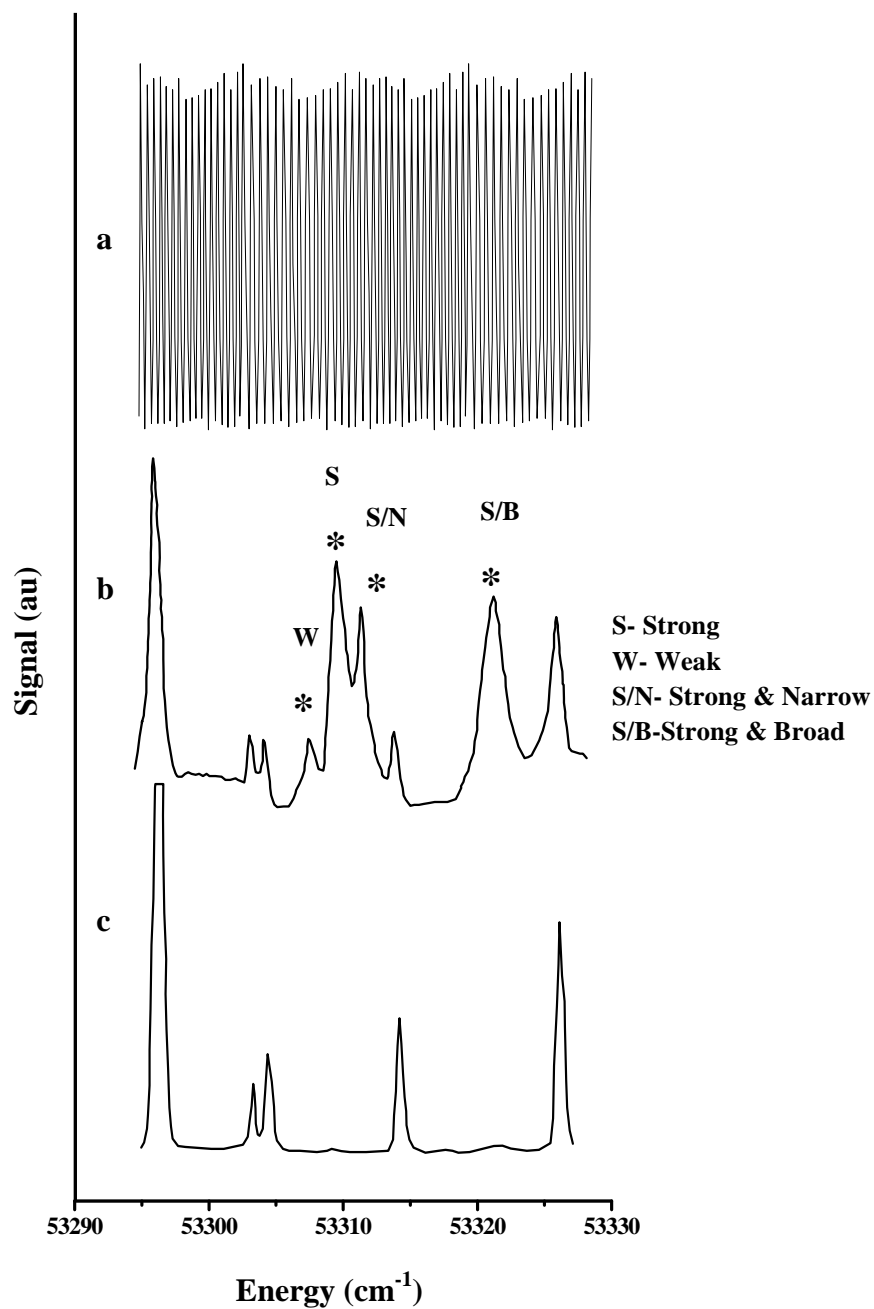


Fig. 4.9: A portion of typical three-color, three-photon autoionization spectra using scheme D in the energy region 53295–53327 cm⁻¹

- a. Fabry-perot etalon fringes**
- b. Autoionization spectra with autoionization resonances marked with asterisk (*)**
- c. Two color spectra recorded by blocking second laser (λ_2)**

Table 4.1 Spectroscopic data for uranium atomic (U I) and ionic (U II) lines used in the analysis (see text for references).

Wavelength of lines (nm)/ Ionic state	Lower level energy (cm ⁻¹)	Lower level degeneracy (g _i)	Upper level energy (cm ⁻¹)	Upper level degeneracy (g _k)	g _i f _{ik}	A _{ki} (s ⁻¹)	Upper level energy (eV)	Signal Intensity (au)
496.73 (U I)	3800	15	23926	17	0.16	2.54×10 ⁶	2.97	1110
530.85(U I)	3800	15	22633	15	0.093	1.47×10 ⁶	2.81	830
562.15(U I)	3800	15	21584	13	0.092	1.49×10 ⁶	2.68	1404
597.63(U I)	3800	15	20529	17	0.22	2.41×10 ⁶	2.55	3636
599.94(U I)	3800	15	20464	15	0.088	1.09×10 ⁶	2.54	1590
621.53(U I)	3800	15	19885	15	0.14	1.61×10 ⁶	2.47	4090
637.24(U I)	3800	15	19489	17	0.30	2.90×10 ⁶	2.42	6524
605.17(U II)	914	10	17434	12	0.013	1.97×10 ⁵	2.16	836

Table 4.2 Electron number density measurement using several uranium atomic (U I) lines and uranium ionic line (U II) at 605.17 nm.

Wavelength of U I line (nm)	Electron number density (cm ⁻³)
496.73	2.97×10 ¹¹
530.85	2.64×10 ¹¹
562.15	3.40×10 ¹¹
597.63	2.98×10 ¹¹
599.94	2.97×10 ¹¹
621.53	3.50×10 ¹¹
637.24	2.83×10 ¹¹

Table 4.3 New autoionization resonances using three-color, three-photon photoionization spectroscopy in a hollow cathode discharge tube.

Sr No	Energy Levels (cm ⁻¹)	Observed by Scheme	Probable J Values	Signal strength/ Signal width
1	52870.75	A	5-8	M
2	52888.75	A	5-8	S
3	52894.25	A	5-8	M
4	52915.25	A	5-8	W
5	52924.00	A	5-8	M/N
6	52937.25	A	5-8	M/B
7	52946.75	A	5-8	M
8	52958.25	A	5-8	W
9	52958.75	A	5-8	W
10	52960.25	A	5-8	W
11	52961.75	A	5-8	M
12	52982.75	A	5-8	M/B
13	52988.75	A	5-8	M
14	53009.19	A	5-8	W
15	53011.19	A	5-8	M
16	53012.69	A	5-8	M
17	53015.69	A	5-8	W
18	53019.19	A	5-8	W

19	53021.19	A	5-8	S/N
20	53033.19	A	5-8	W
21	53037.59	A,D	5,6	M
22	53041.82	D	2-6	M/B
23	53044.44	D	2-6	S/N
24	53047.15	B	2-6	S/N
25	53048.19	A	2-6	M/B
26	53049.65	B,C	4-6	M
27	53054.15	B	2-6	M
28	53055.65	C	4-6	S
29	53059.19	A,C	5,6	M/B
30	53060.69	A,D	5,6	S
31	53064.44	A	5-8	M
32	53070.17	B	2-6	M
33	53074.15	C	4-6	W/B
34	53079.69	A	5-8	S
35	53082.69	A,C	5,6	S
36	53084.32	B,D	2-6	M
37	53088.69	A	5-8	S
38	53095.67	B	2-6	W
39	53098.19	A,B	5,6	S
40	53100.94	A,B	5,6	S

41	53107.07	D	2-6	S/N
42	53108.32	C,D	4-6	M
43	53112.19	A	5-8	S
44	53114.19	A	5-8	S
45	53115.32	D	2-6	M/B
46	53117.19	A	5-8	W
47	53123.82	D	2-6	S/N
48	53125.69	A	5-8	S/N
49	53129.82	C,D	4-6	M/B
50	53133.15	C	4-6	S
51	53134.69	A,C	5,6	S
52	53138.15	C	4-6	S
53	53139.82	B,C	4-6	M
54	53140.65	B	2-6	W
55	53142.92	B	2-6	W
56	53143.32	D	2-6	S/N
57	53144.15	C	4-6	S/B
58	53146.15	C	4-6	S
59	53148.65	C	4-6	S
60	53153.90	B	2-6	S/N
61	53155.19	A	5-8	S
62	53160.19	A,C	5,6	S

63	53161.82	B,D	2-6	S/N
64	53164.69	A,D	5,6	S
65	53167.15	C	4-6	M
66	53170.69	A	5-8	S
67	53173.07	D	2-6	W/B
68	53177.69	A,C	5,6	M
69	53180.32	D	2-6	S/B
70	53187.57	B,D	2-6	S/N
71	53190.57	C,D	4-6	S/N
72	53198.82	D	2-6	S/B
73	53201.42	B	2-6	M
74	53207.57	D	2-6	M
75	53208.90	C	4-6	W
76	53214.15	C	4-6	S
77	53224.32	B,D	2-6	S/N
78	53238.65	B	2-6	M
79	53245.07	D	2-6	S/B
80	53251.07	D	2-6	M
81	53257.07	B,D	2-6	S
82	53259.07	B	2-6	M/B
83	53267.32	B	2-6	W
84	53268.15	B,C	4-6	S/B

85	53268.9	D	2-6	M
86	53272.15	C	4-6	S/B
87	53276.32	D	2-6	S
88	53282.90	C	4-6	M/B
89	53288.57	D	2-6	S
90	53294.65	C	4-6	S/B
91	53303.90	C	4-6	S/B
92	53307.57	B,D	2-6	W
93	53309.57	D	2-6	S
94	53311.57	D	2-6	S/N
95	53313.65	C	4-6	M/B
96	53317.32	B	2-6	S
97	53321.57	B,D	2-6	S/B
98	53328.65	C	4-6	M/B
99	53335.15	B,C	4-6	W
100	53339.07	B,C	4-6	M/B
101	53340.65	C	4-6	W
102	53347.65	C	4-6	S/B

S- Strong, M- Medium, W- Weak, N- Narrow, B- Broad, S/N- Strong and Narrow etc.

Chapter 5

Laser-induced breakdown spectroscopy

5.1. Introduction

The laser-induced fluorescence, photoionization and optogalvanic spectroscopy techniques are very sensitive elemental analysis techniques. When online, remote and multi-elemental analysis is the concern, laser-induced breakdown spectroscopy found to be superior to any other technique. Laser-induced breakdown spectroscopy (LIBS) is also called as laser-induced plasma spectroscopy (LIPS), laser spark spectroscopy (LSS) and laser optical emission spectroscopy (LOES). Laser-induced breakdown spectroscopy (LIBS) has been evolving since last five decades [1]. It has become very popular in the last decade owing to its numerous advantages, such as rapidity, multi-elemental analysis, minimal sample preparation, minimal sample destruction, low cost, versatility of being applied to a wide range of materials without any pre-processing and flexibility of the experimental set-up. It has a strong potential for in situ and real time analysis. LIBS plasma is generated when a high-power pulsed laser is focussed on a solid, liquid or gaseous sample with irradiance $> 1 \times 10^8 \text{ Wcm}^{-2}$ and the light emitted from the plasma is used to determine the elemental composition of the sample.

The LIBS experimental setup usually employs a pulsed laser (typically tens to hundreds of mJ per pulse) and a focusing lens to vaporize a small amount of a sample and generate plasma over the sample surface. The plasma light is collected and a spectrometer disperses the light emitted by excited atomic and ionic species present in the plasma. A detector records the emission signals followed by digitization and displaying the results.

The spectral data analysis provides the chemical species composition and relative species of the sample abundance. Thus setting up LIBS apparatus to perform a LIBS measurement is simple. One focuses a laser pulse on a sample, which can be a gas, liquid, aerosol or solid, to form plasma and the spectra emitted are used to determine the sample's elemental constituents. LIBS can be used in any sample like, metals, rocks, glasses, sand, teeth, bones, weapons, powders, hazardous materials, liquids, plants, biological materials, polymers, etc. Moreover, LIBS can be performed at various scenarios like atmospheric pressure, in a vacuum, at the depths of the ocean, or at extra-terrestrial sites. LIBS can respond in less than a second, using a single laser shot, remotely, to indicate if a spilled white powder is innocuous or hazardous. Samples need not be fluoresce, or infrared (IR) active for performing LIBS, which is a unique characteristic of this method. Because a pulsed laser beam initiates the LIBS plasma, there is no physical contact with the sample; laboratory and open-path standoff applications are readily employed. The LIBS phenomenon represents a well organized engine to convert the chemical information of the target material to light information that can be captured efficiently and analyzed thoroughly by modern spectroscopic instrumentation and data analysis software. The LIBS spectrum reveals immediate qualitative information about sample constituent. Quantitative information of elemental composition of a sample can be obtained either through calibration based LIBS analysis or calibration free analysis of LIBS experiments. In the recent past, it has been extensively used for multi-element analysis of metals and alloys [2,3], art works [4], cultural heritage targets [5], environmental samples [6], and geological [7], biomedical [8] and nuclear materials [9].

In this Chapter, the quantitative elemental analysis of a steel sample using calibration-free laser-induced breakdown spectroscopy (CF-LIBS) has been discussed [2]. The time-resolved spectra from atomic and ionic emission lines of the steel elements are recorded by an Echelle grating spectrograph coupled with a gated intensified charge-coupled device camera (ICCD), which are used for the plasma characterization and the quantitative analysis of the sample. The time delay with respect to the laser pulse where the plasma is in local thermodynamic equilibrium as well as optically thin, necessary for the elemental analysis, is deduced.

Quantitative analysis of unknown samples is conventionally performed using calibration-based LIBS (CB-LIBS) method in which the composition of an unknown sample is determined by comparing the analyte line signals with spectral intensities from the calibration curves [10-16] of emission line intensity ratios versus elemental concentrations using many matrix-matched reference samples with known compositions. This method requires reference samples with a matrix having composition similar to the unknown sample. Ciucci et al. [17] have developed an alternative method, calibration-free LIBS (CF-LIBS) method, for quantitative elemental analysis of a given sample. In this method, the elemental composition of a sample is determined from the LIBS spectrum using computational methods in analyzing the basic physics of the plasma process through the estimation of the plasma temperature and electron number density, assuming that the plasma composition represents exactly the composition of the sample, i.e. stoichiometric ablation and the plasma is optically thin and is in local thermodynamic equilibrium (LTE). They [17] have carried out the quantitative analysis of seven elements in a Al sample. The relative uncertainties in elemental concentration for Al (97.25 wt%)

and Zn (0.1%) was 0.36% and 26% respectively. All the elements in the alloy were detected and quantitatively determined in a wide dynamic range from 250 ppm to 96%. Since its inception, the CF-LIBS method has been applied by several research groups across the world to the analysis of metallic alloys, such as Al-based [17-20], Fe-based [18,20,21], Cu-based [20,22-26] and Au-based [20,25,27] alloys as well as non-metallic samples, such as soils, rocks and glasses [20,25,28-30], human hair [31], coral skeletons [32] and environment samples [33]. Several CF-LIBS techniques have been developed and reported in the literature in the past.

Tognoni et al. [34] have focused on the applications of CF-LIBS method in their review article. They have nicely summarized qualitative results reported in the literature, which are obtained in the analysis of various materials and in the wide range of experimental conditions. They have emphasized on the departure from the nominal compositional values by defining a parameter “distance” and calculated the distance for most of the cited articles in their review article. The distance is being defined as [34],

$$\text{distance} = \sum_{i=1}^N \text{abs} |M_i - C_i|,$$

where the index i runs over all the N elements present in a sample. M_i and C_i represent the measured and certified elemental concentrations respectively. They have used the distance as a monitor of global quality of the CF-LIBS results. The global performance of this analytical method is sketched in a table. The available literature suggests that the CF-LIBS method is more accurate in analyzing metallic alloys rather than rocks or dielectric. The calculated distances vary from 0.9 in metal alloy samples to 73 for rock and soil samples.

Hann and Omenetto [35] have discussed the topic like ablation efficiency, LTE, measurements of temperature and electron number density in their review article. Considerations on the use of Stark broadening and laser-induced fluorescence and absorption are also discussed along with detector calibration and plasma-particle interaction.

The advantage of the CF-LIBS method developed by Ciucci et al. [17], which is used in the above mentioned works, is that it can be applied to any samples without the matrix problem. But, this method requires detecting at least one line of each element in the plasma with known atomic data. Gomba et al. [36] have developed a CF-LIBS procedure different from that of Ciucci et al. [17] to quantify the contents of the elements through the estimation of plasma temperature, electron number density and relative number densities of the neutral and singly ionized ionic species in the LIBS plasma by making use of the experimental spectral line intensities in the time window where the plasma is optically thin and is in LTE. CF-LIBS may be a very important tool for many analytical problems, especially in rapid screening of unknown samples. It can only provide a qualitative estimation of the trace components. This is an intrinsic limit of CF-LIBS because even a small uncertainty in major component is translated into a huge relative error affecting the minor component. However, this limit can be bypassed if the internal standard is available.

Owing to the economic and technical importance of steel in a wide field of industrial applications, home appliances and medical technology, the steel manufacturers are bound to provide customers the chemical composition of steel. Because of the growing demand for real-time, in-situ analytical results in steel industry, LIBS has

received increasing attention of several research groups for compositional analysis of steel [10-12,18,20,21,37-42]. Sattmann et al. [10] have investigated LIBS of steel samples using multiple Q switch Nd:YAG laser pulses and carried out the quantitative analysis using the CF-LIBS. Aragon et al. [11] have studied the experimental conditions and procedure for quantitative analysis of steel in argon at atmospheric pressure using an infrared Nd:YAG laser (1060 nm) and obtained satisfactory analytical results using CB-LIBS with the limit of detection (LOD) in the range of 6-80 ppm. They have carried out elemental analysis of C, Si, Cr and Ni. For Ni, the concentration range of 0.0025% to 2.3% was studied. The relative uncertainty of the CB-LIBS determined values of this element was in the range of 1.2 to 24%. Similar results were obtained for other elements present in the sample. Bassiotis et al. [12] have carried out CB-LIBS analysis in steel samples in air at atmospheric pressure. They have performed measurements with a Q-switched Nd:YAG laser (1064 nm wavelength) and optimized experimental parameters to improve the linearity of the calibration curves for LIBS analysis. They have obtained LOD for Mn as 113 ppm. Togoni et al. [18] have studied the effect of experimental aberrations and accuracy of spectral data using CF-LIBS, assuming that the analytical plasma is ideal. They have studied iron-based and aluminum-based metallic alloys. For a binary iron alloy (Fe-75%, Mn-25%) sample, the relative uncertainty was 1.9% and 5.6% respectively. The distance calculated by Tognoni et al. [34] for this iron and aluminum alloy based samples was 2.8 and 1.8 respectively. Their simulation showed that an acceptable uncertainty of 1% in major component corresponds to very large uncertainty values in minor component affecting the results of this component. Herrera et al. [20] have analyzed Al, Zn, Cu-Ni, Ti, Ni, Cu-Zn alloys and soils using CF-LIBS. Their results

showed that the best accuracy (5% relative uncertainty) is achieved for the matrix elements, while for the remaining components in the sample (major, minor or trace composition), results were considered semi quantitative with < 200% relative uncertainty. Bullajic et al. [21] have developed a model for automatic correction of self-absorption effect in the CF algorithm. The self-absorption corrected CF-LIBS improved the precision and accuracy. Quantitative results in steel samples showed distance 2.5-5.3 as mentioned by Tognoni et al. [34]. Davies et al. [37] have carried out quantitative analysis of steel samples in air at atmospheric pressure using CB-LIBS method with a Q-switched Nd:YAG laser (1064 nm wavelength) at an irradiance of about 10^9 Wcm^{-2} and detected the traces of Cr, Cu, Mn, Mo, Ni, Si and V down to relative concentrations of about 200 ppm. This remote analytical technique has been implemented successfully for measurements in the hostile environment of nuclear reactor building. Aguilera et al. [38] have measured line intensities of neutral atom and ion emission from LIBS plasma produced with a Q-switched Nd:YAG laser (1064 nm wavelength) at irradiances in the range $7.1 \times 10^9 - 7.1 \times 10^{11} \text{ Wcm}^{-2}$ when the laser beam was focussed on steel samples in air at atmospheric pressure and in the range $3 \times 10^8 - 3 \times 10^9 \text{ Wcm}^{-2}$ when the laser beam was defocussed on the steel samples with the lens focal plane behind the samples. They have used the Saha-Boltzman plot to estimate plasma temperature as well as electron number density from the corresponding intercept values, hence provided a variant in the original CF-LIBS quantitative analysis. Palanco and Laserna [39] have developed an instrument for quantitative analysis of steel samples using LIBS and evaluated capability for a fast quality assessment in steel factories. They have used a Q-switched Nd:YAG laser (1064 nm wavelength) at an irradiance of $5.7 \times 10^9 \text{ Wcm}^{-2}$ on steel samples and

carried out elemental analysis of Fe, Cr, Ni, Cu, Mo, Ti and Mn with relative uncertainty of 0.15, 1.0, 1.6, 2.5, 5.3, 7.5 and 6.3 % respectively. Ismail et al. [40] have performed a detailed study of the plasma parameters in LIBS experiments on aluminium and steel alloys using a Q-switched Nd:YAG laser (1064 nm wavelength). Lopez-Moreno et al. [41] have studied the quantification of elemental compositions of steel samples using CB-LIBS with a higher-power microchip Nd:YAG laser (1064 nm wavelength) for enhancing the applicability of the LIBS technique to process monitoring in the steelmaking industry. They have considered non-gated operation of the signal detector and obtained LOD below 100 ppm in most cases.

Vrenegor et al. [42] have analyzed high-alloy steel samples containing nine elements using the CB-LIBS method with a Q-switched Nd:YAG laser (1064 nm wavelength) irradiating the samples. They have compared the results under the influence of two different laser burst modes and two different burst energies using CB-LIBS. They have achieved mean residual deviations values lower than 1 wt% for most of the analytes. For the Ni mean residual deviation was 0.13 wt% which gave a relative uncertainty of 1.2% relative to mean Ni concentration value of 11.1 wt%. They could improve LIBS analysis on high alloy steel samples by a factor of two for matrix and minor elements using interelement correlation.

We have employed a Q-switched Nd:YAG laser (532 nm wavelength) on a steel sample placed in air at atmospheric pressure. We have extended the procedure developed by Gomba et al. [36] for quantitative analysis of two-element Li-Al alloy to multi-element steel (Fe, Cr, Ni, Mg and Si) sample. For the quantification of elemental contents in the steel sample, we have developed an algorithm relating the experimentally

measured spectral intensity values at a time delay where the LIBS plasma is optically thin and in LTE with the basic physics parameters of the plasma. Using the algorithm we have determined the concentrations of Fe, Cr, Ni, Mg and Si in the steel sample. The analytical results obtained from the CF-LIBS method agree well with the certified values of the elements in the sample with a relative uncertainty $< 5\%$.

5.2. Experimental setup

A schematic diagram of the experimental set-up used for LIBS study is shown in Fig. 5.1. An Echelle grating spectrometer coupled with a gateable ICCD camera (Andor Mechelle ME 5000) was used to record the emission spectrum. The spectrometer covers a wide wavelength range 200-975 nm in a single spectrum with a good wavelength resolution (0.05 nm). Low-pressure Hg-Ar lamps which give narrow emission lines from 200-1000nm with accurately known wavelengths has been used for wavelength calibration. Since our spectrograph-detector system is provided with its own data processing software, all calibrations have been done using this software. Mechelle and calibration source has been connected using optical fiber. It was insured that the detector is not saturated. Detector exposure time and gain can be reduced, if detector is saturated. The procedures given in user guide from the manufacturer have been followed. Fig.5.2 shows the wavelength calibrated spectra of Hg-Ar lamp. This figure shows sharp-well resolved lines (the 577-579 nm doublet, for example) of mercury and argon spread over a selected wavelength range of 250-800 nm, which clearly indicates the resolution and range of the system.

Once the wavelength calibration is done, the spectrograph was intensity calibrated using the NIST certified Deuterium-Quartz-Tungsten- Halogen lamp. The intensity

calibrations lamp is supplied with calibration data, which contains a list of irradiance outputs at different wavelengths at a specified distance from the lamp. The lamp has been connected to spectrograph by optical fiber. A background (with no light sources) has been recorded. Then the spectrums of lamps have been recorded by switching on Deuterium source and QTH source one by one. Once this is done, the configuration files have been saved for future usage. Once, the intensity calibration is done, intensity calibrated spectra of Hg-Ar lamp was taken once again. It is shown in Fig. 5.3. However, it can be seen from the both spectra that the 254 nm mercury line, which should be very strong as in Fig. 5.3 (in fact the strongest mercury line) appears only slightly more intense than the 436 nm line in Fig 5.2. This happens because, Echelle gratings produce spectra in several orders, and the efficiency varies across diffraction orders. The relative intensities now more or less match the values given in the NIST Tables i.e. 253.7 nm/436.8 nm \sim 75. Once, the spectra shown in Fig. 5.3 is obtained showing strong 254 mercury line and maintaining the NIST provided intensity ratios, the intensity calibration procedure is complete and the instrument is supposed to be ready for future quantitative spectroscopic analysis.

We have followed Noll [43] for the terms and notations, which are widely agreed upon in the LIBS community. A flash lamp pumped Q-switched Nd:YAG laser (Quantel YG 980) at the second harmonic wavelength $\lambda=532$ nm with pulse duration $\tau_L=7$ ns and repetition rate $\nu_{rep}=20$ Hz was focused normally onto a polished and cleaned steel sample, placed in air at atmospheric pressure using a planoconvex lens with a focal length $f=100$ mm. The focal spot of laser beam was always located on the surface of the sample so that the distance Δs between the position of the beam waist and the surface of

the sample was always zero. We have used 532 nm visible laser radiation for the sake of ease in the alignment. The manufacturer certified elemental compositions of the steel sample used are: Fe (72.4%), Cr (18.3%), Ni (8.03%), Mn (0.82%) and Si (0.33%). The sample, mounted vertically on a X-Y-Z translation stage, was moved manually to perform each measurement on a new part of the sample surface. The laser beam with pulse energy $E_L=70$ mJ was focussed to a focal spot diameter (beam waist width $d_{\sigma 0}$) of about 1 mm measured from the observed ablation spot size on the steel sample. This yields the average laser irradiance at the sample surface equal to $\sim 1 \times 10^9$ Wcm⁻², sufficient for inducing the plasma on the steel surface but insufficient for air breakdown in front of the sample. This laser irradiance, which is same as used by Davies et al. [37], is above the plasma ablation threshold since the line emission from the plasma formed during laser ablation of steel in air has been measured for laser irradiances $\geq 3 \times 10^8$ Wcm⁻² by Aguilera et al. [38]. The spatially integrated plasma light emission was collected and imaged onto the spectrograph slit using an optical-fibre-based collection system. This emission collection assembly (ECA) was positioned at a distance of about 20 cm from the plasma, making an angle 45° to the laser beam. The spectrally dispersed light from the spectrograph was collected by a thermoelectrically cooled ICCD camera which is sensitive in the whole UV-VIS-NIR region, converting the spectral signal into digital signal. The detector was gated in synchronization with the laser pulse to record time-resolved emission spectrum. The detector integration time was limited to 1000 ns to avoid saturation of the detector whereas four delay times of 800, 900, 1000 and 1200 ns were chosen for recording the plasma emission spectra, avoiding the high intensity continuum emission at the early times of the plasma formation. One LIBS spectrum at a

given delay time is derived from an integration of 120 laser pulses to minimize the effects of pulse-to-pulse variations from run to run and for improving the signal-to-noise ratio. In order to obtain enough reproducibility of the results, we have analyzed four sets of such emission spectra recorded at a given delay time. The average line intensity values are calculated as the mean of line intensities from the four spectra, which has been used in the present work for the LIBS analysis.

5.3. Plasma characterization

For quantitative elemental analysis from the LIBS spectral line intensities, it is essential to characterize the time-evolving LIBS plasma in terms of its temperature and electron number density and find out the time window where the LIBS plasma is optically thin and in LTE. Based on plasma spectroscopy, the Boltzmann plot method yields the temperature T and the Saha-Boltzmann equation method yields the electron number density n_e of plasma, which is optically thin as well as in LTE [44]. We briefly present below the relevant equations for characterizing the LIBS plasma using line intensities of the LIBS spectrum.

5.3.1 Determination of plasma temperature T

The spatially integrated spectral line intensity of the k - i electronic transition of the species in charge state Z ($Z = 0$ for neutral atoms, $Z = 1$ for singly-ionized atoms, etc.) of element α in optically thin and LTE plasma is given as [44]

$$I_{ki,Z}^{\alpha} = F n_Z^{\alpha} \frac{g_{k,Z}^{\alpha} A_{ki,Z}^{\alpha}}{\lambda_{ki,Z}^{\alpha} P_Z^{\alpha}} \exp\left(-\frac{E_{k,Z}^{\alpha}}{k_B T}\right), \quad (1)$$

where $F = \frac{hcL}{4\pi}$, L is the characteristic length of the plasma, h is the Planck constant, c is the speed of light, k_B is the Boltzmann constant, $E_{k,Z}^\alpha$ and $g_{k,Z}^\alpha$ are the energy and degeneracy of the upper energy level k respectively, $A_{ki,Z}^\alpha$ is the transition probability and $\lambda_{ki,Z}^\alpha$ is the transition wavelength of the k - i transition, P_Z^α is the partition function and n_Z^α is the number density of the species in ionization stage Z . By taking the natural logarithm, Eq. (1) can be rewritten as

$$\ln\left(\frac{I_{ki}^\alpha \lambda_{ki}^\alpha}{g_k^\alpha A_{ki}^\alpha}\right) = -\frac{E_k^\alpha}{k_B T} + \ln\left(\frac{F n_Z^\alpha}{P_Z^\alpha}\right). \quad (2)$$

If the term on the left-hand side is plotted against E_k for two or more transition lines, the linear plot obtained is called the Boltzmann plot where the integral intensity of each spectral line is represented by a point in the Boltzmann plane. This plot yields straight line with a slope of $(-1/k_B T)$. Thus, the slope of the Boltzmann plot yields the plasma temperature T .

5.3.2 Determination of electron number density n_e

The electron number density using atom and ion spectral lines emitted from the plasma is determined employing the Saha-Boltzmann equation for the line intensities of the species in two consecutive charge states Z and $Z+1$ of a particular element as [36]

$$n_e = \frac{I_Z'}{I_{Z+1}}, 6.04 \times 10^{21} (T_{eV})^{3/2} \times \exp[(-E_{k,Z+1} + E_{k,Z} - \chi_Z) / k_B T] \text{ cm}^{-3}, \quad (3)$$

where $I'_Z = \frac{I_Z \lambda_{ki,Z}}{g_{k,Z} A_{ki,Z}}$ and χ_Z is the ionization energy of the species in the ionization

stage Z . T_{eV} is the plasma temperature in eV. The electron number density is experimentally determined using Eq. (3).

5.3.3 Determination of density ratio of the species of a particular element

The Saha Equation relating the concentrations in the two consecutive charge states Z and $Z+1$ of a particular element α is written as [36]

$$\frac{n_e n_{Z+1}^\alpha}{n_Z^\alpha} = 6.04 \times 10^{21} T_{eV}^{3/2} \frac{P_{Z+1}^\alpha}{P_Z^\alpha} \exp\left(-\frac{\chi_Z^\alpha}{T_{eV}}\right) \text{cm}^{-3}, \quad (4)$$

This equation determines the value of the density ratio of the species in two consecutive charge states of a particular element, using experimentally determined values of T and n_e .

5.3.4 Determination of density ratio of the species of different elements

The density ratio of the species in different charge states of two elements is determined from the Saha-Boltzmann equation for the line intensities of the species in different charge states of two elements α and β as [36]

$$\frac{n_Z^\alpha}{n_{Z+1}^\beta} = \frac{I_{\alpha,Z}'}{I_{\beta,Z+1}'} \frac{P_{\alpha,Z}(T)}{P_{\beta,Z+1}(T)} \exp\left(-\frac{E_k^{\beta,Z+1} - E_k^{\alpha,Z}}{k_B T}\right). \quad (5)$$

5.3.5 Criterion for optically thin and LTE plasma

The condition for the validity of the LTE is often checked with the McWhirter's [45,46] criterion,

$$n_e (\text{cm}^{-3}) \geq 1.6 \times 10^{12} T(K)^{1/2} [\Delta E(\text{eV})]^3, \quad (6)$$

which provides the lowest limit of the electron number density for a homogeneous plasma to be in LTE. Here ΔE is the largest energy gap of the transition lines. There are

papers, which demonstrate the existence of regions of different temperatures and densities in the LIBS plasma [47]. The criterion whether the LIBS plasma is optically thin is obtained from the intensity ratio of two lines of a particular element in the same charge state Z which can be expressed using Eq. (1) as

$$\frac{I_1}{I_2} = \left(\frac{\lambda_{nm,Z}}{\lambda_{ki,Z}} \right) \left(\frac{A_{ki,Z}}{A_{nm,Z}} \right) \left(\frac{g_{k,Z}}{g_{n,Z}} \right) \exp\left(-\frac{E_{k,Z} - E_{n,Z}}{k_B T}\right), \quad (7)$$

where I_1 is the line intensity from the k - i transition and I_2 is that from the n - m transition. If we consider two emission lines having the same upper level or as close as possible, the temperature effect of the Boltzmann factor on the reproducibility of the line intensity ratio is minimized and at the same time the consideration of the efficiency factor of the collecting system is avoided. Neglecting the exponential factor in that condition, one can find out the theoretical value of the intensity ratio of the two lines by using the atomic parameters of the transitions. By matching this theoretical intensity ratio with the measured values at different delay times, one finds out the time window where the plasma is optically thin.

5.4. Quantitative elemental analysis

For quantitative elemental analysis using the CF-LIBS method, we have followed the CF-LIBS procedure developed by Gomba et al. [36] where the concentrations of the elements are determined by matching theoretically obtained values of n_e and relative number densities of the neutral and singly ionized ionic species of a particular element as well as different elements in the plasma with those experimentally determined from Eqs. (3), (4) and (5) using the spectral line intensities in a time window where the LIBS

plasma is optically thin and in LTE. The used CF- LIBS procedure is mentioned in the following.

The total number density of element α is written as

$$\begin{aligned} n_{tot}^{\alpha} &= n_0^{\alpha} + n_1^{\alpha} + n_2^{\alpha} +n_Z^{\alpha} \\ &= n_0^{\alpha} \left[1 + \sum_{Z=1}^{Z_N} \left(\frac{n_Z^{\alpha}}{n_0^{\alpha}} \right) \right], \end{aligned} \quad (8)$$

where n_Z^{α} is the number density of the species of element α in charge state Z ($Z = 0$ for neutral atoms, $Z=1$ for singly-ionized atoms, etc.). The element α contributes to the total n_e with n_e^{α} electrons from the atoms in different charge states, equal to the sum of all ionic state contributions, i.e.

$$n_e^{\alpha} = n_1^{\alpha} + 2n_2^{\alpha} + 3n_3^{\alpha} + = \sum_{Z=1}^{Z_N} Z n_Z^{\alpha} \quad (9)$$

Let us define the functions S_Z^{α} and R_Z^{α} as

$$S_Z^{\alpha} = \frac{n_e n_{Z+1}^{\alpha}}{n_Z^{\alpha}} = 6.04 \times 10^{21} T_{eV}^{3/2} \frac{P_{Z+1}^{\alpha}}{P_Z^{\alpha}} \exp\left(-\frac{\chi_Z^{\alpha}}{T_{eV}}\right) \text{ cm}^{-3} \quad (10)$$

and

$$R_Z^{\alpha} = \frac{n_Z^{\alpha}}{n_0^{\alpha}} \quad (11)$$

The function R_Z^{α} can be rewritten as

$$R_Z^{\alpha} = \frac{n_Z^{\alpha}}{n_0^{\alpha}} = \frac{n_1^{\alpha}}{n_0^{\alpha}} \frac{n_2^{\alpha}}{n_1^{\alpha}} \frac{n_Z^{\alpha}}{n_{Z-1}^{\alpha}} = \frac{S_1^{\alpha}}{n_e} \frac{S_2^{\alpha}}{n_e} \frac{S_Z^{\alpha}}{n_e} = \prod_{j=1}^Z \frac{S_j^{\alpha}}{(n_e)^Z}. \quad (12)$$

n_e^{α} , n_Z^{α} and $n_Z^{\alpha} / n_{Z+1}^{\beta}$ can be expressed in terms of R_Z^{α} as

$$n_e^\alpha = \frac{n_{tot}^\alpha \sum_{Z=1}^{Z_N} Z R_Z^\alpha}{1 + \sum_{Z=1}^{Z_N} R_Z^\alpha} \quad (13)$$

$$n_Z^\alpha = \frac{n_{tot}^\alpha}{1 + \sum_{Z=1}^{Z_N} R_Z^\alpha} R_Z^\alpha \quad (14)$$

$$\frac{n_Z^\alpha}{n_{Z+1}^\beta} = \frac{n_0^\alpha}{n_0^\beta} \frac{R_Z^\alpha}{R_{Z+1}^\beta} \quad (15)$$

The total electron number density n_e of the plasma is obtained by summing up of electron contributions from all the elements:

$$n_e = \sum_{\alpha=1}^M n_e^\alpha, \quad (16)$$

where M is the total number of elements in the sample. Using T obtained from the Boltzmann plot and a proposed (initial) set of $n_{tot}^{\alpha'}$ of all the elements, n_e is calculated, incorporating electron contributions from all the elements, starting from its default value until convergence is reached. The convergence is accepted when the ratio of difference of the last and previous values is $\leq 10^{-4} \%$. The converged value is taken as the theoretical value of n_e . Then, the values of $\frac{n_{Z+1}^\alpha}{n_Z^\alpha}$ and $\frac{n_Z^\alpha}{n_{Z+1}^\beta}$ are calculated. These calculations are carried out for a variable set of $n_{tot}^{\alpha'}$ of all the elements to find out an appropriate set of

$n_{tot}^{\alpha'}$ of all the elements that results in the theoretical estimates of n_e , $\frac{n_{Z+1}^\alpha}{n_Z^\alpha}$ and $\frac{n_Z^\alpha}{n_{Z+1}^\beta}$ very

close ($\leq 1\%$) to the experimentally measured values. These elemental concentrations are then stored. The relative concentration of element α is then obtained as

$$c^{\alpha} = \frac{n_{tot}^{\alpha}}{\sum_{\alpha'} n_{tot}^{\alpha'}}, \quad (17)$$

in terms of molar fractions or as

$$c^{\alpha} = \frac{n_{tot}^{\alpha} \mu_{\alpha}}{\sum_{\alpha'} n_{tot}^{\alpha'} \mu_{\alpha'}}, \quad (18)$$

in terms of mass abundance, where μ_{α} is the atomic weight of element α . Based on the above procedure, we have developed a CF-LIBS algorithm for the quantification of elemental contents in a steel sample. A schematic diagram of the algorithm is shown in Fig. 5.4.

5.5. Results and discussion

5.5.1 Emission spectra

In order to arrive at the proper time window for quantitative analysis, where the LIBS plasma is optically thin and in LTE, we have recorded four sets of LIBS spectra of the steel sample at each of the four delay times of 800, 900, 1000 and 1200 ns respectively relative to the laser pulse. The average line intensity values, calculated as the mean of line intensities from the four spectra, have been used for the LIBS analysis. Fig. 5.5 shows typical experimental LIBS spectra of a steel sample at a delay time of 1000 ns. We have chosen the wavelength range from 250 to 550 nm in Fig. 5.5 A, covering the atomic lines of Fe, Cr, Ni, Mn and Si chosen for the plasma characterization and the compositional analysis. In Fig. 5.5 B, we have chosen the wavelength range from 232 to

242 nm to show the ionic lines of Fe used in the analysis. Since Fe is a major element with a content of more than seventy percent, its rich atomic and ionic transitions make the spectrum much crowded, overlapping with lines of the other elements and making the spectral analysis much tedious. As mentioned in Fig. 5.5, eight Fe I and three Fe II emission lines, which are well resolved, non-resonant and have minimal spectral interference with other spectral lines in a complex steel spectrum, are chosen for the plasma characterization in the present work. Aydin et al. [48] have discussed line selection criterion in detail. These lines along with their spectroscopic parameters, taken from the NIST atomic database [49], are shown in Table 5.1. The non-resonant atomic emission lines of other elements (Cr, Ni, Mn and Si), which are used in the quantitative analysis, along with their spectroscopic parameters are also given in the table.

5.5.2 Time delay for optically thin and LTE plasma

To infer the time delay where the plasma is optically thin, we have considered two Fe I emission lines, one at 425.08 nm and the other at 432.58 nm. The first emission line at 425.08 nm is chosen owing to its upper energy level (4.473 eV) and its degeneracy (7) being same as that of the second emission line. The transition probability of the first emission line is $1.02 \times 10^7 \text{ s}^{-1}$ and that of the second emission line is $5.16 \times 10^7 \text{ s}^{-1}$ as provided in NIST data [49,50]. The theoretical value of the intensity ratio for this couple of lines is calculated from Eq. (7) to be equal to 0.20. Since the values of the transition probabilities chosen are uncertain in range of 10% [50], the overall uncertainty in the theoretical line intensity ratio of two lines is in the range 20%, owing to two transition probabilities involved in Eq. (7). Thus, the theoretical intensity ratio of the two lines chosen is 0.20 ± 0.04 . From the measured average intensities of these Fe I lines with

relative error in the measurement of each of the line intensities in the range of 10%, the experimentally measured intensity ratios of this couple of lines are 0.17 ± 0.03 , 0.23 ± 0.05 , 0.25 ± 0.05 and 0.13 ± 0.03 at delay times of 800, 900, 1000 and 1200 ns respectively. Thus, the LIBS plasma produced in this work is optically thin (within the theoretical and experimental errors) at all the four delay times considered.

We have applied the McWhirter's criterion [Eq. (6)] to obtain the lowest limit of n_e for which the plasma will be in LTE. In our case ΔE is ~ 5.0 eV (Table 5.1). Using $T \sim 10^3$ K (as mentioned in section 5.3) at 1000 ns delay time, the lowest limit of n_e for the plasma to be in LTE, as obtained from Eq. (6), is $\sim 2 \times 10^{16} \text{ cm}^{-3}$. The measured value of n_e equal to $9.8 \times 10^{16} \text{ cm}^{-3}$ (as mentioned in section 5.4) is more than the lowest limit, satisfying the assumption of LTE prevailing in the plasma at 1000 ns delay time. Thus, the LIBS plasma in the present work is optically thin as well as in LTE at 1000 ns delay time. Hence, we have carried out further LIBS analysis at a delay time of 1000 ns.

5.5.3 Plasma temperature

We have generated the Boltzmann plot (Fig. 5.6) at a delay time of 1000 ns using seven Fe I lines mentioned in Table 5.1. The 425.08 nm line is not used because it has the same upper energy level as that of 432.58 nm line. The slope of the plot gives $T = 0.875$ eV (10150 K). The relative error in the measurement of T corresponding to a relative error in the measurement of line intensities and a relative error in the measurement of the transition probabilities may be estimated from the error analysis of Eq. (2) as

$$\frac{\delta T}{T} = \frac{k_B T}{E} \left(\frac{\delta I}{I} + \frac{\delta A}{A} \right). \quad (19)$$

The error in our measurement of line intensities is in the range of 10% and the reported errors in the transition probabilities are in the range 10%. Considering the lowest upper energy level used in the present work, for which $E=3.7$ eV and $T= 0.875$ eV (measured), the resultant relative error in the temperature measurement is about 5%. Thus the value of T obtained from the Boltzmann plot is 0.875 ± 0.044 eV (10150 ± 510 K).

5.5.4 Electron number density

Using the measured intensity ratio of Fe I and Fe II lines at a given delay time, the electron number density n_e is determined from Eq. (3). We have considered five intensity ratios, Fe I 346.59 nm and Fe II 233.28 nm, Fe I 355.49 nm and Fe II 233.28 nm, Fe I 361.88 nm and Fe II 233.28 nm, Fe I 346.59 nm and Fe II 233.80 nm and Fe I 346.59 nm and Fe II 241.33 nm and determined five values of n_e at a given delay time. The arithmetic mean of the five values of n_e is taken as the average value of n_e at that particular delay time. The average value of the electron number density at a delay time of 1000 ns is thus determined to be $9.8 \times 10^{16} \text{ cm}^{-3}$. The spread in the five values of n_e gives a relative uncertainty of $\sim 10\%$ in its measurement. Thus the value of n_e is $(9.8 \pm 1.0) \times 10^{16} \text{ cm}^{-3}$.

5.5.5 Density ratios of the species of particular and different elements

We have determined the density ratio $n_{\text{Fe II}}/n_{\text{Fe I}}$ from Eq. (4) using the measured values of T and n_e at a delay of 1000 ns and the corresponding partition function from the NIST atomic database [49]. Its value is determined as 6.7. Using Eq. (5), the intensities of Cr I, Ni I, Mn I, Si I and Fe II lines at a delay of 1000 ns and their spectroscopic parameters, taken from the NIST database [49], the density ratios $n_{\text{Cr I}}/n_{\text{Fe II}}$, $n_{\text{Ni I}}/n_{\text{Fe II}}$, $n_{\text{Mn I}}$

$I/n_{Fe II}$ and $n_{Si I}/n_{Fe II}$ are determined from Eq. (5). These experimental results are given in Table 5.2. The experimental values of T and n_e determined are also given in the table.

5.5.6 Quantitative elemental analysis

Like many reported articles [34], we have studied one steel sample and applied the CF-LIBS algorithm developed in this work (Fig. 5.4) for its quantitative elemental analysis. In the CF-LIBS algorithm, we have varied the values of n_{tot}^{Fe} , n_{tot}^{Cr} , n_{tot}^{Ni} , n_{tot}^{Mn} and n_{tot}^{Si} each in the range 10^{14} - 10^{17} cm^{-3} and calculated the theoretical values of n_e , $n_{Cr I}/n_{Fe II}$, $n_{Ni I}/n_{Fe II}$, $n_{Si I}/n_{Fe II}$, $n_{Mn I}/n_{Fe II}$ and $n_{Fe II}/n_{Fe I}$ in the LIBS plasma, which match well ($\leq 1\%$) with the experimental results when $n_{tot}^{Fe} = 8.7 \times 10^{16}$ cm^{-3} , $n_{tot}^{Cr} = 2.3 \times 10^{16}$ cm^{-3} , $n_{tot}^{Ni} = 9.4 \times 10^{15}$ cm^{-3} , $n_{tot}^{Mn} = 1.1 \times 10^{15}$ cm^{-3} , and $n_{tot}^{Si} = 8.1 \times 10^{14}$ cm^{-3} are considered. Using these density values we have determined the fractional molar concentrations of Fe, Cr, Ni, Mn and Si in the steel sample. The values of Fe, Cr, Ni, Mn and Si in the steel sample obtained from the CF-LIBS analysis along with their certified values are shown in Table 5.3. The residual deviation (i.e. the deviation of CF-LIBS determined values from the certified values) for Fe, Cr, Ni, Mn, Si in our measured values are 0.26, 0.42, 0.22, 0.04 and 0.01 wt % respectively. The distance as defined by Tognoni et al. [34] for our measurements is 0.95. For the appraisal of LIBS performance, the relative uncertainty of the elemental content value is determined by dividing the residual deviation with the certified value. The relative uncertainties for all the elements are also given in the table. It is noted from the table that the analytical results obtained from the CF-LIBS method agree well with the certified values of the elements with a relative uncertainty $< 5\%$. The

relative uncertainties (or distance) for our measurements are comparable to those reported in the literature on steel samples [11,18,20,21,34,39,42] and other metallic alloys [34].

5.6. Conclusions

A CF-LIBS algorithm for a multi elemental steel relating the experimentally measured spectral intensity with the basic physics of the plasma for the quantitative analysis of materials has been developed. One steel sample has been used and the CF-LIBS algorithm developed in this work for its quantitative elemental analysis has been applied for analysis. The concentrations of Fe, Cr, Ni, Mn and Si in the sample are determined. The LTE and optically thin plasma conditions, necessary for the quantitative elemental analysis, have been determined using the time-resolved spectral intensities of Fe I lines from the LIBS plasma. The density ratio of the species in different charge states of the elements (Fe, Cr, Ni, Mn and Si) in the steel sample using the line intensities of the species in different charge states of the two elements have also been determined. The quantitative analysis of a certified steel sample using the CF-LIBS technique has been successfully carried out. The elemental concentrations obtained from the CF-LIBS technique are in good agreement (with a relative uncertainty $< 5\%$) with the certified values as well as with those reported in the literature. It is concluded that accurate quantitative analysis can be achieved using the CF-LIBS technique by an appropriate choice of experimental conditions.

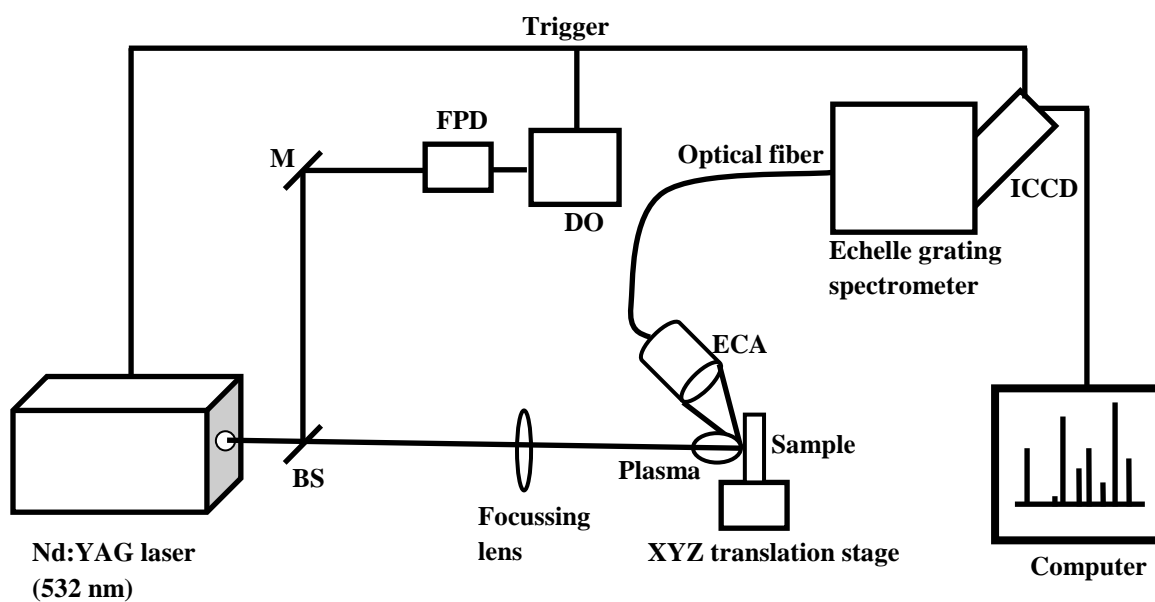


Fig. 5.1: Experimental set-up for LIBS studies

BS - Beam splitter, DO - Digital oscilloscope, ECA - Emission collection assembly, FPD - Fast photo diode, M - Mirror

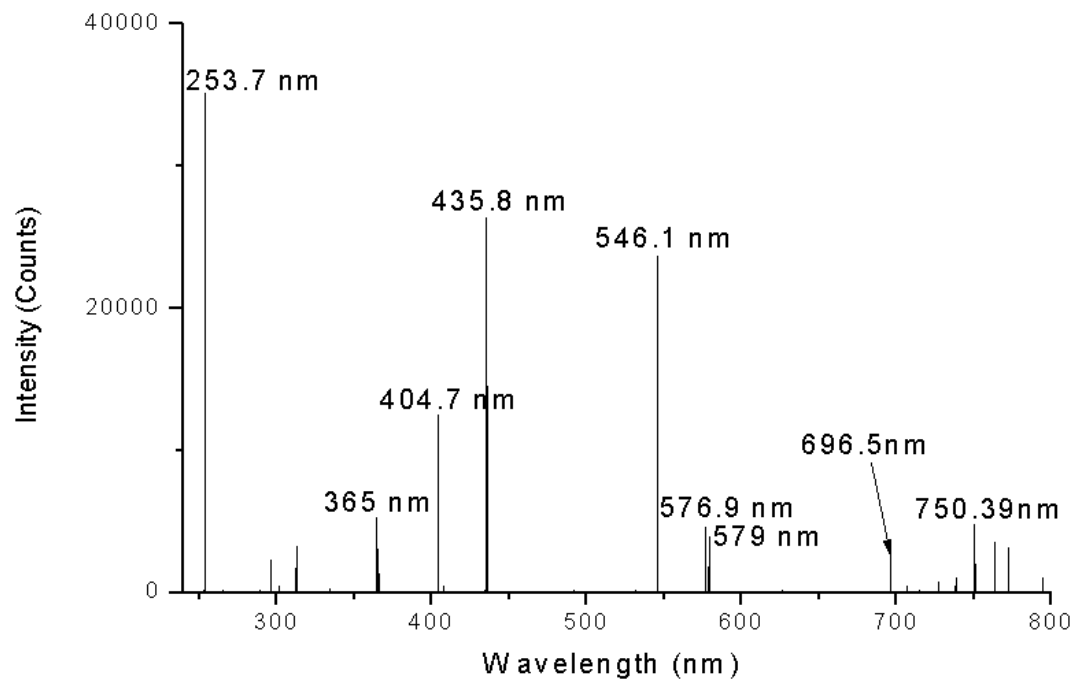


Fig. 5.2: Spectrum of Hg-Ar lamp before intensity

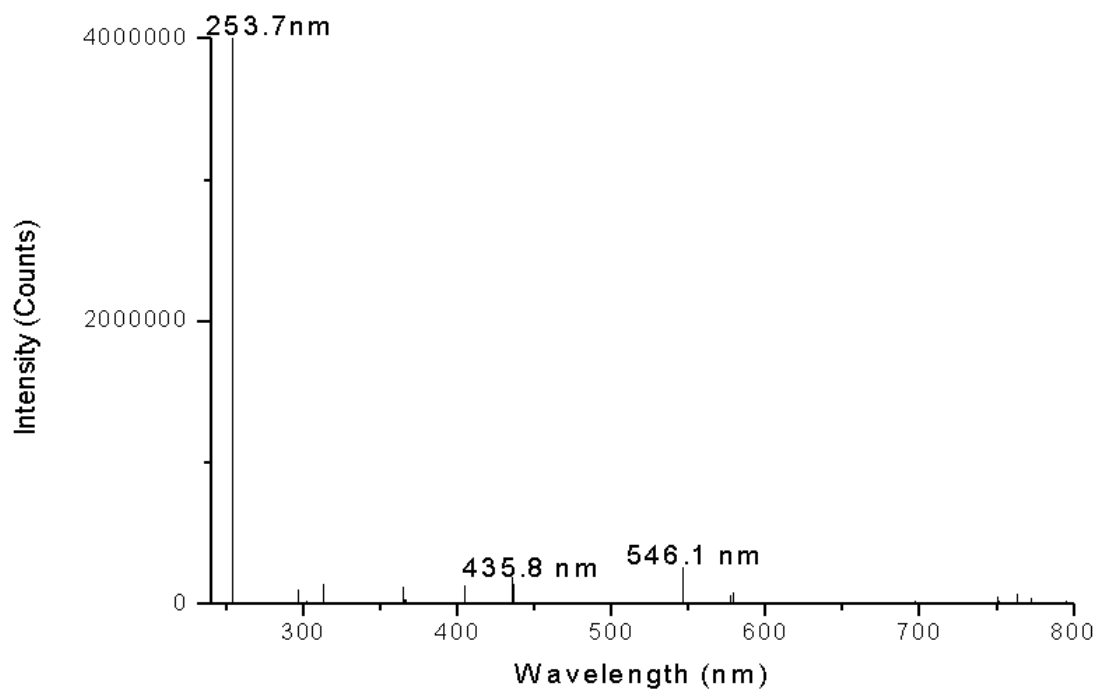


Fig. 5.3: Spectrum of Hg-Ar lamp after intensity calibration

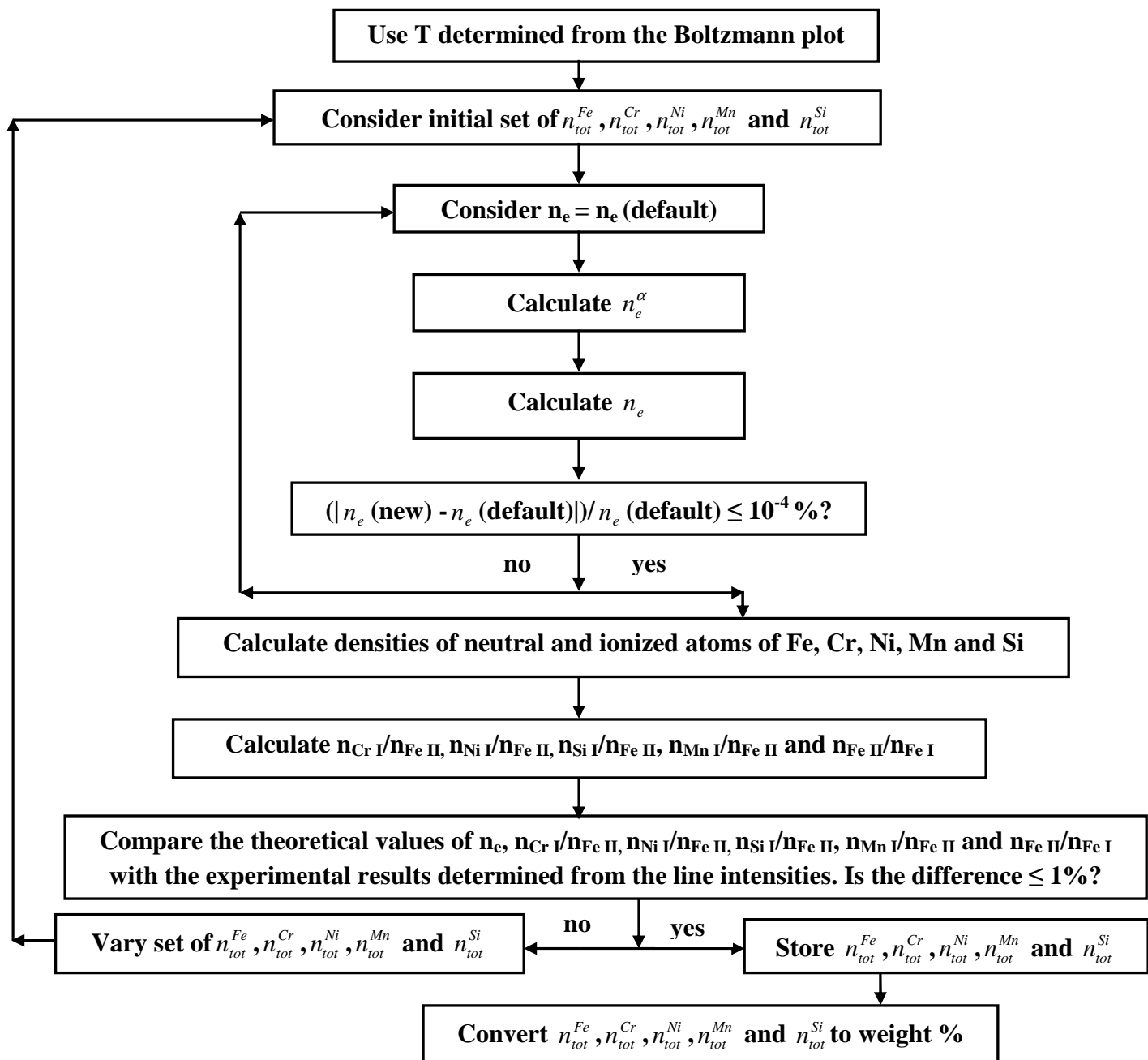


Fig. 5.4: Schematic diagram of the CF-LIBS algorithm

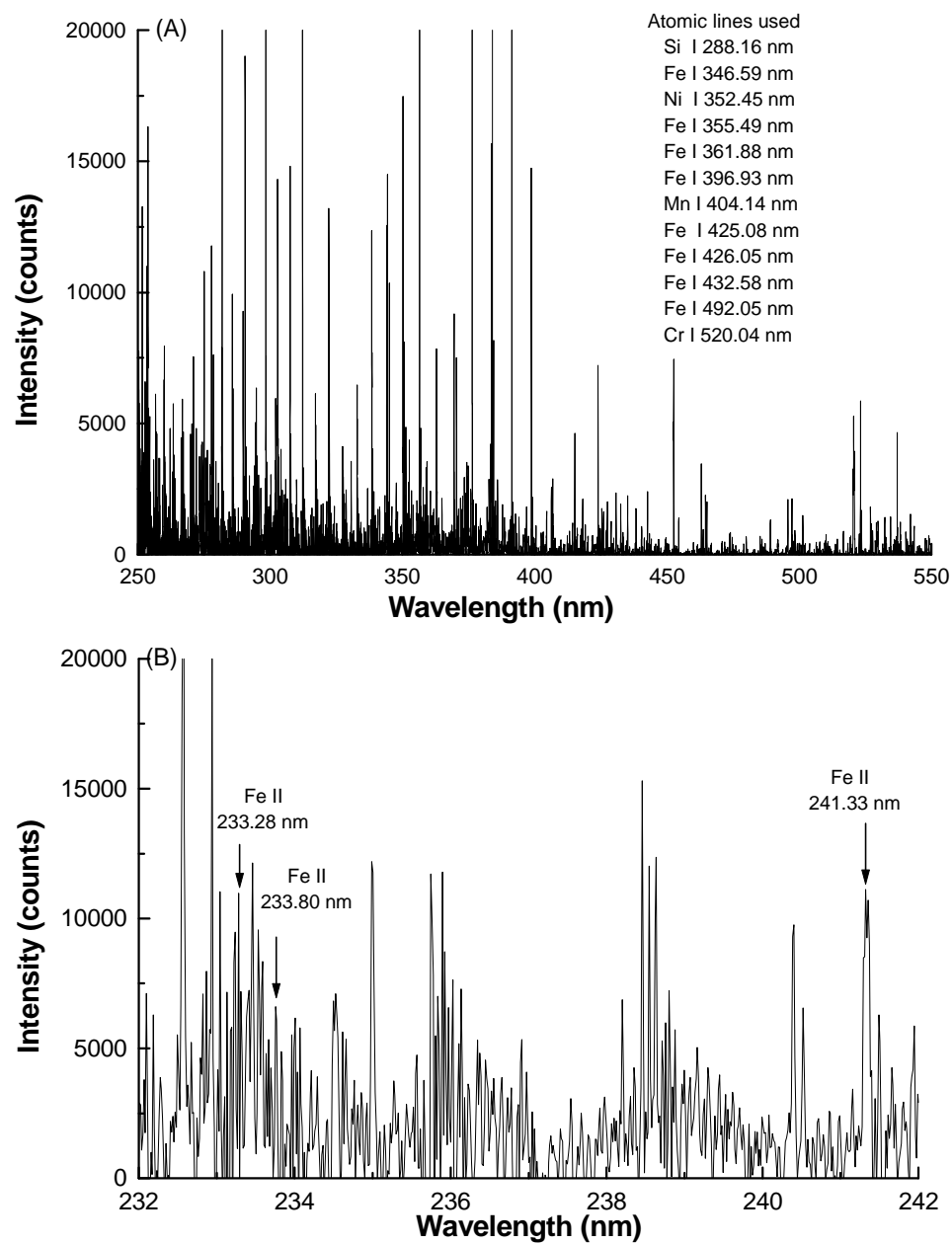


Fig. 5.5: LIBS spectra of a steel sample at a delay time of 1000 ns, covering (A) atomic lines of Fe, Cr, Ni, Mn, and Si (B) ionic lines of Fe used in the analysis

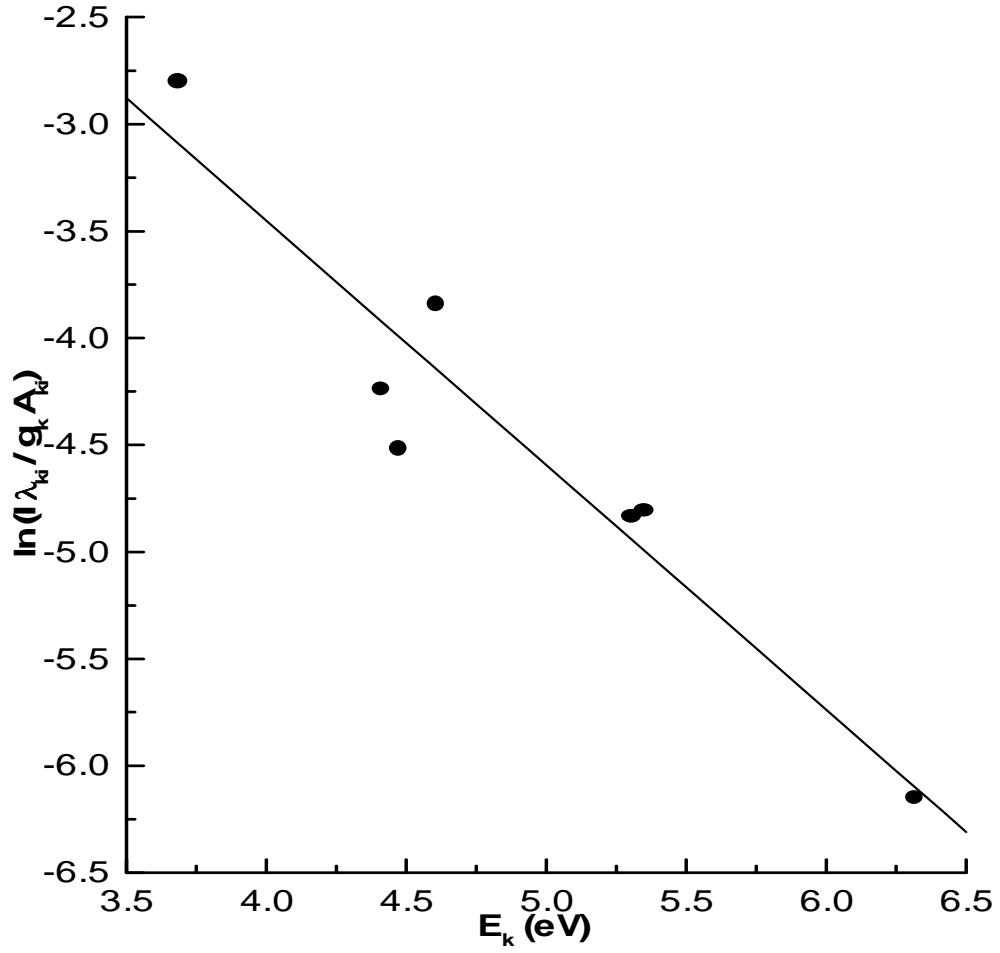


Fig. 5.6: Boltzmann plot made using seven Fe I transitions, considering the intensities at a delay time of 1000 ns. The continuous line represents the results of a linear best fit. The slope gives the temperature equal to 0.875 ± 0.044 eV

Table 5.1 Wavelength, lower and upper energy levels, upper level degeneracy, transition probability for the atomic and ionic emission lines used in the analysis.

Atom/ion	Wavelength (nm)	Upper level energy (eV)	Lower level energy (eV)	Upper level degeneracy	Transition probability (s ⁻¹)
Fe I	346.59	3.686	0.110	3	1.19×10 ⁷
Fe I	355.49	6.319	2.832	13	1.40×10 ⁸
Fe I	361.88	4.415	0.990	7	7.22×10 ⁷
Fe I	396.93	4.608	1.485	7	2.26×10 ⁷
Fe I	425.08	4.473	1.557	7	1.02×10 ⁷
Fe I	426.05	5.308	2.399	11	3.99×10 ⁷
Fe I	432.58	4.473	1.608	7	5.16×10 ⁷
Fe I	492.05	5.352	2.832	9	3.58×10 ⁷
Fe II	233.28	5.361	0.048	6	1.31×10 ⁸
Fe II	233.80	5.408	0.107	4	1.13×10 ⁸
Fe II	241.33	5.257	0.121	4	1.02x10 ⁸
Cr I	520.84	3.321	0.941	7	5.06 x10 ⁷
Ni I	352.45	3.542	0.025	5	1.0 x10 ⁸
Mn I	404.14	5.181	2.114	10	7.87 x10 ⁷
Si I	288.16	5.082	0.781	3	2.17 x10 ⁸

Table 5.2 Values of T, n_e , $n_{Cr\ I}/n_{Fe\ II}$, $n_{Ni\ I}/n_{Fe\ II}$, $n_{Si\ I}/n_{Fe\ II}$, $n_{Mn\ I}/n_{Fe\ II}$ and $n_{Fe\ II}/n_{Fe\ I}$ in the LIBS plasma determined from the LIBS spectral line intensities as experimental results at a delay time of 1000 ns.

T (eV)	n_e (cm ⁻³)	$n_{Cr\ I}/n_{Fe\ II}$	$n_{Ni\ I}/n_{Fe\ II}$	$n_{Si\ I}/n_{Fe\ II}$	$n_{Mn\ I}/n_{Fe\ II}$	$n_{Fe\ II}/n_{Fe\ I}$
0.875	9.8×10^{16}	3.24×10^{-2}	3.01×10^{-2}	4.67×10^{-3}	5.80×10^{-3}	6.7

Table 5.3 Comparison of the elemental contents of the steel sample obtained from the CF-LIBS analysis with their certified values and the corresponding relative uncertainty.

Element	Certified concentration (wt %)	LIBS determined concentration (wt %)	Relative uncertainty (%)
Fe	72.40	72.66	0.4
Cr	18.30	17.88	2.3
Ni	8.03	8.25	2.7
Mn	0.82	0.86	4.9
Si	0.33	0.34	

Summary and future scope of work

During the course of work on this thesis, various laser spectroscopic techniques including laser-induced fluorescence, laser-induced photoionization, laser optogalvanic and laser-induced breakdown spectroscopy, have been developed for the measurements of atomic parameters and quantitative elemental analysis. For the first time, laser-induced fluorescence and laser-induced photoionization techniques are used simultaneously to develop new methodologies. It is established that both techniques should be used in a complimentary way for identification of atomic energy levels. The results obtained using simultaneous laser-induced fluorescence and photoionization techniques have been analyzed using density matrix formalism. This has led us to develop new methodologies for the measurements of important atomic parameters. All these experiments have led to the identification of new energy/autoionization levels of uranium and samarium atoms and the assignment of total angular momentum values to these levels. The radiative lifetimes of high-lying energy levels, and excited-level-to-excited-level absolute transition probabilities, photoionization/ photoexcitation cross-sections are also determined for many atomic transitions of uranium and samarium. These experiments provided extensive atomic data on uranium and samarium.

A new calibration-free laser-induced breakdown spectroscopy approach has been developed for multi-elemental composition analysis. An algorithm relating the experimentally measured spectral intensity values with the basic physics of the plasma is developed. This technique has been used to analyze elemental concentrations of a steel sample.

The experiments have been carried out using uranium and samarium. But, the techniques developed here have universal applicability wherever complex spectra are involved. These techniques can be utilized to generate accurate atomic data in the unexplored regions for other materials of interest.

The simultaneous laser-induced fluorescence and photoionization experimental setup can be modified by introducing a time-of-flight-mass-spectrometer in the experimental setup for detecting the photoion signal instead of using parallel plate configuration. It will not only improve the sensitivity of the photoionization signals but also allow performing the isotope selective photoionization experiments. Effect of magnetic field and laser polarization on isotope selective excitation can also be studied using this type of experimental setup.

The accurate quantitative analysis is possible using the calibration free laser-induced breakdown spectroscopy technique. This technique can be very useful, where online elemental composition analysis is required. This type of technique is quite useful and explored for online monitoring of the materials of nuclear interest. Uranium vitrified glass materials in nuclear waste management and reprocessing plants can be analyzed using this technique.

To improve the signal-to-noise-ratios, laser-induced breakdown spectroscopy can be coupled with laser-induced fluorescence. Here the first laser pulse can be used to create a vapor plume and the second laser pulse can be tuned to a resonant absorption line of the species of interest re-excites the plume. It helps in improving the limit of detection.

References

Chapter 1

1. M. Dolg, “Lanthanides and Actinides”, Max-Planck Institut fur Physik, Komplexer Systems, Dresden, 2002, Encyclopedia of computational chemistry, Wiley online library, DOI: 10.1002/0470845015.cla001 (Published online: 15 April 2002).
2. A. K. Pulhani, “Laser Spectroscopic Investigations of Lanthanides and Actinides”, Ph. D. Dissertation, Mumbai University, India (2011).
3. W. F. Meggers, “Review of Reviews of Atomic Spectroscopy”, Appl. Opt., **2** 657-664 (1963).
4. F.S. Tomkins and M. Fred, “The Argonne thirty-foot spectrograph”, Spectrochim Acta **6**, 139-143 (1954).
5. F.S. Tomkins and M. Fred, “Wavelength measurements with a concave grating spectrograph”, Appl. Opt., **2** 715-724 (1963).
6. P. G. Wilkinson, “A high resolution spectrograph for the vacuum ultraviolet”, J. of Mol. Spectroscopy, **1** 288 –305 (1957).
7. W. F. Meggers, C. H. Corliss, B. F. Scribner, “Table of spectral line intensities- Part 1, Arranged by elements”, National Bureau of standards, Monograph **32** (1961).
8. C. H. Corliss, W.R. Bozman, “Experimental transition probabilities for spectral lines of seventy elements”, National Bureau of standards, Monograph **53**, (1962).
9. W. F. Meggers, C. H. Corliss, B. F. Scribner, “Table of spectral line intensities- Part 1, Arranged by wavelengths”, National Bureau of standards, Monograph **145**, (1975).
10. W. C. Martin, R. Zalubas, and L. Hagan, “Atomic energy levels – the rare earth elements”, National Bureau of Standards, Monograph **60**, (1978).

11. J. Connes, H. Delouis, P. Connes, G. Guelachvili, J. Maillard and G. Michel, "Spectroscopie De Fourier Avec Transformation U' Un Million De Points" *Nouv. Rev. Opt. Appl.*, **1** 3-22 (1970).
12. J. Blaise, Mark Fred, Ralph G. Gutmacher, "Term analysis of the spectrum of neutral plutonium, Pu I", *J. Opt. Soc. Am.*, **3** 403-418 (1986).
13. P. Luc and S. Gerstenkorn, "Fourier transform spectroscopy in visible and ultraviolet range", *Appl. Opt.*, **17** 1327-1331 (1978).
14. A. P. Thorne, C. J. Harris, I. Jones Wynne, R. C.M. Learner and G. Cox, "A Fourier transform spectrometer for the vacuum ultraviolet: Design and Performance", *J. Phys. E*, **20** 54- 60 (1987).
15. Anne Thorne, "High resolution Fourier transform spectrometry in the visible and ultraviolet regions" Invited Lecture, *J. of Analytical Atomic spectroscopy*, **13** 407-411 (1998).
16. Ulf Litzen, "How Fourier Transform Spectroscopy can be used for measurement of atomic parameters of astrophysical importance" *ASP Conference Series*, **81** 167-181 (1995).
17. C.V. Shank, "Physics of dye lasers" *Reviews of Modern Physics*, **47** 649-659 (1975).
18. *Laser Spectroscopy, Basic Concepts and Instrumentation*, Wolfgang Demtroder, Edition, Springer Verlag ISBN-13: 9788181282057 (2003) .
19. *Handbook of Laser-Induced Breakdown Spectroscopy*, D. A. Cremers, L. J. Radziemski, John Wiley & Sons Ltd., England (2006).
20. E. C. Jung, Do-Young Jeong, Kyuseok Song, Jongmin Lee, "High-resolution optogalvanic spectroscopy of Gd I", *Opt. Commun.*, **141** 83-90 (1997).

21. L. A. Hackel, C. F. Bender, M. A. Johnson and M.C. Rushford, "Hyperfine structure measurements of high-lying levels of uranium", J. Opt. Soc. Am., **69** 230-232 (1979).

Chapter2

1. G.S. Janes, I. Itzkan, C.T. Pike, R.H. Levy and L. Levin. Post deadline paper at CLEO, Washington, D.C., “Two-photon laser-isotope separation of atomic uranium-spectroscopic studies, excited state lifetimes, and photoionization cross-sections”, AVCO Everett. Rep. **408**, (1975).
2. L. R. Carlson, J. A. Paisner, E. F. Worden, S. A. Johnson, C. A. May, and R. A. Solarz. “Radiative lifetimes, absorption cross sections, and the observation of new high-lying odd levels of ^{238}U using multistep laser photoionization”, J. Opt. Soc. Am., **66** 846-853 (1976).
3. G. S. Hurst, M. G. Payne, S. D. Kramer, J. P. Young, “Resonance ionization spectroscopy and one atom detection”, Reviews of Modern Physics, **51** 767-819 (1979).
4. V. S. Letokhov, “Laser photoionization spectroscopy of single atoms and molecules”, Optica Acta, **32** 1191-1210 (1985).
5. G. I. Bekov, “Resonance ionization spectroscopy”, American Institute of Physics Proceedings, **329** 9-14 (1995).
6. W. Ruster, F. Ames, H. J. Kluge, E. W. Otten, D. Rehlau, F. Scheerer, G. Herrmann, C. Muhleck, J. Riegel, H. Rimke, P. Sattelberger and N. Trautmann, “A resonance ionization mass spectrometer as an analytical instrument for trace analysis”, Nuclear Instruments and methods in Physics Research A, **281** 547-558 (1989).
7. H. Rimke, G. Herrmann, M. Mang, C. Muhleck, J. Riegel, P. Sattelberger, N. Trautmann, F. Ames, H. J. Kluge, E. W. Otten, D. Rehlau, W. Ruster and F. Scheere, “Principle and Analytical Applications of Resonance Ionization Mass Spectrometry”, Mikrochim Acta, **111** 223-230 (1989).

8. K. Wendt, K. Blaum, B. A. Bushaw, C. Gruning, R. Horn, G. Huber, J. V. Kratz, P. Kunz, P. Muller, W. Nortershauser, M. Nunnemann, G. Passler, A. Schmitt, N. Trautmann, A. Waldek, "Recent developments in and applications of resonance ionization mass spectrometry", *Fresenius J Anal. Chem.*, **364** 471-477 (1999).
9. K. Wendt, K. Blaum, Ch. Geppert, R. Horn, G. Passler, N. Trautmann, B. A. Bushaw, " Laser resonance ionization for efficient and selective ionization of rare species", *Nuclear Instrument and Methods in physics research B*, **204** 325-330 (2003).
10. V. S. Letokhov, *Laser photoionization spectroscopy*, Academic Press, Orlando, ISBN-13: 9780124443204 (1987).
11. G.S. Hurst, M.G. Payne, *Principles and applications of resonance ionization spectroscopy*, Adam Hilger, Bristol, ISBN-13: 9780852744604 (1988).
12. K. Wendt, "Trace isotopic determination by laser spectroscopic techniques", *Journal of Nuclear Science and Technology*, **6** 30-36 (2008).
13. V. K. Mago, B. Lal, A. K. Ray, R. Kapoor, S. D. Sharma, P. R. K. Rao "Two-colour three-step photoionisation of uranium," *J. Phys, B* **20** 6021 (1987).
14. M. Miyabe, I.Wakaida, "Identification of single-colour multiphoton ionization transitions of atomic gadolinium," *J. Phys. B* **30** 4193 (1997).
15. B. A. Bushaw, W. Nortershauser, K. Blaum, K. Wendt, " Studies of narrow autoionizing resonances in gadolinium," *Spectrochim. Acta. B* **58** 1083 (2003).
16. H. J. Kluge, B. A. Bushaw, G. Passler, G. Wendt, N. Trautmann, J.Fresenius, "Resonance ionization spectroscopy for trace analysis and fundamental research" *Anal. Chem.* **350**, 323 (1994).

17. L. Pibida, W. Nortershauser, J. M. R. Hutchinson, B. A. Bushaw, "Evaluation of resonance ionization mass spectrometry for the determination of ^{135}Cs / ^{137}Cs isotope ratios in low-level samples," *Radiochim. Acta* ; **89**, 161 (2001).
18. G. Ewald, W. Nortershauser, A. Dax, S. Gotte, R. Kirchner, H. J. Kluge, T. H. Kuhl, R. J. Sanchez, A. S. Wojtasek, B. A. Bushaw, G. W. F. Drake, Z. C. Yan, C. H. Zimmerman, "Nuclear charge radii of Li-8, Li-9 determined by laser spectroscopy," *Phys. Rev. Lett.* **93**, 113002 (2004).
19. W. Nortershauser, A. Dax, G. Ewald, S. Gotte, R. Kirchner, H. J. Kluge, T. H. Kuhl, R. Sanchez, A. Wojtaszek, B. A. Bushaw, G. W. F. Drake, Z. C. Yan, C. Zimmerman, "First measurement of the nuclear charge Radii of short-lived lithium isotopes," *Hyperfine Interactions* **162**, 93 (2006).
20. H-J Kluge, "Resonance ionization mass spectroscopy for nuclear research and trace analysis," *Hyperfine Interaction* **37**, 347 (1987).
21. L. Pibidaa, C. A. McMahon, B. A. Bushaw, "Laser resonance ionization mass spectrometry measurements of cesium in nuclear burn-up and sediment samples," *Appl. Radiat. Isotopes* **60** 567 (2004).
22. K. Wendt, K. Blaum, C. Geppert, P. Muller, W. Nortershauser, A. Schmitt, P. Schumann, N. Trautmann, B. A. Bushaw, "Laser based techniques for ultra trace isotope production, spectroscopy and detection," *Hyperfine Interactions* **162**, 147 (2006).
23. M. G. Payne, Lu. Deng, "Applications of resonance ionization mass spectrometry," *Rev. Sci. Instrum.* **65**, 2433 (1994).
24. K. Wendt, K. Blaum, B. A. Bushaw, C. Grüning, R. Horn, G. Huber, J. V. Kratz, P. Kunz, P. Müller, W. Nörtershäuser, M. Nunnemann, G. Passler, A. Schmitt, N.

Trautmann, A. Waldek, Recent developments in and applications of resonance ionization mass spectrometry,” *Fresenius J. Anal Chem* **364**, 471 (1999).

25. B. M. Suri, K. Dasgupta, P. N. Bajaj, K. G. Manohar, R. Talukdar, P. K. Chakraborti, and P. R. K. Rao, “Observation of new high-lying odd levels of U I in a two-color multiphoton ionization spectrum,” *J. Opt. Soc. Am B* **4**, 1835-1836 (1987).

26. K. Dasgupta, K. G. Manohar, P. N. Bajaj, B. M. Suri, R. K. Talukdar, P. K. Chakraborti, and P.R.K. Rao "Understanding single-color multiphoton ionization spectra by pump probe technique," *J. Opt. Soc. Am. B* **5** 1257-1260 (1988).

27. K.G. Manohar, P.N. Bajaj, B.M. Suri, R. Talukdar, K. Dasgupta, P.K.Charaborti, and P. R. K. Rao, “Observation of autoionization resonances in uranium by step-wise laser photoionization,” *Appl. Phys. B* **48**, 525-530 (1989).

28. M. Miyabe, M. Oba, and I. Wakaida, “Highly excited odd-parity levels of atomic uranium,” *J. Phys. B* **33**, 4957-4972 (2000).

29. E. Miron, R. David, G. Erez, S. Lavi, and L. A. Levin, “ Laser spectroscopy of U I using stepwise excitation and fluorescence detection, *J. Opt. Soc. Am.* **69**, 256-264 (1979).

30. M. L. Shah, R. C. Das, P. K. Mandal, D.R. Rathod, Vas Dev, K. G. Manohar. B. M. Suri, “Measurement of photoexcitation cross-sections of uranium by saturation method,” *Pramana-J Phy.* **75**, 1141-44 (2010).

31. R.C. Das, P.K. Mandal, M.L. Shah, A.U. Seema, D.R. Rathod, Vas Dev, K.G. Manohar, B.M. Suri, “Measurements of radiative lifetime of high-lying odd parity energy levels of U I,” *J. Quant. Spec. & Radiative Transfer* **113**, 382–386 (2012).

32. A. Petit, R. Avril, D. L'Hermite and A. Pailloux, "Measurement of oscillator strengths in uranium using laser techniques," *Physica Scripta*. **T 100**, 114-119 (2002).
33. R. W. Solarz, J. A. Paisner, L. R Carlson, C. A. May and S. A. Johnson, UCRL-50021-74 (1975).
34. L. A. Hackel, M. C. Rushford, " Lifetime, branching ratio, and absolute transition probability of the 6395.42 °A transition of ²³⁸U I," *J. Opt. Soc. Am.***68**,1084–1087 (1978).
35. R. Avril, A. Petit, J. Radwan, E. Vors, " The spectroscopy of uranium within the "SILVA" program,". *Proc.SPIE*, **1859**, 38–48 (1993).
36. Iain R McNab and Ralph C Shiell, "Laser spectroscopy" *Phys. Educ.*, **29** 164 -169 (1994).
37. N. Omenetto, "Laser-induced atomic fluorescence spectroscopy: a personal viewpoint on its status,needs and perspectives", *Spectrochimica Acta B*, **44** 131-146 (1989).
38. Peter Stchur, Karl X. Yang, Xiandeng Hou, Tao Sun, Robert G. Michel, "Laser excited atomic fluorescence spectrometry – a Review" *Spectrochimica Acta Part B*, **56** 1565-1592 (2001).
39. Jonghoon Yi, Jin- Tac Kim, Hyunmin Park, Sipyo Rho, Yongjoo Rhee, Jongmin Lee and Moon-Gu Baik "Monitoring of Gadolinium Photoionization process by using Fluorescence measurements" *Journal of Korean Physical Society*, **37** 707-712 (2000).
40. F. Orsitto, M. Borra, F. Coppotelli, G. Gatti, and E. Neri, "Molecular Density measurements by laser-induced fluorescence spectroscopy", *Review of Scientific Instruments*, **70** 921-924 (1999).

41. R. McWilliams, H. Boehmer, D. Edrich, L. Zhao, D. Zimmerman, “Laser-induced fluorescence measurements for plasma processing”, *Thin Solid films*, **506-507** 665-668 (2006).
42. M. Oba, K. Akaoka, M. Miyabe, and I. Wakaida, “Zeeman effect of atomic uranium in the high lying odd levels measured by laser induced fluorescence spectroscopy” *Eur. Phys. J. D*, **10** 349-352 (2000).
43. M. Oba, K. Akaoka, M. Miyabe, and I. Wakaida, “Isotope shift and hyperfine structure of the highly excited atomic uranium” *Eur. Phys. J. D*, **21** 255-260 (2002).
44. S. Rochester, C. J. Bowers, D. Budker, D. DeMille, and M. Zolotarev, “Measurement of lifetimes and tensor polarizabilities of odd-parity states of atomic samarium”, *Phys. Rev. A*, **59** 3480-3494 (1999).
45. N. N. Kolachevskii, A. V. Akimov, N. A. Kiselev, A. A. Papchenko, V. N. Sorokin, S. I. Kanorskii, “ Resonances of coherent population trapping in samarium vapours” *Quantum Electronics*, **31** 61-66 (2001).
46. Myoung-Kyu Oh, Wonshik Choi, Jin-Ho Jeon, Moonjoo Lee, Youngwoon Choi, Sangbum Park, Jai-Hyung Lee, Kyungwon An, “ Measurement of hyperfine structures and isotope shifts in the $4f^5 5d 6s^2$ and $4f^6 6s 6p$ of Sm I”, *Spectrochimica Acta B*, **59** 1919 - 1926 (2004).
47. T. Kondo, D. Angom, I. Endo, A. Fukumi, T. Horiguchi, M. Iinuma, and T. Takahashi, “ Stark spectroscopy of high-lying odd parity levels in atomic samarium” *Eur. Phys. J. D*, **25** 103-111 (2003).
48. T. D. Wolfenden and P. E .G. Baird, “An experimental search for enhanced parity non-conserving optical rotation in samarium”, *J. Phys B*, **26** 1379 – 1387 (1993).

49. Kyuseok Song, Hyunki Cha and Jongmin Lee, “Determination of samarium by the two-colour three-photon resonance ionization mass spectrometry” *J. Anal. At. Spectrometry*, **13** 1207-1210 (1998).
50. M. L. Grossbeck, “Development of Improved burnable poisons for commercial nuclear power reactors”, Oak Ridge National laboratory, Available at <http://neri.ne.doe.gov/docs/01annualreport/ANFProgressRpts.pdf>
51. B. Blagoev, V. A. Komarovskii and N.P. Penkin, “Lifetimes of excited states of samarium atom,” *Opt. Spectrosk.* **42**, 424-426 (1977).
52. P. Hannaford and R. M. Lowe, “Radiative lifetimes of low-lying levels in Sm I,” *J. Phys. B*, **18**, 2365-2370 (1985).
53. C. J. Bowers, D. Budker, E. D. Commins, D. Demille, S. J. Freedman, A.-T. Nguyen, S.-Q. Shang and M. Zolotarev, “Experimental investigation of excited-state lifetimes in atomic ytterbium,” *Phys. Rev. A* **53**, 3103-3109 (1996).
54. M. Song, Y. P. Li, W. X. Peng, Z. K. Jiang, C. Guo and Y. N. Yu, “Radiative lifetime measurements on Pr atoms by observing time-resolved laser-induced fluorescence,” *Eur. Phys. J. D* **2**, 115-116 (1998).
55. S. Rochester, C. J. Bowers, D. Budker, D. DeMille, and M. Zolotarev, “Measurement of lifetimes and tensor polarizabilities of odd parity states of atomic samarium,” *Phys. Rev. A*, **59**, 3480-3494 (1999).
56. H. Xu, Z. Jiang and H. Lundberg, “Lifetime measurements in neutral and singly ionized vanadium,” *J. Opt. Soc. Am. B* **23**, 2597-2600 (2006).
57. V. Fivet, P. Palmeri, P. Quinet, E. Biemont, H. L. Xu and S. Svanberg, “Radiative lifetimes and transition probabilities in Ta I,” *Eur. Phys. J. D* **37**, 29-35 (2006).

58. S. E. Bisson, B. Comaskey and E. F. Worden, "Method to measure excited-level-to-excited-level branching ratios and atomic transition probabilities by time-resolved laser photoionization spectroscopy," *J. Opt. Soc. Am. B*, **12**, 193-202 (1995).
59. E. Langlois and J. M. Gagne, "Optogalvanic Detection of the Zeeman Effect in a Hollow Cathode Discharge," *J. Opt. Soc. Am. B* **4**, 1222 (1987).
60. A. K. Pulhani, M. L. Shah, Vas Dev and B. M. Suri, "High-lying even-parity excited levels of atomic samarium," *J. Opt. Soc. Am. B* **22**, 1117-1122 (2005).
61. T. Jayasekharan, M. A. N. Rizvi and G. L. Bhale, "Observation of new even-parity states of Sm I by resonance ionization mass spectrometry," *J. Opt. Soc. Am. B* **13**, 641-648 (1996).
62. J. Liejuan, J. Chunyang, Z. Zhiyao and L. Fucheng, "Studies of high-lying even-parity levels of Sm I: energies and isotope shifts," *J. Opt. Soc. Am. B* **10**, 1317 (1993).
63. P. T. Greenland, D. N. Travis and D. J. H. Wort, "Studies of high-lying even-parity levels of Sm I: energies and isotope shifts," *J. Phys. B* **23**, 2945 (1990).
64. V. A. Komarovskii and Yu. M. Smirnov, "Experimental study of the absolute values of electronic transition probabilities in a samarium atom," *Opt. Spectrosc.* **80**, 357-361 (1996).
65. M. L. Shah, A. K. Pulhani, G. P. Gupta, and B. M. Suri, "Measurements of radiative lifetimes, branching fractions, and absolute transition probabilities in atomic samarium using laser-induced fluorescence," *J. Opt. Soc. Am. B* **27**, 423 (2010).
66. A. K. Pulhani, M. L. Shah, G. P. Gupta, and B. M. Suri, "Measurement of total angular momentum values of high-lying even-parity atomic states of samarium by

spectrally resolved laser-induced fluorescence technique,” *Pramana J-Phys.* **75**, 1135-39 (2010).

67. W.C. Martin, R. Zalubas, and L. Hagan, “Atomic Energy Levels – The rare earth elements” *Natl. Bur. Stand. (U.S. Rep. NSRDS-NBS 60* (1978).

68. E. Biemont, H. P. Garnir, U. Litzen, K. Nielsen, P. Quinet, S. Svanberg, G. M. Wahlgren and Z. G. Zhang, “Radiative lifetime and oscillator strength determinations in Sm III,” *Astronomy and Astrophysics* **399**, 343-349 (2003).

69. M. E. Wickliffe, J. E. Lawler and G. Nave, “Atomic transition probabilities for Dy I and Dy II,” *J. Quant. Spectos. Radiat. Transfer* **66**, 363-404 (2000).

70. 26. T. Jayashekharan, M. A. N. Razvi, G. L. Bhale, “Investigations of new high-lying even-parity energy levels of the samarium atom below its first ionization limit,” *J. Opt. Soc. Am. B* **17**, 1607-1615 (2000).

71. H. Sufen, Z. Sen, M. Shimin, Q. Jizhen, C. Xing, “Investigation of highly excited states of Sm,” *J. Quant. Spectrosc. Radiat. Transfer* **43**, 75-79 (1990).

72. L. Jia, C. Jing, Z. Zhou, F. Lin, “Studies of high-lying even-parity levels of Sm i: energies and isotope shifts,” *J. Opt. Soc. Am. B* **10**, 1317-1320 (1993).

73. A. I. Gomonai, O. I. Plekan, “Single-colour resonance three-photon ionization of samarium Atoms,” *J. Phys. B: At. Mol. Opt. Phys.* **36**, 4155-74 (2003).

74. J. W. Qin, C. J. Dai, Y. Xiao, Y. H. Zhao, “Experimental study of highly excited even-parity bound states of the Sm atom,” *Chin. Phys B* **18**, 3384-3394 (2009).

75. Y. H. Zhao, C. J. Dai, S. W. Yi, “Study on even-parity highly excited states of the Sm atom,” *J. Phy B: At. Mol. Opt. Phys.*, **44**, 195001(7pp) (2011).

76. M. Li., C. J. Dai, J. Xie, J. “Photoionization spectra of even-parity states of Sm atom with multistep excitation,” *Quant. Spectrosc. Radiat. Transfer* **112**, 793-799 (2011).
77. M. Li., C. J. Dai, J. Xie, “Even-parity states of the Sm atom with stepwise excitation,” *Chin. Phys. B* **20**, 0632049 (2011).
78. A. C. Sahoo, M. L. Shah, P. K. Mandal, A. K. Pulhani, G. P. Gupta, Vas Dev and B. M. Suri, “Measurement of radiative lifetime in atomic samarium using simultaneous detection of laser-induced fluorescence and photoionization signals,” *Pramana – J. Phys.*, **82**, 403-408 (2014).

Chapter 3

1. A. K. Pulhani, "Laser Spectroscopic Investigations of Lanthanides and Actinides", Ph. D. Dissertation, Mumbai University, India (2011).
2. P. W. Milonni and J. H. Eberly, "Lasers," John Wiley and Sons, New York, ISBN-13: 9780471627319V (1988).
3. B. W. Shore, The Theory of Coherent Atomic Excitations, John Wiley and Sons, New York, Vol. 1, ISBN-13: 9780471613985, Vol. 2, ISBN-13: 9780471524168 (1990).
4. B. A. Bushaw, W. Nortershauser, K. Wendt, "Lineshapes and optical selectivity in high-resolution double-resonance ionization mass spectrometry, Spectrochim. Acta B **54** 321 (1999).
5. G. P. Gupta, A. K. Pulhani, and B. M. Suri, "Comparison of ^{138}La : ^{139}La -isotope-ratio-enhancement calculations by use of spectral-simulation and density-matrix methods, " J. Opt. Soc. Am. B **21**, 436-441 (2004).
6. P. Zoller and P. Lambropoulos, "Laser temporal coherence effects in two-photon resonant three-photon ionization," J. Phys. B, 13, 69 (1980).
7. Bo-nian Dai and P. Lambropoulos, "Selective ionization: Effects of power broadening, laser bandwidth, and interaction time on selectivity," Phys. Rev. A 34, 3954 (1986).
8. S. N. Dixit, P. Zoller and P. Lambropoulos, "Non-Lorentzian laser line shapes and the reversed peak asymmetry in double optical resonance," Phys. Rev. A 21, 1289 (1980).
9. S. N. Dixit, P. Lambropoulos and P. Zoller, "Spin polarization of electrons in two-Photon resonant three-photon ionization," Phys. Rev. A 24, 318 (1981).

10. S. N. Dixit and P. Lambropoulos, "Theory of photoelectron angular distributions in resonant multiphoton ionization," *Phys. Rev. A* **27**, 861 (1983).
11. A. K. Pulhani, M. L. Shah, V. Dev, and B. M. Suri, "High lying even-parity excited levels of atomic samarium," *J. Opt. Soc. Am. B* **22**, 1117-1122 (2005).
12. Y. Jonghoon, J. T. Kim, P. Hyuamin, R. Sipyo, R. Yongjoo, and L. Jongmin, "Monitoring of the gadolinium photoionization process by using fluorescence detection," *J Korean Phys. Soc.* **37**, 707-712 (2000).
13. M. Broglia, F. Catoni, and P Zampetti, "Simultaneous detection of optogalvanic and fluorescence signals in a uranium hollow-cathode lamp," *J. Opt. Soc. Am. B* **2**, 570-573 (2010).
14. M.L. Shah, A.C. Sahoo, A.K. Pulhani, G.P. Gupta, B.M. Suri, and Vas Dev, "Investigations of high-lying even-parity energy levels of atomic samarium using simultaneous observation of two-color laser-induced fluorescence and photoionization signals," *68*, 235 (1-8) (2014).
15. C. E. Burkhardt, J. L. Libbert, J. Xu, and J. J. Leventhal, "Absolute measurement of photoionization cross sections of excited atoms: Application to determination of atomic beam densities," *Phys Rev A* **38**, 5949-5952 (1988).
16. K. W. McLaughlin and D. M. Duqutte, "Absolute photoionization cross section of excited titanium" *J. Opt. Soc. Am B* **9**, 1953-1958 (1992).
17. M. L. Shah, G. P. Gupta, V. Dev, B. Dikshit, M. S. Bhatia, B. M. Suri, "Measurement of photoionization cross-section in atomic uranium using simultaneous observation of laser-induced photoionization and fluorescence signals," *J. Opt. Soc. Am B* **29**, 600 (2012).

18. K.G. Manohar, P.N. Bajaj, B.M. Suri, R. Talukdar, K. Dasgupta, P.K. Charaborti, and P. R. K. Rao, “Observation of autoionization resonances in uranium by step-wise laser photoionization,” *Appl. Phys. B* **48**, 525-530 (1989).
19. 20. G. P. Gupta and B. M. Suri, “Effects of laser linewidth on an effective method for excitation in three-level atomic systems by two optimally detuned counter propagating pulsed lasers,” *Phys. Rev. A* **77**, 023419-1-5 (2008).
20. L. Radziemski, R. Solarz, and J. A. Paisner, *Laser Spectroscopy and Its Applications*, (Dekker, New York, 1987).
21. T. Asano, N. Uetake, and K. Suzuki, “Mean atomic velocities of uranium, titanium and copper during electron beam evaporation,” *J. Nucl. Sci. Technol.* **29**, 1194-2000 (1992).
22. L. R. Carlson, J. A. Paisner, E. F. Worden, S. A. Johnson, C. A. May, and R. W. Solarz, “Radiative lifetimes, absorption cross sections, and the observation of new high-lying odd levels of ^{238}U using multistep laser photoionization,” *J. Opt. Soc. Am.* **66**, 846-853 (1976).
23. E. Miron, R. David, G. Erez, S. Lavi, and L. A. Levin, “Laser spectroscopy of U I using stepwise excitation and fluorescence detection,” *J. Opt. Soc. Am.* **69**, 256-264 (1979).
24. V. Dev, M. L. Shah, A. K. Pulhani, and B. M. Suri, “Two-color photoionization spectroscopy of uranium in a U Ne hollow cathode discharge tube,” *Appl. Phys. B* **80**, 587-594 (2005).

25. S. Lévesque, J.-M. Gagné, and F. Babin, “Single-color photoionization optogalvanic spectroscopy in U-Xe and U-Ne hollow-cathode discharges,” *Canadian J. Phys.* **76**, 207- 244 (1998).
26. M.L. Shah, A .C. Sahoo, A .K. Pulhani, G.P. Gupta, B. Dikshit, M.S. Bhatia, B.M. Suri, “Measurements of excited-state-to-excited-state transition probabilities and photoionization cross- sections using laser-induced fluorescence and photoionization signals,” **142**, 9-16 (2014).
27. M. L. Shah, A. K. Pulhani, G. P. Gupta, B. M. Suri, “Measurements of radiative lifetimes, branching fractions, and absolute transition probabilities in atomic samarium using laser-induced fluorescence,” *J. Opt. Soc. Am. B* **27**, 423-431 (2010).
28. A.I. Gomonai, E. Yu Remeta, “ Investigation of highly excited states of samarium,” *Opt.and Spectros.***112**,15-23 (2012).
29. W. J. Qin, C. J. Die, Y. J.Xiao,“Multistep excitation of autoionizing states of samarium atoms” *Quant. Spec. Radiant Trans.*;**111**, 63-70 (2010).
30. H. Sufen, M. Shimin, Z. Sen, C. Zing, X. Yunfei, “Observation and measurement of autoionization spectra of atomic samarium” *Chinese Phys. Lett.*;**2**, 64-67 (1989).
31. H. Park, H. Kim, J. Yi, J. Han, Y. Rhee, J. Lee, “The odd parity autoionization states of samarium atoms determined by three-step excitation” *J. Korean Phys. Soc.*,**33**, 288-291 (1998).

Chapter 4

1. B. Barbieri and N. Beverini, “Optogalvanic spectroscopy,” *Reviews of Modern Phys.*, **62**, 603-644 (1990).
2. M.L. Shah, B.M. Suri, and G.P. Gupta, “Spectroscopic measurements of plasma temperatures and electron number density in a uranium hollow cathode discharge lamp,” *Eur. Phys. J. D* **69**: 16. DOI: 10.1140/epjd/e2014-50704-3 (2015).
3. M. L. Shah, P. K. Mandal, Vas Dev, and B. M. Suri, “Study of even-parity autoionization resonances of atomic uranium by three-color optogalvanic spectroscopy,” *J. Opt. Soc. Am. B* **29**, 1625-1630 (2012).
4. N.E. Annemie, G. Renaat, M. Joost, “Gas discharge plasmas and their applications,” *Spectrochim. Acta B* **57**, 609 -658 (2002).
5. J.P. Young, R.W. Shaw, C.M. Barshick, J.M. Ramsey, “Determination of actinide isotope ratio using glow discharge optogalvanic spectroscopy,” *J. Alloys and Compounds* **62**, 271-273, (1998).
6. D. Zhechev, N. Parvanova, “Anomalous optogalvanic signal spectroscopic applications,” *Opto-Electronics Review* **11**, 31 (2003).
7. B. Smeets, “Laser Frequency Stabilization using an Fe-Ar Hollow Cathode Discharge Cell” (The Netherlands Reports, 2003).
8. S. Caroli, “The hollow cathode emission source, “A survey of the past and a look into the future ,” *Prog. Analyt. Atom. Spectrosc.* **6**, 253 (1983)
9. Vas Dev, M.L. Shah, A.K. Pulhani, B.M. Suri, “Two-color photoionization spectroscopy of uranium in a U-Ne hollow cathode discharge tube,” *Appl. Phys. B* **80**, 587-594 (2005).

10. P.K. Mandal, A.U. Seema, R. C. Das, M.L. Shah, Vas Dev, B. M. Suri, "Observation of even-parity autoionization states of uranium by three-colour photoionization optogalvanic spectroscopy in U-Ne hollow cathode discharges ," J. Quan. Spectrosc. Radiat. Transfer **124**, 79-85 (2013)
11. A.K. Pulhani, M.L. Shah, Vas Dev, B. M. Suri, "High-lying even-parity excited levels of atomic samarium," J. Opt. Soc. Am. B **22**, 1117-1122 (2005).
12. M.L. Shah, A. K. Pulhani, G.P. Gupta, B.M. Suri, "Measurements of radiative lifetimes, branching fractions, and absolute transition probabilities in atomic samarium using laser-induced fluorescence ," J. Opt. Soc. Am B **27**, 423-431 (2010).
13. R.C. Das, P.K. Mandal, M.L. Shah, A.U. Seema, D.R. Rathod, Vas Dev, K.G. Manohar, B.M. Suri, "Measurements of radiative lifetime of high-lying odd parity energy levels of U I ," J. Quant. Spectrosc. Radiat. Transfer **113**, 382-386 (2012).
14. M.L. Shah, G.P. Gupta, Vas Dev, B. Dikshit, M.S. Bhatia, B. M. Suri, "Measurement of photoionization cross-section in atomic uranium using simultaneous observation of laser-induced photoionization and fluorescence signals ," J. Opt. Soc. Am B **29**, 600-606 (2012).
15. J.V.D. Jonkers, J.A.M. Mullen, "The excitation temperature in (helium) plasmas ," J. Quant. Spectrosc. Radiat. Transfer **61**, 703-709 (1999).
16. H.R. Griem, Principles of Plasma Spectroscopy (Cambridge University Press, 1997).
17. W. Zyrnicki, J. Mierzwa, "Spectroscopic study of of a hollow cathode discharge operating at direct and high frequency currents – temperature measurements ," Spectrosc. Lett. **19**, 1079-1089 (1986).

18. G. Henrion, M. Fabry, M. Remy, "Determination of oscillator strengths for U_I and U_{II} Lines," J. Quant. Spectrosc. Radiat. Transfer **37**, 477-499 (1987).
19. S. Mahmood, N.M. Shaikh, M.A. Kalyar, M. Rafiq, N.K. Piracha, M.A. Baig, "Measurements of electron density, temperature and photoionization cross sections of the excited states of neon in a discharge plasma," J. Quant. Spectrosc. Radiat. Transfer **110**, 1840-1850 (2009).
20. B.N. Sismanoglu, K.G. Grigorov, R. Caetano, M.V.O. Rezende, Y.D. Hoyer, "Spectroscopic measurements and electrical diagnostics of microhollow cathode discharges in argon flow at atmospheric pressure ," Eur. Phys. J. D **60**, 505-516 (2010).
21. S.H. Nabavi, A.J. Koohian, "Spectral method for excitation temperature measurement in hollow cathode lamp plasma" Mod. Phys. **2**, 40-43 (2011).
22. J.M. Gomba, C.D. Angelo, D. Bertuccelli, G. Bertuccelli, "Spectroscopic characterization of laser induced breakdown in aluminium-lithium alloy samples for quantitative determination of traces ," Spectrochim. Acta B **56**, 695-705 (2001).
23. M.L. Shah, A.K. Pulhani, G.P. Gupta, B.M. Suri, "Quantitative elemental analysis of steel using calibration-free laser-induced breakdown spectroscopy," Appl. Opt. **51**, 4612-4621 (2012).
24. NIST Atomic Spectra Database, <http://physics.nist.gov>
25. G.W.F. Drake, Atomic, Molecular and Optical Physics Handbook (Academic Press, New York, 1996) .
26. R. W. Solarz, C. A. May, C. R. Carlson, E. F. Worden, S. A. Johnson, J. A. Paisner, "Detection of Rydberg states in atomic uranium using time-resolved stepwise laser photoionization," Phys. Rev. A **14**, 1129-1136 (1976).

27. A. Coste, R. Avril, P. Blancard, J. Chatelet, D. Lambert, J. Legre, "New Spectroscopic Data on High-Lying Excited Levels of Atomic Uranium," *J. Opt. Soc. Am* **72**, 103-109 (1982).
28. K. G. Manohar, P. N. Bajaj, B. M. Suri, R. Talukdar, K. Dasgupta, P. K. Chakraborti, P. R. K. Rao, "Observation of autoionization resonances in uranium by step-wise laser photoionization," *Appl. Phys. B* **48**, 525-530 (1989).
29. V. K. Mago, B. Lal, A. K. Ray, S. D. Sharma, P. R. K. Rao, "Single-Colour Photoionisation Studies in Uranium I," *J. Phys. B: At. Mol. Phys.* **20**, 6021-6030 (1987).
30. M. Miyabe, M. Oba, I. Wakaida, "Highly excited odd-parity levels of atomic uranium," *J. Phys. B : At. Mol. Opt. Phys.* **33**, 4957-4972 (2000).
31. B. A. Bushaw, W. Nortershauser, K. Blaum, K. Wendt, "Studies of narrow autoionizing resonances in gadolinium," *Spectrochimica Acta Part B* **58**, 1083-1095 (2003).
32. B. A. Bushaw, Raeder, S. L. Ziegler, K. Wendt, "Triple-resonance autoionization of uranium 33. P. G. Schumann, K. D. A. Wendt, B. A. Bushaw, "High-resolution triple-resonance autoionization of uranium isotopes," *Spectrochimica Acta B* **60** 1402-1411 (2005).
34. M. Broglia, F. Catoni and P. Zampetti, "Optogalvanic Detection of uranium high-lying levels," *Journal de physique, Colloque* **C7** 251-259 (1983).
35. M. Broglia, F. Catoni, A. Montone and P. Zampetti, "Galvanic detection of laser photoionization in hollow-cathode discharges: Experimental and theoretical study," *Phys. Rev. A* **36**, 705-14 (1987).

36. O. Kujirai , Y. Ogawa, “Observation of even-parity autoionization states of lutetium atom by optogalvanic spectroscopy, Journal of physical society of Japan, **67**, 1056-1057 (1998).
37. O..Kujirai , Y. Ogawa, “Study of Odd-Parity Autoionization States of Praseodymium Atom by Optogalvanic Spectroscopy,” Journal of physical society of Japan, **69**, 2845-2849 (2000).
38. O. Kujirai, Y. Ogawa, “Study of Even-Parity Autoionization States of Samarium Atom by Laser Optogalvanic Spectroscopy,” Journal of physical society of Japan, **72**, 1057-1068 (2003).
39. A. P. Marathe, K. G. Manohar, B. N. Jagatap, “New even parity autoionisation levels of UI,” J. Phys.: Conf. Ser. **80**, 012032 (2007).

Chapter 5

1. D. A. Cremers, L. J. Radziemski, Handbook of Laser-Induced Breakdown Spectroscopy (John Wiley & Sons Ltd., England, 2006).
2. M. L. Shah, A. K. Pulhani, G. P. Gupta, B. M. Suri, "Quantitative elemental analysis of steel using calibration-free laser-induced breakdown spectroscopy", *Applied Optics*, **51**, 612-4621(2012).
3. Y. N. Ledney, A. V. Yakovlev, T. A. Labutin, A. M. Povov, N. B. Zorov, "Selection of an analytical line for determining lithium in aluminum alloys by laser induced breakdown spectrometry," *J. Anal. Chem.* **62**, 1151-1155 (2007).
4. V. Burakov, V. Kiris, A. Klyachkovskaya, N. Kozhukh, S. Rainkov, "Application of emission spectrometer with laser sampler with micro analysis of pigments from Hubert Robert's canvas painting," *Microchim. Acta* **156**, 337-342 (2007).
5. A. Giakoumaki, K. Melessanaki, D. Anglos, "Laer-induced breakdown spectroscopy in archaeological-science applications and prospects," *Anal. Bioanal. Chem.* **387**, 749-760 (2007).
6. F. Capitelli, F. Colao, M. R. Provenzano, R. Fantoni, G. Brunetti, N. Senesi, "Determination of heavy metals in soils by laser induced breakdown spectroscopy," *Geoderma* **106**, 45-62 (2002).
7. B. Salle, D. A. Cremers, S. Maurice, R. C. Wiens, " Laser-induced breakdown spectroscopy for space exploration applications: Influence of ambient pressure on the calibration curves prepared from soil and clay samples," *Spectrochim. Acta B* **60**, 479-490 (2005).
8. O. Samek, D. C. S. Beddows, H. H. Telle, G. W. Morris, M. Liska, J. Kaiser,

“Quantitative analysis of trace metal accumulation in teeth using laser-induced breakdown spectroscopy,” *Appl. Phys. A* **69**, S179-S182 (1999).

9. J. P. Singh, F. Y. Yueh, H. Zhang, K. P. Karney, “A preliminary study of the determination of uranium, plutonium and neptunium by laser-induced breakdown spectroscopy,” *Rec. Res. Dev. Appl. Spectrosc.* **2**, 59-67 (1999).

10. R. Sattmann, V. Sturm, R. Noll, “Laser-induced breakdown spectroscopy of steel samples using multiple Q-switch Nd:YAG laser pulses,” *J. Phys. D: Appl. Phys.* **28**, 2181-2187 (1995).

11. C. Aragon, J. A. Aguilera, F. Penalba, “Improvements in Quantitative Analysis of Steel Composition by Laser-Induced Breakdown Spectroscopy at Atmospheric Pressure Using an Infrared Nd:YAG Laser,” *Appl. Spectrosc.* **53**, 1259-1267 (1999).

12. I. Bassiotis, A. Diamantopoulou, A. Giannoudakos, F. R. Kalantzopoulou, M. Kompitsas, “Effects of experimental parameters in quantitative analysis of steel alloy by laser-induced breakdown spectroscopy,” *Spectrochim. Acta B* **56**, 671-683 (2001).

13. J. D. Winefordner, I. B. Gornushkin, T. Correll, E. Gibb, B. W. Smith and N. Omenetto, “Comparing several atomic spectrometric methods to the super stars: special emphasis on laser induced breakdown spectrometry, LIBS, a future super star,” *J. Anal. At. Spectrom* **19**, 1061-1083 (2004).

14. B. Salle, D. Cremers, S. Maurice, R. Wiens, P. Fichet, “Evaluation of a compact spectrograph for in-situ and stand-off Laser-Induced Breakdown Spectroscopy analyses of geological samples on Mars missions,” *Spectrochim. Acta B* **60**, 805-815 (2005).

15. G. Cristoforetti, S. Legnaioli, V. Palledchi, A. Salvetti, E. Tognoni, P. A. Benedetti, F. Brioschi, F. Ferrario, “Quantitative analysis of aluminium alloys by low-energy, high-

Repetition rate laser-induced breakdown spectroscopy,” *J. Anal. At. Spectrom.* **21**, 697-702 (2006).

16. G.P. Gupta, B.M. Suri, A. Verma, M. Sunderaraman, V.K. Unnikrishnan, K. Alti, V.B. Kartha, C. Santhosh, “Quantitative elemental analysis of nickel alloys using calibration-based laser-induced breakdown spectroscopy,” *J. Alloys and Comp.* **509**, 3740-3745 (2011).

17. A. Ciucci, M. Corsi, V. Palleschi, S. Rastelli, A. Salvetti, E. Tognoni, “New Procedure for Quantitative Elemental Analysis by Laser-Induced Plasma Spectroscopy,” *Appl. Spectrosc.* **53**, 960-964 (1999).

18. E. Tognoni, G. Cristoforetti, S. Legnaioli, V. Palleschi, A. Salvetti, M. Mueller, U. Panne, Gornushkin, “A numerical study of expected accuracy and precision in calibration-free Laser-Induced Breakdown Spectroscopy in the assumption of ideal analytical plasma,” *Spectrochim. Acta B* **62**, 1287-1302 (2007).

19. K. K. Herrera, E. Tognoni, N. Omenetto, Y. B. Gornushkin, B. W. Smith, J. D. Winefordner, “Comparative study of two standard-free approaches in laser-induced breakdown spectroscopy as applied to the quantitative analysis of aluminium alloy standards under vacuum conditions,” *J. Anal. At. Spectrom.* **24**, 426-438 (2009).

20. K. K. Herrera, E. Tognoni, N. Omenetto, B. W. Smith, J. D. Winefordner, “Semi-quantitative analysis of metal alloys, brass and soil samples by calibration-free laser-induced breakdown spectroscopy: recent results and considerations,” *J. Anal. At. Spectrom.* **24**, 413-425 (2009).

21. D. Bullajic, M. Corsi, G. Cristoforetti, S. Legnaioli, V. Palleschi, A. Salvetti, E. Tognoni, "A procedure for correcting self-absorption in calibration-free laser-induced breakdown spectroscopy," *Spectrochim. Acta B* **57**, 339-353 (2002).
22. V. S. Burakov, V. V. Kiris, P. A. Naumenkov, S. N. Raikov, "Calibration-free laser spectral analysis of glasses and copper alloys," *J. Appl. Spectrosc.* **71**, 740-746 (2004).
23. F. Colao, R. Fantoni, V. Lazic, I. Caneve, A. Giardini, V. Spizzichino, "LIBS as a diagnostic tool during the laser cleaning of copper based alloys: experimental results," *J. Anal. At. Spectrom.* **19**, 502-504 (2004).
24. I. Fornarini, F. Colao, R. Fantoni, V. Lazic, V. Spizzichino, "Calibration analysis of bronze samples by nanosecond laser induced breakdown spectroscopy: A theoretical and experimental approach," *Spectrochim. Acta B* **60**, 1186-1201 (2005).
25. V. S. Burakov, S. N. Raikov, "Quantitative analysis of alloys and glasses by a calibration-free method using laser-induced breakdown spectroscopy," *Spectrochim. Acta B* **62**, 217- 223 (2007).
26. J. A. Aguilera, C. Aragon, G. Cristoforetti, E. Tognoni, , "Application of calibration-free laser-induced breakdown spectroscopy to radially resolved spectra from copper-based alloy laser-induced plasma," *Spectrochim. Acta B* **64**, 685-689 (2009).
27. M. V. Belkov, V. S. Burakov, V. V. Kiris, N. M. Kozhukh, S. N. Raikov, "Spectral standard-free laser micro analysis of gold alloys," *J. Appl. Spectrosc.* **72**, 376-381 (2005).
28. F. Colao, R. Fantoni, V. Lazic, A. Paolini, F. Fabbri, G. G. Ori, L. Marinangeli, A. Baliva, "Investigation of LIBS feasibility for in situ planetary exploration: an analysis on Martian rock analogues," *Planet. Space Sci.* **52**, 117-123 (2004).

29. B. Salle, J. I. Lacour, P. Mauchien, P. Fichet, S. Maurice, G. Manhes, "Comparative study of different methodologies for quantitative rock analysis by Laser-Induced Breakdown Spectroscopy in a simulated Martian atmosphere," *Spectrochim. Acta B* **61**, 301-313 (2006).
30. A. De Giacomo, M. Dell'Aglia, O. De Pascale, S. Longo, M. Capitelli, "Laser induced breakdown spectroscopy on meteorites," *Spectrochim. Acta B* **62**, 1606-1611 (2007).
31. M. Corsi, G. Cristoforetti, M. Hidalgo, S. Legnaioli, V. Palleschi, A. Salvetti, E. Tognoni, C. Vallebona, "Application of laser-induced breakdown spectroscopy technique to hair tissue mineral analysis," *Appl. Opt.* **42**, 6133-6137 (2003).
32. S. Pandhija, A. K. Rai, "In situ multielemental monitoring in coral skeleton by CF-LIBS," *Appl. Phys. B* **94**, 545-552 (2009).
33. S. Pandhija, N. K. Rai, S. N. Thakur, "Containment concentration in environmental samples using LIBS and CF-LIBS," *Appl. Phys. B* **98**, 231-241 (2010).
34. E. Tognoni, G. Cristoforetti, S. Legnaioli, V. Palleschi, "Calibration-free laser-induced breakdown spectroscopy: state of the art," *Spectrochim. Acta B* **65**, 1-14 (2010)
35. D. W. Hahn, N. Omenetto, "Laser-induced breakdown spectroscopy (LIBS), Part I: Review of basic diagnostics and plasma-particle interactions: Still-challenging issue within the analytical plasma community," *Appl. Spectrosc.* **64**, 335A-366A (2010).
36. J.M. Gomba, C.D' Angelo, D. Bertuccelli, G. Bertuccelli, "Spectroscopic characterization of laser induced breakdown in aluminium-lithium alloy samples for quantitative determination of traces," *Spectrochim. Acta B* **56**, 695-705 (2001).

37. C. M. Davies, H. H. Telle, D. J. Montgomery, R. E. Cobert, "Quantitative Analysis using remote laser-induced breakdown spectroscopy (LIBS)," *Spectrochim. Acta B* **50**, 1059-1075(1995).
38. J. A. Aguilera, C. Aragon, F. Penalba , "Plasma shielding effect in laser ablation of metallic samples and its influence in LIBS analysis," *Applied Surface Sci.* **127**, 309-314 (1998).
39. S. Palanco, J.J. Laserna., "Full automation of a laser-induced breakdown spectrometer for quality assessment in the steel industry with sample handling, surface preparing and quantitaive analysis capabilities," *J. Anal. At. Spectrom.* **15**, 1321-1327 (2000).
40. M. A. Ismail, H. Imam, A. Elhassan, H. Imran, A. Elhassan, W. T. Youniss, M A. Harith, "LIBS limit of detection and plasma parameter of some elements in two different metallic matrices," *J. Anal. At. Spectrom.* **19**, 489-494 (2004).
41. C. Lopez-Moreno, K. Amponsah-Manager, B. W. Smith, I. B. Gornushkin, N. Omenetto, S. Palanco, J.J. Laserna, J. D. Winefordner, "Quantitative analysis of low-alloy steel by microchip laser induced breakdown spectroscopy," *J. Anal. At. Spectrom.* **20**, 552-556 (2005).
42. J. Vrenegor, R. Noll, V. Sturm, "Investigation of matrix effects in laser-induced breakdown spectroscopy plasmas of high-alloy steel for matrix and minor elements," *Spectrochim. Acta B* **60**, 1083-1091 (2005).
43. R. Noll, "Terms and notations for laser-induced breakdown spectroscopy," *Anal. Bioanal. Chem.* **385**, 214-218 (2006).
44. H. R. Griem, *Principles of Plasma Spectroscopy* (Cambridge University Press, Cambridge, 1997).

45. R. W. P. McWhirter, in Plasma Diagnostic Techniques, R. H. Huddleston and S. L. Leonard, Eds., Chap. 5, pp. 201-264 (Academic press, New york, 1965).
46. G. Cristoforetti, A. D. Giacomo, M. Dell’Aglia, S. Legnaioli, E. Tognoni, V. Palleschi, N. Omenetto, “Local thermodynamic equilibrium in laser-induced breakdown spectroscopy: beyond the Mcwhirter criterion,” Spectrochim. Acta B **65**, 86-95 (2010).
47. R. Wester, R. Noll, “Heuristic modeling of spectral plasma emission for laser-induced breakdown spectroscopy,” J. Appl. Phys. **106**, 123302 1-123302 10 (2009).
49. U. Aydin, P. Roth, C. D. Gehlen, R. Noll, “Spectral line selection for time-resolved Investigation of laser-induced plasmas by an iterative Boltzman plot method,” Spectrochim. Acta B **63**, 1060-1065 (2008).
49. NIST Atomic Spectra Database, <http://physics.nist.gov>.
50. T. R. O’Brian, M. E. Wickliffe, J. E. Lawler, W. Whaling, J. W. Brault, “Lifetimes, transition probabilities and level energies in Fe I,” J. Opt. Soc. Am B **8**, 1185-1201 (1991).